An *in-situ* analytical scanning and transmission electron microscopy investigation of structure-property relationships in electronic materials

A DISSERTATION
SUBMITTED TO THE FACULTY OF THE GRADUATE SCHOOL
OF THE UNIVERSITY OF MINNESOTA
BY

Andrew James Wagner

IN PARTIAL FULFILLMENT OF THE REQUIREMENTS
FOR THE DEGREE OF
DOCTOR OF PHILOSOPHY

Advisors: K. Andre Mkhoyan and Uwe R. Kortshagen

August, 2014

© Andrew James Wagner 2014
ALL RIGHTS RESERVED

Acknowledgements

I would like to thank my advisors, Professors K. Andre Mkhoyan and Uwe Kortshagen, for the opportunity to work in their labs and for affording me the freedom to pursue projects of such wildly varying focus. Being amongst Andre's first students, he has maintained an active and encouraging presence in our work while pushing us to go beyond our own expectations. While always expecting more from us, it was not unusual for him to show up in the lab in the evening and invite us out for a beer after a long days work. Professor Kortshagen and the lab have offered a bottomless depth of knowledge of the plasma sciences and nanoparticle synthesis. It has been a great pleasure to work under his guidance and alongside such great researchers as Zachary Holman, Rebecca Anthony, Federico Galli, Richard Liptak, Lance Wheeler, Jason Trask, Lin Cui, Nicolaas Kramer, and many others. All were instrumental in my accomplishments in the lab and I must also thank Fede for the many beers and delicious late-night pasta.

I appreciate the contributions of my committee to the final steps to my PhD. Professor William Gerberich has been an unofficial third advisor. I have enjoyed our interactions and appreciated his wisdom and mastery of mechanical properties. I thank Professor Michael Tsapatsis for finding the time to sit on my committee during a particularly busy couple of months and for presenting me with a particularly challenging project as I have one foot out the door. I thank Professor Stephen Campbell for sitting as external committee member, reader, and chair.

Dr. Aloysius Gunawan and Dr. Anudha Mittal joined me as Andres first students. We created an electron microscopy preparation lab out of an equipment graveyard. Al demonstrated a work ethic, discipline and determination to be admired. He mastered skills quickly and with authority, providing me in the first years with an essential resource. And I should not forget that his same discipline in the gym motivated me in

part to get back in shape while finding a much-needed refuge from the lab for an hour or two each night. Anudha Millie Mittal was ever the optimist when it came to the work of others. I am grateful for her confidence in my work and for putting up with my antics in the lab. Michael Odlyzko has been with us most of the way as well. Sharing my obsession with caffeination and good beer, we have had our fair share of lengthy conversations in and out of the lab. Dr. Jong Seok Jeong joined our group three years ago. His focus, efficiency, and mastery of the art of microscopy are something to be admired. I owe a great debt to Dr. Douglas Stauffer for introducing me to mechanical properties and working with me on *in-situ* experiments. Eric Hinstala has joined me for countless hours on the microscope as we navigated the PicoIndenter, crushing countless nano-things and complementing my microscopy with his knowledge of mechanical properties. Prashant Kumar, just beginning his third year, has provided a great deal of insight and critical analysis of my recent work. He has a bright future ahead. I worked alongside Rahool Gadkari for two years as he completed a Masters degree. We worked on a difficult project and made great progress while becoming good friends. Ryan Wu, Claire Teresi, Pranav Suri, and Jacob Held are younger students whose curiosity has challenged and grown my knowledge and ability to teach.

I owe countless thanks to those who guided my path toward graduate school. While interning at Micron Technology (Boise, ID) my mentor Michel Koopmans and supervisor Bill Polinsky, not to mention the fantastic engineers and operators alongside whom I worked, gave me more responsibility and encouragement than any sophomore deserved. While working as a research assistant at North Dakota State University in my home town of Fargo, ND Rob Sailer, Dr. Douglas Schulz, and Chris Braun likewise guided me through a challenging and rewarding experience. They introduced me to atmospheric plasma processing and its application to materials science while treating me to some unforgettable post-work entertainment.

My senior year I had the great fortune of meeting Professor Davide Mariotti, a visiting professor at RIT whose expertise happened to be atmospheric plasmas. For the next year I worked with Davide on my senior design and continuing research, growing a body of knowledge on plasma physics and diagnostics while designing and testing my own atmospheric microplasma reactor. His confidence in my abilities made possible much of what I have since accomplished.

Last and certainly not least I thank my family for supporting me through the entirety of my education. My mother supported four children through college with more than she needed to. My grandmother has maintained an unbreakable optimism in all of her children and grandchildren and we have all taken great comfort in her support. My aunts, uncles, and cousins have likewise been greatly supportive, even bringing me food following a pre-qualifying exams bout with appendicitis. I thank Sarah for tolerating and even supporting my long and irregular schedule for the last three and a half years all while she worked her way through medical school.

Dedication

To my mother, who raised four children to work hard and helped put us all through way too much school.

Abstract

As electronic and mechanical devices are scaled downward in size and upward in complexity, macroscopic principles no longer apply. Synthesis of three-dimensionally confined structures exhibit quantum confinement effects allowing, for example, silicon nanoparticles to luminesce. The reduction in size of classically brittle materials reveals a ductile-to-brittle transition. Such a transition, attributed to a reduction in defects, increases elasticity. In the case of silicon, elastic deformation can improve electronic carrier mobility by over 50%, a vital attribute of modern integrated circuits. The scalability of such principles and the changing atomistic processes which contribute to them presents a vitally important field of research.

Beginning with the direct observation of dislocations and lattice planes in the 1950s, the transmission electron microscope has been a powerful tool in materials science. More recently, as nanoscale technologies have proliferated modern life, their unique ability to spatially resolve nano- and atomic-scale structures has become a critical component of materials research and characterization. Signals produced by an incident beam of high-energy electrons enables researchers to both image and chemically analyze materials at the atomic scale. Coherently and elastically-scattered electrons can be collected to produce atomic-scale images of a crystalline sample. New specimen stages have enabled routine investigation of samples heated up to 1000 °C and cooled to liquid nitrogen temperatures. MEMS-based transducers allow for sub-nm scale mechanical testing and ultrathin membranes allow study of liquids and gases. Investigation of a myriad of previously "unseeable" processes can now be observed within the TEM, and sometimes something new is found within the old.

High-temperature annealing of pure a-Si:H films leads to crystallization of the film. Such films provide higher carrier mobility compared to amorphous films, offering improved photovoltaic performance. The annealing process, however, requires exceptionally high temperature (>600 °C) and time (tens of hours), limiting throughput and costing energy. In an effort to fabricate polycrystalline solar cells at lower cost, large ($\tilde{3}0$ nm) silicon nanocrystals were incorporated into hydrogenated amorphous silicon (a-Si:H) thin films. When annealed, the embedded nanocrystals were expected to act as

heterogeneous nucleation sites and crystallize the surrounding amorphous matrix. When observed in the TEM, an additional and unexpected event was observed. At the boundary between the nanocrystal and amorphous matrix, nanocavities were observed to form. Continued annealing resulted in movement of the cavities away from the nanocrystal while leaving behind a crystalline tail. The origins and fundamental mechanisms of this phenomenon were examined by *in-situ* heating TEM and *ex-situ* crystallographic TEM techniques. We demonstrate a mechanism of solid-phase crystallization (SPC) enabled by nanoscale cavities formed at the interface between an hydrogenated amorphous silicon film and embedded 30 nm to 40 nm Si nanocrystals. The nanocavities, 10 nm to 25 nm across, have the unique property of an internal surface that is part amorphous and part crystalline, enabling capillarity-driven diffusion from the amorphous to the crystalline domain. The nanocavities propagate rapidly through the amorphous phase, up to five times faster than the SPC growth rate, while pulling behind a crystalline tail. It is shown that twin boundaries exposed on the crystalline surface accelerate crystal growth and influence the direction of nanocavity propagation.

The mechanical properties and mechanisms of plasticity in these same silicon nanocubes have also been investigated. The strain-dependent mechanical properties and the underlying mechanisms governing the elastic-plastic response are explored in detail. Elastic strains approaching 7% and flow stresses of 11 GPa were observed, significantly higher than that observed in other nanoscale volumes of Si. *In-situ* imaging revealed the formation of 5 nm dislocation embryos at 7% strain, giving way at 20% strain to continuous nucleation of leading partial dislocations with {111}-habit at the embryo surface.

Contents

Acknowledgements **i**

Dedication **iv**

Abstract **v**

List of Tables **xi**

List of Figures **xii**

1 Introduction **1**

2 Methods **4**

2.1 The transmission electron microscope 4

2.2 Conventional transmission electron microscopy 5

2.2.1 Illumination system of a TEM 6

2.2.2 Imaging system of a TEM 6

2.2.3 Aberrations 7

2.2.4 The contrast transfer function 12

2.2.5 Bright-Field TEM 13

2.2.6 Diffraction in CTEM 14

2.2.7 Dark-Field TEM 15

2.2.8 Dislocation imaging 15

2.3 Scanning transmission electron microscopy 16

2.3.1 Imaging with STEM 16

2.3.2 Bright-Field STEM 17
2.3.3 Annular dark-field STEM 18
2.4 Spectroscopy in the (S)TEM 19
2.4.1 Electron energy-loss spectroscopy 19
2.4.2 Energy-dispersive X-ray spectroscopy 24
2.5 Aberration-corrected TEM 24
2.6 *In-situ* heating 24
2.7 *In-situ* mechanical testing 26
2.8 Specimen preparation techniques 27
2.8.1 Drop-casting 28
2.8.2 Direct deposition of nanoparticles and thin films 28
2.8.3 Mechanical wedge polishing 29
2.8.4 Small-angle cleaving technique 30
2.8.5 Focused-ion beam 32
2.8.6 Ion milling 35
2.8.7 Specimen Contamination 37
2.9 Electron microscopes at University of Minnesota 39
2.9.1 FEI Tecnai G2 T12 (S)TEM 39
2.9.2 FEI Tecnai G2 F30 (S)TEM 39
2.9.3 FEI Tecnai G2 F30 Cryo (S)TEM 39
2.9.4 FEI Titan G2 60-300 (S)TEM 40
2.9.5 FEI Quanta 200 3D dual-beam FIB 42
2.9.6 Jeol 6500 and 6700 FEG SEMs 42
2.10 Si NC synthesis 42

3 Nanocavity-enhanced crystallization of silicon **46**
3.1 Introduction 46
3.2 Background 49
3.2.1 Solid-Phase Crystallization 49
3.2.2 The role of hydrogen in solid-phase crystallization of silicon . . . 50
3.2.3 Anisotropic SPC 52
3.3 Methods 53

3.3.1 Layer-by-layer Deposition 53
3.3.2 Specimen Preparation 57
3.3.3 *In-situ* Heated-Stage TEM 58
3.3.4 *Ex-situ* TEM 60
3.3.5 Raman Spectroscopy 60
3.4 Results and discussion 61
3.4.1 Origin of Propagating Nanocavities 61
3.4.2 Surface diffusion along the curved nanocavity surface 64
3.4.3 Twinning and identification of twinned crystals by transmission electron microscopy 67
3.4.4 The {113} surface 71
3.4.5 Twin-mediated growth 73
3.4.6 Size and temperature dependence of nanocavity propagation . . 75
3.4.7 Nanocavity propagation kinetics 79
3.4.8 Predicting thin film crystallization rates 81
3.5 Conclusion 83
3.6 Future Directions 84

4 Mechanical Properties of Si Nanocrystals 86
4.1 Introduction 86
4.2 Methods 91
4.2.1 Substrate preparation. 91
4.2.2 Si NC synthesis. 92
4.2.3 Preparation for *in-situ* experiments 92
4.2.4 *In-Situ* Compression. 93
4.2.5 Calculation of True Stress and True Strain 93
4.3 Results and discussion 95
4.3.1 Mechanical properties of Si Nanocubes 95
4.3.2 Investigating the mechanisms of plasticity in Si nanocubes 105
4.3.3 *In-situ* and *post-mortem* analysis of plasticity 107
4.3.4 The role of back stress in small volume strengths 120
4.3.5 Indenter Stability 126

4.4 Conclusion 128
4.5 Future Directions 128

5 Changes in electronic structure of strontium titanate under uniaxial compression 130

5.1 Introduction and Background 130
5.2 EELS fine structure of STO 132
5.3 STO nanopillar fabrication 134
5.4 Combined nanopillar STEM-EELS and compression 138
5.5 Discussion and Future Directions 138

References 142

A Acronyms 165

B Simulation of screw dislocations and stacking faults 167

List of Tables

3.1 Parameters for a-Si:H deposition and Si nanocrystal synthesis. 56

3.2 Diffusivity data for the amorphous Si surface. 67

4.1 Mechanical properties for oxide-free and oxide-coated Si nanocubes. . . 104

List of Figures

2.1 (a) Ray diagram of the illumination system of an (S)TEM operating in imaging mode [1]. (b) Image of one of two FEI Tecnai F30 in the Characterization Facility of the University of Minnesota. 7

2.2 Ray diagrams of the imaging systme in CTEM operation (a) in diffraction and (b) bright-field imaging modes. In both cases, the paths of electron beams are the same before the intermediate lens. In diffraction mode, the intermediate lens uses the back focal plane of the objective lens as the object while imaging mode uses the image plane of the objective lens [1]. 8

2.3 (a) High-resolution CTEM image of epitaxial growth of 50 nm Si-doped InAs on 3 nm intrinsic InAs on GaSb viewed along the [110] zone axis and (b) a corresponding SAD pattern. GaSb and InAs are both zinc blende structures with lattice constants of 6.10 Å and 6.06 Å, respectively. . . . 9

2.4 (a) Ray diagram demonstrating distorted wave fronts and bending rays near the lens edge more than those near the axis. The minimum image size is then defined by the disc of least confusion. (b) Ray diagram demonstrating chromatic aberration due dependent on incident electron energy. 10

2.5 The effects of spherical aberration on the focusing of electrons (a) in real space and (b) in reciprocal space. In real space, spherical aberration focuses electrons farther from the optic axis more strongly than those passing through the lens center. In reciprocal space, spherical aberration causes a radial phase shift of a plane wave entering the lens. 12

2.6 Contrast transfer function representative of a Tecnai F30 with $C_s = 1.2$ mm operating at 300 keV with defocus of (a) 600 Å and (b) 1000 Å [2]. . . . 13

2.7 (a) Ray diagram of (S)TEM operating as a scanning transmission electron microscope [1] and (b) image of the UofM Characterization Facility's FEI Titan 60-300. (c) Schematic of the probe scan coils of a STEM. Deflections of the electron beam by the first scan coil are returned to the optic axis through the front focal plane of the final condensor lens with an angle that determines displacement of the focused beam without tilting the it as it is rastered across the specimen [1]. 17
2.8 Comparison of the contrast transfer function for ADF-STEM and BF-CTEM for the same spherical aberration and accelerating voltage. While the BF-CTEM CTF begins to oscillate rapidly about 0 at moderate frequencies, the ADF-STEM CTF remains positive while gradually approaching zero. Reproduced from Kirkland [3]. 18
2.9 FTIR of 10%nom. B-doped Si nanocrystals as produced, after annealing, after oxidation, and after HF-vapor etching. Oxidation and annealing lead to a plasmon resonance peaked around 1700 cm^{-1}. Courtesy Nicolaas Kramer. 21
2.10 STEM-EELS of fresh and aged 10%nom. B-doped Si nanocrystals. (a) Survey image of a chain of Si nanocrystals extending off carbon grid over vacuum. (b) Sub-pixel-scanned ADF-STEM image during spectrum imaging. (c) High-loss spectrum image. (d) Background-subtracted Si $L_{2,3}$ and B K edges of fresh and aged nanocrystals. (e) The B K edges of fresh particles and particles aged for two days with comparison of core and edge of particle. A red-shift in edge onset from 187.2 eV to 180.2 eV is observed in conjunction with the plasmon resonance in FTIR. Particles were synthesized by Nicolaas Kramer and Katelyn Schramke. 23
2.11 (a) Image of Hysitron PI95 PicoIndenter and closeup of the sample region. (b) Diagram and image of the MEMS transducer design. (c) Schematic of the four capacitive comb devices. Adapted from Oh *et al* [4]. 26
2.12 (a) Schematic of an ideal wedge after wedge-polishing and (b) optical micrograph of the thin edge of a Si wedge. 29

2.13 (a) Low-magnification ADF-STEM image of the thin tip of a SACT-cleaved Al_2O_3-back-filled ZnO nanoparticle film on Si. (b) High-magnification ADF-STEM image of ZnO particles in Al_2O_3 matrix. (c) EDX maps of Zn and Al from the SACT specimen [5]. 31
2.14 TEM specimen prepared by FIB. (a) Lift-out of a lamella using an Omniprobe and (b) conventional TEM-BF image of the specimen [6]. 33
2.15 STEM analysis of the recovered products. (A) TEM-BF image, (B) STEM-ADF image and (C-F) corresponding STEM-EDX maps(C) Mg K, (D) Si K, (E) Fe K, and (F) O Kare presented. STEM-ADF and EDX maps were obtained simultaneously. (G-J) SAED patterns and (K-N) EDX spectra were also obtained from the positions indicated in (A) [6]. 34
2.16 (a) Schematic of an ion-beam thinning machine. Argon gas enters two ionization chambers where ion beams are accelerated towards the specimen in equal and opposite direction. The specimen is tilted for low-angle impingement [1]. (b) The Fischione 1010 ion mill in the UMN Characterization Facility. 36
2.17 (a) ADF-STEM image of an InAs/GaSb FIB lamella created with 30 keV Ga^+ ions and (b) the same lamella after thinning and polishing with 1.5 keV Ar ions. 36
2.18 (a) Image of the high-vacuum heating system. A custom Leybold BMH70 pumping station has been modified to send an output to a temperature controller. Signal setpoint is based on set pressure, delay time, and heater on time. (b)-(d) IImages of the disassembled vacuum system displaying the tungsten filament and sample carrier. Filament sits above sample which is inserted on carrier via dovetail. 38

2.19 (a) Unfiltered HAADF-STEM image of InAs grown on GaSb, acquired at 200 keV with 50 pA probe current, 12 µs dwell time, 23 mrad convergence angle, and 54 mrad inner acceptance angle. (c) The same image Fourier-filtered to remove information below 0.8 Å. The reduced intensity at the interface, plotted as a horizontally averaged line scan on the inset right, suggests an interface comprised of the lighter elements Ga and As. (c) STEM-EDX line scan created from a spectrum image and averaged along the (100) plane. The oscillations in the line scan correlate with the respective atomic position. The mismatch in Ga:Sb ratio suggests improper k-factors for quantization. The relative increase of Ga and As across the interface correlate with the reduced intensity observed in the HAADF-STEM image. (d) The FFT of the HAADF-STEM image demonstrating image resolution of 0.9 Å. 43
2.20 (a) Schematic of NC plasma reactor. (b) Still-frame images of plasma, adopted in part from [7]. 44
2.21 (a) ADF-STEM and (b) HR-TEM images of cubic Si nanocrystals. (c) ADF-STEM image of cuboctahedral Si nanocrystals. (d) Normalized size distribution of cubic and cuboctahedral Si nanocrystals as measured by ADF-STEM. 45
3.1 (a) Schematic of Si nanocrystals in the a-Si:H film. A 20 nm bottom layer of a-S:H is deposited followed by deposition of Si nanocrystals. A 100 nm top layer of a-Si:H embeds the nanocrystals in a continuous film. (b) A plan-view TEM image of the nanocrystals embedded in film. The particles, about 30 nm across are surrounding by a larger ring of contrast in part due to the conformal deposition on top of the nanocrystals. (c) A higher-magnification TEM image of an embedded nanocrystal. 47
3.2 *In-situ* TEM image series of seeded a-Si:H film while annealing. (a) As-deposited 120 nm a-Si:H films containing rounded Si nanocrystals. (b) Elongated cavities form near the seed while ramping to 640 °C in 15 minutes. (c) The cavities become rounded within a few minutes at the soak temperature and (d) begin moving away from the nanocrystal at a rate of 1-15 nm min^{-1} leaving behind tails of crystalline Si. 48

3.3 (a,b) Kink-like steps at the edge of a (111) terrace and (c) a reconstructed (100) surface comprised of {111} terraces terminated by $[1\bar{1}0]$ ledges. Reproduced from Spinella [8] and Williams and Elliman [9]. 50
3.4 (a) Schematic of attachment on the (110) and (111) surfaces demonstrating how 3-atom nucleation events can occur in two orientations on the (111) surface, denoted N and T. (b) Schematic of a re-entrant twin edge. Two-atom nucleation events across the boundary which expand by single-atom attachment. From Drosd and Washburn [10]. 52
3.5 Solid-phase crystallization in thin film a-Si is anistropic due to fast- and slow-growth surfaces. (a,b) Crystallites with a $\langle 112 \rangle$ direction in plane but whose {111} planes are inclined exhibit elongated, rod-like growth. (c,d) Crystallites that possess {111} planes in the film plane exhibit fast, isotropic growth. From Spinella *et al* [8]. 53
3.6 (a) Dual-plasma reactor for layer-by-layer deposition of a-Si:H with embedded Si nanocrystals. Separate plasma reactors allow independent control of a-Si:H deposition and nanocrystals synthesis. (b) Seeded a-Si:H films are grown layer-by-layer. A bottom layer of a-Si:H is deposited, followed by nanocrystal deposition, which are then embedded in a continuous film by additional a-Si:H deposition. 54
3.7 Picture of a-Si:H film deposition reactor 55
3.8 (a) Plan-view TEM image of a Si nanocube embedded in a 120 nm a-Si:H film. (b,c) Cross-section TEM images of embedded Si nanocrystals in a-Si:H. A parabolic porous region extends from near the base of each nanocrystal towards the a-Si:H surface. (d,e) Cross-section SEM images of as-deposited film. In (d) the material within the parabolic region remains after cleaving. In (e) the material within the parabolic region was removed by cleaving. Scale bars are (a) 25 nm and (b-e) 50 nm. . . 56

3.9 Liftout-free FIB lamella preparation process for cross-section TEM analysis. (a) A Si mesa mounted to a TEM grid. (b) SEM top-view image of a seeded a-Si:H film on Si mesa. The raised surface is bordered by the mesa sidewalls which appear bright. Scale bar is 50 μm (c) Schematic of lamella formation. A protective Pt layer was deposited over the region of interest prior to FIB cutting. (d) Optical images of lamellae and corresponding low-magnification TEM image of a single lamella. 59
3.10 TEM image series of a 120 nm a-Si:H film with embedded cubic Si nanocrystals annealed at 625 °C. The nanocrystals act as heterogeneous nucleation sites. No other nucleation was observed to occur. Images acquired at (a) 0 hours, (b) 1 hour, and (c) 2 hours. Scale bar is 1 μm. Images courtesy Curtis Anderson [11] 61
3.11 Crystal fraction with respect to annealing time at 650 °Cfor a-Si:H films of varying seed concentration. Inclusion of seeds reduces τ_0 and τ_c by more than half. Courtesy Jason Trask [12]. 62
3.12 (a,d) HAADF-STEM images of a 31 nm cubic nanocrystal (a) and a 39 nm cuboctahedral nanocrystal (d). (b,e) Cross-section TEM images of a-Si:H films with embedded cubic and a cuboctahedral nanocrystal seeds, respectively. A parabolic porous region extends from the base of the nanocrystal seeds towards the a Si:H surface which forms due to shadowing of the top layer deposition. Cuboctahedral seeds (e) have a more significant porosity at their bases which develop into nanocavities up to a few tens of nm in size upon annealing. The seeds lack well-defined boundaries due to epitaxy during deposition of the top a-Si:H layer. (c,f) Drawings of the porous region surrounding the embedded nanocrystals. Scale bars are 20 nm. 63
3.13 A kinetic Monte Carlo simulation of isotropic deposition and surface diffusion. (a)-(d) Cross-sections of increasing depth with the nanocube, red, in center. A thin paraboloid of voids are incorporated into a growing film beginning at the nanocube base and extending outward and upward to the surface. 64

3.14 (a) BF-STEM and (b) ADF-STEM images of a seeded film containing crystalline tails. The tip of the crystalline tail appears dark in the ADF-STEM image. The reduced intensity of this region confirms voided nature of the cavity as the film is otherwise uniform in thickness and composition. 65

3.15 Film composition by (a) ADF-STEM, (b) STEM-EDX and (c) STEM-EELS of a nanocavity in an a-Si:H film. The EDX spectrum recorded from region indicated in (a) and EEL spectrum obtained from a similar location suggest only Si is present. Scale bar is 10 nm. 65

3.16 Heated-stage TEM image series of a propagating nanocavity heated to 640 °C. Each frame is roughly two minutes apart. The nanocavity shape is highly dynamic while maintaining overall volume. The propagation of the nanocavity is seen to be linear over length scales of 100 nm or more suggesting oriented growth. Scale bar is 100 nm. 68

3.17 (a) High-resolution TEM image of a nanocavity along its [011] zone axis. Two $\Sigma3\{111\}$ twin boundaries, indicated by yellow arrows, terminate at the rear of the nanocavity. The crystalline surface contains $\{111\}_{M,T}$ and $\{113\}_T$ facets. (b,c) Schematics of a crystalline surface containing one twin. Diffusion of surface atoms across the free energy landscape ends in attachment and growth of the crystalline surface, accelerated by preferential nucleation sites along the exposed twin boundary. Scale bar is 10 nm. 69

3.18 (a) A partial stereogram for a-Si crystal and its first order twins centered on the [112] zone axis. Each dotted circle represents 15° of rotation away from the [112] zone axis. (b) Co-linear zone axes of a host crystal and its first-order twins listed with the rotation angle α relative to the host crystal. 70

3.19 (a) A selected area diffraction pattern of [110] Si with contrast inverted for clarity. (b) A schematic SADP for a crystal twinned on the $\{\bar{1}1\bar{1}\}$ plane. (c) The resulting SADP for twinning on both visible {111} planes. Adapted from [13]. 72

3.20 Schematic comparing the crystalline surface composed of (a),(c) only {111} surfaces and (b),(d) {111} and {113} surfaces. The {113} surface provides high diffusivity compared to a {111}-terraced surface, promoting growth. 72

3.21 CBED patterns along the crystalline tail as marked in (a) the BF-TEM image with e-beam aligned along the seed crystals [110] zone axis. Changes in growth direction are outlined with ovals. (b)-(f) CBED patterns from the areas indicated by the yellow circles in (a) with outlines of identified zone axis patterns color corded to regions outlined in (a). (b) A first-order twin is present, visible as parallel bands in the TEM image. (c) A new first-order twin activates, coincident. (d) The blue pattern disappears while the green pattern remains. (e) The blue pattern reappears with growth. (f) The grain is oriented along a $\langle 114 \rangle$ zone axis suggesting the grain is rotated by first-order twinning. CBED patterns are inverted for clarity. (g) SAD pattern of the entire crystalline tail. Scale bars are 20 nm in (a) and 5 nm^{-1} in (b)-(g). 74

3.22 (a)-(c) SADPs along the $[011]_M$, $[101]_M$, and $[114]_M$ zone axes of a seed crystal. Growth along the first segment of the crystalline tail coincides with twinning on $(11\bar{1})_M$ planes. A change in growth direction coincides with twinning on $(111)_M$ planes. (d)-(f) BF-TEM images for the respective SADPs. (g) Outline of crystal grains. The black line surrounds the crystalline tail and seed, the red line surrounds a grain with twinning on $(11\bar{1})_M$ planes, and the green line surrounds a grain with twinning on $(111)_M$ planes. (h-j) DF-TEM images using 220-type reflections of the seed crystal (blue squares). (l)-(n) DF-TEM images using 220-type reflections of $(11\bar{1})_M$-twinned grains (green triangles). (q) DF-TEM images using 220-type reflection of $(111)_M$-twinned grains (green triangle). (k),(o) DF-TEM images using the 111-type reflections of $(111)_M$-twinned grains (magenta pentagon and teal hexagon). Scale bars are 5 nm^{-1} in (a)-(c) and 100 nm in (d)-(q). 76

3.23 Growth velocities for SPC along the fast and slow axes offset from 0 nm by $\pm$ 0.5 nm, respectively, and the propagation velocities for nanocavities of different size at 620 to 660 °C. 77
3.24 Plan-view BF-TEM image of embedded Si nanocrystal seeds in a-Si:H (a) as-deposited and (b) after annealing for 70 minutes at 640 °C. The nanocavity has propagated approximately 1 µm leaving behind it a crystalline tail. (c-e) A cartoon of the film evolution while annealing. A porous region near the base of the seed coalesces into tens-of-nm-sized nanocavities at elevated temperature. The cavity surface, part amorphous and part crystalline, promotes mass transfer from the amorphous to the crystalline domain. The receding amorphous surface and growing crystalline surface creates a crystalline tail as the nanocavity propagates through the film. Scale bar is 50 nm. 78
3.25 (a) A cartoon showing nanocavities of different size at an a/c interface. (b) After a period of time, the larger cavities, possessing greater twin boundary length, propagate faster leading to formation of crystalline tails. 80
3.26 Growth velocities, experimental uncertainties, and fits for propagation velocities for nanocavities of different size at 620 to 660 °C. 81
3.27 Extrapolation of nanocavity-accelerated crystallization. (a) Experimental crystallization curves for 100 nm thick a-Si:H films annealed at 650 °C. (b) Schematic of a Si nanocrystal embedded in a Si film and having a single nanocavity, modeled as sphere-like growth from the seed in addition to conical growth of the crystalline tail. (c) Calculated crystallization curves at 650 °C based on Equation 3.12. Experimental SPC growth velocity was used to model 100 nm and 1 μm thick films having a density 40 seeds μm^{-2} and 4 seeds μm^{-2}, respectively, and a growth ratio $r = 5$. 84

4.1 (a) Elastic limit, (b) yield stress, and (c) modulus versus critical length scale for nanoscale silicon structures. Reduction in size results in an increase in elastic limit from bulk, $\epsilon_{Si,bulk} = 0.01$; an increase in yield stress from bulk, $\sigma_{bulk} = 5.3$ GPa, towards the ideal strength, $\sigma_{th} = 16$ GPa [14]; and a reduction in modulus, $E_{bulk} = 160$ GPa. Derived from ▲ Gerberich *et al* [15], ⬢ Ostlund *et al* [14], ▼ Namazu *et al* [16], ◆ Tsuchiya *et al* [17], and ◀ Zhu *et al* [18]. 89
4.2 TEM images of {100} Si nanocubes oriented such that its (a) [110] direction and (b) [100] direction is along the beam direction. (c) Cartoon illustrating the truncated nature of the Si nanocubes. 92
4.3 True stress versus true strain curve as determined from instantaneous contact width (red) and using a fitted contact area (blue). The fit matches the experimental contact width and hence stress at high and low strains with only slight deviation in the region of the load drop. When contact width could not be measured the contact width was determined using Equation 4.4 and the instantaneous displacement as measured *in-situ*. 95
4.4 Representative true stress versus true strain curves for [001]-compressed nanocubes of varying size. Linear-elastic response was consistently observed to about 7±1% strain, followed by a deviation from ideal up to 20±3% with corresponding yield strengths of 7.3 ± 1.2 GPa and 11.2 ± 1.4 GPa, respectively. The upper yield point was followed by a load drop with measurable hardening beginning around 40% strain. 96
4.5 True stress versus true strain curves for [001]-compressed nanocubes of varying size. Hardening rates varied considerably amongst the compressed nanoparticles. 96
4.6 True stress versus true strain curves of a 38 nm particle whose $[0\bar{1}1]$ direction is oriented along the electron beam and whose slip planes are parallel to the beam direction, corresponding to the respective frames on the next page. 98

4.6 (contd.) *In-situ* TEM image series of a 38 nm particle whose $[0\bar{1}1]$ direction is oriented along the electron beam and whose slip planes are parallel to the beam direction, corresponding to the stress-strain curves on the preceding page. 99
4.7 *In-situ* TEM image series and true stress versus true strain curve of a 40 nm particle whose [100] direction is oriented along the electron beam and whose slip planes are inclined to the beam direction. 100
4.8 *In-situ* TEM image series and true stress versus true strain curve of a 39 nm $[0\bar{1}1]$-oriented particle, seen prior to compression in left frame with CBED pattern inset. (A) Symmetric strain contours are observed to extend from the compressed surfaces. (B) Irregular contrast near the compressed surfaces appears as the true stress-true strain relationship deviates from linear. (C) Sharp contrast bands on {111}-habit planes appears at the upper yield point. The bands multiply as strain increases, until (D) complex dislocation activity is observed beyond 40% strain. The *post-mortem* image, right, is seen with accompanied CBED pattern inset. The nanocube stuck to the indenter, limiting imaging however the CBED pattern shows slight grain rotation, most clearly seen in the 220 reflections. 101
4.9 Strain limits versus nanocube size demonstrating a large elastic strains ϵ_{PEL} of 7% and strains at the upper yield point ϵ_{UYP} approaching 20%. No clear size effect is present. Solid symbols are oxide-free nanocubes while open symbols have a thin native oxide. 102
4.10 True stress versus nanocube size at transition from perfectly elastic to elastic-plastic σ_{PEL} and at the upper yield point σ_{UYP}. Contract stresses at σ_{PEL} approach 7 GPa and at σ_{UYP} exceed 11 GPa. Solid symbols are oxide-free nanocubes while open symbols have a thin native oxide. . . . 102
4.11 Measured modulus with respect to nanocube size during (black) loading and (red) unloading. Solid symbols are oxide-free nanocubes while open symbols have a thin native oxide. Bulk modulus for Si(100) $E_{Si(100)}$ is represented by the dashed line. 103

4.12 Repeat compression of a 45 nm Si nanocube plotted as (a) load-displacement and (b) true stress - true strain. Particle height was measured between compressions. The first compression was aborted upon observation of {111}-habit contrast. Subsequent compressions were terminated at a target displacement of 5 nm. 104
4.13 Thompson tetrahedron and schematic of slip planes in the Si nanocubes. (a) $[\bar{1}10]$ projection with [001] pointing down. (b) HR-TEM image of a 38 nm [110]-oriented nanocube. (c) View along the $[\bar{1}10]$ direction with the $(\bar{1}\bar{1}1)$ and (111) slip planes active and (d) the respective Thompson tetrahedron defining slip planes and slip directions with Greek letters indicating each slip plane. (e) View along the [110] direction with the (111) slip plane highlighted and (d) its Thompson tetrahedron. The directions with highest Schmid factors highlighted by dashed red line. . 106
4.14 Schematic of dislocation half loops on {111} slip planes. A half loop nucleating on the compressed surface grows across the slip plane and terminates at the free corner of the truncated cube. The limited resolved lateral shear stress may prevent the screw segments of a perfect dislocation from leaving the crystal. Alternatively, a partial dislocation loop, being predominantly straight as preferred in high Peierls barrier systems, may grow across the entire crystal, leaving behind a stacking fault. . . . 107
4.15 *In-situ* TEM image series and true stress versus true strain curve of a 45 nm particle whose [110] direction is oriented along the electron beam and whose slip planes are inclined to the beam direction. A 5 nm embryo forms at the upper contact surface at 8 s, marked by red brace, as the stress-strain curve deviates from perfectly elastic. At the upper yield point, {111}-habit contrast develops, extending from the embryo to the opposing corner. Parallel contrast bands form on the lower contact surface. 109
4.16 Representative true stress versus true strain data for [100]-compressed nanocubes of varying size. For post-mortem HR-TEM analysis, the compression was aborted as soon as dislocation activity was observed in the TV-rate acquisition. 110

4.17 (a) Post-mortem focal series reconstruction and (b) respective (111) Fourier-filtered image of [$\bar{1}$10]-oriented 36 nm nanocube compressed to Point C in Figure 4.8 revealing two stacking faults. The red lines highlight the faulted nature of the top-left and bottom-right portions of the nanocube with respect to the center region. 110
4.18 (a) Ball and stick model of a single (1$\bar{1}$1) [10$\bar{1}$] screw dislocation in a [110]-oriented 37 nm nanocube and (b) the resulting amplitude of the exit wave. (c),(d) Magnified view of the screw dislocation. 112
4.19 (a) Ball and stick model of a single (1$\bar{1}$1) [1$\bar{1}\bar{2}$] partial dislocation in a [110]-oriented 37 nm nanocube and (b) the resulting amplitude of the exit wave. (c),(d) Magnified view of the partial dislocation. 113
4.20 A comparison of the (1$\bar{1}\bar{1}$)-filtered amplitude of the focal series reconstruction with the amplitude of the exit wave reconstructions for inclined (1$\bar{1}$1) [10$\bar{1}$] screw dislocations and (1$\bar{1}$1) [1$\bar{1}\bar{2}$] stacking faults in a 37 nm nanocrystal. Simulations were performed for an accelerating voltage of 200 keV, C_s of 2.0 mm, coherent incident wave function, α of 10 mrad, Δf between −200 nm and 200 nm with 20 nm defocus step. 114
4.21 (a) Post-mortem focal series reconstruction and (b) respective ($\bar{1}\bar{1}$1) Fourier-filtered images of [$\bar{1}$10]-oriented 28 nm nanocube compressed past the load drop after yield. Numerous, closely spaced, stacking faults on its (111) planes can be observed, highlighted in (c,d). 115
4.22 *In-situ* DF-TEM image of Si nanocube under [001] compression. Nanocube is oriented such that its [110] zone axis is along the beam direction, g = 2$\bar{2}$0. The full, inclined slip plane, highlighted in red in 17.820 s frame, can be seen starting across the width of the top surface and extending to a corner of the lower surface of the nanocube whose outline is in blue. . 116

4.23 *Post-mortem* DF-TEM images of a $[01\bar{1}]$-oriented 41 nm Si nanocube after [001] compression. (a),(b) Pre-compression HR-TEM image and a corresponding CBED pattern. (c),(d) *Post-mortem* TEM image and a corresponding CBED pattern. Contrast bands are visible on $(11\bar{1})$ planes in the TEM image and as slight streaks along the [111] direction in the CBED pattern. (e) A selected area diffraction pattern aligned such that the diamond indenter contributes minimal diffraction. Additional spots along the [111] direction are indicative of faulting on $(11\bar{1})$ planes. (f) DF-TEM images using the $\bar{1}\bar{1}\bar{1}$, $1\bar{1}\bar{1}$, and $0\bar{2}\bar{2}$ reflections and the faulted $\bar{1}\bar{1}\bar{1}_T$ and $0\bar{2}\bar{2}_T$ reflections. 118
4.24 *In-situ* TEM image series and true stress versus true strain curve of a 30 nm particle whose [100] direction is oriented along the electron beam and whose slip planes are parallel to the beam direction. {110}-habit contrast can be observed. Downward translation of the contrast is sporadic in the video hinting at movement of Lomer locks (i.e. pinned {111}-habit dislocations). 119
4.25 Calculated contact stress versus (blue) initial sphere radius of compressed spheres or (red) plastic zone diameter of nanoindentation of bulk silicon. Original data from [19, 20]. 122
4.26 True stress versus true strain curves, calculated back stress, and effective stress for (a) a 26 nm and (b) a 37 nm nanocube. (c) Table of mean effective stress for all nanocubes examined. The mean effective stress was found to be 11.8 GPa. 125
4.27 A comparison of force versus displacement curves for pillars with small lateral vibration, teal and violet, and after damping of the vibration well below 1 nm, red and green. Regular load-drops in the loading curve which could be mistakenly interpreted as pop-in events from dislocation bursts during stable compression rather than unresolved shear stresses contributing to deformation. 127

5.1 (a) Schematic of perovskite structure under biaxial compression and tension. (b) Strain phase diagram of $(001)_p$-oriented $SrTiO_3$. (c) A lattice constant number line of available ferroics and perovskite substrates. Few substrates are available near the R-T ferroelectric transition for $SrTiO_3$, limiting investigation of material properties across the transition. Adapted with permission from Schlom *et al* [21, 22] and Haeni *et al* [23]. 131
5.2 EELS spectrum acquired from the pillar in Figure 5.5 prior to compression with dispersion of 0.1 eV channel^{-1}. The Ti $L_{2,3}$ edge at 454 eV consists of the L_3 and L_2 peaks which are each split by the Coulomb field generated by the surrounding O atoms. The O K edge at 527 eV contains information related to bonding of oxygen with neighbor Ti and Sr atoms and is sensitive to bond length and bond angle. 133
5.3 (a) As-fabricated nanopillar of STO produced by FIB milling with a 30 keV ion beam and, inset, a higher mangification image of the sidewall revealing a 15 nm amorphous layer and an additional 15 nm damaged layer. (b) The same pillar after etching in 300:1 BOE for 30 s. The amorphous layer has been removed but a nanocrystalline layer has developed. (c) The same pillar following an additional 60 s etch. (d-f) ADF-STEM images and (g,h) correlated STEM-EDX spectra of the nanocrystalline layer and the un-covered core at the tip of the pillar, respectively. The nanocrystalline material appears to be precipitation of insoluble products during etching. 136
5.4 (a) BF-TEM and (b) DF-TEM using a g = 200 reflection of a nanopillar etched in a DI:HF:HCl solution. The pillar has well-developed crystalline surfaces and no sign of surface defects. (c) A HR-TEM image of the pillar tip demonstrating a the crystalline surface, composed of many surface steps but free of any apparent amorphous or damaged layer. 137
5.5 (a) Low-magnification ADF-STEM image of the diamond indenter approaching an STO pillar. (b) Higher-magnification image as the indenter is aligned with the pillar. 139

5.6 (a) ADF- and HAADF-STEM images of the pillar with the faceted surface visible in the HAADF-STEM image and an ADF-STEM image of the compressed nanopillar. (b) ADF/HAADF-STEM scans during spectrum imaging, rotated 90°from orientation in (a). (b) Core-loss spectra of the Ti $L_{2,3}$ edge during compression and (c) difference maps between the local spectrum and a reference spectrum acquired before compression. No clear change of state is seen in this early work. 140
B.1 Multislice through-focal series of screw dislocations and stacking faults in a [110]-oriented 37 nm nanocube having no tilt about the $[1\bar{1}\bar{1}]$ direction. 171
B.2 Multislice through-focal series of screw dislocations and stacking faults in a [110]-oriented 37 nm nanocube having 1° about the $[1\bar{1}\bar{1}]$ direction. 172
B.3 Multislice through-focal series of screw dislocations and stacking faults in a [110]-oriented 37 nm nanocube having 2° about the $[1\bar{1}\bar{1}]$ direction. 173
B.4 Multislice through-focal series of screw dislocations and stacking faults in a [110]-oriented 37 nm nanocube having 4° about the $[1\bar{1}\bar{1}]$ direction. 174

Chapter 1

Introduction

While much early research using transmission electron microscopes focused on biological applications [24], their utility in the physical sciences also grew rapidly. Achieving resolution of a few nanometers by the 1940s, TEMs, made it possible to observe and study the nanoscale structures which define fundamental properties of materials in the world around us. It was not until 1934 that three independent papers attributed plasticity in crystals to dislocations [25–27]. While they had been studied indirectly through processes such as chemical etching for years even before their conception [28], it was not until 1956 that the transformative work of Peter Hirsch *et al* [29] and Walter Bollman [30] provided the first direct imaging of dislocations by dislocation contrast in the TEM. That same year Menter [31] imaged directly the crystal lattice and end-on edge dislocations in platinum phthalocyanine [32].

The application of electron microscopy to materials science matured rapidly from this early work. Their use extends from most basic application of imaging the local mass thickness in ultra-thin specimens (no more than a few hundred nanometers and preferably far less) to the probing of the local atomic structure of crystals and defects. Diffraction contrast in the TEM allows the study of location and nature of crystalline defects. Dark field techniques can likewise probe defects in addition to examination of grain structure in polycrystalline materials. As electron sources and optic improved, so did spatial resolution. At high magnifications, phase contrast imaging allows direct imaging of a crystalline lattice, though the interpretation of such images must not be approached carelessly. The integration of complementary spectroscopic techniques such

as electron energy-loss spectroscopy (EELS) and energy-dispersive X-ray spectroscopy (EDX) expanded their use to the probing of the chemical structure of materials.

Some of the earliest applications of TEM in materials science were *in-situ* experiments. The work of Hirsch *et al* [29] involved the imaging of moving dislocations in thin metal foils under the thermal stresses of the 100 keV electron beam. The first *in-situ* tensile experiments were performed by Wilsdorf in 1958 [33], confirm previously theorized dislocation mechanisms. In the following few decades, the advent of high-voltage electron microscopes (HVEMs) operating at accelerating voltages in the 1 MeV range catalyzed the study of thick foils of FCC and BCC metals [34]. These instruments, however, create significant radiation damage and are not trivial to operate and maintain. Today most microscopes have accelerating voltages of 100 to 300 keV, allowing the study of materials of moderate thickness with generally tolerable damage.

Today, modern microscopes can routinely achieve sub-nm and even sub-Åspatial resolutions. Recent advances in electronics and fabrication techniques have ushered an era of *in-situ* microscopy where dynamic experiments can be performed directly in the TEM. These include observation of materials under straining [35,35–49], heating [50–52], cooling [53–55], or other external stimuli [56–58]. In addition, environmental stages such as liquid- and gas-cells have been developed, which allow observation of chemical reactions [52, 59–63].

Much of the work contained herein relies on the advances in *in-situ* TEM. Using modern heating and mechanical deformation stages, dynamic processes are observed as they occur using the electron microscope. Chapter 3 examines crystallization processes in hydrogenated amorphous silicon (a-Si:H) during thermal annealing. Thin films of a-Si:H were seeded with cubic Si nanocrystals. Upon annealing it was found that small cavities formed which began propagating through the films, leaving behind crystalline tails. The origins of this phenomenon and the processes enabling it were studied by both *in-situ* and *ex-situ* TEM techniques. Chapter 4 examines the elastic-plastic response of silicon nanocubes under uniaxial compression. The development of a mechanically actuated, load-displacement sensing stage [4, 59] have enabled the observation and qualification of discrete, nanoscale mechanical processes. The mechanical response of Si nanocubes were correlated with the mechanisms atomistic mechanisms of plasticity.

- Chapter 2 provides an introduction to the common theme of my research: electron microscopy and its applications. I provide a background to each technique and in some cases use examples of my work to demonstrate its application.

- Chapter 3 discusses an *in-situ* heating investigation of a crystallization process in hydrogenated amorphous silicon whereby porous regions at the interface of the amorphous film and nanocrystal inclusions which, when annealed, lead to propagating nanocavities having crystalline tails. By imaging the crystallization process *in-situ*, insights to the kinetics of growth are found while *ex-situ* analysis probes crystallography of the crystalline tails and nanocavity surfaces.

- Chapter 4 examines the mechanical response of 25 to 65 nm {001} silicon nanocubes compressed in the TEM. The elastic-plastic response to deformation is examined as it relates to size scale, demonstrating large elastic strains and flow stresses approaching the theoretical strength. These results are compared to *post-mortem* HR-TEM imaging to determine the nature of dislocations accommodating plasticity.

- Chapter 5 describes the preliminary investigation of the changing electronic response of strontium titanate nanopillars when as they are strained inside the TEM. The approach to fabricating sub-50 nm pillars of a complex oxide without surface damage is described and initial *in-situ* straining and STEM-EELS acquisition is discussed.

Chapter 2

Methods

This chapter provides a description of the tools and methodologies used in my research. The transmission electron microscope (TEM) has been the principal tool and the TEM, its components, and its applications will be described in some detail here. For a more thorough description of the TEM, see the texts by Williams and Carter [1], Reimer and Kohl [64], and Fultz and Howe [65].

2.1 The transmission electron microscope

Today, state of the art transmission electron microscopes allow nearly-routine characterization of materials at the atomic scale, which could scarcely be imagined 150 years ago. Towards the end of the 19th century our understanding of optics and electromagnetism grew and provided the impetus for the development of electron microscopy. Enabled by the development of the cathode ray tube by Robert Crookes in the 1870s, J. J. Thompson experimentally discovered the electron in 1897 by measuring the mass of cathode rays. Heinrich Hertz demonstrated that cathode rays act as waves in 1887, providing experimental proof of Maxwell's theory of electromagnetism, and in 1892 demonstrated that cathode rays can pass through thin metal foils. The work of Ernst Abbé, a pioneer in physical optics, defined the resolution limit of a microscope based on diffraction-limited optics and the wavelength of the source. As it is possible to generate electrons with wavelengths vastly smaller than those of visible light, Abbe's resolution criterion predicted a new domain of microscopy. Following the invention of the electromagnetic

lens by Hans Busch in 1926, the first electron microscope was developed by German researcher Ernst Ruska and his doctoral advisor Max Knoll in 1931, earning Ruska a Nobel Prize in Physics over 50 years later. His first microscope had a resolution worse than an optical microscope, but advances quickly changed that. Initially of interest to study biological specimens, a flurry of research around the world led to the first commercial production of transmission electron microscopes by Seimens in 1939 and Philips in 1946 [66].

Likely the most familiar form of transmission electron microscopy to scientists and engineers is the technique more accurately called conventional transmission electron microscopy, or conventional TEM, which is discussed in Section 2.2. This is in contrast to scanning transmission electron microscopy (STEM), which is discussed in Section 2.3.

2.2 Conventional transmission electron microscopy

The resolution of a microscope is defined by minimum distance between two distinguishable objects. Ernst Abbé, a pioneer of physical optics, defined the diffraction-limited resolution limit as the radius of the Airy disc

$$d = \frac{\lambda}{2NA}, \tag{2.1}$$

where the numerical aperture, $NA = n \sin\theta$, defines the angles over which the microscope accepts light. For an optical microscope the wavelength λ is within 350 nm to 650 nm giving a minimum resolution of about 0.5 µm. In 1923 de Broglie demonstrated that all particles, including electrons, have a wavelength associated with their momentum $\lambda = {}^{h}/_{m\nu}$ where m and ν are the relativistic mass and velocity of the particle. Three years later, Hans Busch invented the electromagnetic lens, making it possible to focus electrons of an electron microscope which was first built five years later by Max Knoll and Ernst Ruska in 1931. By emitting electrons from a heated filament and accelerating them using static potentials, electrons can be focused using electromagnetic lenses much like light. Large potentials can accelerate electrons to greater than one half the speed of light. For a conventional transmission electron microscope with an electron accelerating voltage in the range of 100 keV to 300 keV, resulting in λ less than 0.05 Å, modern TEMs can approach spatial resolutions of 1 Å to 5 Å [1].

In conventional TEM, specimen imaging is performed by created a collimated and coherent electron beam which interacts with the sample and is collected on the transmitted side using an objective lens and projection system. This is in contrast to scanning transmission electron microscopy (STEM), which is discussed in Section 2.3. A conventional TEM, an example of which is shown in Figure 2.1b, is comprised of an electron source, a condenser system to guide the electron beam to the sample, an objective system to form a diffraction pattern or image, and a projection system to provide for magnification. In the next following subsections, the components and capabilities of conventional TEM are discussed.

2.2.1 Illumination system of a TEM

The illumination system of a conventional TEM guides electrons originating at the electron source, i.e. gun system, to the specimen such that a coherent and collimated beam of electrons passes through the specimen. An example ray diagram of an (S)TEM operating in conventional TEM mode can be found in Figure 2.1a. The gun crossover is excited in such a way that an image of the electron source is positioned at the back focal plane of the C1 lens, providing the object for the C1 lens and producing a demagnified image of the source at the back focal plane of the C2 lens. The C2 lens is then focused to produce an image of the C1 crossover at the front focal plane of the upper objective lens. The upper objective lens is then excited such that the transmitted beam is highly collimated, with a convergence angle less than 10^{-4} mrad. Operators of the TEM should take caution as it can be easy, if harmful to one's data, to converge the beam in order to provide greater intensity at the camera as the coherent nature of the incident beam will be lost.

2.2.2 Imaging system of a TEM

The imaging system refers to the optics located on the transmitted side of the specimen. In CTEM, the imaging system is designed to form diffraction patterns and images. The lower objective lens takes the exit wave of the electron beam after passing through the sample and form a diffraction pattern in the back focal plane and image in the image plane of the projection system. The most common type of diffraction condition is that

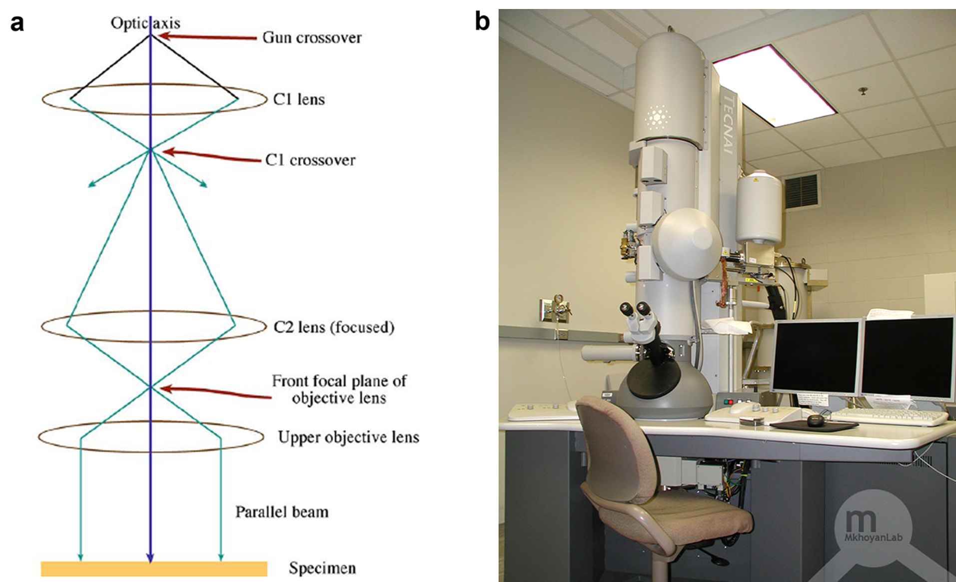

Figure 2.1: (a) Ray diagram of the illumination system of an (S)TEM operating in imaging mode [1]. (b) Image of one of two FEI Tecnai F30 in the Characterization Facility of the University of Minnesota.

of selected-area diffraction (SAD), which is formed by illuminating the specimen with a collimated beam of electrons as shown in Figure 2.2a and placing an aperture around the region of interest in the back focal plane of the objective lens. This back focal plane is used as the object for the intermediate lens, resulting in the dot-like features, i.e. diffracted beams from crystallographic structure of the specimen, in SAD patterns. An example high-resolution CTEM image of InAs grown on GaSb and a representative SAD pattern can be seen in Figure 2.3.

2.2.3 Aberrations

The ultimate resolution of a microscope, ignoring all aberrations, is called the diffraction-limited condition and is defined in terms of the Rayleigh criterion as discussed earlier. Diffraction of a point source results in an image consisting of a radially-symmetric, angular-dependent intensity called the Airy disc. When the image of two point sources are brought together, each with the profile of the Airy disc which is defined by a Bessel function, the resolution is determined by the resultant contrast of the superposition of

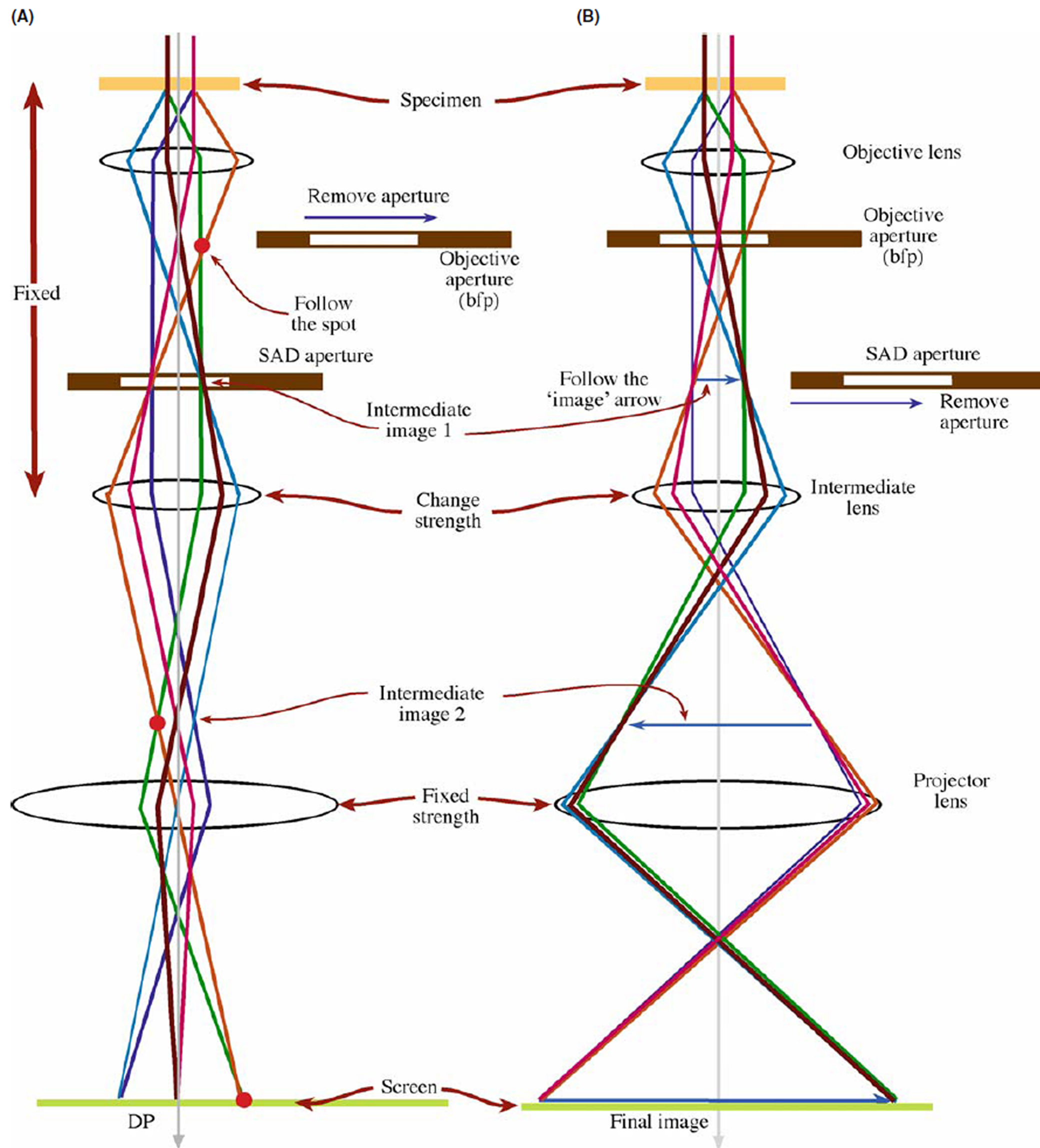

Figure 2.2: Ray diagrams of the imaging systme in CTEM operation (a) in diffraction and (b) bright-field imaging modes. In both cases, the paths of electron beams are the same before the intermediate lens. In diffraction mode, the intermediate lens uses the back focal plane of the objective lens as the object while imaging mode uses the image plane of the objective lens [1].

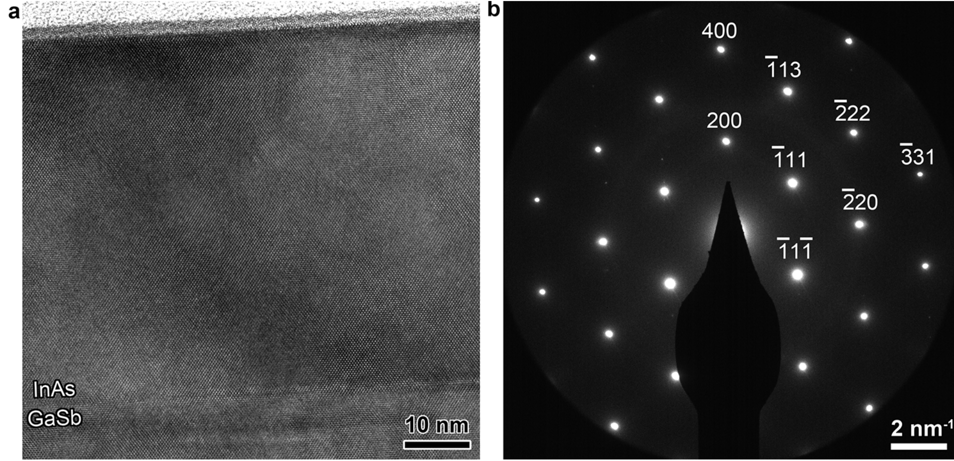

Figure 2.3: (a) High-resolution CTEM image of epitaxial growth of 50 nm Si-doped InAs on 3 nm intrinsic InAs on GaSb viewed along the [110] zone axis and (b) a corresponding SAD pattern. GaSb and InAs are both zinc blende structures with lattice constants of 6.10 Å and 6.06 Å, respectively.

the spread intensity of each image. Defining the resolution limit as the point where the intensity between the two images is 80% of their peaks leads to a diffraction-limited resolution of $r_{th} = 1.22\lambda/\beta$ where β is the maximum angle of collection of the objective lens aperture.

In traditional electron microscopes, achieving diffraction-limited resolution is prevented by aberrations induced by imperfect lenses and incoherent electron sources. The inability of electromagnetic lenses to focus rays of different axial positions to the same point, cause a point object to be imaged as a disk of finite size, referred to as spherical aberration. Ray diagrams representing a lens with spherical aberration can be seen in Figure 2.4a. As can be seen from this ray diagram, the point object P is imaged at the Gaussian plane as a large disc. Calculation of the diameter of this disk along the optic axis leads to the determination of a position outside the Gaussian image plane having the minimum diameter, termed the "plane of least confusion." Scherzer determined that the defocus required to image this condition is defined by $\Delta f = (C_s\lambda)^{1/2}$, where Δf is the objective lens defocus, C_s is the spherical aberration coefficient, and λ is the electron wavelength. The resulting spherical aberration-limited resolution is

$$r_{sph} = C_s\beta^3. \tag{2.2}$$

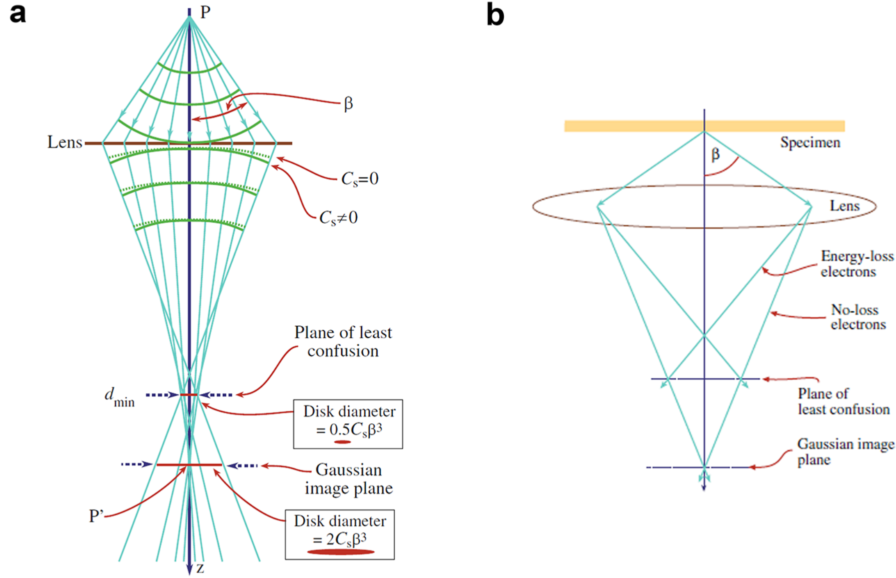

Figure 2.4: (a) Ray diagram demonstrating distorted wave fronts and bending rays near the lens edge more than those near the axis. The minimum image size is then defined by the disc of least confusion. (b) Ray diagram demonstrating chromatic aberration due dependent on incident electron energy.

The combination of diffraction-limited resolution r_{th} and spherical aberration r_{sph} leads to a probe-limited resolution of

$$r = \left(r_{th}^2 + r_{sph}^2\right)^{1/2}. \tag{2.3}$$

Assuming optimal selection of collection angle as described more thoroughly in [1] or any other text on TEM, the practical achievable resolution is then

$$r_{min} = 0.91\left(C_s\lambda^3\right)^{1/4}. \tag{2.4}$$

An electromagnetic lens, providing a static field, bends electrons of lower energy more strongly, resulting in chromatic aberration, depicted in Figure 2.4b. The small energy spread of an electron beam, about 0.3 eV for a cold FEG up to about 1.0 eV for a thermionic source, creates an almost negligible effect on resolution in a non-spherical aberration corrected microscope [64]. Inelastic scattering in the specimen, particularly in thick specimens, can create wide and significant spread in transmitted electron energies,

limiting resolution to

$$r_{chr} = C_c \frac{\Delta E}{E_0} \beta \tag{2.5}$$

where C_c is the chromatic aberration coefficient, ΔE is the energy loss of the electrons, E_0 is the incident beam energy, and β is the maximum angle of collection of the objective lens aperture. Zero-loss filtered imaging using an energy filter such as the Gatan GIF2002 on the Characterization Facility's FEI Tecnai F30 Cryo (S)TEM can reduce the effects of chromatic aberration to that of the incident energy spread by filtering out all inelastically scattered electrons.

Familiar to anyone who has used a scanning electron microscope is astigmatism, which is a non-uniform magnetic field about the optic axis causing an angular change in defocus. Astigmatism is easily corrected by octupole compensating field lenses referred to as the stigmators.

The description of aberrations above has been described as they affect the propagation of electron paths in real space, however the aberrations can also be considered as error induced in the phase of the propagating wave front. The dominant aberration in a thin specimen, spherical aberration, affects the path length through the phase distortion function, or aberration function, $\chi = (2\pi/\lambda)\,\delta$. The aberration function can be expanded in terms of deviation from the optic axis as [3]

$$\chi = \frac{2\pi}{\lambda}\delta = \frac{2\pi}{\lambda}\left(\frac{1}{2}C_1\alpha^2 + \frac{1}{4}C_3\alpha^4 + \frac{1}{6}C_4\alpha^6 + \cdots\right), \tag{2.6}$$

where $\alpha = \sqrt{\alpha_x^2 + \alpha_y^2}$ is the convergence angle determined by the condenser aperture. The terms C_1, C_2, and C_3 refer to the defocus, third-order spherical aberration coefficient, and fifth-order spherical aberration coefficient, respectively. C_3 is the spherical aberration coefficient commonly referred to as C_s. A comparison of the real space and reciprocal space treatments of spherical aberration can be seen in Figure 2.5.

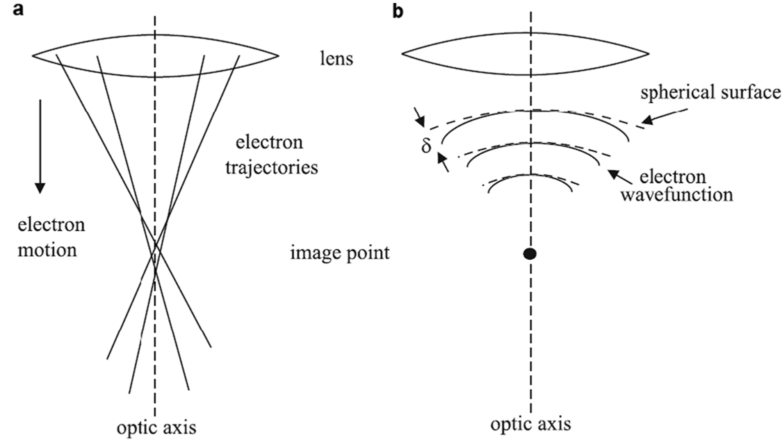

Figure 2.5: The effects of spherical aberration on the focusing of electrons (a) in real space and (b) in reciprocal space. In real space, spherical aberration focuses electrons farther from the optic axis more strongly than those passing through the lens center. In reciprocal space, spherical aberration causes a radial phase shift of a plane wave entering the lens.

2.2.4 The contrast transfer function

The aberration function introduced in Section 2.2.3 create modulations in the spatial frequency of the incident wave function through the phase shift relation [3]

$$H_o(K) = \exp\left[-i\chi * (K)\right] = \cos\left[-\chi(K)\right] - i\sin\left[-\chi(K)\right], \tag{2.7}$$

where $a = \lambda k$ and $K = k\left(C_s\lambda^3\right)^{1/4}$. $H_o(K)$, referred to as the modulation transfer function or contrast transfer function (CTF) describes how the objective lens transfers the incident wave function after it passes through the sample. Example contrast functions representative of the Characterization Facility F30 with SuperTWIN lens and operating at 300 keV can be found in Figure 2.6.

Depending upon the defocus and beginning at moderate frequencies, the contrast transfer function can be seen to oscillate about zero. Contribution of frequencies when H_oK is positive will destructively interfere with that of frequencies whose H_oK is negative. It is therefore important to tune defocus such that the first crossover, determined by λ, Δf, and C_s, is moved to as high a frequency as possible while higher frequencies are excluded from the image by use of an appropriately selected objective aperture.

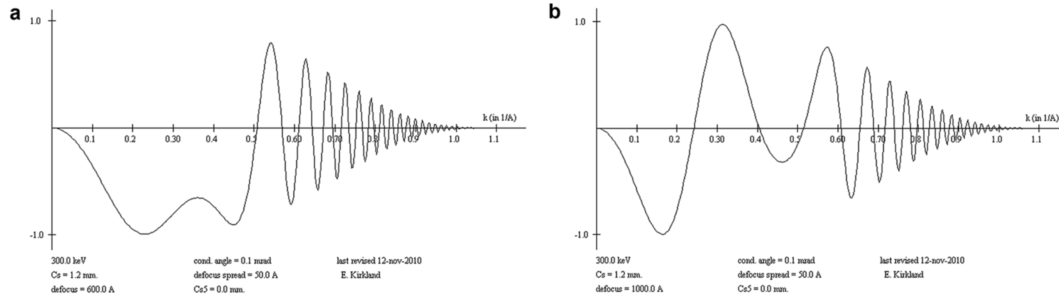

Figure 2.6: Contrast transfer function representative of a Tecnai F30 with $C_s = 1.2\,\mathrm{mm}$ operating at 300 keV with defocus of (a) 600 Å and (b) 1000 Å [2].

While lack of an objective aperture may yield a qualitatively higher resolution image, interpretation of atomic structure from such an image must be made with caution.

2.2.5 Bright-Field TEM

The centering of the objective diaphragm about the optic axis leads to the bright-field TEM (BF-TEM) mode of operation. Selection of an aperture with objective aperture acceptance angle α typically within the range of 5 mrad to 20 mrad leads to strong scattering and diffraction contrast while eliminating the destructive contribution of positive components of the CTF. When high resolution is desired, the operator must also take care in selection of beam convergence angle. While often requiring greater beam intensity at high magnifications, the larger convergence angle of a focused beam leads to partial coherence of the incident beam and greater attenuation of the CTF, reducing the first crossover and reducing point resolution.

Reduction of the objective aperture acceptance angle $\alpha$to include only the direct beam will lead to strong mass-thickness and diffraction contrast at the expense of phase contrast. By increasing α to include one or more Bragg reflections, strong diffraction contrast can be utilized to image high-resolution lattice fringes down to about 1 Å in a modern FEG CTEM. The source of high-resolution information in the TEM can be derived from wave-optical theory of imaging, described in detail in Chapter 28 of Williams and Carter [1], Chapters 7 and 9 of Reimer and Kohl [64], and Chapters 3 and 5 of Kirkland [3].

2.2.6 Diffraction in CTEM

Diffraction patterns in the STEM provide information on local crystal structure. The selected area aperture, located in the first image plane below the specimen, can be placed around a region of interest. The condenser system is then aligned such that a parallel probe passes through the specimen. The SAD aperture excludes rays originating from regions outside the aperture, providing a diffraction pattern of focused spots only of the region of interest.

The minimum region of interest of an SAD aperture is limited by spherical aberration, limiting practical spatial selection to around 100 nm. Spherical aberration results in delocalization of the diffraction information in the back focal plane. As the SAD aperture is reduced in size, greater contributions of surrounding material as well as loss of local diffraction information will result. A more thorough discussion can be found in Chapter 11 of Williams and Carter [1].

To collect diffraction information with greater spatial resolution convergent beam electron diffraction (CBED) can be employed [67]. In CBED, the probe is converged on the sample and placed over a region of interest. The convergence angle and spatial resolution are then determined by the pre-specimen optics - a combination of gun lens, condenser lenses, and pre-field of the objective lens. A larger spot size will provide a smaller probe, however with larger convergence angle. The large convergence angle relative to SAD results in loss of coherence in the diffraction pattern. The diffraction spots will appear as discs with diameter related to the convergence angle.

Changes in strain can be derived from CBED patterns with a spatial resolution of approximately 5 nm by measuring the distortion of high-order Laue zone (HOLZ) lines, located in the zero disk, from their ideal relaxed position in the bulk [68–70]. The HOLZ lines result from scattering of the incident beam due to intersection of a lattice plane at its Bragg angle θ_B. Scattering over all possible directions of θ_B forms a reflection, called the excess line, and at an angle $-\theta_B$ a corresponding dark line, the defect line, which can be observed in the zero disc. The Bragg angle is highly susceptible to changes in the local lattice which can be compared to simulated CBED patterns for strain determination.

Identification of twinning and faulting by CBED analysis can be rather complicated. The overlap of the discs can obfuscate the relatively weak reflections resulting

from stacking faults or nanotwins. An alternative approach is that of microprobe-STEM or nanodiffraction. In each case the condenser system is aligned to maximize demagnification of the source while spreading the beam to achieve reduced convergence angle [71–73]. Two-condenser systems can achieve spatial resolutions lesss than 10 nm with α less than 1 mrad while three-condensor systems such as the FEI Titan can achieve spatial resolutions on the order of 1 nm. Changes in orientation can be mapped by correlating simulation of the crystal diffraction pattern to experimental results at each position as used by Yu *et al* [74] to study the twist of a CdSe nanorod along its axis.

2.2.7 Dark-Field TEM

In dark-field TEM (DF-TEM) the primary beam is removed by the objective diaphragm at the focal plane of the objective lens, leading to contrast only from scattered electrons. In the case of twinning and stacking faults in Si, DF-TEM imaging can prove especially useful. Selection of a unique Bragg reflection can provide contrast of twinned grains and stacking faults contained within a matrix crystal. This is discussed in greater detail in Section 3.4.3.

2.2.8 Dislocation imaging

Important to the work described in both Chapter 3 and Chapter 4 is the ability to identify the presence of defects within a crystal. Diffraction contrast can be most easily identified through the use of the so-called near two-beam condition [1,64]where a strong Bragg scattering condition applies for a single reflection is then tilted slightly away such that a large excitation error exists between the Ewald sphere and the reflection's relrod. The strain field around a dislocation will locally bend the lattice on one side of the dislocation into a strong Bragg condition while the opposite side will bend further away. The result in a BF-TEM image is a sharp dark band along the dislocation while the DF-TEM image will have a sharp bright band. Such an approach, called "weak-beam dark field" imaging can resolve dislocations with a resolution below 3 nm [1].

Alternatively, line defects such as edge-on stacking faults or edge dislocations can be imaged directly by high-resolution TEM. Interpretation of high-resolution images of defects can be hazardous, however, when the defect is not oriented directly along

the beam direction. It can also be complicated by instrument aberrations, particularly spherical aberration, which lead to delocalization effects in the phase contrast. Focal series reconstructions of HR-TEM image series acquired in discrete defocus increments can be used to determine the amplitude of the exit wave [75–77], an approach used in Chapter 4 to examine the structure of deformed Si nanocubes. Simulation of numerous possible dislocation structures were also performed using the Multislice algorithm implemented by Kirkland [3] to guide interpretation of *in-situ* and post-mortem images.

2.3 Scanning transmission electron microscopy

In scanning TEM (STEM) mode, depicted in Figure 2.7 [1], electron optics converge the beam to a small, incoherent probe on the order of one angstrom in diameter. In this ray diagram the C1 lens is strongly excited while the C2 lens is weakened. The upper objective lens then acts as a third condenser lens focusing the C1 crossover on the specimen as a highly demagnified image of the source with large convergence angle. As probe size is critical for resolution in STEM, the type of source is extremely important. While the image of the source is demagnified two or more times as it passes through the condenser system, starting with a small source is essential.

As the FEI Tecnai F30s and FEI Titan at the University of Minnesota operate as both conventional and scanning TEMs, they utilize Schottky field-emission guns (SFEGs). This is as opposed to the thermionic emission source of the FEI T12 which is dedicated to conventional TEM. SFEGs use a zirconium oxide-coated tungsten probe having a sharp tip, relying on both heating and strong electric field to produce electrons. Thermionic emission guns, on the other hand often rely on LaB_6 crystals. The sharp tip of the tungsten filament coupled with the sharp field gradient at this tip promotes intense emission of electrons from a small area resulting in a small, bright source.

2.3.1 Imaging with STEM

The focused probe generated in STEM can be rastered across the sample using scan coils as depicted in Figure 2.7c. Unlike in scanning electron microscopy, where the scan coils are positioned after the condensor system, the scan coils in STEM are designed such that the incident angle of the probe on the specimen remains the same. This is

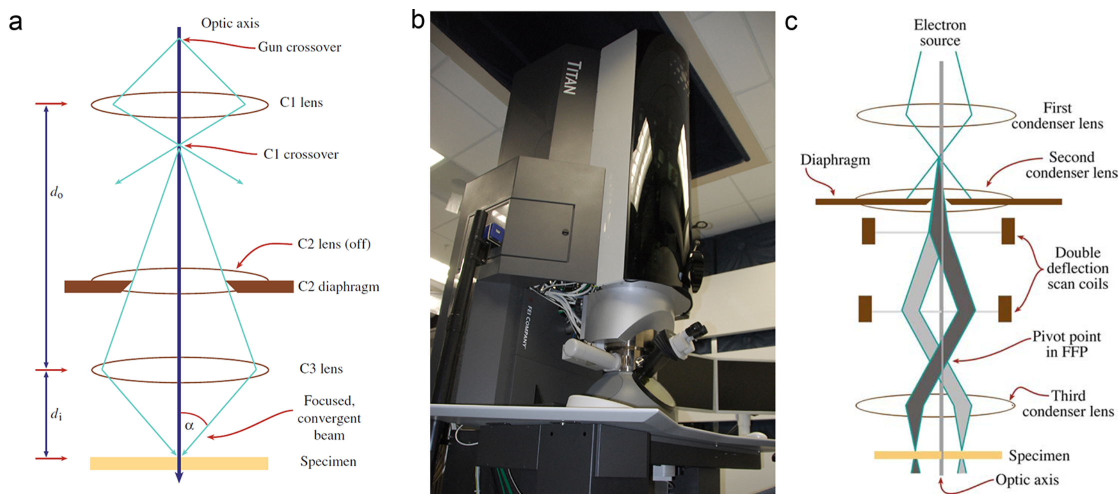

Figure 2.7: (a) Ray diagram of (S)TEM operating as a scanning transmission electron microscope [1] and (b) image of the UofM Characterization Facility's FEI Titan 60-300. (c) Schematic of the probe scan coils of a STEM. Deflections of the electron beam by the first scan coil are returned to the optic axis through the front focal plane of the final condensor lens with an angle that determines displacement of the focused beam without tilting the it as it is rastered across the specimen [1].

accomplished by placing the a pair scan coils before the final condenser lens. The first scan coil deflects the beam away from the optic axis while the second scan coil returns the beam to the optic axis through a pivot point at the front focal plane of the final condenser lens. The angle produced by the scan coils causes a displacement of the probe on the specimen while maintaining an electron trajectory along the optic axis.

Images can then be formed in a serial manner from the various signals produced at each point in the scan area. These include the unscattered electrons resulting in a bright-field STEM image, low-angle-scattered electrons creating a dark-field diffraction contrast image, high-angle scattered electrons to from a high-angle dark-field image, collection of the inelastically-scattered electrons to form electron energy-loss spectra, or collecting of the generated x-rays to produce an energy-dispersive x-ray spectra.

2.3.2 Bright-Field STEM

Collection of the electrons scattered at low angles, smaller than the probe convergence angle, is referred to as bright-field STEM (BF-STEM) and results in a phase contrast

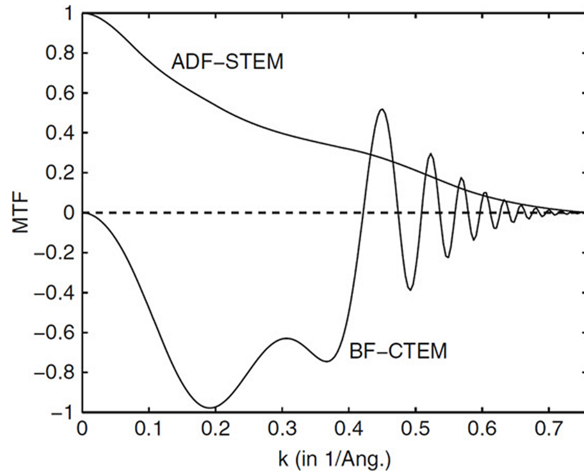

Figure 2.8: Comparison of the contrast transfer function for ADF-STEM and BF-CTEM for the same spherical aberration and accelerating voltage. While the BF-CTEM CTF begins to oscillate rapidly about 0 at moderate frequencies, the ADF-STEM CTF remains positive while gradually approaching zero. Reproduced from Kirkland [3].

image that is similar to that observed in BF imaging in CTEM. Alternatively, annular detectors can be placed about the optic axis, resulting in collection of scattered electrons and forming a dark-field image.

2.3.3 Annular dark-field STEM

Annular dark-field (ADF-STEM) imaging utilizes a detector with inner and outer acceptance angles such that Bragg scattered electrons are collected, generating a diffraction contrast image. Scattering due to phonons and lattice distortions are also collected, providing significant image contrast and enabling strain mapping, crystal orientation mapping, and imaging of individual light dopant atoms and vacancies [78–81]. Interpretation of ADF-STEM images is also simplified by the fact that the contrast transfer functions in ADF-STEM does not oscillate about 0 as was described in Section 2.2.4 and illustrated in Figure 2.8. The lack of modulation about 0 results from the loss of coherency of the incident electrons due to the focused probe. The result is an ability to more directly interpret ADF-STEM images without the need to perform the meticulous simulations as required in conventional TEM.

Electron interaction with crystals is complicated by plural scattering events and coherent scattering due to periodicity of the lattice, i.e. dynamical scattering. These effects can be minimized by increasing the inner angle of the detector, which decreases contribution of diffracted beam at the expense of intensity [82], discussed in Section 2.3.3.

High-angle ADF (HAADF) imaging utilizes a large inner angle so that predominately incoherent nuclear scattering is collected. Annular dark field (ADF) imaging utilizes incident electrons that are elastically scattered at large angles. The intensity for each position of the probe is determined by integration of the diffraction pattern across the detector. The incoherent Rutherford scattering of electrons by an isolated atom are defined by a scattering cross-section varying approximately as the atomic number Z^2 and providing so-called "Z-contrast imaging" condition [68]. HAADF imaging provides benefits over bright field imaging such as high Z-contrast and the lack of contrast reversal with defocus due to a contrast transfer function (CTF) that is always positive, simplifying image interpretation [83]. The effectiveness of this imaging mode has been demonstrated by resolution of individual dopant atoms in a silicon crystal [84] and anomalies in local thermal vibrations of a crystal [85].

2.4 Spectroscopy in the (S)TEM

2.4.1 Electron energy-loss spectroscopy

As the time-varying electric field of the incident electron beam passes through the specimen it interacts over a large range of frequencies, from the infrared to the X-ray. These interactions result from electron excitations within the specimen with incident electrons losing energy $\Delta E = E_f^e - E_i^e$ equal to the difference in energies of the excited electron in its final and initial states. EELS separates in energy the inelastically scattered electrons with a magnetic prism which are then collected on a CCD. Inelastic collisions are strongly forward scattered, allowing ADF imaging, EDX, and EELS to be performed simultaneously with precise determination of atomic position [86].

The zero loss peak (ZLP) contains primarily unscattered electrons and its FWHM is the energy resolution of the EEL spectrum [1]. The low-loss spectrum, 0.50 eV, is due to weakly bound outer-shell excitations, i.e. plasmon-loss, and valence-to-conduction band transitions. From this spectra the localized dielectric constant, band gap, and

band structure can be derived [87]. The core-loss spectrum, 50 eV to 100 eV, results from core electron excitations to empty states above the Fermi level. These transitions are highly localized and elemental- and site-specific. Whereas the low-loss excitations are a collective process of the electron gas, core-loss transitions are well-approximated by a single-electron transition. Coupling EEL spectra with modeling of allowed core-shell transitions can therefore identify composition and coordination [87, 88]. Study of the near-edge fine structure of the core-loss spectra can determine changes in bonding near an interface with a resolution below 1 nm. These capabilities have demonstrated, for example, spatially resolved EELS at an Si-SiO_2 interface, identifying a silicon transition from the $Si4^{+}$ state in the oxide to Si^{2+}, bound to two silicon and two oxygen, at the interface and to Si_O on the c-Si side of the interface due to symmetry breaking of the conduction band with a near-edge shoulder identified as defect sites [86, 89].

The near-edge fine structure can be described by single-electron theory as excitation of an electron from an inner shell to an unoccupied state [90, 91]. Using the dipole approximation, the near-edge fine structure can then be described by Fermi's Golden rule, i.e. a double-differential cross-section simplified as [90]

$$J_c\left(E\right) = \frac{d^2\sigma}{d\omega dE} = \frac{8\alpha_0^2 R^2}{E m_0 \nu^2}\left(\frac{1}{\theta^2 + \theta_E^2}\right)\frac{df}{dE}, \tag{2.8}$$

where σ is the scattering cross-section, $R = \left(m_o e^4/2\right)\left(4\pi\epsilon_0\hbar\right)^{-2} = 13.6\,\text{eV}$ is the Rydberg energy, θ_E is the characteristic angle for scattering, approximated as $\theta_E = {}^{E}/{}_{2E_0}$, and ${}^{df}/{}_{dE}$ is the generalized oscillator strength per unit of energy loss E. Having a well-defined energy and angular momentum, EELS is therefore sensitive to specimen orientation and provides an angular- and energy-dependent density of unoccupied states weighted by its transition probability for the given scattering atom and its bonding to neighboring atoms.

Silicon nanocrystals have attracted much attention for applications in light-emitting devices and photovoltaics due to the ability to tune their opto-electronic properties with size and morphology. The ability to dope nanocrystals provides an additional means of controlling through changes in free carrier concentration [92–95]. Recently, doping of Si nanocrystals resulting in localized surface plasmon resonances (LSPRs) were reported for the first time. Using STEM-EELS, the incorporation of boron in 5 nm

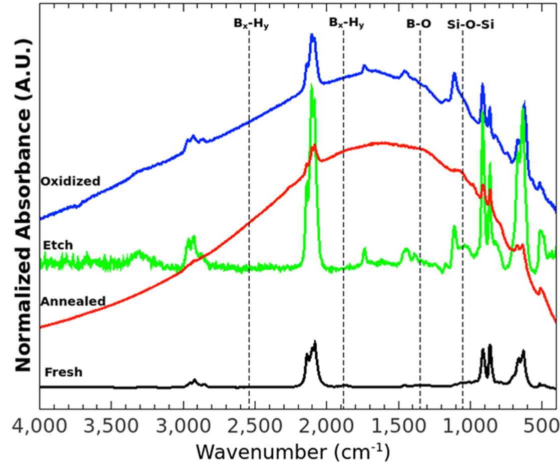

Figure 2.9: FTIR of 10%nom. B-doped Si nanocrystals as produced, after annealing, after oxidation, and after HF-vapor etching. Oxidation and annealing lead to a plasmon resonance peaked around 1700 cm^{-1}. Courtesy Nicolaas Kramer.

to 10 nm Si nanocrystals and its role in LSPR is being examined. These small B-doped Si nanocrystals exhibit no LSPR immediately after synthesis, however when allowed to oxidize or subjected to annealing a strong plasmonic response develops Figure 2.9. Using the high spatial and energy resolution of the monochromated Titan, Section 2.9.4, operating at a voltage of 80 keV we are exploring the role of boron and oxidation in this plasmonic response by probing the fine structure of the Si $\mathrm{L}_{2,3}$ and B K edges. Nanocrystals were synthesized in a flow-through plasma reactor using silane and borane as precursor gases. Particles were deposited directly on holey carbon grids and isolated particles suspended over vacuum such as those seen in Figure 2.10a are selected for STEM-EELS spectrum imaging. Figure 2.10b,c show the sub-pixel scanned ADF-STEM image and core-loss map, respectively. The low-loss spectrum, not pictured, was used for alignment of the spectra within the spectrum image prior to pixel summing.

The Si $L_{2,3}$ and B K edges at 99 eV and 188 eV both exhibit well defined near-edge fine structure providing a fingerprint of the local environment of the scattering atoms. The Si $L_{2,3}$ has an abrupt edge onset which is defined by transitions from the $2p$ orbital to unoccupied s- and d-states. Spin-orbit coupling splits these peaks into two, with a separation of 0.6 eV, but it requires exceptional energy resolution to be resolved. Such effects can be much stronger in other materials, as described in Chapter 5. The sp^3

hybridization of silicon also allows $2p-3p$ transitions, making a significant contribution to the ELNES. Reduced thickness of Si, for example in nanoparticles, leads to loss of long-range order and surface effects which blur these structures. The Si $L_{2,3}$ edge is sensitive to the electronegativity of atoms to which it is bonded, causing a chemical shift of about 2 eV for boron to 6 eV for oxygen [96]. Additional peaks at 108 eV and 115 eV are associated with Si-O-Si bonds [97, 98]. Beginning around 150 eV is a broad beak corresponding to the $L_{2,3}$ ionization edge [99].

The B K edge is a favorite for those studying EELS due to its characteristic sharp "white lines" and relatively high scattering cross-section, though about the Si $L_{2,3}$ edge is about five times higher. Metallic boron has an edge onset around 188 eV with broad, poorly defined features. Oxides, carbides, and nitrides of boron, however develop strong peaks at 192 eV and 198 eV owing to sp^2 hybridization and the $\sigma*$ and $\pi*$ orbitals, respectively. Chemical shifting can occur due to core hole effects, i.e. an unscreening of the nuclear charge as the a localized core electron is excited into an unoccupied position, leading to shifts as high as 2 eV in cubic-BN.

Preliminary findings, Figure 2.10d, have revealed a large red-shift in the B K edge onset of 7 eV. The cause of such a large red-shift is not currently known and such red-shift has been observed for boron in any other materials system. A sharper onset is observed for the oxidized particles, Figure 2.10e while the broad peak centered about 200 eV is absent in the aged particles. The shift has been observed in nanocrystals allowed to oxidized for as little as 7 h, comparable to the time required for observation of a plasmonic response in FTIR. While not conclusive, it appears that the large shift in core-loss onset is associated with the plasmonic response. With improvements in performance of the EEL spectrometer, changes in the fine structure of the Si $L_{2,3}$ and B K will be examined over time and with special consideration of projected dopant position. While etching eliminates the plasmonic response, subsequent annealing causes it to return, suggesting a strong role of the surface and oxidation states coupled with the presence of boron, also necessitating study of the O K edge. Correlation of these effects with changes in fine structure will elucidate role of dopant incorporation in the particles as it relates to modifications in the nanoparticle electron structure.

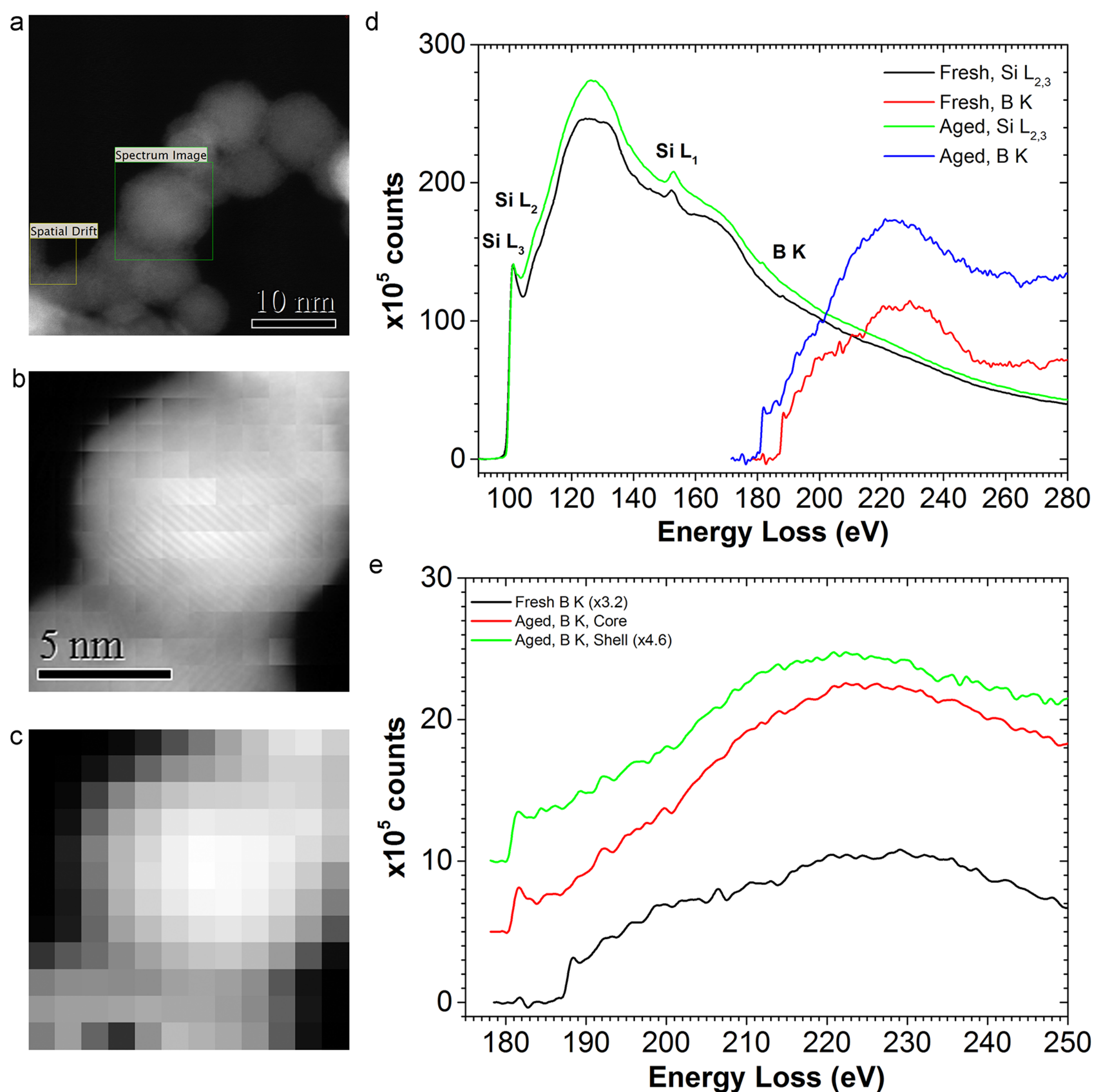

Figure 2.10: STEM-EELS of fresh and aged 10%nom. B-doped Si nanocrystals. (a) Survey image of a chain of Si nanocrystals extending off carbon grid over vacuum. (b) Subpixel-scanned ADF-STEM image during spectrum imaging. (c) High-loss spectrum image. (d) Background-subtracted Si $L_{2,3}$ and B K edges of fresh and aged nanocrystals. (e) The B K edges of fresh particles and particles aged for two days with comparison of core and edge of particle. A red-shift in edge onset from 187.2 eV to 180.2 eV is observed in conjunction with the plasmon resonance in FTIR. Particles were synthesized by Nicolaas Kramer and Katelyn Schramke.

2.4.2 Energy-dispersive X-ray spectroscopy

Inelastic scattering of an incident electron with an inner-shell electron can result in ejection of that electron into an unoccupied, leaving a hole in the inner shell. When an outer shell electron relaxes into the unoccupied hole of the ionized atom the excess energy is emitted as an Auger electron or an X-ray. The energy of the electron or X-ray is then characteristic of the energy difference between the initial and final states of the relaxed electron. These characteristic energies are unique to the allowed electronic transitions between orbitals. The collection of the X-rays or Auger electrons can then provide a fingerprinting of the irradiated material. In the case of STEM, the chemical resolution is defined by the size of the electron probe as it passes through an electron transparent specimen. An example of such capabilities in an FEI Titan are described in Section 2.9.4.

2.5 Aberration-corrected TEM

The state of the art in TEM has advanced rapidly in the last twenty years thanks to the development of spherical aberration correctors. A primary limitation of spatial resolution in TEMs has spherical aberration C_s, which in symmetric electromagnetic lenses is always positive as proved by Scherzer [100]. In 1947 the use of multipole lenses to produce fields with negative C_s to correct for the positive C_s induced by the rest of the optical column, proposed again by Scherzer [101]. It was not until the late 1990s, though, that electronics and signal processing had advanced to the point that the numerous lenses and correction algorithms could be integrated into a commercial instrument. As it is not a focus of this work, the science behind aberration correction will be left to existing literature [102–105].

2.6 *In-situ* heating

Heating experiments performed *in-situ* in the TEM utilized a Gatan 652 double-tilt heating holder inserted into the FEI Tecnai F30 Cryo (S)TEM. The Gatan 652 is a furnace-style heating holder, utilizing resistive heating across the specimen “cup” which is separated from the rest of the holder by ceramic beads. The specimen is held in place

by a hex screw and temperature feedback is provided by a thermocouple incorporated in the furnace. The 652 temperature controller was replaced by a Keithley Instruments 2611A sourcemeter and temperature was calibrated to applied voltage by slowly ramping voltage and measuring temperature. Heating to greater than 600 °C requires a slow ramp on the order of 30 min to aid in thermal equilibrium. The 652 is susceptible to substantial lateral thermal drift upon heating and cooling, requiring the operator to track a region of interest while ramping.

The Characterization Facility has also procured a Protochips Aduro four-electrode heating and electrical holder. Using a thin SiC nanoparticle membrane suspended over vacuum on a silicon chip, the Aduro utilizes Joule heating of the SiC membrane by applied voltage. The extremely small volume of the SiC membrane, the carbon support film, and the specimen means that the temperature can be ramped up and down rapidly, on the order of a few seconds. Most thermal drift is in the Z direction, minimizing the need to use the stage to track X-Y movement, instead allowing the operator to adjust only in Z or defocus. The current technology, however uses an open loop system whereby each chip is individually calibrated using an infrared microscope. This proved problematic in the thin film heating experiments due to the deposited film's differing thermal emissivity. The specimen, within the vacuum of the column, dissipates the majority of its energy by radiation when heated, rather than convection or conductivity through the large, thin membrane. Radiative heat transfer obeys the Stefan-Boltzmann law, $P = \epsilon\sigma A T^4$, where P is radiated power, ϵ is emissivity, σ is a proportionality constant, A is surface area, and T is temperature. In the case of the SiC membrane, ϵ is roughly 0.85 to 0.95, while the emissivity of silicon varies drastically from 0.1 at room temperature to 0.7 above 500 °C [106, 107]. It should also be noted that consideration of thin film effects must also be considered [108]. In any case, the reduced emissivity compared to that of the calibrated SiC carbide leads to a greater retention of applied energy and therefore an underestimate of the actual temperature. This was seen experimentally as the 100 nm a-Si:H films flash-crystallized at temperatures where the crystallization process should take many hours. Nevertheless, such heated stage platforms provide an excellent vehicle for studying isolated materials such as nanoparticles at high-resolution and high-temperature. Access to infrared microscopes

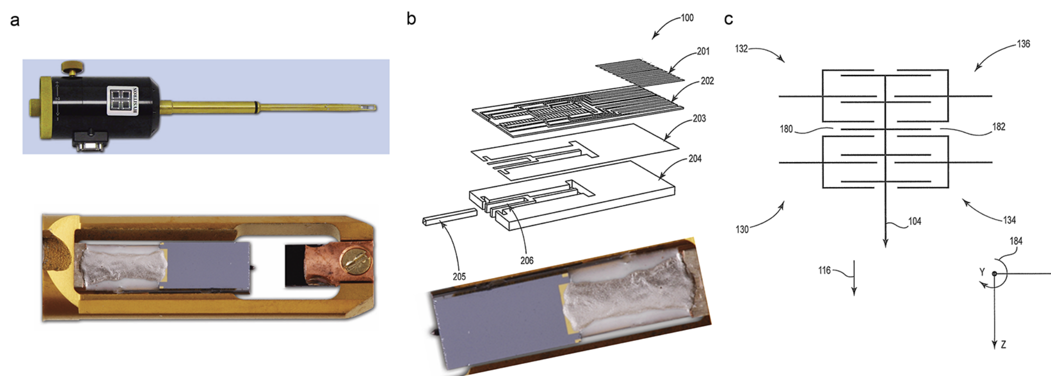

Figure 2.11: (a) Image of Hysitron PI95 PicoIndenter and closeup of the sample region. (b) Diagram and image of the MEMS transducer design. (c) Schematic of the four capacitive comb devices. Adapted from Oh *et al* [4].

for "benchtop" calibration of thin film specimens or closed-loop Joule-heating holders such as the new FEI NanoEx-i/v should eliminate such practical challenges.

2.7 *In-situ* mechanical testing

The Hysitron PI95 PicoIndenter is a uniaxial deformation holder designed for *in-situ* compression or tensile testing of materials inside the TEM. The PI95, Figure 2.11a, is comprised of a diamond indenter placed on a 3-axis moveable stage within the center of the TEM holder. Coarse mechanical adjustments on the back end of the holder allow for gross movement of the stage up to a few hundred microns in the TEM Y- and Z- axes and insertion/retraction over many millimeters along the TEM X-axis. Partway along the indenter stage is a 3-axis piezoelectric crystal enabling fine, nm-scale, adjustment over many microns for alignment of the diamond indenter with the specimen.

The indenter itself is comprised of a micromachined comb drive, aka "MEMS transducer," allowing fine uniaxial displacement of the indenter, Figure 2.11b. The MEMS tranducer allows for closed-loop feedback of instantaneous load and displacement and can be actuated to apply load to a specimen through displacement- or load- control. The micromachined comb drive itself consists of four banks of microfabricated comb capacitors, depicted in Figure 2.11c. One set of the combs are attached to the diamond indenter while the other set are secured to the substrate. The entire assembly is held

in place by MEMS springs, stabilizing the drive unit orthogonal to the indentation axis while providing a spring-force resistance to displacement in the indentation axis.

The force exerted by the capacitor is proportional to the overlapped comb area, comb spacing and applied voltage as given by

$$F_d = \frac{\epsilon bh}{2d^2} V^2, \tag{2.9}$$

where F_d is the electrostatic force , ϵ is the permittivity of free space, b is the comb width, h is the comb height, d is the comb spacing, and V is the applied bias. The exceptionally large surface area of comb capacitors allows for greater sensitivity in the comb spacing, and hence sensitivity to load. In the case of the MEMS transducer design employed by Hysitron, four banks of differential capacitors are used to determine the instantaneous displacement of the indenter as per the equation for capacitance combination ratio [4]

$$CCR_I = \{(C_A + C_D) - (C_B + C_C)\} \, / \, \{(C_A + C_D) + (C_B + C_C)\} \tag{2.10}$$

which is calibrated to the spring constant of the stabilizing springs as determined by load- and displacement-controlled actuation of the free indenter in vacuum.

Use of the MEMS-based system has grown rapidly since its introduction. Having load and displacement resolutions of 0.02 µN and 0.2 nm with maximum instantaneous excursions of about 0.1 µN and 1 nm, extremely precise information on load and displacement can be coupled with the imaging, diffraction, and spectroscopy capabilities provided by the (S)TEM. Unprecedented insights into the nano- and atomic-scale responses to mechanical deformation have resulted [38,40,41,43,44,46,47,109–114] as will be explored in Chapter 4 and Chapter 5.

2.8 Specimen preparation techniques

Preparation of specimens for electron microscopy can often be as challenging as the microscopy itself. Not only must each specimen be of the appropriate thickness, typically much less than 100 nm, but it must represent the material of interest without deformation, structural changes, or contamination. Some samples, such as the nanocrystals

synthesized by plasma reactors in the Kortshagen group, can be easily deposited directly on TEM grid. Others, such as the formation of sub-50 nm pillars of a complex oxide for the *in-situ* experimentation discussed in Chapter 5 require careful FIB milling followed by chemical etching and decontamination. Drop-casting of colloidal suspensions is generally quite trivial, but the solvents used can leave unwelcome hydrocarbon contamination that must be addressed. For every material of interest there often exists a number of choices in specimen preparation, but choosing the right can be as critical as the analysis to be performed. In this section various specimen preparation techniques utilized through my time at the University of Minnesota are discussed.

2.8.1 Drop-casting

Drop casting of colloidal solutions of nanoparticles or nanosheets suspended in solvent directly onto TEM grids can result in well-distributed nanoparticles for individual high-resolution analysis or particle sizing. Often, however, agglomeration of particles can complicate analysis. Appropriate choice of solvent and controlled rate of evaporation can aid in distribution of particles on the TEM grid, even generating monolayers and superlattices.

2.8.2 Direct deposition of nanoparticles and thin films

The gas-phase synthesis of nanoparticles and thin films such as those studied in Chapter 3 and Chapter 4 allows facile preparation of TEM specimens by depositing particles or films directly onto TEM grid. Exposure time of the grid to the particle beam or film deposition plasma then controls the density or thickness of the specimen. This process has a distinct advantage over drop-casting in that solvents can be entirely avoided. Grids can be decontaminated immediately prior to deposition by heating to 125 °C or more in vacuum for a few hours. The samples can then be quickly loaded into the TEM without worry of contamination under the electron beam. The particles can then be studied as close to their as-synthesized state as possible or allowed to, for example, oxidize or be subjected to heat treatment directly on the TEM grid.

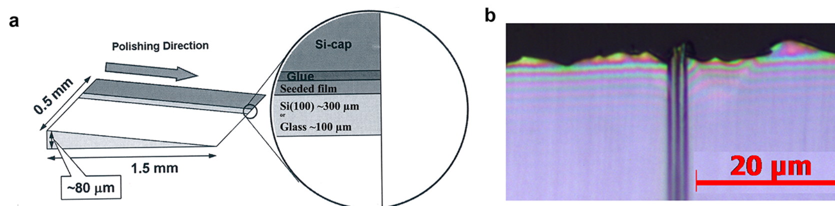

Figure 2.12: (a) Schematic of an ideal wedge after wedge-polishing and (b) optical micrograph of the thin edge of a Si wedge.

2.8.3 Mechanical wedge polishing

The wedge-polishing method, described well by Voyles *et al* [115], can be employed to examine specimen cross-sections of region of interest that is extremely thin (20 nm to 100 nm). A wedge schematic and experimental wedge of Si with oxide can be seen in Figure 2.12a. Ideal materials are crystalline and well-bonded to a hard substrate such as silicon.

Samples are cleaved into small sections typically 1 cm on a side. The side of interest is then glued to a support substrate, typically a Si(100) wafer piece, using M-Bond^{TM} 610 epoxy-phenolic resin. Two specimens can also be glued to each other, doubling the available electron-transparent material per wedge. The glue-line thickness must be minimized in order to ensure mechanical stability of the sample during mechanical polishing. Pressure is applied to the specimen using a spring-loaded, custom-designed clamping system to minimize the glue-line thickness. The clamping system is placed in a vacuum oven at 100 °C for one hour to cure the glue. The specimen is subsequently adhered to microscope slide using Crystalbond^{TM} wax. A dicing saw is used to cut the specimen into small square pieces about 2 x 2 mm. The small pieces are removed from the glass slide and washed in acetone and rinsed in methanol. A small piece is chosen for further preparation and the rest are set aside for later use. The small specimen is adhered to a glass stub with super glue. The specimen is oriented so that the glue line will run parallel with the rotation during polishing.

Specimens are polished into a wedge using an Allied High Tech TechPrep polishing wheel with Multiprep sample holding assembly. The glass stub is mounted to the Multiprep assembly which can be tilted at 0.02° increments to variable angle of incline with respect to the polishing wheel. Diamond lapping films of progressively finer grid

(30, 15, 6, 3, 1, 0.5, and 0.1 µm grit sheets) are used to create a smooth, uniform surface. During lapping, the assembly oscillates along the radius of the polishing wheel to maximize use of the polishing pad and the user holds a Kimwipe against the polishing pad to remove debris from the polishing process. At the end of each step, the surface is examined by optical microscope to confirm a smooth surface. For fully crystalline specimens, a subsequent step using 0.02 µm colloidal silica slurry placed on a cloth pad can used to smooth the surface, but can create unwanted contamination.

Upon completion of the first side, the specimen is removed from the glass stub by soaking in acetone and then rinsed in methanol. Care must be taken so as not to damage the polished surface as the specimen is re-glued to the glass stub, polished side down, with the glue-line oriented parallel to the polisher rotation. The glass stub is attached to the holding assembly and tilted 2 to 4° with respect to the polishing wheel so that the polishing direction will be towards the wedge tip, as seen in Figure 2.12. Again, the wedge is polished with lapping films of decreasing roughness. The specimen inspected by optical microscope, however this is appropriate down to about 0.5 µm films after which the fringing effect due to varying thickness at the optically transparent wedge tip, Figure 2.12b, is relied upon for end-point determination.

After finishing the second side, the sample is dismounted and glued using M-Bond to a 3 mm copper washer for handling and insertion into the TEM. After polishing the second side, the sample is extremely thin and must be handled with care. For mounting, the specimen is left in the dish used for washing and placed on a height-adjustable stage positioned under an optical microscope. The copper washer is held above the stage and in-focus by a vacuum wand. The stage is slowly raised until the wedge, positioned so that the wedge tip is towards the center of the washer, makes contact with the glue. The stage is then lowered and the grid cured in the vacuum oven on a Teflon block for 1 hour at 100 °C.

2.8.4 Small-angle cleaving technique

The small angle cleaving technique offers a much faster alternative to the wedge polishing method, particularly when there is an abundant supply of the material of interest. While the electron transparent area is typically limited to a few hundred nanometers, the procedure can yield many samples with relatively little work as compared to the

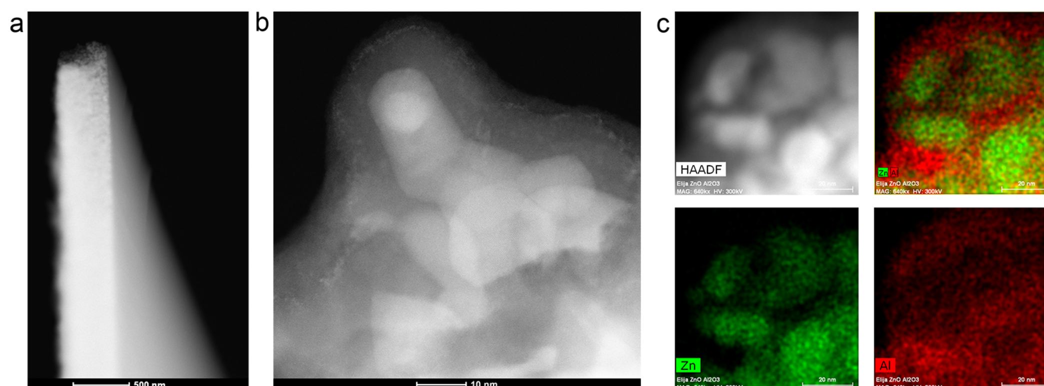

Figure 2.13: (a) Low-magnification ADF-STEM image of the thin tip of a SACT-cleaved Al_2O_3-back-filled ZnO nanoparticle film on Si. (b) High-magnification ADF-STEM image of ZnO particles in Al_2O_3 matrix. (c) EDX maps of Zn and Al from the SACT specimen [5].

wedge polishing method. Such an approach was recently used to study the composition thin films of gas-phase deposited ZnO nanocrystals in-filled with an ALD Al_2O_3, shown in Figure 2.13 [5].

The small-angle cleaving technique relies on thinning a crystalline substrate to the point that it can be fractured along non-preferred crystallographic plane at a shallow angle to an easy-cleave plane resulting in a long, thin wedge whose tip is electron transparent [116]. A typical approach is as follows: Bulk samples are cleaved to smaller than 1 cm^2 and bonded film-side down to a parallel polishing fixture using CrystalBond 509. The samples are then thinned to less than 100 µm using an Allied Multiprep and 30 µm diamond lapping film. The sample is oriented to the polishing direction such that scratches were aligned approximately 10° from the easy-cleave [110] direction. Using a metal ruler and diamond scribe, deep scratches are created along the polishing direction approximately 1 mm apart. The sample is then removed from the polishing fixture using acetone and placed in a petri dish containing a glass slide. The specimen is carefully cleaved along the scratches using tweezers and the edge of the glass slide. These pieces are then cleaved again along the easy-cleave plane using the tweezers and edge of the glass slide. Samples having a sharp tip are mounted to slot-type Mo TEM grids using MBond 510 epoxy.

2.8.5 Focused-ion beam

Focused ion beam milling is used in microscopy for site-specific imaging, deposition, and more importantly removal of material from a larger specimen. Ions are accelerated to high energy, typically 1 keV to 30 keV, and focused through a series of lenses much like the electron beam of a scanning electron microscope to image. The most common ion source is gallium due to its low melting point, low volatility, and low vapor pressure. The ion beam can be focused to very small probes, allowing imaging and local sputtering of material with a resolution smaller than 5 nm. The instrument at the University, an FEI Quanta 200 3D, described in Section 2.9.5, is a dual-beam system incorporating a vertical electron column and an ion column rotated by 52° with a coincident eucentric point, allowing electron beam imaging and ion beam milling of material. Electron-transparent cross-sections created from larger samples, referred to as lamella, can be produced with relative ease, used to study thin films in Chapter 3, in addition to more complex structures such as nanopillars utilized in Chapter 5. A comprehensive description of the instrument and methodology can be found in the book by Giannuzzi and Stevie [117].

While regularly used to create electron-transparent cross-section of electronic materials such as the heteroepitaxial films of InAs grown on GaSb discussed in Section 2.9.4, FIB milling finds use in a variety of applications. In collaboration with Zhang *et al* [6] we looked at the micron-scale disproporationation of phases in an iron silicate material compressed in a diamond anvil cell to over 90 GPa at temperatures exceeding 2200 K. These complex samples microporous, 30 µm diameter by 4 µm thick, and very rare - presented a unique challenge to prepare by FIB.

An example lamella during liftout and after thinning is found in Figure 2.14. The products from the $(Mg_0.85Fe_0.15)SiO_3$ (Fs15) starting material examined in the paper were synthesized at 101 GPa and 2200 K to 2400 K in a Ne medium and subsequently decompressed and recovered to ambient conditions for *ex-situ* transmission electron microscopy (TEM) study. An FEI Quanta 200 3D focused ion beam (FIB) instrument was used for the preparation of TEM specimens. A lamella of approximately 10x5x2 µm was cut by FIB from the center potion of the laser heated spot in the recovered sample. The lamella was attached to a tungsten needle by platinum welding and lifted out with an Omniprobe Figure 2.14a. The lamella was then welded to a Cu grid and further

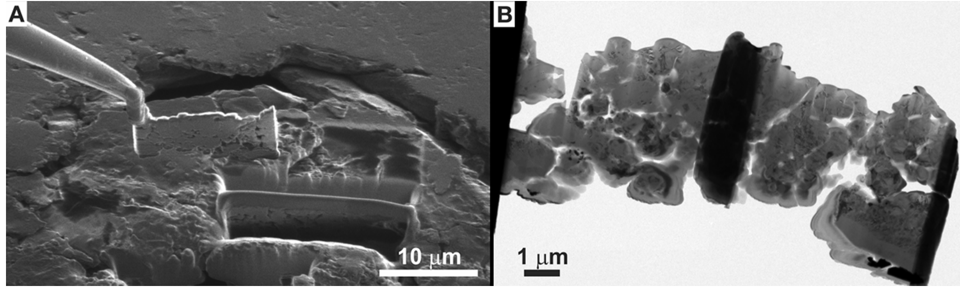

Figure 2.14: TEM specimen prepared by FIB. (a) Lift-out of a lamella using an Omniprobe and (b) conventional TEM-BF image of the specimen [6].

thinned to about 200 nm for TEM analysis Figure 2.14b. The bright-field (BF) and annular dark-field (ADF) scanning transmission electron microscopy (STEM) images were obtained using a FEI Tecnai G2 F30 S-TEM equipped with an energy dispersive x-ray (EDX) spectrometer operated at accelerating voltage of 300 keV. The STEM has semi-convergent angle of 9 mrad and ADF detector inner angle of 31 mrad. The EDX mapping with a size of 100x50 pixel^2 was performed at a scanning rate of 500 ms/pixel with drift correction. Each individual EDX spectrum was collected for 60 s.

The sample section demonstrated both compositional and phase heterogeneities. To explore the nature of the heterogeneities and their correlation to the in-situ XRD data, we performed STEM-EDX mapping, compositional analysis, and selected area electron diffraction (SAED) for each phase (Figure S5). The EDX data suggested that $MgSiO_3$ is the dominant phase in position 1 Figure 2.15k and the BF image and SAED pattern indicate that the phase is well crystallized Figure 2.15a,g, confirming the Fe-depletion in the pv phase. A small piece of crystalline SiO2 was found in the position 2 Figure 2.15h,l, consistent in quenchable structure and overall quantity with the excess SiO_2 in the starting composition and the *in-situ* XRD observations. Unlike the quenchable crystalline $MgSiO_3$ pv, the ultrahigh-pressure H phase is highly unstable at ambient conditions and further decomposed during the sample preparation process for STEM Figure 2.15i-j,m-n, so its properties must be studied in-situ at high pressures. The SAED patterns show that the iron-oxide rich phase in position 3 is crystallized Figure 2.15e, i, and m and the iron-free phase in the neighboring position 4 is amorphous Figure 2.15j. Nevertheless, the integrated composition of the iron-oxide crystals and the coexisting amorphous phase is close to the Fe-rich $(Mg,Fe)SiO_3$.

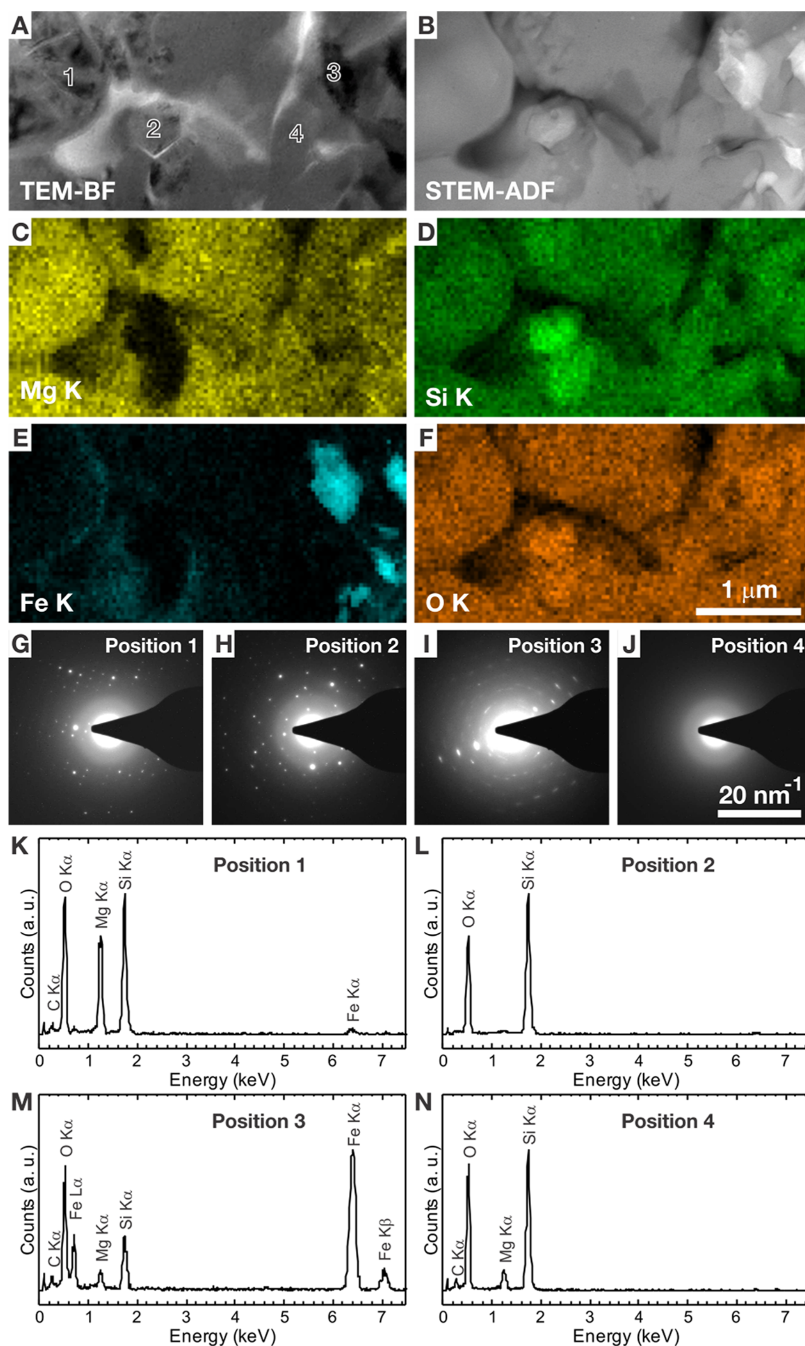

Figure 2.15: STEM analysis of the recovered products. (A) TEM-BF image, (B) STEM-ADF image and (C-F) corresponding STEM-EDX maps(C) Mg K, (D) Si K, (E) Fe K, and (F) O Kare presented. STEM-ADF and EDX maps were obtained simultaneously. (G-J) SAED patterns and (K-N) EDX spectra were also obtained from the positions indicated in (A) [6].

An additional important consideration in preparation of FIB lamellae and nanopillars is that the same process that enables localized sputtering of material also induces local damage and ion implantation of the specimen. This damaged layer can be many tens of nanometers with a 30 keV ion beam, leading to substantial modification of the material of interest when not performed carefully [118–120]. This is highlighted in Chapter 5 where the creation of sub-100 nm pillars without any damaged layer was crucial for the analysis of electronic structure of the original material. Another example of the deleterious effects for lamella formation can be seen in the next section where a follow-up low-energy ion milling step was required to remove a damaged layer which interfered with high-resolution imaging of a crystalline film.

2.8.6 Ion milling

Ion milling involves energetic ion bombardment of a specimen to sputter surface material and can be used to thin samples that are too thick or to remove surface contamination. As opposed to FIB, argon ions are used for ion milling since argon is inert, heavy, and unlike gallium is an uncommon constituent of most materials of interest. The specimen is milled from both sides in order to uniformly thin the film and remove surface contamination. Accelerating voltage, current, specimen temperature, angle of incidence, and sample rotation can be modified to create an ideal recipe for the material of interest. The angle of incidence is typically kept below 10° in order to prevent implantation, however the rate of thinning is reduced with reduction in angle. The sample is rotated to prevent grooving of the sample due to directional bombardment. A higher-energy step of 3 keV to 5 keV is used for thinning and is followed by a lower-energy final step below 2 keV.

The substrate can be cooled with liquid N_2 in order to reduce the risk of specimen heating by the incident ions. The ion energy is kept as low as possible to minimize the inherent implantation of incident ions. The low angle of incidence also serves to reduce this effect. The substrate rotation serves to reduce any surface structure (grooves) due to the anisotropic ion incidence. TEM images of a FIB-milled lamellae of InAs grown on GaSB before and after ion milling can be seen in Figure 2.17. The pre-milled specimen is opaque to the electron beam while the post-milled specimen has a large electron-transparent region.

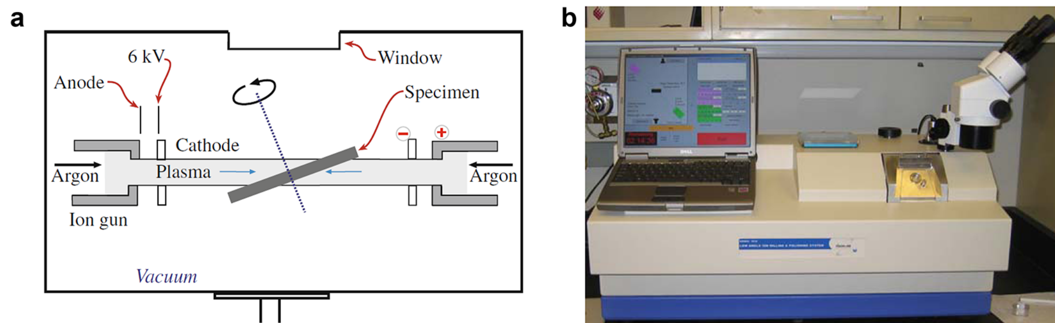

Figure 2.16: (a) Schematic of an ion-beam thinning machine. Argon gas enters two ionization chambers where ion beams are accelerated towards the specimen in equal and opposite direction. The specimen is tilted for low-angle impingement [1]. (b) The Fischione 1010 ion mill in the UMN Characterization Facility.

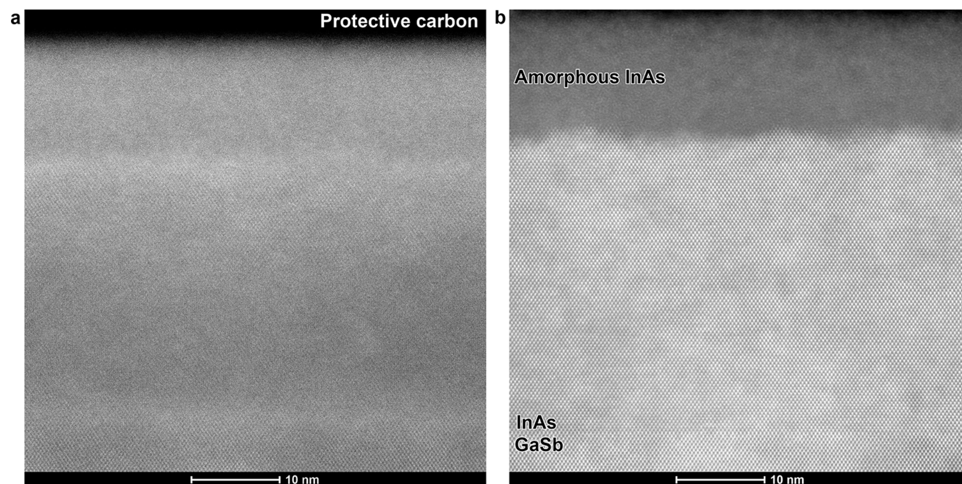

Figure 2.17: (a) ADF-STEM image of an InAs/GaSb FIB lamella created with 30 keV Ga^+ ions and (b) the same lamella after thinning and polishing with 1.5 keV Ar ions.

2.8.7 Specimen Contamination

Buildup of contamination on the sample and TEM holder surfaces is an ever-present nuisance in electron microscopy. As the beam passes through the specimen, hydrocarbons are attracted to the surface, building up and reducing image contrast. Plasma cleaning is a standard method for removal of hydrocarbon contamination on the specimen and TEM holder which is performed immediately before insertion of a specimen into the TEM. The TEM holder, with specimen, is inserted into a vacuum chamber. The holder and specimen are positioned within an inductively coupled oxygen plasma and a mixture of energetic electrons and ions bombard the surface, reacting with hydrocarbons to produce carbon-oxygen complexes which are removed by the vacuum pump.

Plasma cleaning, however, is not always suitable for decontamination of a specimen. The oxygen plasma is highly reactive with carbon, removing the amorphous carbon film of a TEM grid in a matter of seconds. Additionally, specimens of interest such as graphene cannot be cleaned by this method. An effective complement to plasma cleaning is the heating of the specimen under high vacuum in order to remove contamination. A high vacuum system, seen in Figure 2.18, was developed to heat multiple TEM grids by tungsten filament. A steel sample carrier capable of holding seven specimens slides onto a dovetail within the vacuum chamber. The carrier is positioned below a tungsten filament and temperature is monitored by a thermocouple placed on the carrier surface. The pumping system is a custom BMH70 turbo pumping system from Oerlikon Leybold, Inc having a TMP70 turbomolecular pump backed by an oil-free diaphragm pump. The control unit has been customized to send a trigger signal to a silicon-controller rectifier (SRC) based temperature controller which controls a tungsten filament within the vacuum. A trigger pressure, delay time, and heating time can be set. Upon completion, the turbopump remains on until the user vents the chamber with nitrogen for transfer to the TEM holder. Samples can be heated to 100 to 200 °C at a base pressure below 5E-7 torr. Direct heating of TEM grids by the lamp can heat the TEM grid significantly higher than the thermocouple, leading to diffusion of the grid material (e.g. copper) onto the sample. To alleviate this, aluminum foil is placed above the TEM grids to prevent direct radiation of the samples.

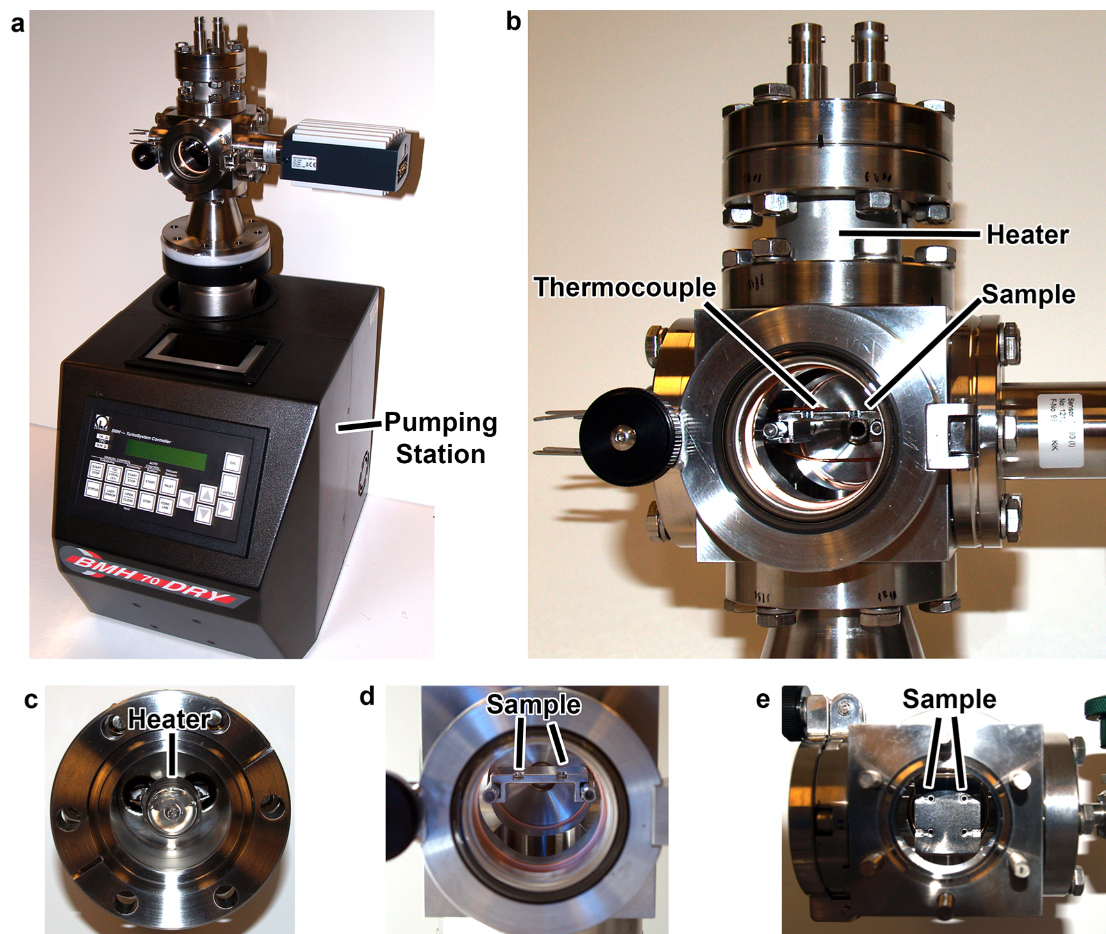

Figure 2.18: (a) Image of the high-vacuum heating system. A custom Leybold BMH70 pumping station has been modified to send an output to a temperature controller. Signal setpoint is based on set pressure, delay time, and heater on time. (b)-(d) IImages of the disassembled vacuum system displaying the tungsten filament and sample carrier. Filament sits above sample which is inserted on carrier via dovetail.

2.9 Electron microscopes at University of Minnesota

The University of Minnesota's Characterization Facility is home to a suite of electron microscopes serving the university and local industry. There are currently seven microscopes capable of conventional TEM operation: a JEOL 1200EX, an FEI Tecnai T12, an FEI Tecnai BioSpirit, two FEI Tecnai F30s, and a probe-corrected FEI Titan 60-300; the latter three also capable of STEM operation.

2.9.1 FEI Tecnai G2 T12 (S)TEM

The workhorse of the Characterization Facility is an FEI Tecnai T12, a thermionic emission TEM operating at 120 keV with CTEM imaging and diffraction and EDX capabilities. This microscope is the first TEM that facility users are permitted to use. Capable of spatial resolutions below 3.5 Å, this instrument satisfies the majority of user needs in determining structure of materials or, for example, examining nanoparticle sizes. The T12 is also equipped with an Oxford INCA EDX system for compositional analysis.

2.9.2 FEI Tecnai G2 F30 (S)TEM

The FEI Tecnai G2 F30 FEG (S)TEM is equipped with Schottky field emission gun, SuperTWIN pole piece (C_s = 1.2 mm), EDX system, and a Gatan Enfina 1000 EEL spectrometer. The instrument is capable of operating at 300, 200, and 100 keV with manufacturer-listed resolution at 300 keV of 2.0 Å point-point in CTEM and 1.9 Å in STEM. The SFEG source provides an energy resolution better than 0.8 eV at 300 keV accelerating voltage. This instrument is shown in Figure 2.1b. *Ex-situ* analysis of the seeded a-Si:H films in Chapter 3 as well as the *in-situ* STEM-EELS experiments of Chapter 5 utilized this instrument.

2.9.3 FEI Tecnai G2 F30 Cryo (S)TEM

The FEI Tecnai G2 F30 FEG Cryo (S)TEM is equipped with Schottky field emission gun, TWIN pole piece (C_s = 2.0 mm), and a Gatan GIF2002 energy filter. The instrument is capable of operating at 300, 200, and 100 keV with manufacturer-listed resolution at 300 keV of 2.4 Å point-point in CTEM and 2.4 Å in STEM. The SFEG

source provides an energy resolution better than 0.8 eV at 300 keV accelerating voltage while the GIF enables EELS mapping in CTEM and STEM. The GIF2002 also has an analog TV-rate camera, typically used for beam alignment, which is used in our experiments for TV-rate image acquisition during *in-situ* experiments. This instrument has proved vital for the *in-situ* heating and deformation experiments discussed in Chapter 3 and Chapter 4

2.9.4 FEI Titan G2 60-300 (S)TEM

The FEI Titan G2 60-300 (S)TEM is equipped with an X-FEG source, analytical Super-TWIN pole piece, monochromator, and DCOR probe corrector. The microscope has CCD camera, a BF-STEM detector, three ADF-STEM detectors, four-quadrant SuperX EDX detector, and Gatan Enfinium ER EEL spectrometer. The microscope is capable of operating at 60, 80, 200, and 300 keV with achieved spatial resolution better than 0.63 Å at 300 keV. The monochromator has allowed us to achieve EELS energy resolution better than 0.15 eV. The Titan has a three condenser lens system which allows parallel illumination in CTEM over a large dose range. The monochromator system likewise allows control over beam dose without adjustment of convergence angle. It is equipped with a CEOS DCOR double C_s corrector, capable of making correction for aberrations including 4th order and 5th order. ADF-STEM images with resolution better than 0.8 Å at 200 keV and 0.65 Å at 300 keV can be routinely achieved. The Gatan Enfinium ER spectrometer provides the unique capability of collecting zero/low-loss and core-loss spectra in effectively simultaneously, greatly expanding the spectroscopic range of STEM-EELS analysis while simplifying alignments of characteristic edges in the spectrum. Combined with the monochromator, fine structure of core-loss spectra can be examined while taking advantage of the high brightness of the Schottky FEG.

The aberration-corrected Titan provides an unprecedented ability to probe the atomic-scale structure of materials through STEM imaging and spectroscopy. For example, the structure and properties of Esaki diodes comprised of InAs:GaSb tunnel junctions were examined to elucidate the differing performance of devices grown by two different groups. The films were comprised of a 50 nm layer of Si-doped InAs, on a 3 nm intrinsic layer of InAs, on a 20 nm layer of Be-doped GaSb grown on a GaSb substrate.

Cross-section specimens were prepared using FIB and then ion milled to remove the FIB-induced damage and further thin the lamellae. The film structure of the poorer performing devices were found to have a 10 nm to 13 nm amorphous layer on a 33 nm to 36 nm layer of crystalline InAs. No planar defects or dislocations were observed in the film, owing to the very small lattice mismatch of GaSb and InAs, about 0.6%. High-resolution imaging of the interface, not shown, revealed an interface comprised of InSb. Geometric phase analysis of the interface showed it to have a 6% increase in atomic spacing across the interface, equal to the lattice mismatch between GaSb and InSb.

The second film, having superior device performance, is seen in Figure 2.19. The unfiltered HAADF-STEM image in Figure 2.19a was low-pass and high-pass filtered with Gaussian cutoffs of 0.8 Å and 60 Å, respectively, seen in Figure 2.19b and its FFT in Figure 2.19d. Highlighting the exceptional value of Z-contrast imaging, the [110] dumbbells of InAs on GaSb can clearly be seen above and below the interface, respectively. The changing Z of the lighter elements Ga (Z = 31) and As (Z = 33) and heavier elements In (Z = 49) and Sb (Z = 51) leads to a substantial change in contrast in the dumbbells above and below the interface. The inset provides an averaged line scan revealing the reduction of intensity across the interface indicating an GaAs interface. This is the opposite observed in the poorer-performing device.

Utilizing the exceptional efficiency of the SuperX EDX detector, spectrum images of the interface were acquired over an area of 11 by 11 nm in five minutes. A line scan with pixels parallel to the (001) GaSb:InAs interface can be seen in Figure 2.19c. The oscillations in each signal match the atomic positions in the lattice. As is clear by the weak contrast, however, the chemical resolution is not equivalent to the imaging resolution as can also be seen when comparing the apparent 3 nm width of the interface in the EDX line scan compared to the atomically abrupt interface in the HAADF-STEM image. The periodicity of the lattice coupled with electron channeling masks the spread of the probe as it passes through the sample. Regarding chemical resolution, inelastic scattering of electrons that have shifted to nearby columns, exacerbated by sample thickness and the large convergence angles used in aberration-corrected STEM, leads to X-ray generation from regions of the specimen outside of the probe position.

GaSb specimens were studied at 200 keV accelerating voltage with a probe current of 50 pA for imaging and 150 pA for EDX. Probe convergence angles of 10 mrad and

23 mrad were used when studying the poorer and superior devices, respectively, giving a spatial resolution of 1.0 Å and 0.8 Å. A measured inner angle of 54 mrad was used for HAADF-STEM imaging. STEM-EDX spectrum images were acquired using Bruker Esprit with a pixel dwell time of 24 µs and summation of 33 frames yielding a total pixel dwell time of about 800 µs.

2.9.5 FEI Quanta 200 3D dual-beam FIB

The FEI Quanta 200 3D dual-beam FIB located within the Nanofabrication Center is a two-column design consisting of thermionic emission electron source and Ga^+ ion source for site-specific milling of material. The electron beam serves to image the region of interest in a non-destructive manner while the ion beam is used to form, for example, electron-transparent lamella for cross-sectional TEM analysis or "FIB pillars" for mechanical deformation testing. The ion beam is currently only capable of 30 keV operation, creating amorphous layers greater than 10 nm with implanted Ga at up to three times this depth. This necessitates post-FIB sample processing such as ion milling or chemical etching to remove the damaged layers.

2.9.6 Jeol 6500 and 6700 FEG SEMs

The two SEMs used in the work here are the JEOL 6500 and 6700 SEMs. Both instruments have Schottky field emission sources. The 6500 includes an EBSD detector, CL detector, and EDX detector. Both systems have secondary and backscattered electron detectors.

2.10 Si NC synthesis

Si nanocrystals were synthesized in a flow-through plasma reactor [121], consisting of a 48 mm diameter, 610 mm long glass tube, Figure 2.20a. Both ends were terminated by grounded ultra-torr fittings. The bottom ultra-torr fitting contained a 6 mm thick stainless steel plate having a small orifice 1 mm in diameter on the plasma side and opening to 4 mm diameter on the exit side. The orifice acted as a convergent-divergent aerodynamic nozzle accelerating the effluent gas, creating an expanding particle beam to which the substrate is exposed. 13.56 MHz RF power was applied to a 6 mm tall ring

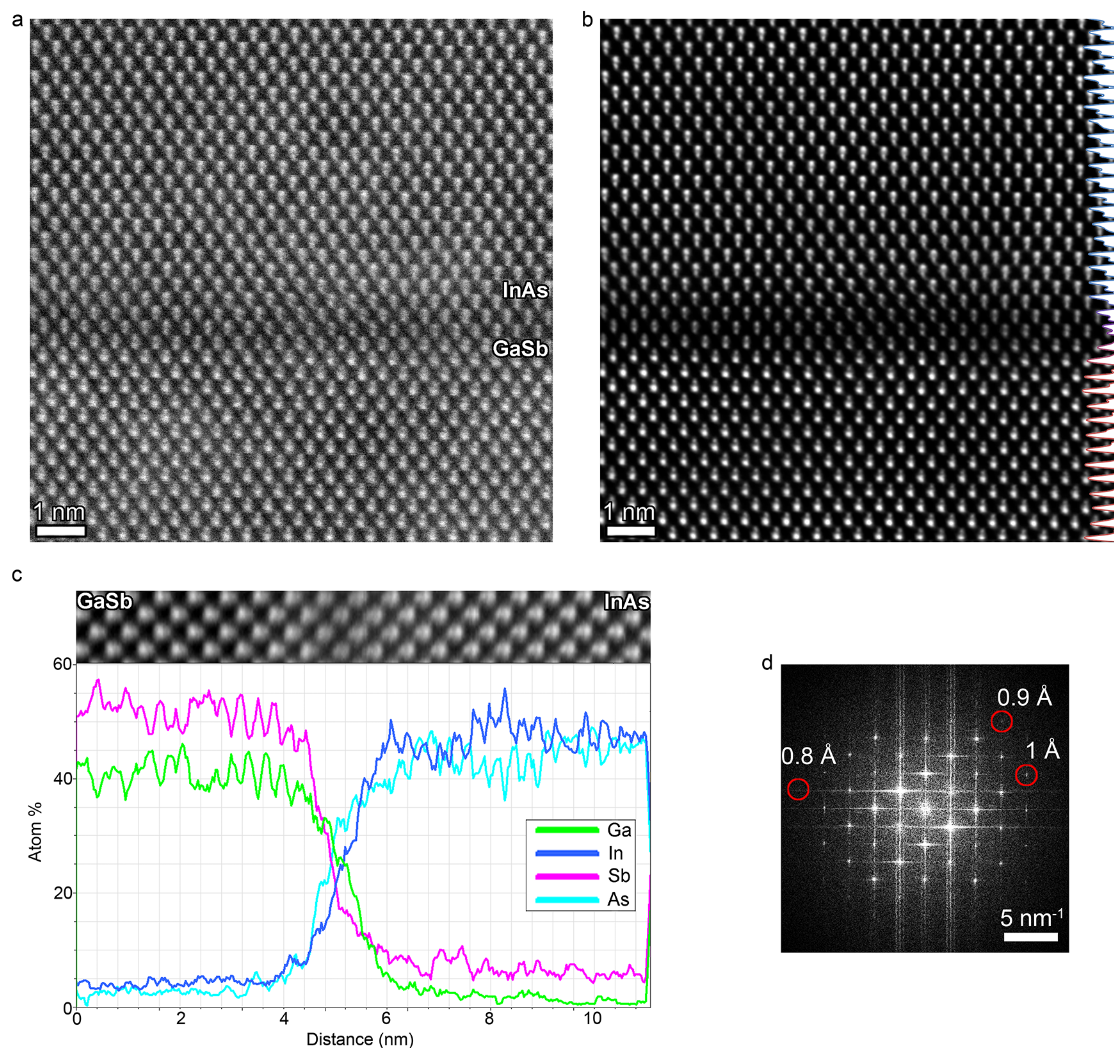

Figure 2.19: (a) Unfiltered HAADF-STEM image of InAs grown on GaSb, acquired at 200 keV with 50 pA probe current, 12 µs dwell time, 23 mrad convergence angle, and 54 mrad inner acceptance angle. (c) The same image Fourier-filtered to remove information below 0.8 Å. The reduced intensity at the interface, plotted as a horizontally averaged line scan on the inset right, suggests an interface comprised of the lighter elements Ga and As. (c) STEM-EDX line scan created from a spectrum image and averaged along the (100) plane. The oscillations in the line scan correlate with the respective atomic position. The mismatch in Ga:Sb ratio suggests improper k-factors for quantization. The relative increase of Ga and As across the interface correlate with the reduced intensity observed in the HAADF-STEM image. (d) The FFT of the HAADF-STEM image demonstrating image resolution of 0.9 Å.

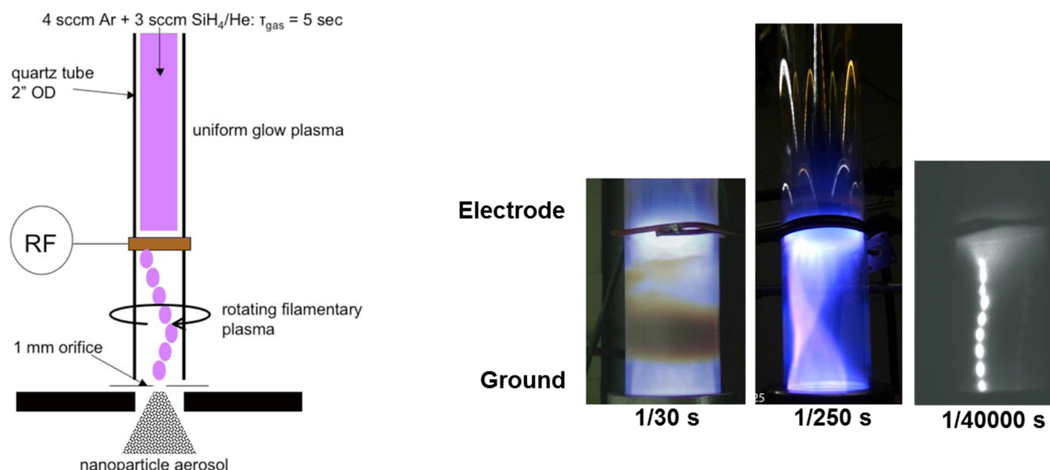

Figure 2.20: (a) Schematic of NC plasma reactor. (b) Still-frame images of plasma, adopted in part from [7].

electrode positioned 152 mm above the orifice, generating a rotating capacitive filamentary discharge between the ring and lower electrodes and a weak, uniform capacitive glow discharge between the ring and upper electrode, Figure 2.20. A shutter positioned 50 mm downstream of the orifice controlled exposure of the substrate to the particles.

A gas flow of 3 sccm 5% SiH_4 in He balance and 4 sccm Ar created a tube pressure of 340 Pa. A plasma discharge was created by an applied rf power of 130 W for cubic nanocrystals and 150 W for cuboctahedral nanocrystals. Annular dark-field scanning transmission electron microscopy (ADF-STEM) images of highly monodisperse 29 $\pm$ 2 nm cubic and 34 $\pm$ 3 nm cuboctahedral nanoparticles that can be readily obtained under these conditions are depicted in Figure 2.21. A high-resolution conventional TEM (HR-TEM) image of a typical cubic Si nanocrystals with no detectable defect inside is shown in Figure 2.21b. The nanocrystals are strongly-faceted and defect-free. It has been shown that the cubic shape with 100 facets is the equilibrium shape of hydrogen-terminated Si nanocrystals [122]. While it is still not clear why under some conditions formation of cuboctahedral nanocrystals become favorable, we observed that experimentally, larger nanocrystals with truncated corners result from higher power applied to ring electrode.

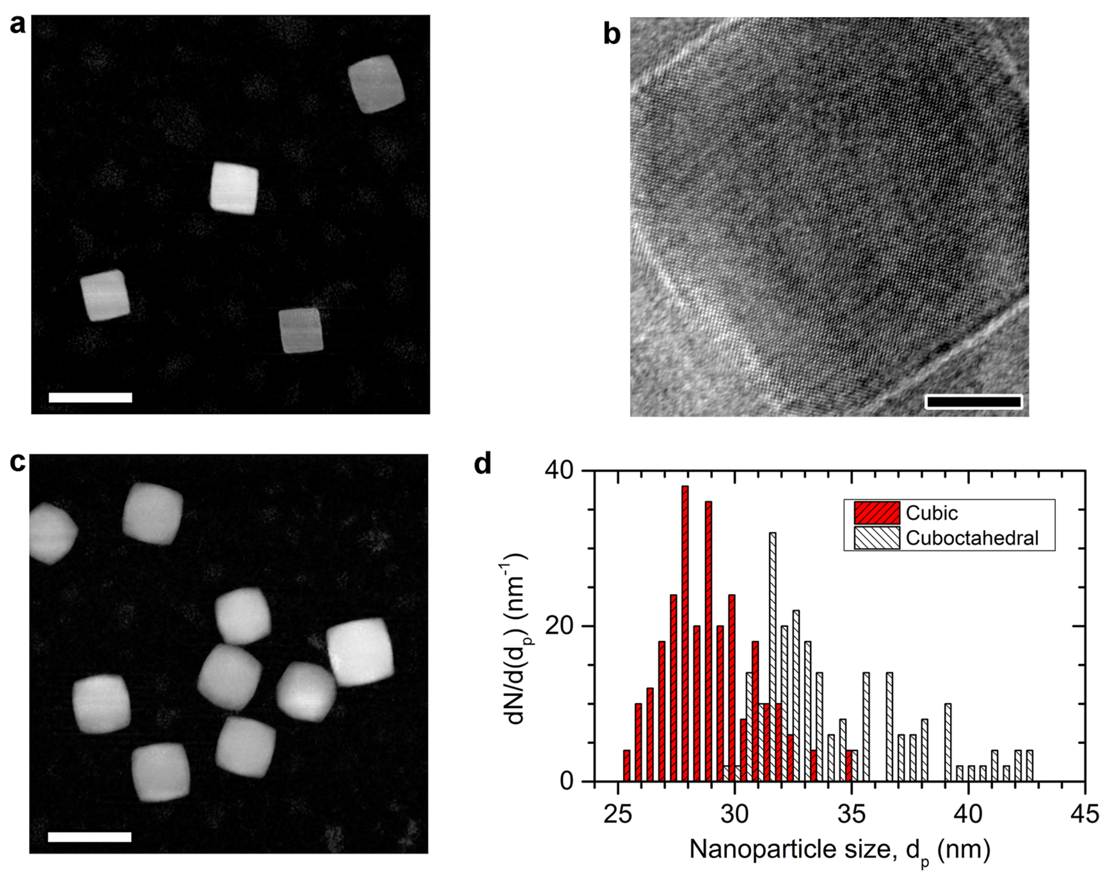

Figure 2.21: (a) ADF-STEM and (b) HR-TEM images of cubic Si nanocrystals. (c) ADF-STEM image of cuboctahedral Si nanocrystals. (d) Normalized size distribution of cubic and cuboctahedral Si nanocrystals as measured by ADF-STEM.

Chapter 3

Nanocavity-enhanced crystallization of silicon

Adapted with permission from Wagner *et al*, “Propagating Nanocavity-Enhanced Rapid Crystallization of Silicon Thin Films” *Nano Letters* **13**, 5735-5739 (2013). Copyright 2013 American Chemical Society.

3.1 Introduction

Crystallization of amorphous thin films is a ubiquitous approach to producing polycrystalline thin films of many materials [123–130]. Among the numerous processes developed, solid-phase crystallization (SPC) produces films with excellent purity, high density and good conformity. SPC proceeds by growth of small crystallites that nucleate in the amorphous matrix during a lengthy incubation period of a few hours or more at temperatures greater than 600 °C for thin film hydrogenated amorphous silicon (a-Si:H). Numerous methods overcome the thermal and temporal limitations of traditional SPC, however each is associated with its own drawbacks such as high film porosity, the incorporation of metallic impurities, or the impracticality for large-scale application [131–134].

Incorporation of crystalline seeds into an a-Si:H film can substantially reduce crystallization time by providing heterogeneous nucleation sites [135, 136]. However, the existing approaches to introducing seeds offer limited control over seed size and aerial

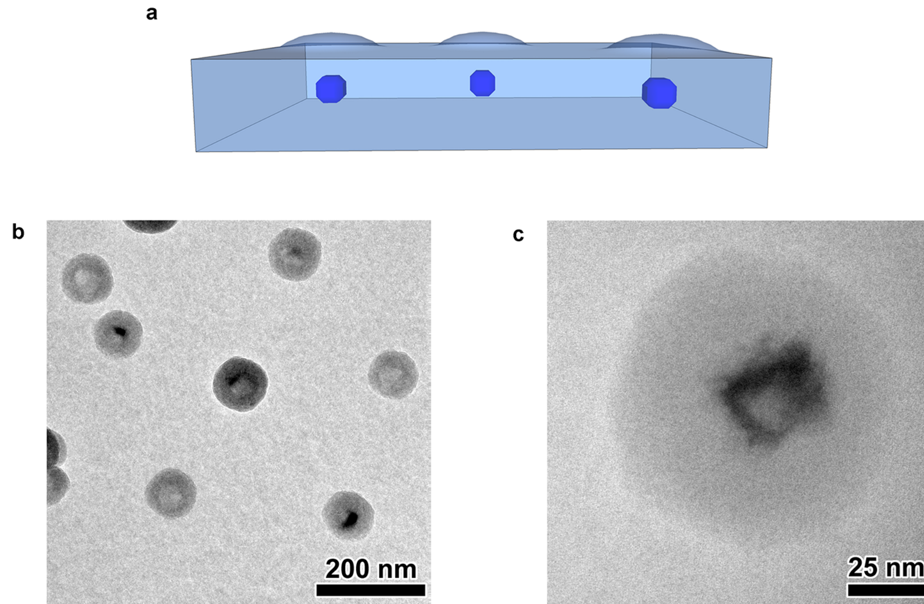

Figure 3.1: (a) Schematic of Si nanocrystals in the a-Si:H film. A 20 nm bottom layer of a-S:H is deposited followed by deposition of Si nanocrystals. A 100 nm top layer of a-Si:H embeds the nanocrystals in a continuous film. (b) A plan-view TEM image of the nanocrystals embedded in film. The particles, about 30 nm across are surrounding by a larger ring of contrast in part due to the conformal deposition on top of the nanocrystals. (c) A higher-magnification TEM image of an embedded nanocrystal.

density. To overcome this challenge, we designed and constructed a dual-plasma reactor in which large silicon nanocrystals are synthesized by a filamentary plasma, injected through an orifice into a plasma enhanced chemical vapor deposition (PECVD) reactor, and there are embedded in a PECVD-grown a-Si:H film containing about 10 at% hydrogen (Figure 3.1). The nanocrystals are highly monodisperse, 30 to 40 nm in size, and cubic or cuboctahedral in shape, depending on the radiofrequency power that is applied for nanocrystal synthesis. The embedded Si nanocrystals acted as heterogeneous nucleation sites for crystal growth while annealing, reducing the crystallization time by up to 90% while providing independent film and particle synthesis.

When cuboctahedral nanocrystals were employed as seeds, we observed through transmission electron microscopy (TEM) the formation of elongated nanoscale cavities at the boundary between the amorphous film and the embedded nanocrystals while

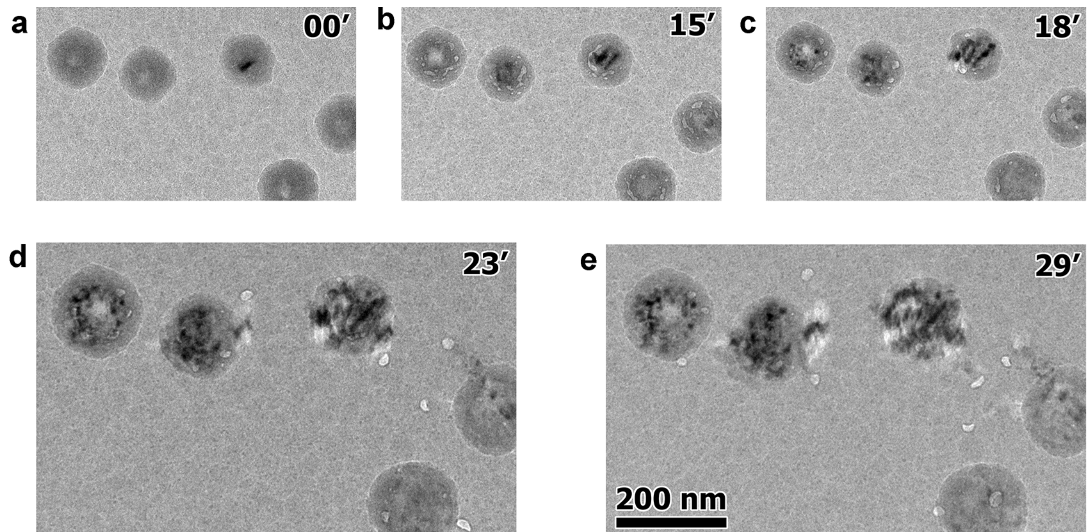

Figure 3.2: *In-situ* TEM image series of seeded a-Si:H film while annealing. (a) As-deposited 120 nm a-Si:H films containing rounded Si nanocrystals. (b) Elongated cavities form near the seed while ramping to 640 °C in 15 minutes. (c) The cavities become rounded within a few minutes at the soak temperature and (d) begin moving away from the nanocrystal at a rate of 1-15 nm min^{-1} leaving behind tails of crystalline Si.

heating to a temperature of 650 °C over 15 minutes (Figure 3.2a,b). These elongated nanocavities become rounded, 5 nm to 30 nm across, within a few minutes (Figure 3.2c) and begin moving through the amorphous film, leaving behind tails of crystalline silicon which continue to grow by SPC (Figure 3.2d). Nanocavities propagate with speeds up to five times faster in the sample plane than the SPC growth (Figure 3.23). For example, at 650 °C nanocavity speeds are between 5 nm min^{-1} and 13 nm min^{-1}, increasing linearly with cavity size, compared to measured growth velocities of 1.2 nm min^{-1} and 4.5 nm min^{-1} for the SPC slow-growth and fast-growth directions, respectively. TEM image sequences of propagating nanocavities in 120 nm films show that the shape of cavities is dynamic with time while the cavity volume appears to remain constant.

3.2 Background

3.2.1 Solid-Phase Crystallization

Solid phase crystallization can be separated into two types: solid-phase epitaxy (SPE) and solid-phase crystallization (SPC). SPE relies on the existence of a well-defined growth front, such as the case of crystallization of amorphous silicon on a clean crystalline silicon substrate. SPC lacks a well-defined growth front and typically requires homogeneous nucleation of a crystalline phase and then proceeds by multiple growth fronts, such as the case of crystallization of a purely amorphous material through a thermal process.

Solid phase epitaxy is modeled by terrace-ledge-kink (TLK) growth. Kink-assisted growth of $\{111\}$ facets with $\langle 110\rangle$-directed edges at the a/c interface occurs through a process of zero mass-transfer diffusion. The preferential a/c boundary in silicon is that of $\{111\}$ surfaces due to low dangling bond density and consequently the lowest free energy, low enough that theoretical approaches to crystal growth of perfect $\{111\}$ surfaces exhibit zero grain growth [8, 9]. Growth of a single (111) terrace, however, proceeds rapidly by diffusion of adatoms along $\langle 110\rangle$ steps on which they move readily due to adjacent dangling bonds lowering the binding energy of adatoms. Adatoms adsorb at kinks, depicted in Figure 3.3a,b, extending the terrace in the $\langle 100\rangle$ direction as steps are filled. Surfaces other than $\{111\}$ are believed to reconstruct into a series of stepped $\{111\}$ terraces which then grow. The lowest formation energy for $\{111\}$ terraces is on $\{100\}$ surfaces [8, 9], resulting in maximum growth rate in the $\langle 100\rangle$ direction as depicted in Figure 3.3c.

Growth of crystalline grains by SPC follows the same principle of minimum energy a/c interfaces, however it has two additional constraints: 1) crystal grains must spontaneously form through thermal processes and 2) growth proceeds on multiple fronts. SPC in amorphous silicon follows classic homogeneous nucleation theory [8, 136–139]. The large surface-to-volume ratio of small crystals (on the order of a nanometer or less in size) results in unfavorable free energy of formation causing small crystals to return to the amorphous phase [139]. The rate of crystal formation and the probability of the crystal growing beyond a critical size are governed by the Gibbs free energies of the bulk crystal and a/c interface relative to the amorphous bulk. Once a cluster grows beyond

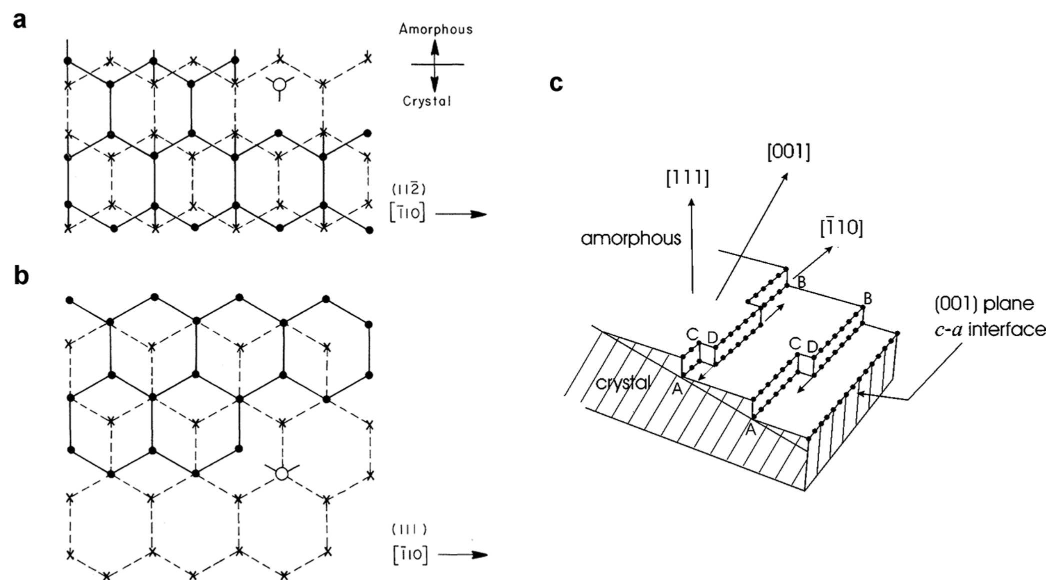

Figure 3.3: (a,b) Kink-like steps at the edge of a (111) terrace and (c) a reconstructed (100) surface comprised of {111} terraces terminated by [1$\bar{1}$0] ledges. Reproduced from Spinella [8] and Williams and Elliman [9].

the critical size, the lowered influence of the differential increase in surface energy per additional surface atom results in solid phase epitaxial growth of the crystalline phase. The reaction rates follow Arrhenius relations whose activation energies are related to the Gibbs free energy of format ion and whose principle rate of reaction is governed by the activation energy for self-diffusion of amorphous silicon.

3.2.2 The role of hydrogen in solid-phase crystallization of silicon

For dehydrogenated amorphous silicon, homogeneous nucleation of crystals above the critical cluster size is immediate at elevated temperatures. The crystallites that form then act as seeds for growth of the entire amorphous film resulting in a broad distribution of final grain sizes between 0.2 to 2.0 μm [140]. High quality amorphous silicon however is most-easily produced by a PECVD process using silane as a precursor resulting films containing about 10 at% hydrogen. Homogeneous nucleation in a-Si:H films is inhibited by the presence of hydrogen. Passivation of dangling bonds in the amorphous silicon lowers the free energy of the amorphous matrix by relaxing the local atomic

structure and consequently increases the free energy of formation of crystalline clusters, thus inhibiting homogeneous nucleation [141, 142]. Hydrogen effusion studies combined with Raman spectroscopy, nuclear magnetic resonance (NMR), and electron paramagnetic resonance (EPR) have elucidated the role of clustered and isolated Si-H bonds in the film [143–145]. It is believed that the isolated Si-H complexes restrict nucleation while the clustered Si-H complexes inhibit growth of crystals. Clustered Si-H evolves from the film readily by Si-H bond breaking and molecular hydrogen formation around 400 °C with a low activation energy for diffusion of 0.02 eV [146] while isolated atomic hydrogen is less mobile with effusion occurring around 580 °C [142, 147]. Upon thermal treatment, the inhibited nucleation time in hydrogenated amorphous silicon results in a characteristic incubation time prior to crystallization of the film. This incubation period can be as long as one hour at 675 °C to more than ten hours at 600 °C roughly half of the total time for crystallization [11, 12].

In order to reduce the characteristic crystallization time of an amorphous film, incorporation of crystalline seeds into the film presented a logical approach, providing a template for crystal growth without the need for homogeneous formation of crystals [11, 135, 136, 148–151]. Transient crystal growth can then proceed immediately by SPC, bypassing the time required for effusion of isolated hydrogen. An additional consequence of this reduction in crystallization time is that homogeneous nucleation of grains can be avoided, reducing the number of nm-sized grains common in SPC silicon. Traditional seeding processes make use of dusty plasmas in which small silicon nanocrystals, 1 nm to 10 nm in size, are formed in the gas phase and are incorporated into the growing a-Si:H film [152]. Optimization of the a-Si:H is restricted by the inherently coupled film growth and nanocrystal formation.

An alternative approach to traditional seeded SPC processes was investigated here. Silicon nanocrystals are produced independent of the film growth and incorporated by a controlled layer-by-layer deposition process. The a-Si:H film is produced in a reactor consisting of two separate plasmas: one to produce the a-Si:H film and the other to create nearly monodisperse cubic silicon nanocrystals of tunable size [121]. This process allows for individual control of both the film and the nanocrystals, greatly expanding control of material properties.

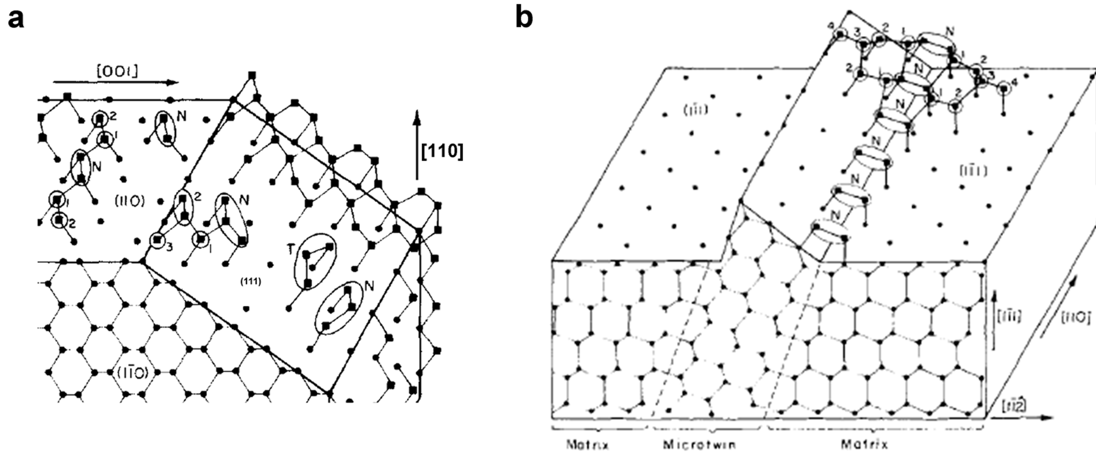

Figure 3.4: (a) Schematic of attachment on the (110) and (111) surfaces demonstrating how 3-atom nucleation events can occur in two orientations on the (111) surface, denoted N and T. (b) Schematic of a re-entrant twin edge. Two-atom nucleation events across the boundary which expand by single-atom attachment. From Drosd and Washburn [10].

3.2.3 Anisotropic SPC

Solid-phase crystallization (SPC) of amorphous Si (a-Si) is controlled by consumption of the amorphous matrix by the more ordered crystalline silicon. This conversion is highly anisotropic owing to the fast and slow growth of high and low energy surfaces, respectively. As the high energy surfaces grow, low energy surfaces develop at their boundaries until the crystal surface becomes terminated by these low energy surfaces. The low-energy, slow-growth {111} surfaces often develop stacking faults and $\Sigma 3$ twin boundaries. Formation of twins preserves nearest-neighbor bond ordering in the lattice, leading to a low stacking fault energy of about 0.03 eV atom^{-1} [10, 153, 154], depicted in Figure 3.4a. Once formed, step nucleation at the re-entrant edge of a twin boundary requires only two atoms compared to three atoms required on the {111} surface, creating preferential nucleation sites and accelerating growth along the $\langle 112 \rangle$ direction, Figure 3.4. New steps can grow rapidly in the lateral direction until forming slow-growth surfaces normal to the $\langle 112 \rangle$ direction and resulting in anisotropic, rod-like growth.

The one-dimensional nature of thin films leads to constrained growth of crystallites. This, coupled with the anisotropic nature of the crystal growth leads to three characteristic crystallite shapes: radially uniform and slow growth, radially uniform and fast

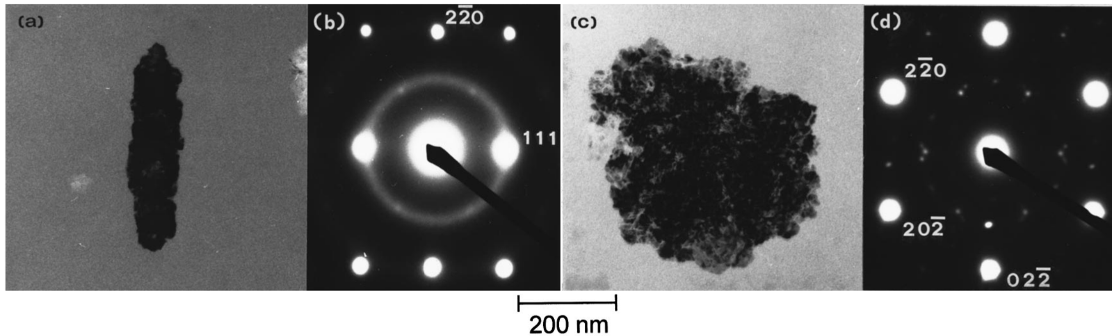

Figure 3.5: Solid-phase crystallization in thin film a-Si is anistropic due to fast- and slow-growth surfaces. (a,b) Crystallites with a ⟨112⟩ direction in plane but whose {111} planes are inclined exhibit elongated, rod-like growth. (c,d) Crystallites that possess {111} planes in the film plane exhibit fast, isotropic growth. From Spinella *et al* [8].

growth, or anisotropic growth. Crystallites whose ⟨112⟩ directions are inclined with respect to the film plane exhibit isotropic slow growth. Crystallites with {111} planes in the plane of the film and containing active twins exhibit isotropic fast growth, Figure 3.5b. Crystallites with {111} planes inclined to the film plane whose ⟨112⟩ directions are in plane with the film will exhibit anisotropic growth with fast growth along the ⟨112⟩ directions, Figure 3.5a.

3.3 Methods

3.3.1 Layer-by-layer Deposition

Seeded a-Si:H films were grown in a vacuum chamber comprised of two separate radiofrequency (rf) plasma reactors; one for a-Si:H film growth and one for Si nanocrystal synthesis (Figure 3.6a). The system is designed such that films can be grown layer-by-layer (Figure 3.6b). A bottom layer of a-Si:H can be grown on a substrate, followed by deposition of a layer of H-terminated Si nanocrystals, which are then embedded in a continuous film by additional a-Si:H deposition.

a-Si:H was deposited by plasma-enhanced chemical vapor deposition (PECVD) in a parallel plate capacitive discharge generated by 13.56 MHz rf power. The reactor, Figure 3.7, consisted of a 100 mm diameter powered electrode positioned 50 mm above a 150 mm diameter grounded electrode. A 152 mm diameter grounded box enclosed the

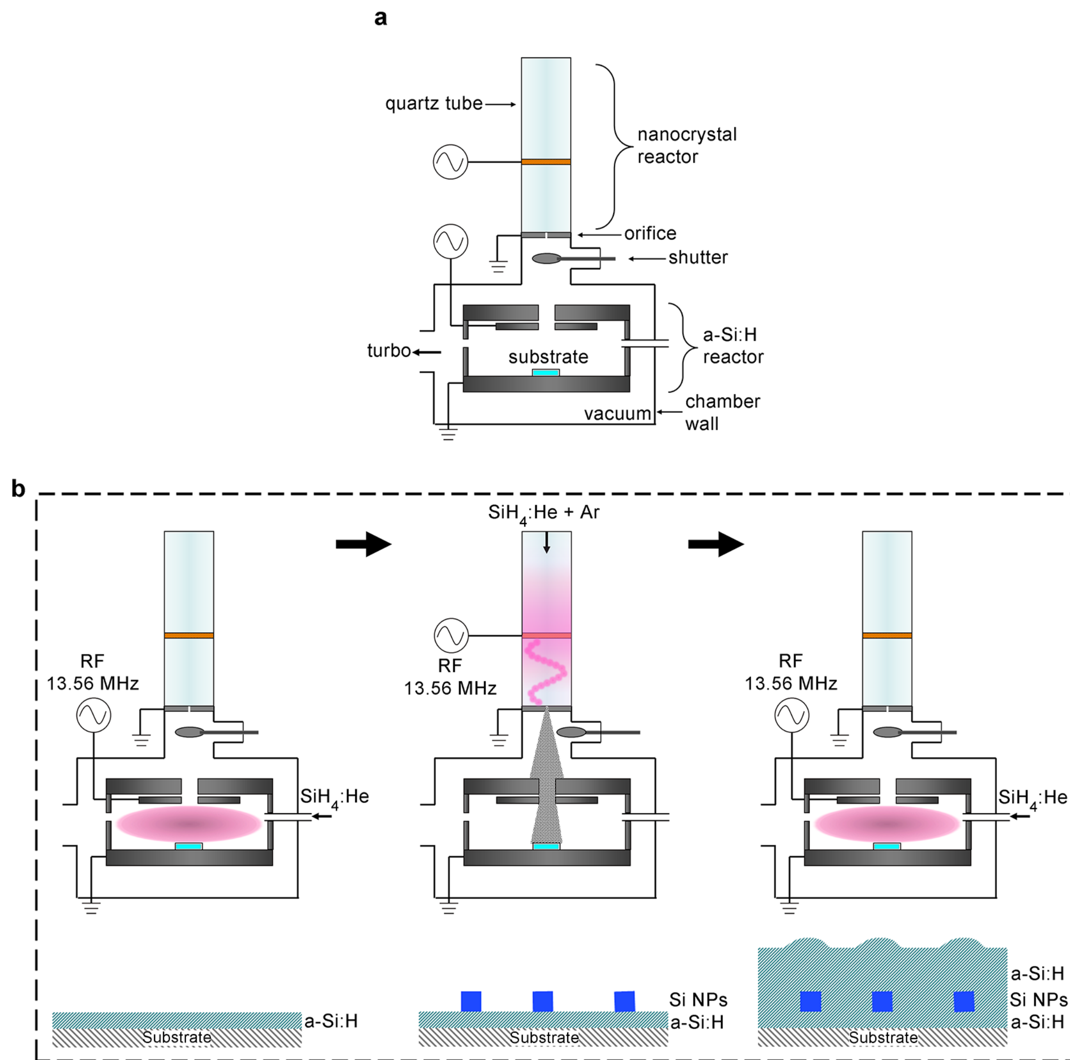

Figure 3.6: (a) Dual-plasma reactor for layer-by-layer deposition of a-Si:H with embedded Si nanocrystals. Separate plasma reactors allow independent control of a-Si:H deposition and nanocrystals synthesis. (b) Seeded a-Si:H films are grown layer-by-layer. A bottom layer of a-Si:H is deposited, followed by nanocrystal deposition, which are then embedded in a continuous film by additional a-Si:H deposition.

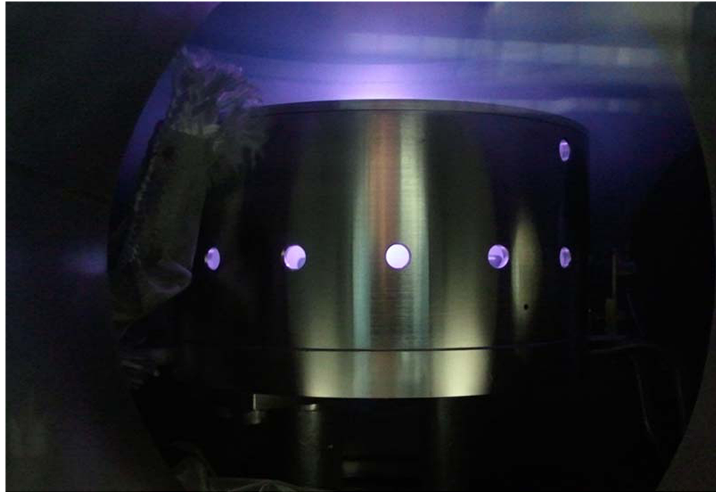

Figure 3.7: Picture of a-Si:H film deposition reactor

powered electrode and discharge. This box acted to support the powered electrode and to reduce the electric field at the substrate. Substrates were placed at the center of the grounded electrode via a load-lock. The PECVD reactor resides within a stainless steel chamber, approximately 25 cm tall and 25 cm in diameter which is evacuated by a turbo pump. Sixteen 6 mm holes in the plasma box allow reactive gas to escape the deposition chamber. Reactive gas enters through a tube inserted through one of the exhaust holes. Two cartridge heaters within the grounded electrode control the substrate temperature. A 13 mm diameter hole in the top center of the reactor allows nanoparticle injection.

A substrate temperature of 250 °C, gas flow of 40 standard cubic centimeter per minute (sccm) 5% SiH_4 in He balance, chamber pressure of 15 Pa, and 1.5 W RF was applied using an Advanced Energy RFX 600 power supply as measured at a vacuum feed through using an MKS VI Probe®, yielding a power density of approximately 3.6 mW cm^{-2} and resulting in a deposition rate of 1.6 nm min^{-1}.

Seeded a-Si:H films were deposited using the conditions provided in Table 3.1. Substrates are placed at the center of the PECVD reactor via a load-lock and heated to the deposition temperature of 250 °C. Typical base chamber pressure is less than 10^{-5} Pa. Once at 250 °C, a 10 minute Ar cleaning plasma is run. The chamber is then evacuated and precursor in carrier gas was injected into the PECVD reactor. A manual gate valve is adjusted to maintain a chamber pressure of 15 Pa. Following bottom layer deposition

Table 3.1: Parameters for a-Si:H deposition and Si nanocrystal synthesis.

	Power	Pressure	Ar	5% SiH_4 in He	Electrode spacing	Substrate Temperature	Time	Deposition rate
	[W]	[Pa]	[sccm]	[sccm]	[mm]	[°C]	[s]	[Seeds/μm²/sec] [Å/min]
Nanocrystal Reactor Cleaning	150	230	4	-	152	-	300	-
Nanocrystal Plasma	130 / 150	320	3	4	152	-	2	2-4
a-Si:H Reactor Cleaning	10	8	40	-	50.4	300	600	-
a-Si:H Plasma	5	15	-	40	50.4	250	var	20

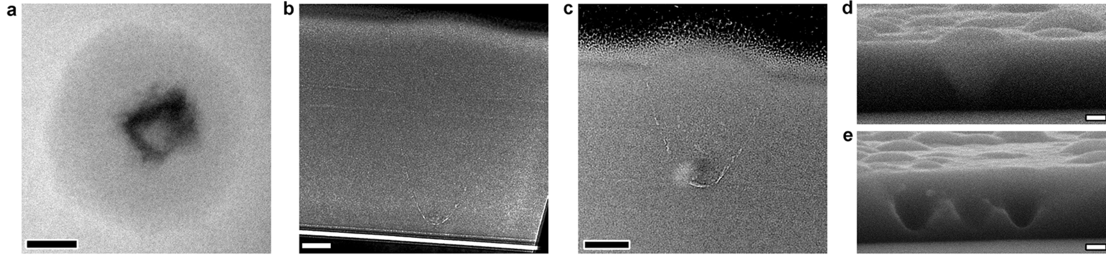

Figure 3.8: (a) Plan-view TEM image of a Si nanocube embedded in a 120 nm a-Si:H film. (b,c) Cross-section TEM images of embedded Si nanocrystals in a-Si:H. A parabolic porous region extends from near the base of each nanocrystal towards the a-Si:H surface. (d,e) Cross-section SEM images of as-deposited film. In (d) the material within the parabolic region remains after cleaving. In (e) the material within the parabolic region was removed by cleaving. Scale bars are (a) 25 nm and (b-e) 50 nm.

the plasma is extinguished and the chamber is evacuated. Nanocrystals are then synthesized as described above. After 1 minute of stable filamentary discharge the shutter was opened, exposing the substrate to the nanocrystal beam. Following nanocrystal deposition the reactor was evacuated and a-Si:H deposition was repeated, embedding the nanocrystals in a continuous film as seen in plan-view and cross section TEM and SEM images in Figure 3.8.

3.3.2 Specimen Preparation

An integral part of microscopy research is specimen preparation. Different analytical techniques require separate specimen preparation methods. Plan-view samples are deposited directly on TEM grids while cross-sectional samples are deposited on a hard substrate for further processing. With regards to the primary tool of this research, the TEM, dynamical scattering due to multiple scattering events complicates image interpretation. Therefore, a total film thickness less than the characteristic distance for multiple electron scattering events, $\lambda_p = 115$ nm for silicon, is preferred [1]. The total film thickness, including amorphous carbon support film, is limited to 150 nm. High resolution TEM studies use a thinner a-Si:H capping layer or undergo ion milling to reduce film thickness.

Films for plan-view TEM were deposited directly onto carbon-coated molybdenum grids (Grid-Tech Mo-400HD). The grids consist of a molybdenum mesh and are covered by a double layer a-C consisting of a lacey carbon sub-layer and a continuous a-C film. The lacey film acts as a support structure for the ultra-thin continuous film and is about 30 nm thick with carbon-free openings on the order of about 10 μm across. The continuous a-C film is 3-5 nm thick, providing large regions for analysis where scattering from the carbon support film is insignificant. Seeded films consisted of a 20 nm bottom layer of a-Si:H, a layer of seed crystals with typical density of 1 to 5 seeds μ m^{-2}, and a 100 nm top layer of a-Si:H. Films for cross-section TEM were deposited on Si(100) mesas (Hysitron Inc., 5-0923) and prepared by a liftout-free focused ion beam (FIB) method using a FEI Quanta 3D 200, detailed below.

Early efforts to examine film cross-sections relied on the wedge-polishing method as well described by Voyles *et al* [115]. The wedge provides an electron-transparent region of increasing lateral thickness at the tip of the specimen, however the amorphous films often delaminated from the substrate during thinning. To facilitate cross-section preparation of TEM specimens a new technique was developed which allows creation of several focused ion beam (FIB) lamellae from a single specimen without the need for liftout or bulk cutaway. This technique provide a result similar to the H-bar technique [1,120], but without the need for any mechanical polishing step. a-Si:H films were deposited on microfabricated Si substrates, Si mesas (Hysitron, Inc. 5-0923), which have a 1.5 μm wide, 2 mm long Si(100) surface elevated 20 μm from the surrounding

substrate (Figure 3.9a). The mesas were produced by masking a strip of silicon and KOH etching the remaining substrate creating 54.7° sidewalls. The Si mesa, passivated with native or thermal oxide, provided an elevated surface wide enough that lamellae formed on the mesa can be considered equivalent to films deposited on flat substrates (Figure 3.9b). Si mesas were mounted using superglue to a TEM grid having a vertical tab, which can be placed in standard TEM holders. FIB lamellae were then made along the length of the strip without need for bulk cutting or liftout. A protective Pt layer was deposited along the mesa by ion beam deposition, acting as a protective coating for the region of interest during ion beam cutting (Figure 3.9c). The lamellae were prepared by ion beam with decreasing current of 300 to 30 nA at 30 keV. Final cutting was performed with a 50 pA and 10 keV ion beam (Figure 3.9c) resulting in lamellae less than 100 nm thick and 10-20 μm long. Figure 3.9d show two optical microscope images of multiple FIB lamellae on a single mesa and a cross-section TEM image of the upper FIB lamella (Figure 3.9d).

3.3.3 *In-situ* Heated-Stage TEM

Heated-stage TEM was performed using a Gatan 652 double-tilt heating holder in an FEI Tecnai G2 F30 (S)TEM with TWIN pole piece operating at 100 keV and equipped with a Gatan 4k x 4k Ultrascan CCD. Temperature was ramped to 650 °C at a rate between 35 and 45 °C min^{-1}, held for one minute, and then set to the soak temperature. Full-frame images were acquired *in-situ* for the duration of the experiment at a rate of one BIN 4 frame per four seconds during temperature ramping and one BIN 1 frame per eleven seconds at the soak temperature. SPC growth velocity and nanocavity propagation speeds were measured every third frame, 33 seconds apart. Fast-growth SPC was identified by elongated crystals extending from the nanocrystal seeds while slow-growth was measured as the expansion of seed crystals having slow, isotropic growth. Nanocavity propagation speed was measured as the displacement of the crystalline surface between frames. When no well-defined crystalline surface was visible, displacements were recorded but excluded from measurement.

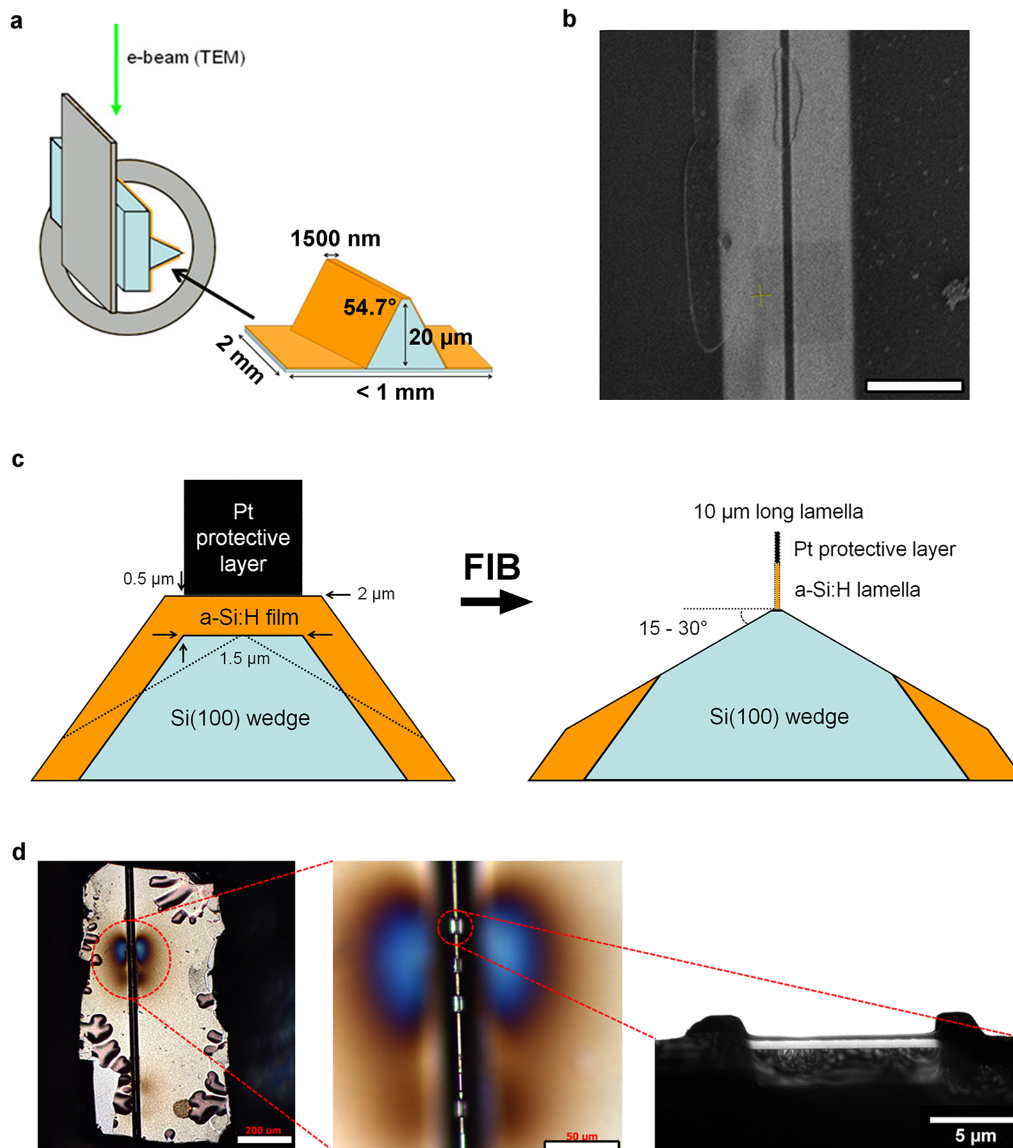

Figure 3.9: Liftout-free FIB lamella preparation process for cross-section TEM analysis. (a) A Si mesa mounted to a TEM grid. (b) SEM top-view image of a seeded a-Si:H film on Si mesa. The raised surface is bordered by the mesa sidewalls which appear bright. Scale bar is 50 μm (c) Schematic of lamella formation. A protective Pt layer was deposited over the region of interest prior to FIB cutting. (d) Optical images of lamellae and corresponding low-magnification TEM image of a single lamella.

3.3.4 *Ex-situ* TEM

Specimens were examined *ex-situ* in an FEI Tecnai G2 F30 (S)TEM with S-TWIN pole piece. The microscope is equipped with a Gatan 2k x 2k Ultrascan CCD camera, Gatan Enfina-1000 electron energy-loss (EEL) spectrometer, and EDAX Si(Li) energy dispersive X-ray (EDX) detector. An accelerating voltage of 100 keV was used for conventional TEM study and 200 keV for STEM investigation. Centered dark-field TEM (DF-TEM) was performed with an on-axis objective aperture and beam tilt. DF-TEM images were acquired for all visible 220 spots. Convergent beam electron diffraction (CBED) patterns were obtained by positioning the beam at select locations along the crystalline tail. Each pattern was used to identify the local crystal structure and relate growth direction with the locally active twin planes. A 50 µm C2 aperture, giving α of 5.5 mrad, was chosen to decrease disc size, helping identification of patterns. Thicker regions of the tail (near the seed) scatter strongly while the small thickness of the crystal near the nanocavity limits interpretation of some diffraction patterns.

3.3.5 Raman Spectroscopy

Raman spectroscopy can identify various atomic bonding configurations in a material by analysis of monochromatic light inelastically scattered by active phonon modes [155, 156]. Crystal fraction can be determined by the shift intensity in a band between 400 and 550 cm^{-1} [8, 157]. Two asymmetric peaks centered around 480 and 517 cm^{-1} correspond to the amorphous and crystalline phases, respectively. Their integrated intensity is related to the crystal fraction by $X_c = {}^{I_c}/_{I_c + \gamma I_a}$ where I_a and I_c are the integrated intensities of the amorphous and crystalline peaks and $\gamma = {}^{I_c \alpha_c}/_{I_a \alpha_a}$ is a constant where α_c and α_c are the respective absorption coefficients at a specific excitation wavelength [157]. Additional peaks corresponding to other modes must also be fit, though not used in this calculation, and are done so using the method described by Smit *et al* [158]. The characteristic time for onset of crystallization τ_0 is defined as the point at which crystal fraction first increases. The characteristic crystallization time τ_c is defined at $X_c = 0.63$ [157]. To determine crystal fractions of seeded and unseeded a-Si:H thin films, the films were deposited on Eagle XG glass (Corning, Inc.), annealed in a N_2-ambient furnace and periodically removed for measurement.

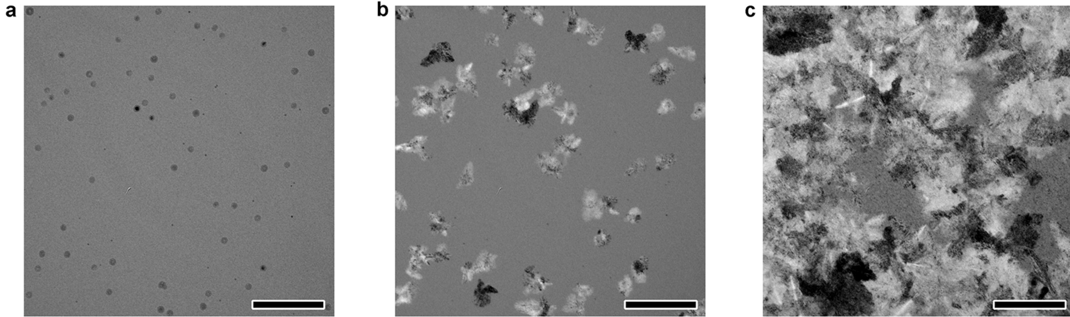

Figure 3.10: TEM image series of a 120 nm a-Si:H film with embedded cubic Si nanocrystals annealed at 625 °C. The nanocrystals act as heterogeneous nucleation sites. No other nucleation was observed to occur. Images acquired at (a) 0 hours, (b) 1 hour, and (c) 2 hours. Scale bar is 1 μm. Images courtesy Curtis Anderson [11]

3.4 Results and discussion

The role of embedded Si nanocrystals as heterogeneous nucleation sites was confirmed by TEM of a-Si:H films with embedded cubic Si nanocrystals annealed at 625 °C (Figure 3.10). Complete crystallization of the films occurred prior to the onset of homogeneous nucleation. Crystallization curves were determined for 100 nm a-Si:H films with and without a layer of 4 cubic Si nanocrystals μm^{-2} annealed at 650 °C (Figure 3.11). The incorporation of nanocrystal seeds reduced the SPC incubation time by an order of magnitude, from 230 minutes to 20 minutes. The characteristic crystallization time τ_c defined at a crystal fraction $X_c = 0.6$ was reduced by 80%, from 400 minutes to 70 minutes. The inclusion of 4 cuboctahedral nanocrystals μm^{-2} reduced τ_c by 90%.

Discussion of observation, in-situ HS-TEM.

3.4.1 Origin of Propagating Nanocavities

Films containing cuboctahedral seed crystals typically exhibited one or more mobile nanocavities per seed while cubic seed crystals seldom induced cavities. To investigate the origin of the nanocavities we prepared cross-sections of as-deposited films containing seed crystals. Films with embedded cubic seeds have thin parabolic regions of porous a-Si:H extending from the base of each seed crystal towards the film surface (Figure 3.12b). Films with embedded cuboctahedral seeds have a similar structure but

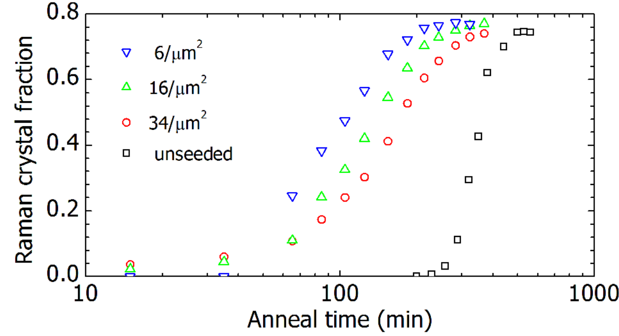

Figure 3.11: Crystal fraction with respect to annealing time at 650 °Cfor a-Si:H films of varying seed concentration. Inclusion of seeds reduces τ_0 and τ_c by more than half. Courtesy Jason Trask [12].

with greater porosity near the base of each nanocrystal seed (Figure 3.12e). Shadowing by the nanocrystals during a-Si:H vapor phase deposition appears to cause cusping of the growing film that results in the formation of small pores as deposition continues [159]. The convex surface of cuboctahedral seed crystals more strongly shadows the deposition resulting in the greater porosity around the base of each nanocrystal (Figure 3.12c-f). During annealing, the porous regions around the nanocrystal bases appear to coalesce into larger nanocavities which by nature of their location between the crystal seeds and the amorphous phase are bound by internal surfaces that are part amorphous and part crystalline.

Large aspect-ratio structures and surface roughness can cause in shadowing of vapor-phase deposition of thin films resulting in the formation of cavities in the growing film [160]. A simple on-lattice kinetic Monte Carlo simulation of deposition of atoms onto a cubic lattice was prepared for a flat (100) substrate containing a cubic-shaped nanocrystal was conducted and the results are presented in Figure 3.13. Atoms were deposited on the surface with isotropic deposition angle and allowed to diffuse based on nearest-neighbor bonding availability using binding energies that yielded a continuous film on a flat surface. While simplistic, it results in a film structure similar to that observed experimentally and to the results of more sophisticated KMC models [161–163].

The cavitated nature of the nanocavities was confirmed by ADF-STEM images (Figure 3.14) which identifies the nanocavities as a region of reduced thickness relative to

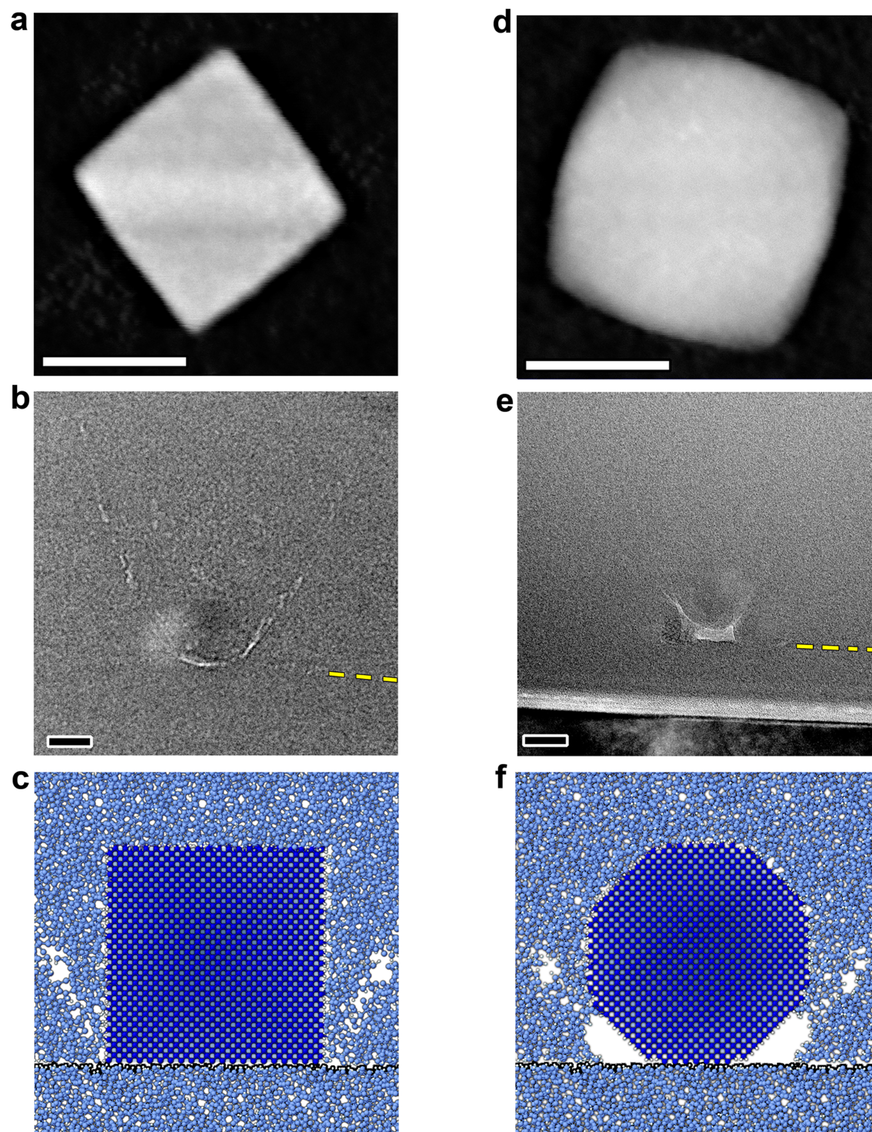

Figure 3.12: (a,d) HAADF-STEM images of a 31 nm cubic nanocrystal (a) and a 39 nm cuboctahedral nanocrystal (d). (b,e) Cross-section TEM images of a-Si:H films with embedded cubic and a cuboctahedral nanocrystal seeds, respectively. A parabolic porous region extends from the base of the nanocrystal seeds towards the a Si:H surface which forms due to shadowing of the top layer deposition. Cuboctahedral seeds (e) have a more significant porosity at their bases which develop into nanocavities up to a few tens of nm in size upon annealing. The seeds lack well-defined boundaries due to epitaxy during deposition of the top a-Si:H layer. (c,f) Drawings of the porous region surrounding the embedded nanocrystals. Scale bars are 20 nm.

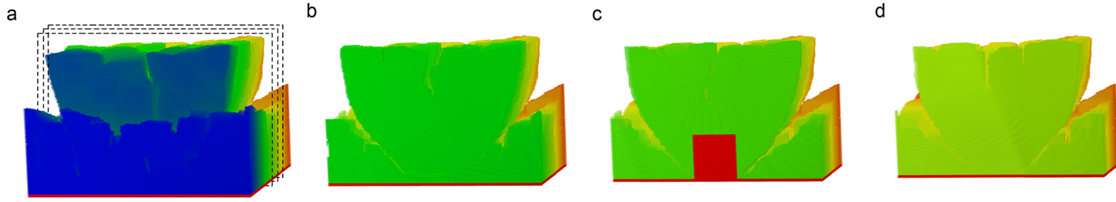

Figure 3.13: A kinetic Monte Carlo simulation of isotropic deposition and surface diffusion. (a)-(d) Cross-sections of increasing depth with the nanocube, red, in center. A thin paraboloid of voids are incorporated into a growing film beginning at the nanocube base and extending outward and upward to the surface.

the surrounding a-Si:H film. Metals such as Al or Ni are known to influence the crystallization of a-Si:H. STEM-EDX of the region surrounding the nanocavities and the crystalline tail suggests only Si is present (Figure 3.15a,b). The Mo signal originates from the TEM grid, the Ta peaks originate from a Ta washer, and the O and C signals result from surface oxide and small carbon contamination. Quantification including the Al Kα_1 at 1.49 keV and Ni Lα_1 and Kα_1 edges at 0.85 keV and 7.48 keV indicate no presence of either. Additionally, no Al $L_{2,3}$ edge (73 eV) was detected in the EEL spectra (Figure 3.15c).

3.4.2 Surface diffusion along the curved nanocavity surface

We propose that the lower chemical potential of atoms on the crystalline silicon surface compared to the amorphous silicon surface acts as the driving force for mass transport from the amorphous to the crystalline part of the surface. The free energy for amorphous and crystalline Si surfaces has been studied both through experiments and simulation, reporting a difference in the range of 0.15-0.23 eV atom^{-1} [164–166]. Mobile atoms on the crystalline surface then become incorporated into the crystalline tail by epitaxy. Based on this mechanism, we calculate the propagation speed for a nanocavity to be 15 nm min^{-1} at 640 °C using the Mullins equation for capillarity-induced diffusion along the amorphous surface [50, 167], and it is comparable to the 10 nm min^{-1} measured experimentally.

The Gibbs-Thomson equation describes the change in chemical potential along a curved surface. Implementing the formulation described by Mullins [168], we can estimate the diffusion towards the crystalline surface. The chemical potential is defined as

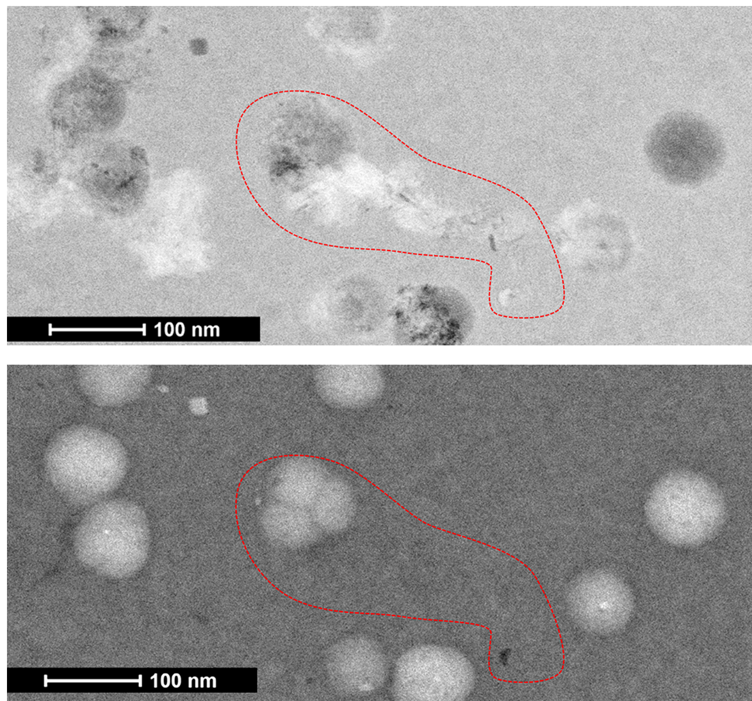

Figure 3.14: (a) BF-STEM and (b) ADF-STEM images of a seeded film containing crystalline tails. The tip of the crystalline tail appears dark in the ADF-STEM image. The reduced intensity of this region confirms voided nature of the cavity as the film is otherwise uniform in thickness and composition.

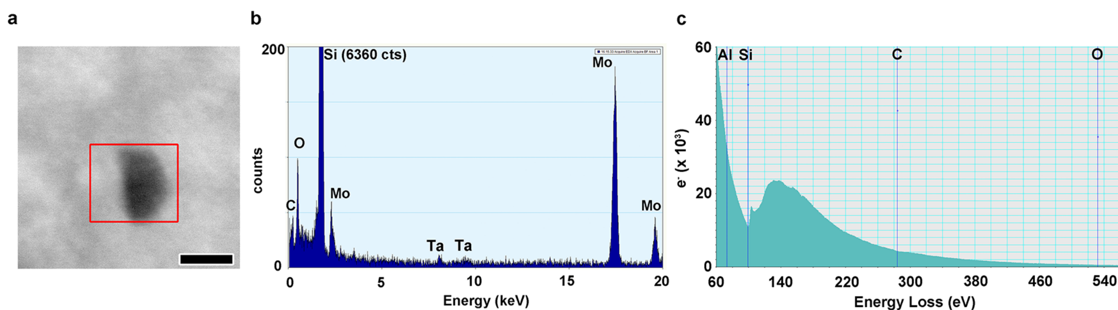

Figure 3.15: Film composition by (a) ADF-STEM, (b) STEM-EDX and (c) STEM-EELS of a nanocavity in an a-Si:H film. The EDX spectrum recorded from region indicated in (a) and EEL spectrum obtained from a similar location suggest only Si is present. Scale bar is 10 nm.

$$\mu(K) = \gamma\Omega K \tag{3.1}$$

where γ is the surface energy, Ω is the atomic volume and K is the local radius of curvature. Ouyang *et al* [169] described the chemical and structural contributions to the surface energy based on size effects. They found the structural component to be negligible above very small cavity sizes (a few nm) while the chemical component modified the surface energy such that:

$$\gamma = \gamma_{bulk}(1 + 2h_0 K) \tag{3.2}$$

where h_0 is the atomic diameter. The atomic flux J along a surface is defined by [159]:

$$\overline{J} = \frac{C_a D_a}{k_B T}(-\Delta\mu) \tag{3.3}$$

where C_a is the adatom surface coverage and D_a is the adatom diffusivity. Combining (3.1)-(3.3) the atomic flux J becomes:

$$\overline{J} = C_a \gamma_{bulk} \Omega \frac{D_a}{k_B T}(1 + 4h_0 K)\frac{\partial K}{\partial s}. \tag{3.4}$$

The total atom transfer to the rear surface is the product of the flux J, the atomic volume Ω, and the interface length l. Assuming a circular surface, the growth rate is

$$\nu_{rear} = \frac{J\Omega l}{A} = \frac{2}{R}\gamma_{bulk} C_a \Omega^2 \frac{D_a}{k_B T}(1 + 4h_0 K)\nabla K \tag{3.5}$$

where $\nabla K = {}^{\partial K}/_{\partial s}$ is the change in local curvature over the first few nm nearest the a/c interface, length is $l = 2\pi R$, and area is $A = \pi R^2$.

The speed, for example of the 17 nm nanocavity discussed in Figure 3.17, was estimated using (i) the surface diffusivity data reported by Sakai *et al* [170] Table 3.2 and (ii) the nanocavitys curvature near the a/c interface of 0.6 nm^{-1} and (iii) the change in curvature of 1 nm^{-2} as measured near the amorphous/crystalline interface. At temperature of 640 °C a growth rate of 15 to 23 nm min^{-1} was found without and with nanocavity size effect, respectively. The calculated growth rate is about 2x the

Table 3.2: Diffusivity data for the amorphous Si surface.

	Diffusion coefficient	Activation energy	Surface energy	Surface coverage	Atomic volume	Temperature	Atomic diameter	Surface density
	cm^2/s	eV	J/m^2		cm^3	°C	nm	cm^{-2}
Sakai *et al.[8]*	43	2.38	1	0.01	2×10^{-23}	625	.2352	10^{15}

experimentally observed speed of 9.4 ± 1.7 nm min^{-1} suggesting that surface diffusion is sufficient and it is not a mediating factor in nanocavity propagation.

3.4.3 Twinning and identification of twinned crystals by transmission electron microscopy

When viewed at moderate magnification over time scales of a few minutes it can be seen that the nanocavity shape is highly dynamic, repositioning itself on the crystalline tail while maintaining overall volume for the duration of the heating experiment, Figure 3.16. The overall propagation of the nanocavity, however, is linear over length scales of 100 nm or more leading to oriented growth with sharp turns. Such dynamic nanocavity shape suggests significant migration of surface atoms while epitaxial growth of the crystalline tail must determine direction of growth.

The high-resolution TEM (HR-TEM) image shown in Figure 3.17 provides a detailed view of the rounded amorphous surface terminating at a faceted crystalline rear surface. Here, the crystalline tail, aligned along its [011] zone axis relative to the incident beam, has two parallel $\Sigma 3$ twin boundaries terminating on the rear of the nanocavity. The main crystal M has a $(11\bar{1})$ facet while the twinned crystal T is composed of a small $(11\bar{1})$ and larger $(\bar{3}\bar{1}1)$ facet. HR-TEM image analysis of many nanocavities showed that the facets are predominately $\{111\}$ and $\{113\}$. Further behind the nanocavity is a region with a superstructure, periodicity $3d_{111}$, characteristic of superposed crystals related by twinning parallel to the electron optic axis [171].

Twins in silicon occur predominately on the $\{111\}$ surfaces due to their low surface energy and the low excess energy of formation, about 0.027 eV atom^{-1} [154], as they preserve nearest neighbor coordination. Twins are planar defects that effectively rotate the twinned crystal by 180° about the $\langle 111 \rangle$. The orientation of these first order twins with a host crystal can be described in matrix form by their orientation relationship

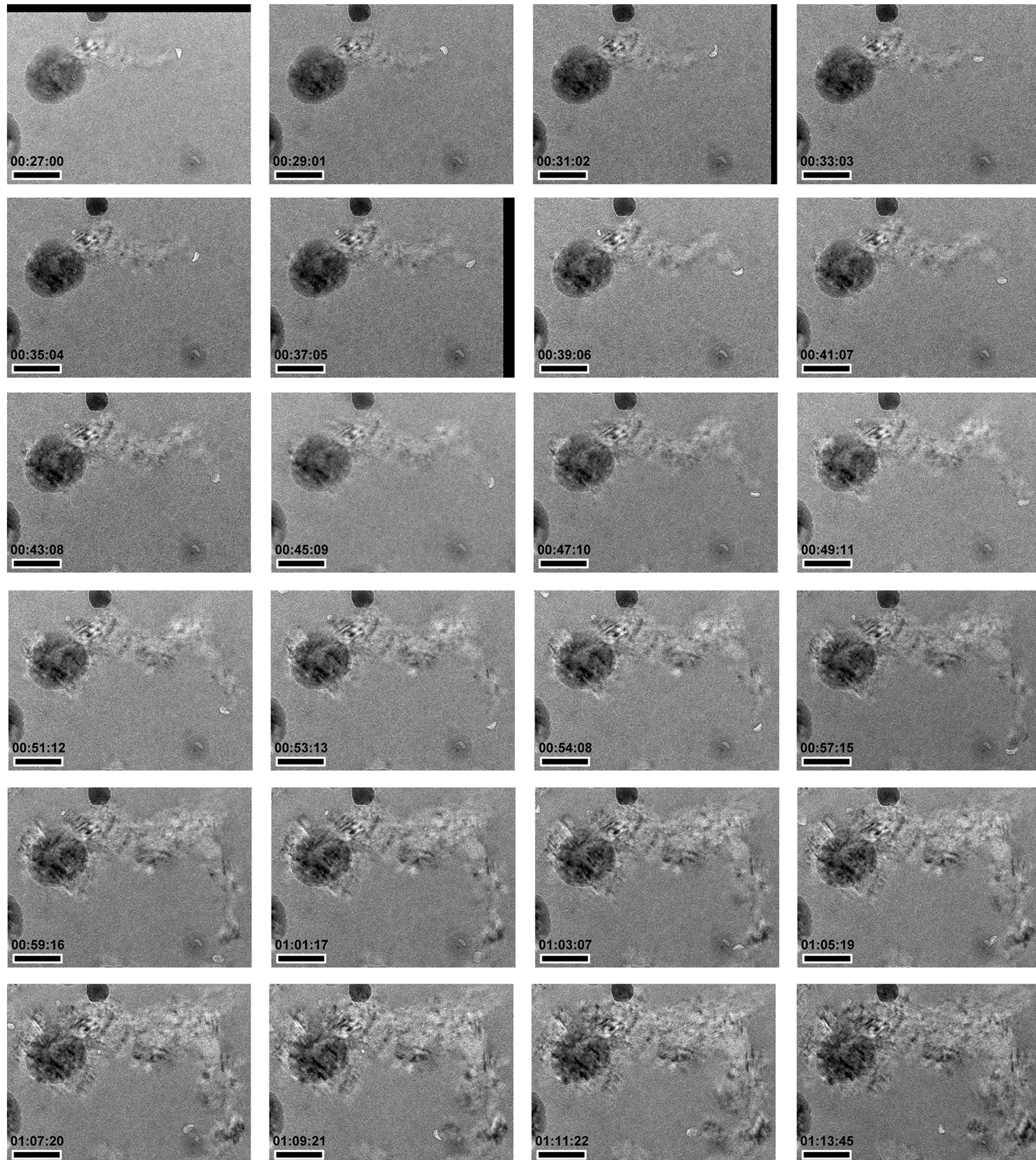

Figure 3.16: Heated-stage TEM image series of a propagating nanocavity heated to 640 °C. Each frame is roughly two minutes apart. The nanocavity shape is highly dynamic while maintaining overall volume. The propagation of the nanocavity is seen to be linear over length scales of 100 nm or more suggesting oriented growth. Scale bar is 100 nm.

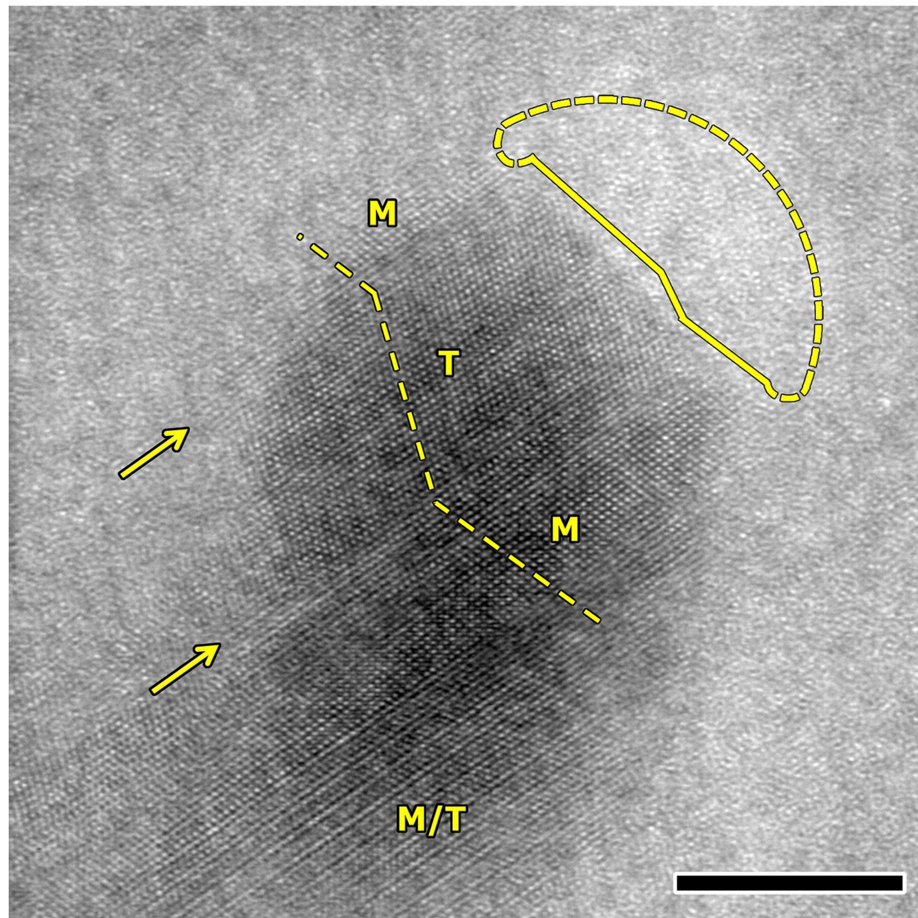

Figure 3.17: (a) High-resolution TEM image of a nanocavity along its [011] zone axis. Two $\Sigma3\{111\}$ twin boundaries, indicated by yellow arrows, terminate at the rear of the nanocavity. The crystalline surface contains $\{111\}_{M,T}$ and $\{113\}_T$ facets. (b,c) Schematics of a crystalline surface containing one twin. Diffusion of surface atoms across the free energy landscape ends in attachment and growth of the crystalline surface, accelerated by preferential nucleation sites along the exposed twin boundary. Scale bar is 10 nm.

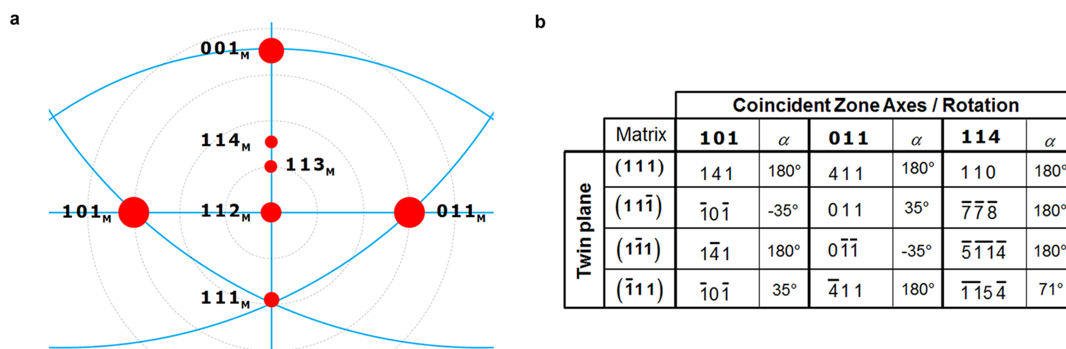

		Coincident Zone Axes / Rotation					
	Matrix	**101**	α	**011**	α	**114**	α
Twin plane	(111)	141	180°	411	180°	110	180°
	$(11\bar{1})$	$\bar{1}0\bar{1}$	-35°	011	35°	$\bar{7}\bar{7}\bar{8}$	180°
	$(1\bar{1}1)$	$1\bar{4}1$	180°	$0\bar{1}\bar{1}$	-35°	$\bar{5}\,\overline{11}\,\bar{4}$	180°
	$(\bar{1}11)$	$\bar{1}0\bar{1}$	35°	$\bar{4}11$	180°	$\overline{11}\,5\,\bar{4}$	71°

Figure 3.18: (a) A partial stereogram for a-Si crystal and its first order twins centered on the [112] zone axis. Each dotted circle represents 15° of rotation away from the [112] zone axis. (b) Co-linear zone axes of a host crystal and its first-order twins listed with the rotation angle α relative to the host crystal.

described here as:

$$T_{11\bar{1}} = \frac{1}{3}\begin{bmatrix} -1 & 2 & -2 \\ 2 & -1 & -2 \\ -2 & -2 & -1 \end{bmatrix} \quad T_{1\bar{1}\bar{1}} = \frac{1}{3}\begin{bmatrix} -1 & -2 & -2 \\ -2 & -1 & 2 \\ -2 & 2 & -1 \end{bmatrix}$$

$$T_{\bar{1}1\bar{1}} = \frac{1}{3}\begin{bmatrix} -1 & -2 & 2 \\ -2 & -1 & -2 \\ 2 & -2 & -1 \end{bmatrix} \quad T_{111} = \frac{1}{3}\begin{bmatrix} -1 & -2 & -2 \\ 2 & -1 & 2 \\ 2 & 2 & -1 \end{bmatrix} \tag{3.6}$$

Twins perpendicular to the $[1\bar{1}0]$ zone axis are visible as a 70.53° angle between the (111) planes across a twin boundary along the $[11\bar{1}]$ direction. The other two twins rotate the crystal such that $\langle 411\rangle$ zone axes become coincident with the $\langle 011\rangle$ of the host crystal. A single $\langle 110\rangle$ zone axis can thus provide information for two of the four twin planes, while $\langle 110\rangle$ zone axes 60° apart can provide information about three of the four and $\langle 110\rangle$ zone axes 120° apart can provide information about all four. Typically only a single $\langle 110\rangle$ zone axis is available due to limitations in sample tilting, though zone axes 60° apart can be accessed in certain cases. A stereographic projection of major zone axes for first order twins near the [112] zone axis of a host crystal is provided in Figure 3.18. A $\langle 112\rangle$ zone axis near 0° tilt provides access to two $\langle 110\rangle$ zone axes in addition to a $\langle 114\rangle$ zone axis within the limits of sample tilt.

Selected area diffraction patterns (SADPs) of Si crystals oriented along a $\langle 110 \rangle$ direction, Figure 3.19a, contains two pair of $\{111\}$ spots. Twinning on either of the $\{111\}$ planes results in a rotation of the crystal revealed as a mirror of the diffraction pattern across the $\{1\bar{1}1\}$ direction. A diffraction pattern containing a common pair of 111 spots indicating the twin plane with additional unique 111 and 220 spots 70.53° apart, mirrored across the twin plane, are depicted in Figure 3.19b. If twinning occurs on both visible $\{111\}$-type planes, two mirror boundaries exist, resulting in the pattern seen in Figure 3.19c. Twins on the inclined $\{111\}$ planes rotate the twinned crustal such that its $\langle 114 \rangle$ zone axis rotates into the beam direction. Examination of 220 and 111 diffraction spot intensities in specimens of well-defined thickness can provide evidence for the presence of out-of-plane twins, however the irregular crystal geometry in SPC crystals such as those of the crystalline tails make this technique impractical.

Dark-field TEM imaging can highlight regions scattering strongly into selected diffraction spots by highlighting regions having unique reflections in the SADP. Using the 111-diffraction spots for DF imaging is complicated by their close proximity to each other and objective aperture size limitations. DF imaging using 220 spots can identify in-plane twins, however the presence of out-of-plane twins is obfuscated. Combining DF imaging with hollow-cone dark field (HCDF) imaging can solve this problem. DF imaging using 220 spots reveal all regions that scatter strongly into the given spot while HCDF imaging about the 111 radius will only reveal areas with $\{111\}$ planes parallel to the beam direction. Regions that are dark in the HCDF image but bright in the DF image can then be identified as oriented along $\langle 114 \rangle$.

3.4.4 The {113} surface

Atomic steps on the slow-growth Si$\{111\}$ surfaces of a nanocavity may act as barriers to growth due to the source of mobile atoms coming from the adjacent amorphous surface. Surface growth would require either extension of a terrace to the amorphous surface or diffusion of mobile atoms up the step as depicted in Figure 3.20a,c. The evolution of $\{113\}$ surfaces, depicted in Figure 3.20b,d, can eliminate this barrier by providing a high-diffusivity surface connecting the amorphous surface to the $\{111\}$ surface, preserving the preferential nucleation sites at the twin boundary. The $\{113\}$ surface is unreconstructed above 600 °C [172] and can be described as bulk-terminated, effectively a series of $\{111\}$

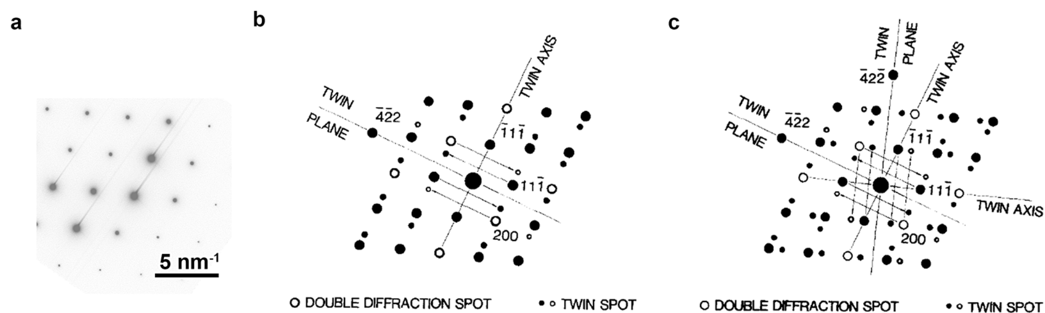

Figure 3.19: (a) A selected area diffraction pattern of [110] Si with contrast inverted for clarity. (b) A schematic SADP for a crystal twinned on the $\{\bar{1}1\bar{1}\}$ plane. (c) The resulting SADP for twinning on both visible {111} planes. Adapted from [13].

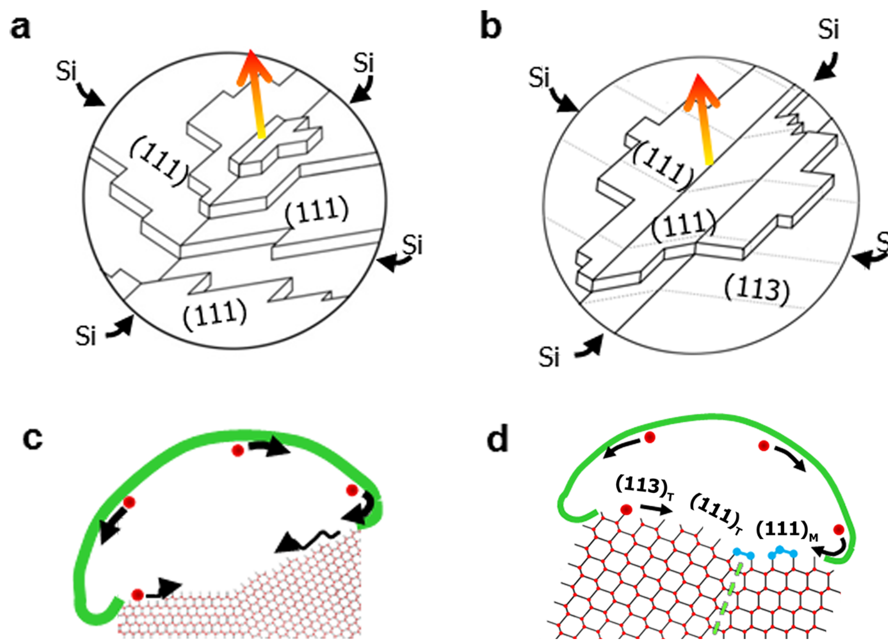

Figure 3.20: Schematic comparing the crystalline surface composed of (a),(c) only {111} surfaces and (b),(d) {111} and {113} surfaces. The {113} surface provides high diffusivity compared to a {111}-terraced surface, promoting growth.

facets a single row long, i.e. composed of alternating (001) and (111) rows. The surface energy of the {113} surface is comparable to the {100} surface with only the {111} surface having lower energy and a growth rate between the two [173, 174].

3.4.5 Twin-mediated growth

A strong dependence of nanocavity growth direction on twinning was found by analyzing the relation of crystalline orientation along the crystalline tails through a combination of TEM imaging and diffraction using the geometric relationships between a matrix crystal M and its first order twins (Figure 3.21). In this example a nanocavity grew from left to right with the seed out of view. Each segment contains bands of contrast parallel to the growth direction as seen in the BF-TEM image aligned near the [110] zone axis of the nanocrystal seed (Figure 3.21a). The first segment, CBED pattern (1), has two [110] zone axis patterns (ZAPs) related by a first-order twin operator whose twin boundary is along the growth direction. As growth direction changed ((2),(3)), one of the two ZAPs was replaced by a new [110] ZAP consistent with a twin boundary along the local growth direction. In (4) a single [110] ZAP was identified. The change in growth direction suggests that a twin boundary not visible in this orientation may be active. In (5) and (6) the [110] ZAPs seen in (2) and (3) were again identified with the same growth direction. A [114] ZAP was identified in (7) correlating with a loss of contrast in the BF-TEM image and consistent with twinning on the invisible (111) planes and termination of the host crystal orientation. Had a mechanism other than first-order twinning contributed to this change in contrast, it would be expected that additional reflections would be present. However, none were identified.

A crystalline tail having extended linear growth with a well-defined change in growth direction can be seen in Figure 3.22. DF-TEM imaging reveals that a single crystalline grain is common between the segments before and after the change in growth direction while each contains twin boundaries along the local growth direction. Selected-area diffraction (SAD) patterns aligned near the $[011]_M$, $[101]_M$, and $[114]_M$ zone axes of the seed crystal M of the crystalline tail, Figure 3.22a-c, the corresponding BF-TEM images, Figure 3.22d-f, and the DF-TEM images corresponding to reflections within these SAD patterns, Figure 3.22h-q, can be interpreted using twin relations. The ZAPs aligned along the $[011]_M$ and $[101]_M$ directions of the host crystal share common $(11\bar{1})_M$ reflections. Visible in both SAD patterns are superposed ZAPs resulting from $\Sigma3(11\bar{1})_M$ twins aligned along the growth direction of the first tail segment. The small width of each twinned crystal, on the order of 10 nm, results in the streaking observed normal to the twin plane in the SADPs. By selecting the respective 220-type reflections, the

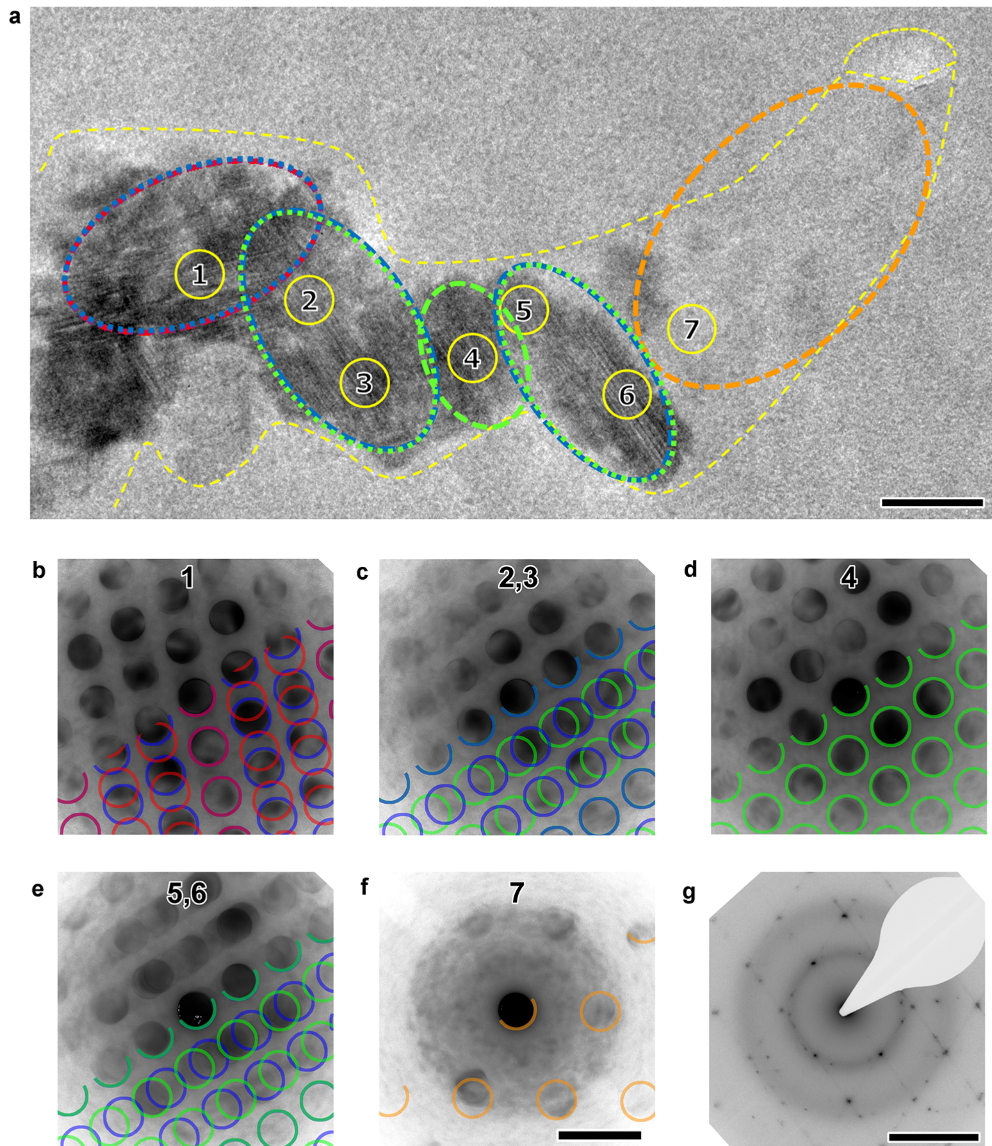

Figure 3.21: CBED patterns along the crystalline tail as marked in (a) the BF-TEM image with e-beam aligned along the seed crystals [110] zone axis. Changes in growth direction are outlined with ovals. (b)-(f) CBED patterns from the areas indicated by the yellow circles in (a) with outlines of identified zone axis patterns color corded to regions outlined in (a). (b) A first-order twin is present, visible as parallel bands in the TEM image. (c) A new first-order twin activates, coincident. (d) The blue pattern disappears while the green pattern remains. (e) The blue pattern reappears with growth. (f) The grain is oriented along a $\langle 114 \rangle$ zone axis suggesting the grain is rotated by first-order twinning. CBED patterns are inverted for clarity. (g) SAD pattern of the entire crystalline tail. Scale bars are 20 nm in (a) and 5 nm^{-1} in (b)-(g).

host crystal M appears bright in the DF-TEM images while the $(11\bar{1})_M$-twinned crystal appears bright in the DF-TEM images. Minor $(\bar{1}11)_M$ twinning is also apparent in the SAD pattern along the zone axis and visible as small grains in the DF-TEM image.

DF-TEM images using the $2\bar{2}0$ reflection of the host crystal along its $[114]_M$ zone axis (Figure 3.22j) reveal a region including the host crystal and extending further along the crystalline tail. The previously identified $(11\bar{1})_M$-twinned crystal provides additional 220 reflections rotated by 60°. DF-TEM images using these reflections highlight the $(11\bar{1})_M$-twinned grain, terminating at the same point along the crystalline tail as observed in the $[011]_M$ and $[101]_M$ SADPs. DF-TEM images using the 111-type reflections (Figure 3.22k,o) reveal a small grain adjacent to the first tail segment. When compared with the 220 DF-TEM images, it can be concluded that this grain is oriented along $[110]_M$ and is consistent with twinning on $(111)_M$ planes. The change in growth direction coincides with the boundary between the host crystal with $(11\bar{1})_M$ twins and the $(111)_M$-twinned grain suggesting that there is a relationship between the two. The orientation of the remaining crystalline tail could not be identified due to the small thickness of the crystal and presumably the activation of higher-order twins.

3.4.6 Size and temperature dependence of nanocavity propagation

Growth velocities for the SPC of nanocrystal seeds embedded in a-Si:H films were measured for temperatures between 620 and 660 °C while heating in the TEM. Activation energies of 3.3 ± 0.5 eV along the slow growth direction and 3.5 ± 0.3 eV along the fast growth direction were found. At 650 °C the slow and fast growth velocities were 1.2 nm min^{-1} and 4.5 nm min^{-1}, respectively. Comparable activation energies and growth velocities have been previously reported [50,139]. The films here were deposited by PECVD and contain approximately 10 at% hydrogen as determined by FrES [12]. Batstone discussed the effect of impurities (e.g. O, H) and roughness of the a/c interface which increase activation energy for crystallization from that of 2.7 ± 0.05 eV as reported solid-phase epitaxy of planar a-Si. The temperature dependence on growth rate was described as a combination of nucleation rate and reordering in the amorphous phase, the latter being influenced by impurities and interface roughness.

The displacement of the rear surface of each nanocavity and its maximum width was measured every third frame and used to determine mean propagation speed. It

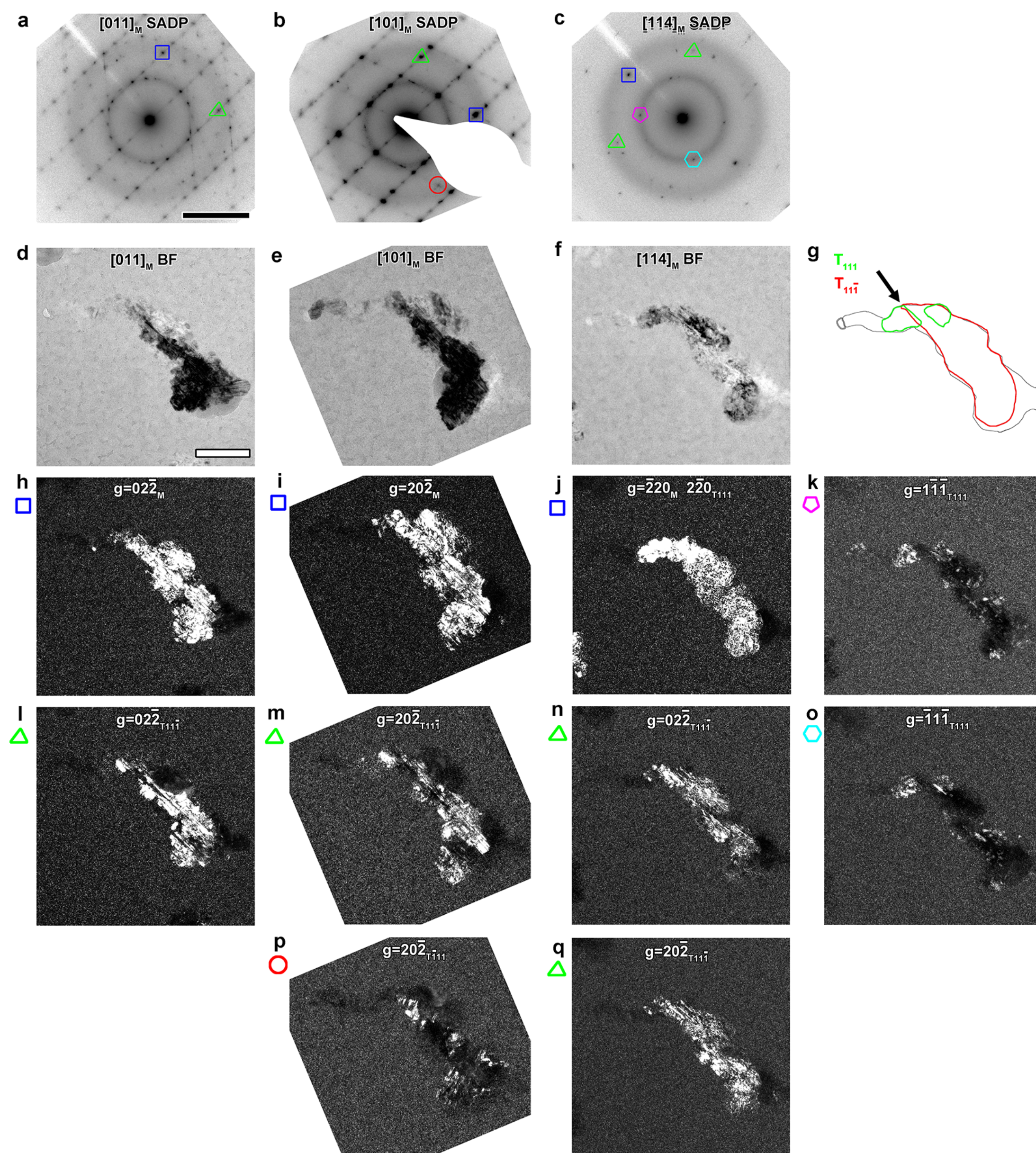

Figure 3.22: (a)-(c) SADPs along the $[011]_M$, $[101]_M$, and $[114]_M$ zone axes of a seed crystal. Growth along the first segment of the crystalline tail coincides with twinning on $(11\bar{1})_M$ planes. A change in growth direction coincides with twinning on $(111)_M$ planes. (d)-(f) BF-TEM images for the respective SADPs. (g) Outline of crystal grains. The black line surrounds the crystalline tail and seed, the red line surrounds a grain with twinning on $(11\bar{1})_M$ planes, and the green line surrounds a grain with twinning on $(111)_M$ planes. (h-j) DF-TEM images using 220-type reflections of the seed crystal (blue squares). (l)-(n) DF-TEM images using 220-type reflections of $(11\bar{1})_M$-twinned grains (green triangles). (q) DF-TEM images using 220-type reflection of $(111)_M$-twinned grains (green triangle). (k),(o) DF-TEM images using the 111-type reflections of $(111)_M$-twinned grains (magenta pentagon and teal hexagon). Scale bars are 5 nm^{-1} in (a)-(c) and 100 nm in (d)-(q).

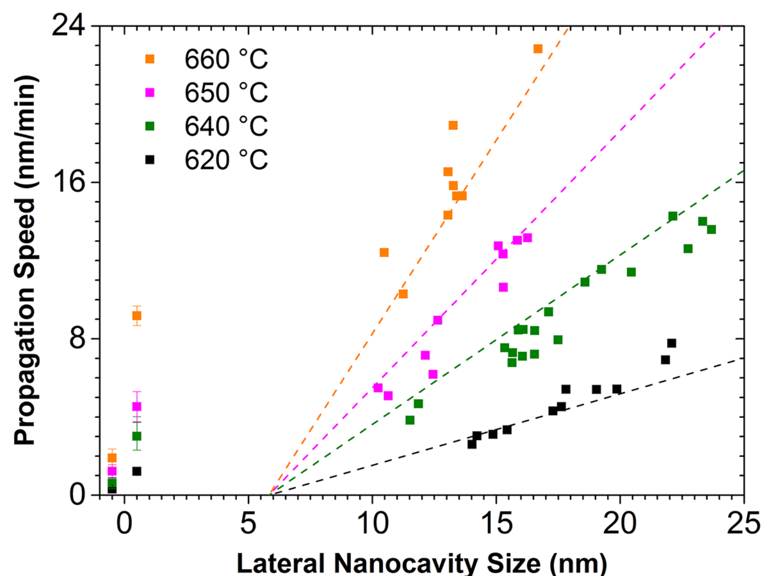

Figure 3.23: Growth velocities for SPC along the fast and slow axes offset from 0 nm by ± 0.5 nm, respectively, and the propagation velocities for nanocavities of different size at 620 to 660 °C.

can be seen, Figure 3.23, that propagation speed increases with size suggesting that diffusion is sufficiently fast for cavity propagation and that some other mechanism determines growth rate. If surface diffusion were the rate limiting step in the nanocavity propagation, the nanocavity speed would vary inversely with nanocavity size due to the increasing crystalline surface area and an approximately linear increase in mass transfer across the a/c interface and emphasized in Equation 3.12. This is reinforced by the dynamic shape of the amorphous surface over time which may result from Rayleigh-Taylor instabilities [175] owing to the growing crystal changing the a/c interface and the influence of local curvature of the amorphous surface on diffusion.

The presence of twins in the crystalline tail, terminating on the cavitys crystalline surface, suggests that nanocavity propagation is mediated by step nucleation at twin boundaries (Figure 3.20)d, which is consistent with the observation of directional nanocavity propagation where a crystalline tail contains multiple segments of linear growth (Figure 3.24). Analysis of dark-field TEM (DF-TEM) images and convergent-beam electron diffraction (CBED) patterns of crystalline tails as discussed in Section 3.4.5 indicates the same.

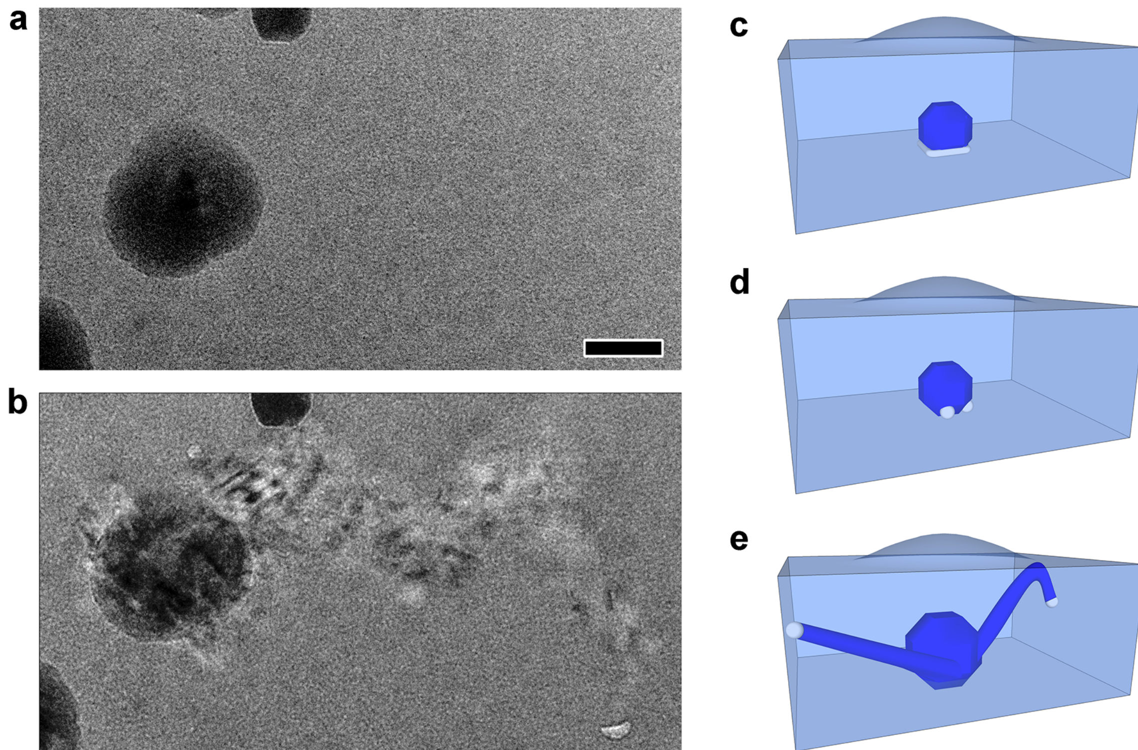

Figure 3.24: Plan-view BF-TEM image of embedded Si nanocrystal seeds in a-Si:H (a) as-deposited and (b) after annealing for 70 minutes at 640 °C. The nanocavity has propagated approximately 1 µm leaving behind it a crystalline tail. (c-e) A cartoon of the film evolution while annealing. A porous region near the base of the seed coalesces into tens-of-nm-sized nanocavities at elevated temperature. The cavity surface, part amorphous and part crystalline, promotes mass transfer from the amorphous to the crystalline domain. The receding amorphous surface and growing crystalline surface creates a crystalline tail as the nanocavity propagates through the film. Scale bar is 50 nm.

Coherent twinning in solid-phase crystallization is often seen in growth of thin film silicon, whiskers, and dendrites and its role in crystallization has been known since the 1960s beginning with the work of R.S. Wagner and others [153,176,177]. Three decades later, the twin-plane reentrant edge (TPRE) on the growth front of SPC silicon were revealed directly high-resolution transmission electron microscopy [178,179]. A review by Spinella [8] explores the theories of nucleation and grain growth of SPC silicon.

3.4.7 Nanocavity propagation kinetics

Nanocavity propagation speed mediated by the presence of twin boundaries is expected to be dependent on length and number of exposed twin boundaries as depicted in Figure 3.25. In crystals grown by SPC, twin boundaries are typically separated by 1-20 nm [50], consistent with our observation of twin boundary spacing within the tails. Small nanocavities may not have twin boundaries on their crystalline surface and therefore not have accelerated growth. The length of twin boundaries will also be dependent on position and generally shorter than the nanocavity size. Additionally, twin boundaries not oriented precisely along the propagation direction will grow across the cavity and into the amorphous matrix and thus no longer contribute to cavity propagation but instead to twin-mediated SPC at the a/c interface. The result is that larger nanocavities, having greater twin boundary length and therefore more nucleation sites, will propagate faster than smaller cavities. Nanocavity propagation will be fastest when directed along the $\langle 112\rangle$ direction of the active twin plane as a single re-entrant edge can continuously support crystal growth. Changes in propagation direction can occur if a new twin boundary develops on exposed $\{111\}$ surfaces.

Nanocavity propagation speeds can be described by the size-dependent Arrhenius equation

$$\nu_{NC}(R,T) = \nu_0 \frac{d_{112}(R - R_c)}{d_{110}} \exp\left(\frac{-E_A}{k_B T}\right) \tag{3.7}$$

where d_{112} and d_{110} are the $\{112\}$ and $\{110\}$ planar spacings, nu_0 is the vibrational attempt frequency, R is the nanocavity size, R_c is a critical cavity size below which enhanced crystallization does not occur, E_A is an effective activation energy, k_b is the Boltzmann constant, and T is temperature. Here the precense of d_{112} in the numerator accounts for surface step height per nucleation event and d_{110} in the denominator

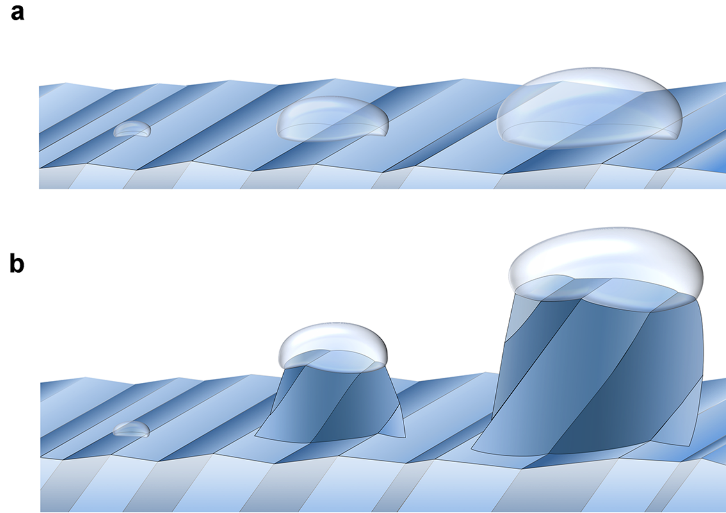

Figure 3.25: (a) A cartoon showing nanocavities of different size at an a/c interface. (b) After a period of time, the larger cavities, possessing greater twin boundary length, propagate faster leading to formation of crystalline tails.

normalizes for the number of nucleation sites. The critical size R_c results from the temporal averaged twin boundary length exposed on the nanocavity surface. The data were weighted by standard deviation in speed for each nanocavity and fitted for each temperature with shared parameters using the Levenberg-Marquardt fitting algorithm [167] in Origin (Origin Lab, Inc.) with an attempt frequency of $\nu_0 = 10^{13}$ Hz [180]. An activation energy of $E_A = 2.33 \pm 0.01$ eV and a critical size of $R_c = 5.15 \pm 0.60$ nm was found. As only temperature and nanocavity size are available as independent variables, fitting of the data with activation energy E_A, critical nanocavity size R_c, and the vibrational attempt frequency ν_0 as fitting parameters results in over-parameterization, which leads to a small change of regression over a wide range of E_A and ν_0. The data were fit using a fixed attempt frequency within the range for surface diffusion [180], 10^{12}-10^{13} Hz, and compared these to the result obtained by allowing for variable attempt frequency (Figure 3.26 and Table 3.2). Adjusting the attempt frequency by an order of magnitude results in a small shift of activation energy of about 0.2 eV. Allowing variable attempt frequency results in value, $10^{15.2}$ Hz. The activation energy only weakly depends on attempt frequency. As growth appears to be limited by nucleation of new terraces, this activation energy can be considered as that for nucleation at a twin boundary.

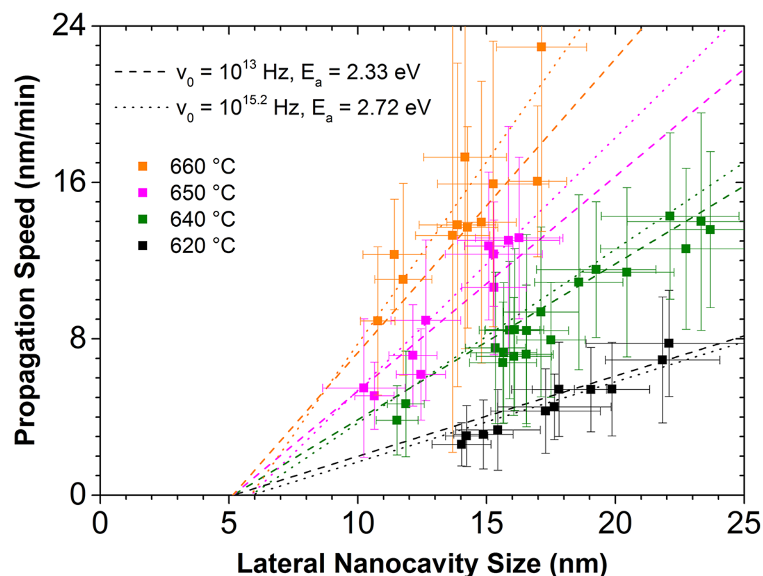

Figure 3.26: Growth velocities, experimental uncertainties, and fits for propagation velocities for nanocavities of different size at 620 to 660 °C.

3.4.8 Predicting thin film crystallization rates

Raman spectroscopy of 100 nm thick a-Si:H films containing 40 cubic nanocrystals μm^{-2} deposited onto and annealed in a nitrogen-filled furnace Figure 3.27a show that SPC incubation time is reduced by up to an order of magnitude, from 300 minutes to 40 minutes at 650 °C, and time to complete crystallization from onset of crystallization is reduced by a factor of two, from 600 minutes to 300 minutes. Complete crystallization of the seeded films occurs prior to the onset of homogeneous nucleation. The reduced rate of crystallization for the seeded samples is a result of fixed seed density whereas unseeded a-Si:H films crystallize via homogeneous nucleation with seed density increasing with time.

Due to the rapid movement of nanocavities through the film, leading to fast growth of crystalline tails, a significant improvement of the crystallization kinetics should be expected. Raman spectroscopy studies of the crystallization revealed reductions in characteristic crystallization time of 90% for 100 nm a-Si:H films containing cuboctahedral Si nanocrystals, respectively. To develop a model for the benefits of such nanocavity-induced crystallization for thicker films we modified the Johnson-Mehl-Avrami-Kolmogorov

(JMAK) model for isothermal crystallization [181] to account for spherulitic growth of nanocrystal seeds and a single crystalline tail modeled as a cone extending from each nanocrystal seed to a nanocavity. The JMAK equation relates the changes in actual crystal fraction to the change of an extended crystal fraction that assumes no impingement of growing crystallites such that

$$df = df^{ext}(1 - f) \tag{3.8}$$

where f is the instantaneous crystal fraction and f^{ext} is the extended crystal fraction. For isotropic growth of a fixed number of uniformly spaced sphere-like nuclei, such as for crystallization of a-Si:H with embedded Si nanocrystal seeds, the extended crystal fraction can be expressed as:

$$f^{ext}(t) = N\frac{4}{3}\pi(\nu_{SPC}t)^3 \tag{3.9}$$

where N is the number density of nuclei, ν_{SPC} is the SPC growth velocity and t is time. Solving Equation 3.8 for f leads to the JMAK equation:

$$f(t) = 1 - \exp(-Kt^n) \tag{3.10}$$

The JMAK equation can be modified to account for the additional crystalline growth due to propagating nanocavities by adding to f_{ext} the volume contribution from the crystalline tail modeled as a cone extending from the growing nanocrystal seed to the nanocavity (Figure 3.27b). The cone length is defined as the difference between the nanocavity propagation speed and SPC growth velocity. The base diameter is defined by SPC growth normal to the surface. With a single nanocavity per seed the contribution of the nanocavity to the extended crystal fraction is:

$$f^{ext}_{cavity}(t) = N\frac{1}{3}\pi R^3 h = N\frac{1}{3}\pi\left[\nu_{SPC}\sin(\alpha)\,t\right]^2(\nu_{cavity} - \nu_{SPC})\,t \tag{3.11}$$

where ν_{cavity} is the nanocavity speed and α is the half angle of the cone. Combining the extended crystal fractions and solving, the crystal fraction f becomes:

$$\nu_{rear} = \frac{J\Omega l}{A} = \frac{2}{R}\gamma_{bulk} C_a \Omega^2 \frac{D_a}{k_B T}(1 + 4h_0 K)\nabla K \quad (3.12)$$

where $r = \nu_{cavity}/\nu_{SPC}$ is the ratio between nanocavity speed and SPC growth velocity.

Applying the experimental SPC growth velocity and nanocavity propagation speeds obtained from heated-stage TEM experiments, we compared the time required to crystallize a 1 μm film containing a layer of nanocrystal seeds. The model is consistent with experimental results in that the presence of nanocrystal seeds reduced the characteristic crystallization time by more than 80%. The addition of nanocavities reduced the crystallization time by another 50%.

This can be further optimized by tuning the density and location of nanocrystals within the film. The addition of nanocavities effectively shifts the S-curve to the left dependent on the size of the starting nanocrystal seed and ratio r of nanocavity speed to SPC speed. Accounting for one nanocavity per nanocrystal seed and a growth ratio $r = 5$ the addition of nanocavities can reduce the characteristic crystallization time τ_c by 50% for a 100 nm a-Si:H film containing a single layer of 4 seeds μm^{-2}, comparable to the experimental results (Figure 3.27c). The model suggests the same aerial density of nanocrystal seeds can reduce τ_c by 35% for a 1 μm film.

3.5 Conclusion

To our knowledge this is the first demonstration of a crystallization process perpetuated by diffusion along an enclosed surface. The surface of nanocavities located at an a/c interface have a chemical potential gradient along which atoms diffuse, resulting in a receding front amorphous surface and a growing rear crystalline surface. Twin boundaries on the crystalline surface provide preferential nucleation sites which accelerate growth. Activation of new twin boundaries influence growth direction of the crystalline tail. As the nanocavities propagate through the film a crystalline tail develops, creating a rapidly expanding a/c interface surface which crystallizes the surrounding film by SPC. The result is a dramatic reduction in crystallization time for amorphous Si films. While perfectly explained using well-understood principles of diffusion and crystal growth, this

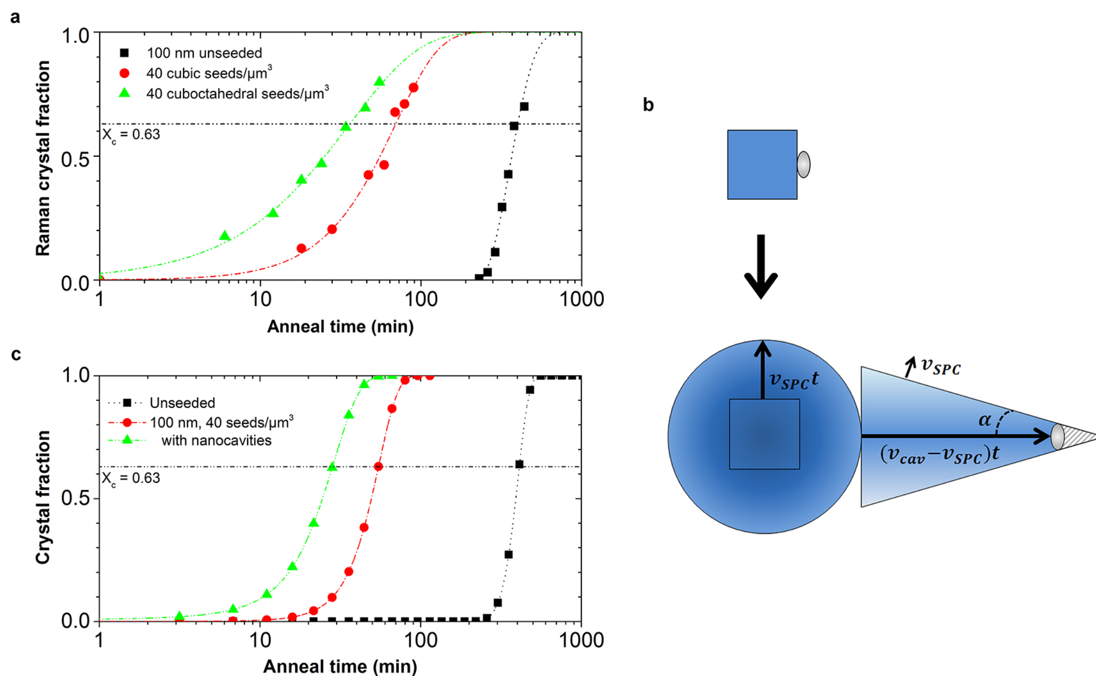

Figure 3.27: Extrapolation of nanocavity-accelerated crystallization. (a) Experimental crystallization curves for 100 nm thick a-Si:H films annealed at 650 °C. (b) Schematic of a Si nanocrystal embedded in a Si film and having a single nanocavity, modeled as sphere-like growth from the seed in addition to conical growth of the crystalline tail. (c) Calculated crystallization curves at 650 °C based on Equation 3.12. Experimental SPC growth velocity was used to model 100 nm and 1 μm thick films having a density 40 seeds μm^{-2} and 4 seeds μm^{-2}, respectively, and a growth ratio $r = 5$.

is to our knowledge the first description of such a process on an enclosed surface which enables effectively perpetual crystal growth using the receding amorphous surface as a source of adatoms. Likely common in any system where voids are present at an a/c boundary, the phenomena was fortuitously discovered in these seeded a-Si:H films where cavity formation was promoted at the nanocrystal/film interface, making it the primary activity observed while heating *in-situ* in the TEM.

3.6 Future Directions

While the development of alternatives to Si-based photovoltaics and thin film devices is much in vogue, silicon-based devices continue to be hold significant share of the

market. Simplifying the processes associated with converting cheaply-produced a-Si:H to crystalline silicon is essential to further reducing costs of device fabrication. Seeding processes as described here are hypothetically expandable to any size film that can be deposited and current efforts within the group aim to demonstrate this applicability. Beyond the potential for enhancing crystallization in silicon films, the kinetics of this process should translate to the crystallization of many other materials in which this process may present new applications.

Chapter 4

Mechanical Properties of Si Nanocrystals

4.1 Introduction

As electronic and mechanical devices scale downward in size and upward in complexity, accurate determination of materials properties in nanoscale volumes becomes increasingly important for meeting new performance and lifetime demands. The change in mechanical and electrical response of dimensionally-confined materials with deformation has created a new challenge for device design while potentially opening the door to a world of new applications [22, 182–187]. At such small length scales, fundamental mechanisms are different and new structure-property relationships are observed. Even the geometrical nature of confinement can have significant effects on deformation mechanisms, so new device architectures will require their own properties measurements. These challenges coupled with stresses induced by fabrication and operation necessitate an intimate understanding of the mechanical behavior. A sized-based ductile-to-brittle transition in silicon has provided a practical and exceptionally valuable use. Strained silicon-based transistors were introduced in the early 2000s, offering improvements in electron and hole mobility with potential to increase drive current by 2 to 4 times [123]. The recently commercialized FINFETs and their potential successor gate-all-around transistors, e.g. nanowire transistors, extend these limits even further [188–190]. The strains for these devices, however, can induce deleterious dislocation generation and

plasticity which must be understood for future device design and prediction of performance [183, 190].

Semiconductors such as silicon, having large Peierls barriers, are brittle materials at room temperature and pressure. Bulk Si has an elastic modulus of 160 GPa and a fracture strength greater than 1 GPa, however it can only sustain elastic strains of about 0.1%. Native defects generate large local stresses approaching the theoretical stress such that small applied stresses can lead to crack formation and propagation. Nucleation of dislocations, which blunt and stabilize cracks in metals, is limited due to the high Peierls barrier reducing their mobility. As the materials dimensions are reduced, the number of native defects and their size is lowered, reducing both the stress concentration and probability of alignment between the defect and the applied stress favorable for cracking. Below some critical size, the number of defects is reduced to an extent that brittle fracture no longer occurs. Instead, the bulk internal stresses increase to a point that the Peierls barrier can be overcome and dislocations can readily pass through the material, leading to a ductile response.

The general trend is that smaller is stronger. It can then be inferred that beyond some size where the defect density is effectively zero, no additional strengthening should occur and the applied stress can approach the theoretical strength. Such strengths have been observed in extremely shallow indentations in materials such as silicon [191] and Permalloy [192], however thorough investigation of such a transition is limited. Additional size effects have been proposed regarding increased ease of surface termination of dislocations, as well as the changing electronic structure in highly confined materials affecting the dislocation mobility since dislocations possess dangling bonds [193].

Exceptional strength and plasticity at the nanoscale has been observed in a diverse set of materials [194–196]. Recent innovations have enabled *in-situ* investigation of mechanical properties in the TEM at a size scale where defect density can approach zero, which is of interest from both fundamental and applied perspectives. The study of intrinsic material properties of matching volumes to atomistic simulations provides needed experimental validation, and also explores the utility of classic structural and electronic materials for new uses at a size commensurate with the scale of their application. The rapid increase in computational power for upscaling of modeling and the downscaling of experiments by improved characterization methods is bridging the

gap between experiment and theory. This has enabled more insightful computational analysis [197–201] and more detailed experimental analysis by conducting experiments *in-situ* in the electron microscope. Numerous approaches to synthesis of metallic nanostructures [44, 46, 109, 202] have led to aggressive study of plasticity in metallic systems, particularly under tensile loading. For example, Oh *et al* [46] and Zheng *et al* [202] have revealed, at the atomic scale, the source-mediated plasticity of aluminum and gold nanowires, respectively.

Silicon, being a ubiquitous component of micro-devices, has been studied extensively via *ex-situ* [15, 192] and *in-situ* [14, 49, 203, 204] mechanical testing. The mechanical properties of silicon nanowires and the atomistic mechanisms contributing to elasticity and plastic deformation have been examined extensively by tensile testing and bending in the electron microscope [18, 205, 206], revealing the strong size dependence of strength and elasticity in nanoscale Si as seen in Figure 4.1. Such nanowires are unsuitable for compression studies. While a ductile-to-brittle transition has been observed in compression of Si nanopillars below a critical size of about 400 nm [14], there have been conflicting reports on plasticity of Si nanowires in tension and bending [42, 205–208]. Stan *et al* [207] demonstrated brittle fracture of Si$[11\bar{2}]$ nanowires with maximum bending stresses of 17 GPa, though the nanowires were found to contain stacking faults and deformation twinning. Wang *et al* [206] present an argument for both perfect and partial dislocation nucleation, propagation and termination, but the challenge of controlling nanowire orientation and defocus during bending makes a confident interpretation of their data difficult. Tensile testing of Si nanowires by Gordon *et al* [208] and Tang *et al* [42] argue that brittle fracture occurs with little to no plastic deformation. In the latter work, Tang *et al* found that the same nanowires under bending accommodated significant plasticity up to 14% bending strain, ultimately forming cracks on the tensile side at bending strains greater than 20%. Hoffmann *et al* [209] found that 100 nm to 200 nm VLS-grown [111] Si nanowires had a 12 GPa fracture strength, though no investigation of plasticity prior to fracture was performed.

In-situ compression of silicon has been limited to a scale of about 100 nm and greater. Compression testing is complicated by a variety of factors. For example, indenter instability transverse to the loading axis leads to unresolved lateral stresses on the specimen

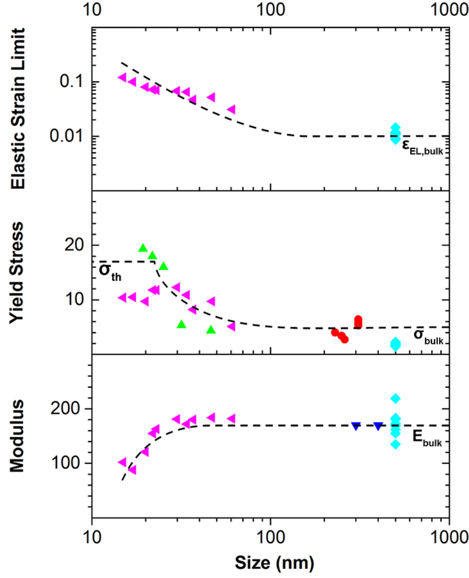

Figure 4.1: (a) Elastic limit, (b) yield stress, and (c) modulus versus critical length scale for nanoscale silicon structures. Reduction in size results in an increase in elastic limit from bulk, $\epsilon_{Si,bulk} = 0.01$; an increase in yield stress from bulk, $\sigma_{bulk} = 5.3\,\mathrm{GPa}$, towards the ideal strength, $\sigma_{th} = 16\,\mathrm{GPa}$ [14]; and a reduction in modulus, $\mathrm{E}_{bulk} = 160\,\mathrm{GPa}$. Derived from ▲ Gerberich *et al* [15], ⬢ Ostlund *et al* [14], ▼ Namazu *et al* [16], ◆ Tsuchiya *et al* [17], and ◀ Zhu *et al* [18].

which complicates the stress state and may possess a component resolved onto the primary slip or cleavage plane. A fixed instability becomes increasingly problematic as the size scale of the specimen is reduced. As two-dimensionally confined structures such as nanopillars are reduced in diameter their length must also be reduced to mitigate the effects of buckling under compression. A number of synthesis methods exist to create high quality silicon nanospheres in this size range [15,20,49,197,210] however this geometry makes it difficult to align a desired crystallographic direction along the compression axis. Such challenges have resulted in *in-situ* tensile and bend testing as the methods of choice. High-aspect ratio structures such as nanowires and FIB pillars can be tested to diameters less than 10 nm [18,202]. Requirements on load-cell stability are eased by the reduced strain-to-displacement ratio of long test structures. Requirements on the stability of the indenter tip are also eased as small vibrations at the point of contact yield minor additional stress and strain on the nanowire. The large surfaces of these

2-dimensionally confined structures, however, increase the probability of native defects which act as stress concentrators.

An important consideration in the examination of tensile and bending tests is the distinct differences between the nature of elastic-plastic response to tensile and compressive deformation. Tensile stress drives irreversible bond breaking, particularly in materials with highly directional bonding such as ionic and covalent solids. Compressive deformation, however, generates large shear stresses which promotes bond switching, a paired bond breaking and reformation process [187]. This likely contributes to the mixed results demonstrated in work on tensile deformation of Si nanowires relative to the repeatably-demonstrated brittle-to-ductile transition in compressed silicon pillars.

The challenge of compressive experiments at the sub-100 nm size scale have motivated significant computational investigation of the mechanical response to deformation in silicon under compressive stresses. Primarily studied using molecular dynamics simulations with modified potentials, a variety of atomistic mechanisms have been proposed as the dominant mechanism at the nanoscale [197–201, 211]. For the low-temperature, high-stress regime at the nanoscale, these models have predicted {111} slip by perfect $\boldsymbol{b} = {}^{a}/{}_{2}\langle 111\rangle$ dislocations [197, 198], $\boldsymbol{b} = {}^{a}/{}_{2}\langle 111\rangle$ dissociated into $\boldsymbol{b} = {}^{a}/{}_{6}\langle 112\rangle$, {110} slip by perfect dislocations with $\boldsymbol{b} = {}^{a}/{}_{2}\langle 110\rangle$ [199], deformation twinning [200, 201], and phase transformation [212]. A detailed review of the predicted and experimentally verified dislocations at varying size scale, applied stress, and temperature can be found in Rabier [213].

Here, we investigate the elastic-plastic response of 25 nm to 65 nm cubic Si nanocrystals under uniaxial $[00\bar{1}]$ compression. The morphology of these cubic particles enables repeatable compression on a well-defined axis, the $[00\bar{1}]$ direction, while rotation of the particle using alpha tilt allows observation of the particle along any direction normal to this axis, such as [110] or [100] zone axes. We demonstrate elastic response up to 7% at 7 GPa in the Si nanocubes with an upper yield point of 11 GPa. We reveal a regime where "smaller is stronger" appears to plateau, suggesting these small crystals are effectively pristine and whose plasticity is mitigated by nucleation of the first dislocations. Using post-mortem analysis in the TEM we investigate the nature of dislocations present within the various stages of deformation and present evidence that

leading $\boldsymbol{b} = a/6\{112\}$ partial dislocations, i.e. stacking faults, are the dominant source of plasticity at this size scale.

4.2 Methods

4.2.1 Substrate preparation.

Sapphire was selected as a substrate to minimize compliance effects during compression. The large modulus of sapphire (340 GPa) relative to silicon (160 GPa) forces most of the deformation into the silicon nanocrystal. C-axis sapphire squares, 10 mm × 10 mm × 0.1 mm, were cleaned in a four step ultrasonic process. The square was placed in a small polypropylene beaker filled with Alconox cleaning solution and sonicated for 15 min. The Alconox drained and flushed with DI water three times. The beaker was then filled with DI water and sonicated again for 15 min and flushed with DI water three times. This was then repeated with acetone and then methanol before being air dried.

The sapphire square was then placed on the sticky portion of a Post-It note and covered with Ross lens tissue and placed tissue-side down on a granite table. The square was then hit through the Post-It with a hard object to shatter the sapphire square. Small shards with sharp tips were selected under an optical microscope and mounted on the Hysitron PicoIndenter "chair" using CrystalBond wax. Silver paste was then applied to the base and sides of the sapphire to mitigate charging while taking great care not to contaminate the surface nearest the sharp tip. The samples were then placed in a vacuum oven heated to 70 °C for at least one hour before deposition.

Greater success in obtaining sharp tips was found using thin, 0.1 mm thickness, sapphire as compared to thicker alternatives. A sharp tip is necessary to eliminate substrate shadowing of the extremely small silicon nanocubes when the samples are placed in the TEM. The Si mesas available from Hysitron were considered, but the increased substrate compliance was deemed too problematic both for mechanical analysis and differentiation of particle and substrate in the TEM.

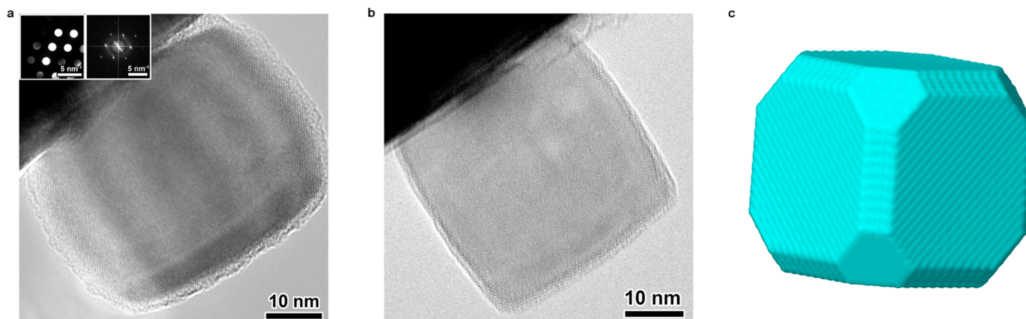

Figure 4.2: TEM images of {100} Si nanocubes oriented such that its (a) [110] direction and (b) [100] direction is along the beam direction. (c) Cartoon illustrating the truncated nature of the Si nanocubes.

4.2.2 Si NC synthesis.

Silicon nanocubes were synthesized in the flow-through plasma reactor described in Section 2.10 using a secondary load-lock system designed for nanocrystal deposition. This load-lock consisted of a differentially-pumped push-pull rod separated from the high-vacuum chamber by a gate valve. Substrates were attached to a small plate on the end of the push-pull rod using polyimide tape. The load-locked was evacuated/vented three times with an Oerlikon EcoDry 15 pump and high-purity nitrogen prior to insertion. A shutter time of two to three seconds was found to produce a satisfactorily sparse coverage for indentation experiments. The dislocation-free cubic Si nanocubes tested , Figure 4.2, were 25 nm to 65 nm in size and had {001} facets with slight asperity [7,214]. The truncation of edges and corners leads to the rounded profile of the NCs aligned such that a $\langle 110 \rangle$ direction is along the electron beam as seen in Figure 4.2b. The edge-to-edge and corner-to-corner versus face-to-face ratios for all nanocubes tested here were both 1.25 as compared to 1.414 and 1.73 for a perfect cube.

4.2.3 Preparation for *in-situ* experiments

Contamination is an ever-present problem in electron microscopy. This is especially true for complex specimen holders such as the Hysitron PI95 PicoIndenter as it has a large surface area exposed to the TEM column. It was necessary to keep the holder under vacuum using a pumping station overnight prior to experiments. Significant carbon

growth, a few tens of nm or more, was occasionally found to occur on the indenter tip after exposure to the electron beam. Plasma cleaning was therefore performed immediately prior to insertion for four minutes using either a Fischione 1020 plasma cleaner or Fischione 1070 NanoClean system operating at 40 Watt power. When this procedure was followed, no carbon buildup on the indenter was observed and column vacuum quickly reached desirable levels.

4.2.4 *In-Situ* Compression.

NCs were compressed by a 50 mm to 500 mm wide flat diamond tip of a Hysitron PI95 PicoIndenter modified for improved lateral stability as described in Section 4.3.5. Compressions were performed in displacement control at a rate of $0.8\,\mathrm{nm\,s^{-1}}$, corresponding to a strain rate of about $10^{-2}\,\mathrm{s^{-1}}$ to $10^{-1}\,\mathrm{s^{-1}}$, which was found to be the slowest stable displacement rate. ZLP-filtered images were acquired using the Gatan 692 TV-rate CCD (25 fps) of a Gatan GIF 2002 attached to an FEI Tecnai F30 (S)TEM with TWIN pole piece having $C_s = 2.0\,\mathrm{mm}$ and operating at 200 keV. Specimens transferred quickly to the TEM remained nominally oxide-free while delays allowed a 1 nm to 2 nm oxide to form, enabling H-terminated and oxide-passivated NCs to be studied. To provide contrast of the $\{111\}\langle 1\bar{1}0\rangle$ slip system, the NC was rotated for view along its $\langle 100\rangle$ or $\langle 110\rangle$ zone axis. Displacement δ_i and contact width w_i were measured in-situ and fitted assuming a square contact area to determine the true stress and strain.

4.2.5 Calculation of True Stress and True Strain

Accurate determination of critical dimensions and their change during mechanical deformation is a significant challenge for nanoscale materials. For example, to determine contact stresses during mechanical deformation by an AFM tip or a nanoindenter, the sample size is typically measured before and, if possible, after deformation with reasonable fitting employed to estimate the instantaneous cross-sectional area. At the size scales considered here, small errors in this estimate can yield drastic over- or under-calculation of stresses. Similarly, the small displacement rates needed to compress nanoscale structures or perform nanoindentation of thin films or bulk samples push the limits of detection. Small errors in measurement can likewise result in large errors

in strain estimates. An extraordinary benefit of performing *in-situ* deformation in the TEM is the ability to directly measure instantaneous critical dimensions for determination of true stress and true strain.

In the experiments performed here, small silicon nanocubes were compressed between a sapphire substrate and small-diameter diamond flat punch. Slight tilting of the substrate and electron transparency of the indenter tip enabled instantaneous measurement of the contact width as well as instantaneous height of the nanocube. The contact stress was calculated to be

$$\sigma_i = {}^{L}\!/_{w_i^2} \tag{4.1}$$

when viewed along a $\langle 100 \rangle$ direction and

$$\sigma_i = {}^{L}\!/_{(\sqrt{2}w_i)^2} \tag{4.2}$$

when viewed along a $\langle 110 \rangle$ direction, where σ_i is the instantaneous contact stress, L is the instantaneous load, and w_i is the instantaneous projected width of contact between the nanocube and indenter.

In the event that the contact surface was obstructed, a displacement-dependent, exponential fitting function to model the asperity of the nanocube surface was employed to determine contact stress. The volume-conserving equation for change in width under large strains

$$\Delta w = -d\left[1 - \left(1 + {}^{\Delta L}\!/_{L}\right)^{-{}^{\nu}\!/_{2}}\right] \tag{4.3}$$

was modified to account for the surface asperity by inclusion of a fitted exponential term such that the instantaneous contact stress σ_i is

$$\sigma_i = {}^{L}\!/_{\left\{w_0 + (R_0 - w_0)\left[1 - \exp\left(-6\epsilon\right)\right](1-\epsilon)^{-\nu/2}\right\}^2} \tag{4.4}$$

where the term w_0 is the initial contact width, R_0 is the initial particle width, and ν is the Poisson ratio for silicon. The term $[1 - \exp(-6\epsilon)]$ accounts for the surface asperity and corrects the contact area at low strains while the Poisson relation $(1-\epsilon)^{-\nu/2}$ corrects for volumetric expansion at large strains. This model was found to be consistent with cases where contact surfaces were visible, as demonstrated in Figure 4.3.

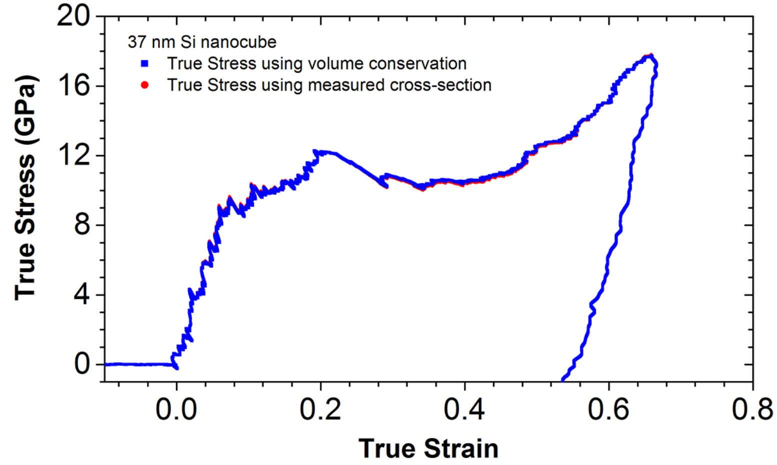

Figure 4.3: True stress versus true strain curve as determined from instantaneous contact width (red) and using a fitted contact area (blue). The fit matches the experimental contact width and hence stress at high and low strains with only slight deviation in the region of the load drop. When contact width could not be measured the contact width was determined using Equation 4.4 and the instantaneous displacement as measured *in-situ*.

4.3 Results and discussion

4.3.1 Mechanical properties of Si Nanocubes

Representative stress-strain curves for particles between 22 nm and 65 nm, compressed to strains greater than 60%, can be found in Figure 4.4 with a complete data set presented in Figure 4.5. A target displacement rate of $0.8\,\mathrm{nm\,s^{-1}}$ was used in all cases. A linear elastic response was observed up to a true strain of $7 \pm 1\%$ with a corresponding true stress exceeding 7.3 ± 1.2 GPa and resulting loading modulus of 110 ± 23 GPa. Stress continued to increase until a true strain of $20 \pm 3\%$ strain, reaching a true stress of 11.2 ± 1.4 GPa. This upper yield strength was followed by a load drop and displacement excursion extending to nearly 30% true strain with true stress reducing to 9.5 ± 1.5 GPa. This stress remained relatively constant until 35% true strain at which point work hardening began. Between true strains of 35% and about 60%, the work hardening is fairly linear before increasing exponentially beyond 60% strain, as is seen in Figure 4.5, due to the accumulation of back stress from trapped dislocations as the compression confines the slip planes from both sides as discussed in Section 4.3.4.

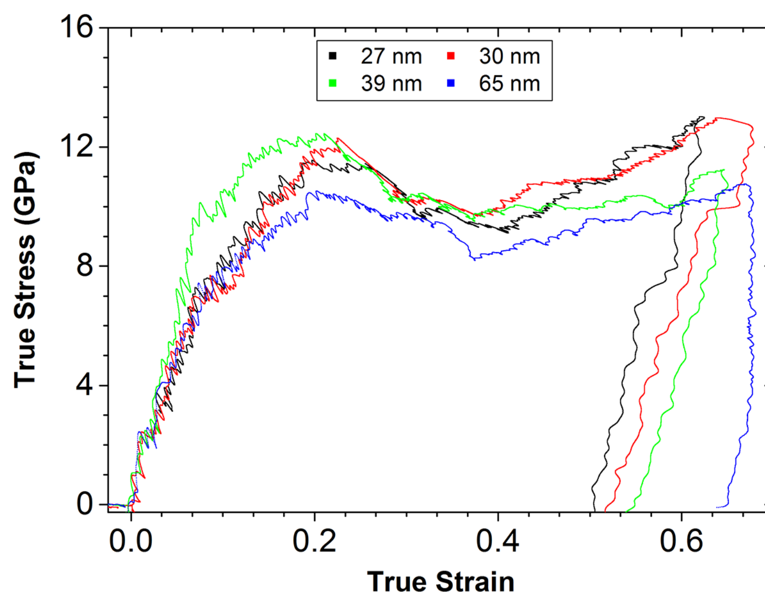

Figure 4.4: Representative true stress versus true strain curves for [001]-compressed nanocubes of varying size. Linear-elastic response was consistently observed to about $7 \pm 1\%$ strain, followed by a deviation from ideal up to $20 \pm 3\%$ with corresponding yield strengths of $7.3 \pm 1.2\,\mathrm{GPa}$ and $11.2 \pm 1.4\,\mathrm{GPa}$, respectively. The upper yield point was followed by a load drop with measurable hardening beginning around 40% strain.

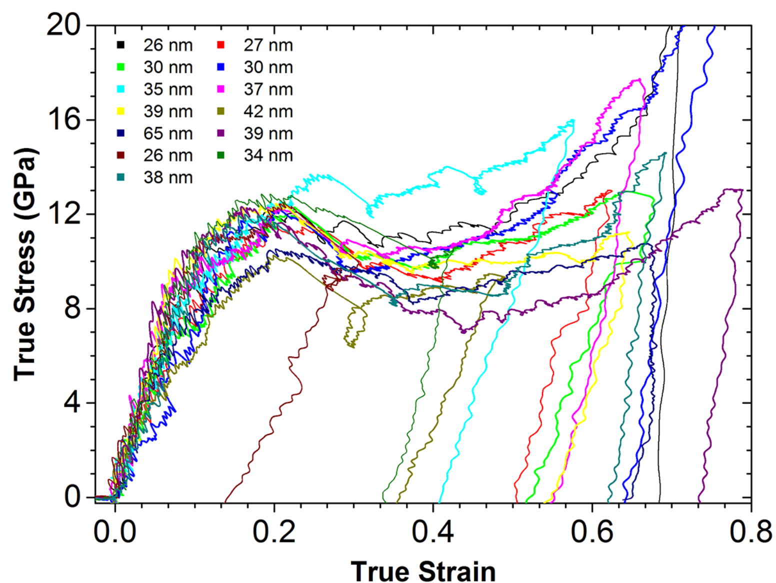

Figure 4.5: True stress versus true strain curves for [001]-compressed nanocubes of varying size. Hardening rates varied considerably amongst the compressed nanoparticles.

Comparing each region of the stress-strain curve with the *in-situ* TEM images of a nominally oxide-free 38 nm nanocube oriented along its $[0\bar{1}1]$ direction, Figure 4.6, we can gain insight to the state of stress and mechanisms governing plasticity. Following initial contact broad strain contours can be seen originating at the contact surfaces, growing across the nanocube as strain is increased. In the [110] projection the contours are bent, highlighting the slight asperity of the nanocube faces. When viewed along the [100] projection, Figure 4.7, the strain contours appear appear parallel to the surface. As the stress-strain curve deviates from linear-elastic response around 7% strain, or 10 s, sharp yet irregular contrast can be observed near the center of contact on the nanocrystal. As the stress-strain curve reaches its maxima, sharp bands of contrast along $\{111\}$ directions abruptly form within one to two frames as the sudden load drop causes a displacement excursion. Continued compression up to around 35% strain results in the development of additional $\{111\}$-habit bands of contrast. Within this range, the bands of contrast flicker while remaining in the same position as they originated hinting that additional dislocation activity may be occurring on these planes. As the stress begins to increase, additional $\{111\}$-habit bands of contrast form until in an interlocking pattern develops hinting that sessile Lomer-Cottrell locks have formed and are impeding dislocation motion, generating a back stress and resultant work hardening. The entire sequence is more concisely demonstrated in Figure 4.8, highlighting each region of the stress-strain curve, and is carefully examined in greater detail in Section 4.3.3.

The elastic response ϵ_{PEL} up to 7% in these sub-70 nm Si nanocubes is substantially larger than observed in other nanoscale crystalline Si systems such as nanowires under tension [17, 48, 204], compression [14, 15, 191, 215], or bending [16, 205–207, 209], Figure 4.1, which demonstrate elastic strains below about 5% and fracture strains below 12%. The upper yield point σ_{UYP} of 11 GPa is comparable to that of the strongest, and smallest, nanowires in these studies and approaches the ideal strength of silicon, $E/10 = 16$ GPa. Contrary to these reports, however, there is no clear size dependence for elasticity, Figure 4.9, strength, Figure 4.10, or modulus Figure 4.11. If we are to consider the nanowire morphology and assume for now that yield in nanoscale silicon is mediated by source nucleation on the surfaces, we can postulate that the large surface areas of nanowires, scaling with diameter, will play a strong role in the increasing strength

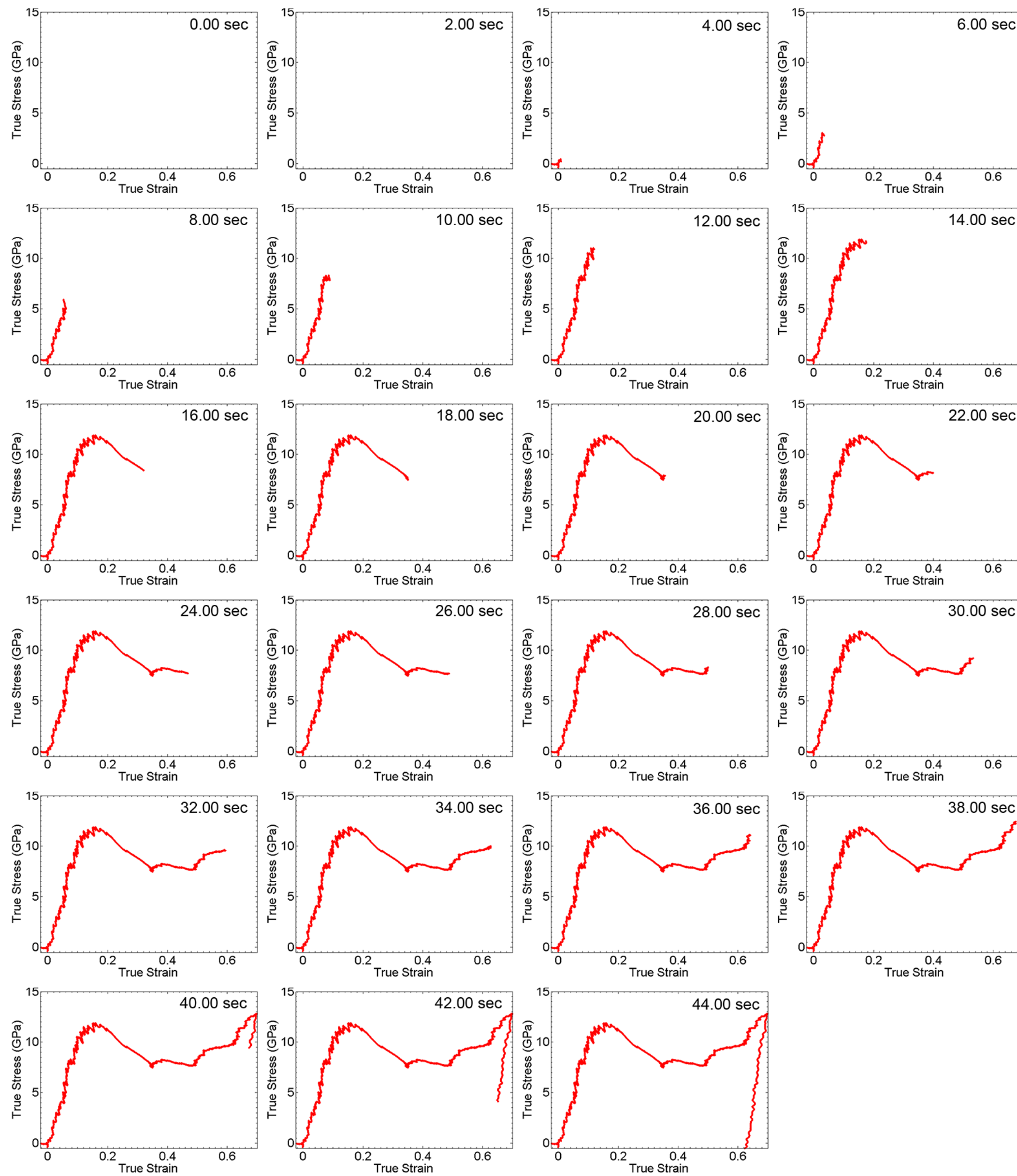

Figure 4.6: True stress versus true strain curves of a 38 nm particle whose $[0\bar{1}1]$ direction is oriented along the electron beam and whose slip planes are parallel to the beam direction, corresponding to the respective frames on the next page.

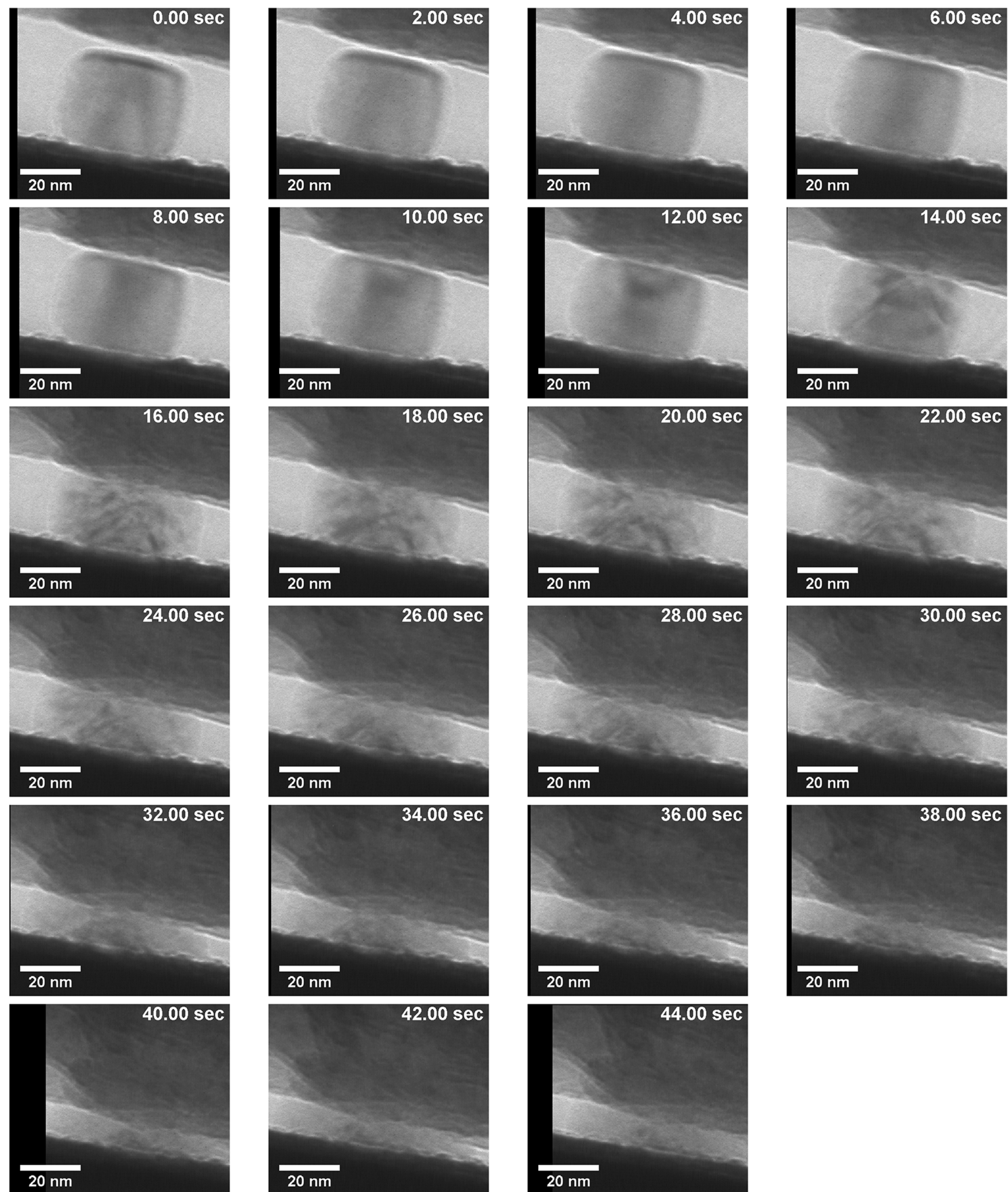

Figure 4.6: (contd.) *In-situ* TEM image series of a 38 nm particle whose $[0\bar{1}1]$ direction is oriented along the electron beam and whose slip planes are parallel to the beam direction, corresponding to the stress-strain curves on the preceding page.

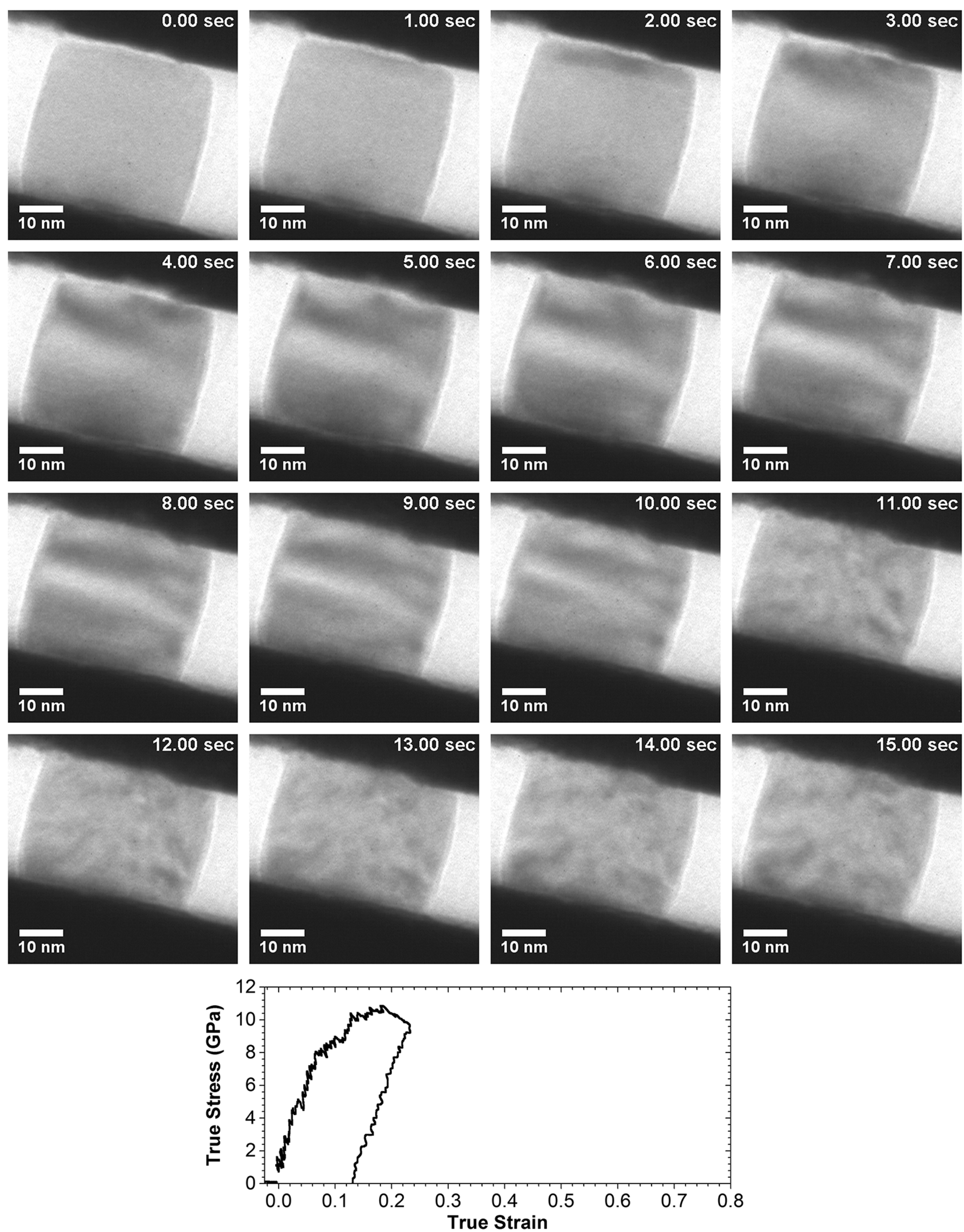

Figure 4.7: *In-situ* TEM image series and true stress versus true strain curve of a 40 nm particle whose [100] direction is oriented along the electron beam and whose slip planes are inclined to the beam direction.

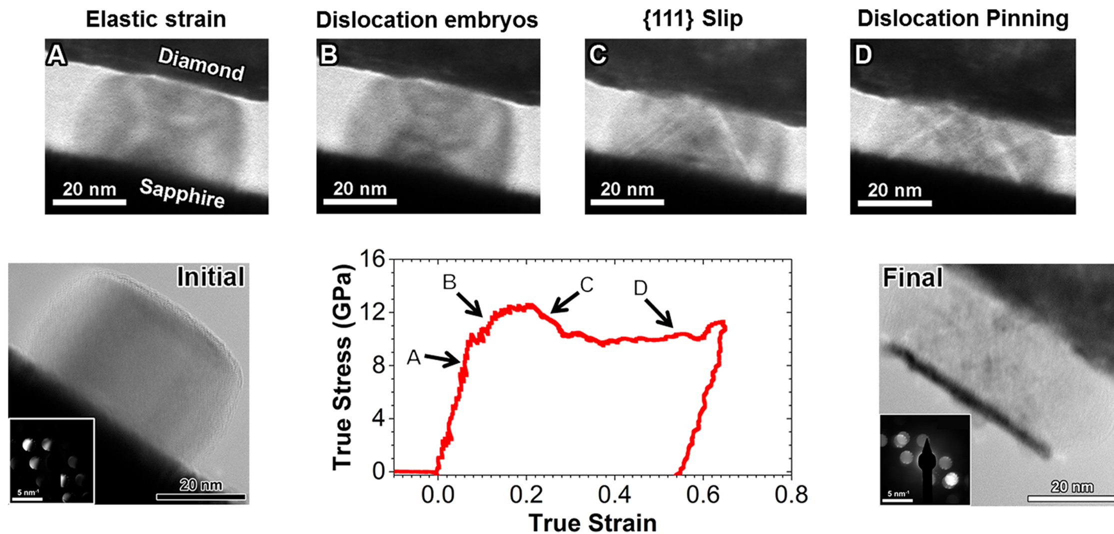

Figure 4.8: *In-situ* TEM image series and true stress versus true strain curve of a 39 nm $[0\bar{1}1]$-oriented particle, seen prior to compression in left frame with CBED pattern inset. (A) Symmetric strain contours are observed to extend from the compressed surfaces. (B) Irregular contrast near the compressed surfaces appears as the true stress-true strain relationship deviates from linear. (C) Sharp contrast bands on {111}-habit planes appears at the upper yield point. The bands multiply as strain increases, until (D) complex dislocation activity is observed beyond 40% strain. The *post-mortem* image, right, is seen with accompanied CBED pattern inset. The nanocube stuck to the indenter, limiting imaging however the CBED pattern shows slight grain rotation, most clearly seen in the 220 reflections.

and elasticity the nanowire experiments. As the diameter is reduced, the absolute surface area decreases dramatically and the number of pre-existing defects is reduced. The reduction of pre-existing defects then increases the applied stresses required to initiate plastic deformation. In the case of silicon nanocubes, the length scale is confined in all three dimensions, resulting in greatly reduced surface area. Large changes in nanocube size result in smaller absolute changes in available surface area and the length scale no longer plays a significant role in determining strength and elasticity. Such considerations are important in nanoscale devices that are confined in three dimensions. The extremely short channel lengths and widths in modern FINFETs, for example, would respond to applied stresses differently than would nanowires whose length are many times greater than their diameter.

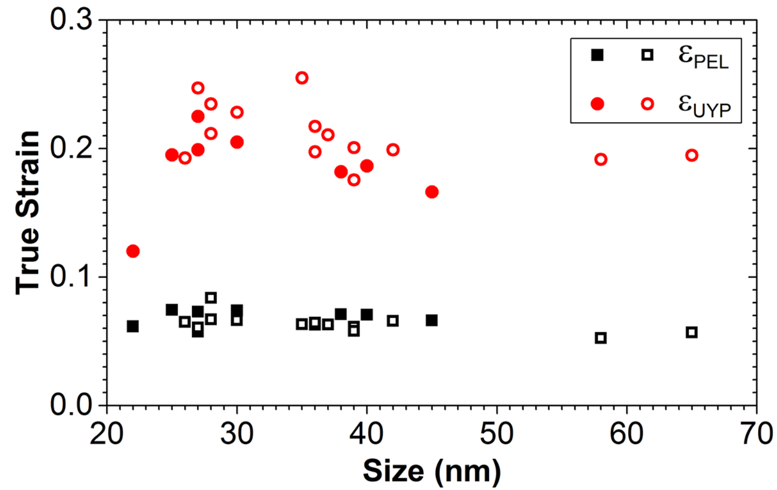

Figure 4.9: Strain limits versus nanocube size demonstrating a large elastic strains ϵ_{PEL} of 7% and strains at the upper yield point ϵ_{UYP} approaching 20%. No clear size effect is present. Solid symbols are oxide-free nanocubes while open symbols have a thin native oxide.

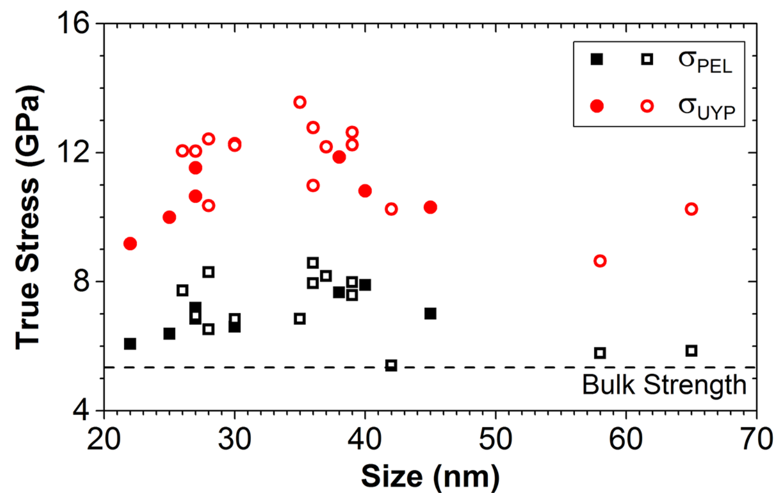

Figure 4.10: True stress versus nanocube size at transition from perfectly elastic to elastic-plastic σ_{PEL} and at the upper yield point σ_{UYP}. Contract stresses at σ_{PEL} approach 7 GPa and at σ_{UYP} exceed 11 GPa. Solid symbols are oxide-free nanocubes while open symbols have a thin native oxide.

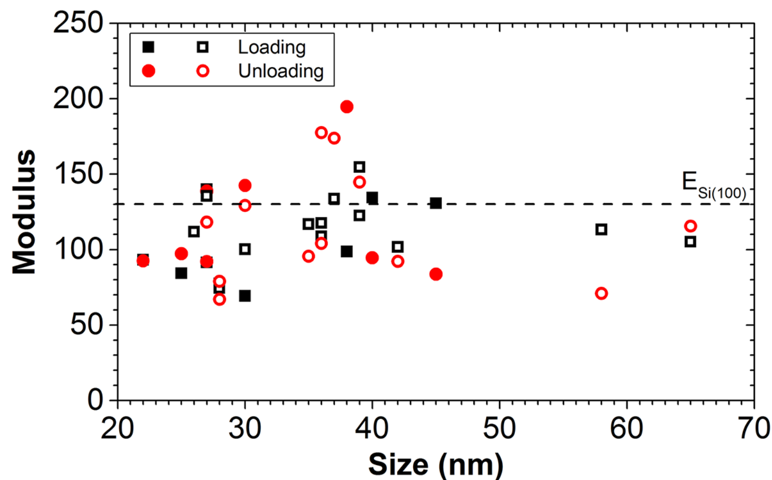

Figure 4.11: Measured modulus with respect to nanocube size during (black) loading and (red) unloading. Solid symbols are oxide-free nanocubes while open symbols have a thin native oxide. Bulk modulus for Si(100) $E_{Si(100)}$ is represented by the dashed line.

Surface nucleation-mediated plasticity was demonstrated by repeated compression of a 45 nm Si nanocube whose stress-strain curves are seen in Figure 4.12. Initial compression of the nanocube was aborted at the first sign of yielding and the nanocube was then repeatedly compressed with displacements of approximately 5 nm. Between each compression the particle height and width were measured and used to offset each curve. The strength of the NC under the initial compression approached 11 GPa as observed in compressions of other nanocubes. On the subsequent compression, plastic response began just below a stress of 7 GPa, comparable to that observed in full, continuous compressions. Such an effect supports an interpretation that the nanocubes represent an effectively defect-free volume of crystalline silicon. An applied stress of 11 GPa is required to nucleate the first planar defects which generate steps on the contact surfaces. These initial steps and respective stress concentration promote plasticity at reduced applied stress on subsequent compression. The repeat loading experiment also demonstrates the stress drop is not the result of time-dependent stress relaxation, and is a real feature of the stress-strain curve for these particles. The mismatch between the unloading particle height at zero load and post-mortem measurement suggests that a significant amount of reverse plasticity occurs on unloading. The contribution of tensile

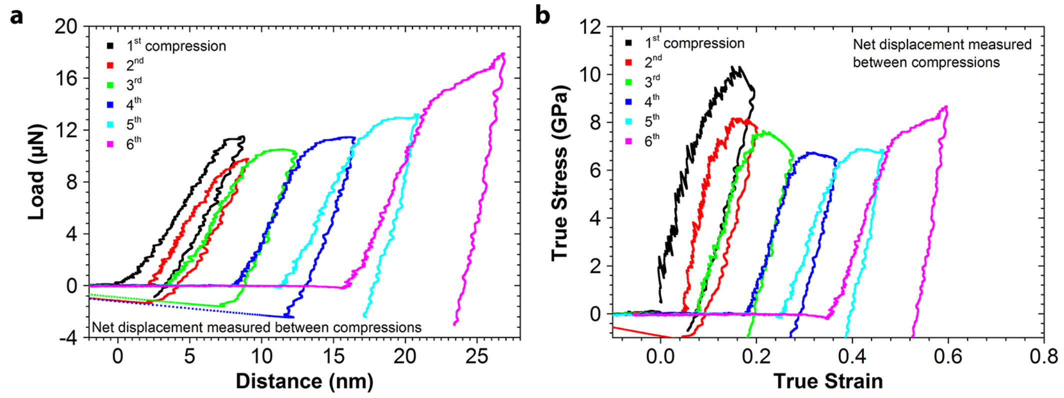

Figure 4.12: Repeat compression of a 45 nm Si nanocube plotted as (a) load-displacement and (b) true stress - true strain. Particle height was measured between compressions. The first compression was aborted upon observation of {111}-habit contrast. Subsequent compressions were terminated at a target displacement of 5 nm.

loading due to indenter-particle adhesion after compression would provide extra means for reverse plasticity but is not explored further here.

While the difference seen between the stress-strain curves of nominally H-terminated and native oxide-coated nanocubes is within the statistical margin of error, Table 4.1, there is a consistent increase in magnitude of strain limits and yield stresses. The opposite effect has been described elsewhere [215, 216]. In these studies, a decrease in yield stress is attributed to nucleation of dislocations on the nanowire sidewalls and the presence of point defects at the crystal-oxide interface which create local stress concentrations. In the present work, dislocation nucleation occurs on the contact surfaces. It is believed that the soft oxide acts to redistribute the load across the contact surface which alleviates local stress gradients and increases the applied stress required for plasticity.

Table 4.1: Mechanical properties for oxide-free and oxide-coated Si nanocubes.

Oxide	$\varepsilon_{elastic}$	StDev	$\sigma_{elastic}$	StDev	ε_{UYP}	StDev	σ_{UYP}	StDev	σ_{LYP}	StDev	$d\sigma/d\varepsilon_{Loading}$	StDev	$d\sigma/d\varepsilon_{Unloading}$	StDev
			GPa				GPa		GPa		GPa		GPa	
0 nm	0.07	0.01	6.8	0.9	0.17	0.04	10.5	1.4	9.2	0.8	104	25	110	42
1 nm	0.07	0.01	7.6	1.3	0.21	0.02	11.6	1.3	9.5	1.6	112	21	125	53

4.3.2 Investigating the mechanisms of plasticity in Si nanocubes

Unlike metallic systems, the covalent nature of silicon bonds leads to a large Peierls barrier and a higher bond energy, meaning the partial reconstruction of bonds in the dislocation core is much more significant energetically. This, coupled with the limited available slip systems, causes dislocations in Si to be straight and oriented along the low-energy $\langle 110 \rangle$ Peierls valleys on the $\{111\}$ slip plane, particularly at low temperatures and high stresses [213]. Given the observed bright-dark contrast bands appear on $\{111\}$-habit planes as would be expected for bond reordering on the $\{111\}$ slip planes. Understanding slip on the $\{111\}$ planes of FCC materials such as these Si nanocubes, Figure 4.13a,b, can be aided by the use of the Thompson tetrahedron. The Thompson tetrahedron provides a visual reference for possible atomic displacements for perfect and partial dislocations. The tetrahedron defines the $\{111\}$ planes of the crystal, the edges define the $\langle 110 \rangle$ directions, and the lines from edge to face center define the $\langle 112 \rangle$ directions. It can be seen that perfect dislocations must follow the tetrahedron edges and partial dislocations, having their burgers vectors along the $\langle 112 \rangle$-type directions, must pass first from a corner to a faulted position at face center before the trailing partial returns the faulted atom to an on lattice position. Considering the [001] compression of these particles, the maximum critically resolved shear stress τ_{crss}, defined by the applied stress times the Schmid factor [217, Ch. 9], is along the direction of the leading partial dislocation. With this in mind, the orientation of the nanocube with respect to the beam direction is such that, the crystal is oriented along its $[\bar{1}10]$ direction when the visible slip planes share an axis with the beam direction. When slip at yield is inclined, the crystal is defined as being viewed along the [110] direction, Figure 4.13d,e. When the crystal is viewed along the [110] direction the maximum τ_{crss} for a leading partial is located in the inclined $\{111\}$ planes, Figure 4.13e,f.

In the case of nucleation of dislocation half-loops on the contact surfaces, we can depict nucleation and growth of dislocation half loops across the available $\{111\}$ planes, Figure 4.14. The higher mobility of the edge component, in additional to the higher resolved shear stresses in this direction, lead to elongation of the half loop and eventual termination on the corners of the opposing side. In the case of perfect dislocations, the lower mobility of the screw component coupled with the relatively small transverse shear stresses due to contact friction may result in trapping of the screw components within

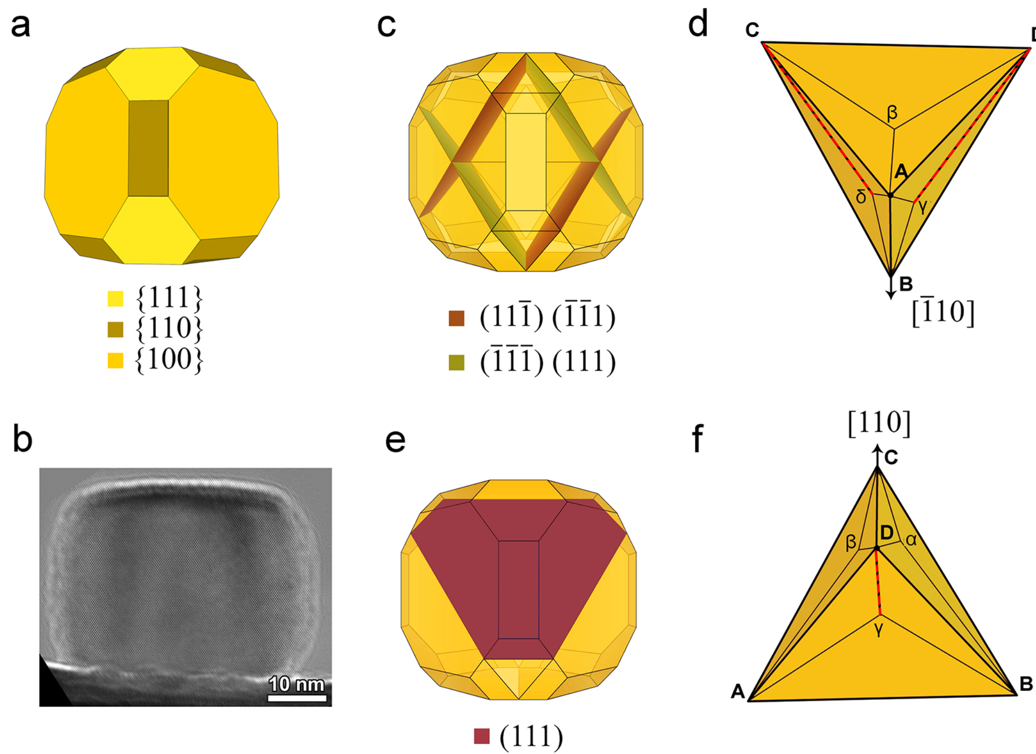

Figure 4.13: Thompson tetrahedron and schematic of slip planes in the Si nanocubes. (a) [$\bar{1}$10] projection with [001] pointing down. (b) HR-TEM image of a 38 nm [110]-oriented nanocube. (c) View along the [$\bar{1}$10] direction with the ($\bar{1}\bar{1}$1) and (111) slip planes active and (d) the respective Thompson tetrahedron defining slip planes and slip directions with Greek letters indicating each slip plane. (e) View along the [110] direction with the (111) slip plane highlighted and (d) its Thompson tetrahedron. The directions with highest Schmid factors highlighted by dashed red line.

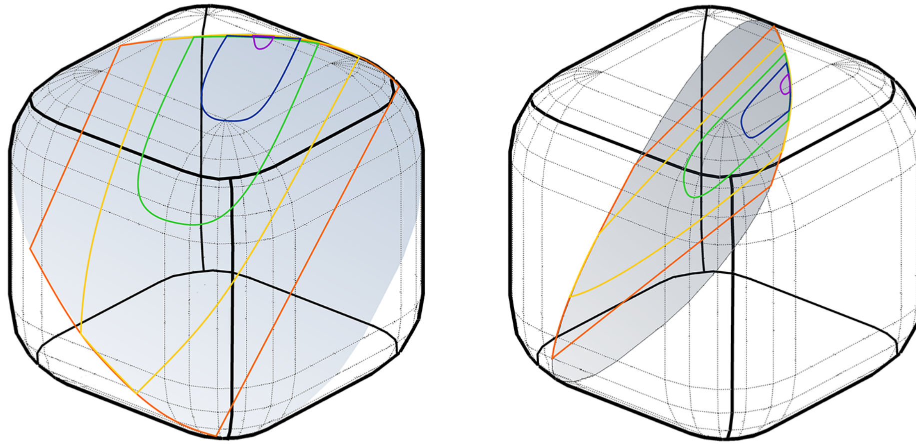

Figure 4.14: Schematic of dislocation half loops on {111} slip planes. A half loop nucleating on the compressed surface grows across the slip plane and terminates at the free corner of the truncated cube. The limited resolved lateral shear stress may prevent the screw segments of a perfect dislocation from leaving the crystal. Alternatively, a partial dislocation loop, being predominantly straight as preferred in high Peierls barrier systems, may grow across the entire crystal, leaving behind a stacking fault.

the dislocation volume, creating a localized stress field visible in the TEM images. If, however, the screw components are able to escape at the particle side walls, it seems improbable that the bright-dark contrast observed could occur from solely the edge component. In the case of formation of leading partial dislocations a slight rotation of the crystal resulting in overlapping crystal on either side of the slip plane and displaced by the burgers vector $\boldsymbol{b} = {}^{a}/_{6}\langle 112 \rangle$, may generate the observed contrast.

4.3.3 *In-situ* and *post-mortem* analysis of plasticity

Incipient plasticity. A kink in the elastic response, which is masked in load-displacement (F-d) data as the change in slope is gradual while the contact area is increasing, is revealed when converted to stress versus strain. This kink corresponds to *in-situ* observation of dislocation embryos at the contact surface. While in most cases, sharp but irregular contrast is observed at the contact surface, the formation of small, 4 nm to 5 nm dislocation embryos have also been observed, Figure 4.15. This embryo is highlighted by Moiré fringes and appears to be the source of {111}-habit planar defects the form at the upper yield point. While often seen in atomistic simulations [218–222], as

far as we are aware this is the first reported experimental observation of embryo nucleation and subsequent dislocation emission. While it was not possible in these studies to determine the exact nature of these embryos, we might postulate that the strong friction stresses created by the compressive contact generate great enough hydrostatic pressure near the center of the contact surface to allow formation of the β-tin phase observed under the confining pressures of nanoindentation [223–229]. Additional work must be done to confirm this hypothesis. Though perhaps not possible to determine experimentally with current state of technology, finite element analysis will help to estimate whether this system can produce large enough confining pressures to induce the phase transformation.

Plastic Flow. To investigate the nature of dislocations in the deformed nanocubes, compressions were performed such that the loading was terminated within the described stages of deformation. Compressions performed up to the first observation of {111}-habit activity and just beyond the displacement excursion were successfully analyzed. Compression beyond the displacement excursion invariably resulted in the nanocube adhering to the indenter tip rather than the substrate. Slight drift of the indenter tip rendered high-resolution or dark-field acquisition impossible. Representative stress-strain curves for these compressions can be found in Figure 4.16 for comparison to the full compressions described earlier. High-resolution TEM focal series imaging, dark-field imaging, and convergent beam electron diffraction were performed to analyze the nature of defects within the deformed nanocubes.

Nanocubes compressed to the point of initial observation of {111}-habit contrast, Point C in Figure 4.8 can be seen in the focal series reconstruction, Figure 4.17a. Two bright-dark bands of contrast on $(\bar{1}\bar{1}1)$ planes extend from the center of the top and bottom contact surfaces towards the opposing corners. Fourier filtering of the (111) reflection indicate that the corners are faulted with respect to the nanocube center, indicative of the formation of leading partial dislocations with Burgers vector $\boldsymbol{b} = {}^{a}\!/_{6}[211]$ type. Red lines aligned along the bright fringes of the lower right portion of the nanocube and extending along the crystal highlight the faulted nature of the crystal. Observation in the *in-situ* TEM images of additional activity on these same planes without substantial multiplication of slip planes between initial slip and the onset of hardening suggests

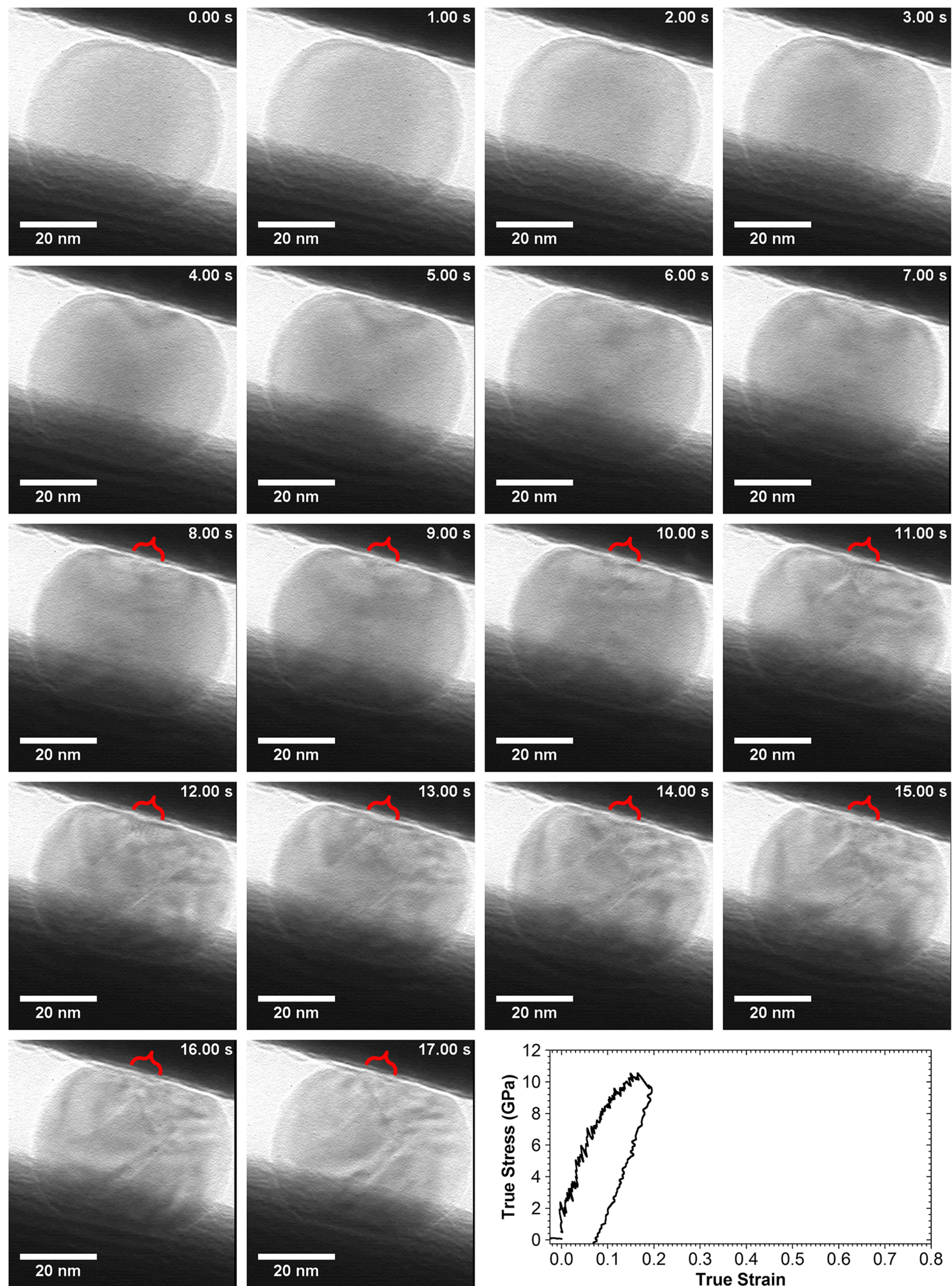

Figure 4.15: *In-situ* TEM image series and true stress versus true strain curve of a 45 nm particle whose [110] direction is oriented along the electron beam and whose slip planes are inclined to the beam direction. A 5 nm embryo forms at the upper contact surface at 8 s, marked by red brace, as the stress-strain curve deviates from perfectly elastic. At the upper yield point, {111}-habit contrast develops, extending from the embryo to the opposing corner. Parallel contrast bands form on the lower contact surface.

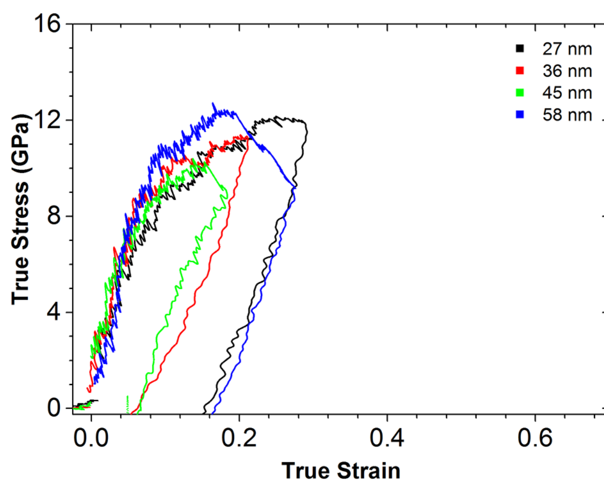

Figure 4.16: Representative true stress versus true strain data for [100]-compressed nanocubes of varying size. For post-mortem HR-TEM analysis, the compression was aborted as soon as dislocation activity was observed in the TV-rate acquisition.

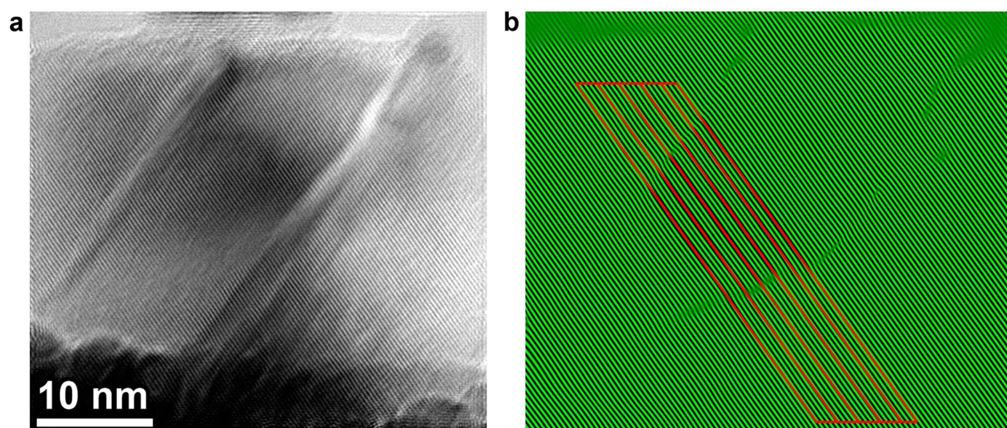

Figure 4.17: (a) Post-mortem focal series reconstruction and (b) respective (111) Fourier-filtered image of $[\bar{1}10]$-oriented 36 nm nanocube compressed to Point C in Figure 4.8 revealing two stacking faults. The red lines highlight the faulted nature of the top-left and bottom-right portions of the nanocube with respect to the center region.

that trailing partials also form but are quickly followed by additional leading partials dislocations.

The {111}-habit contrast observed in [110]-oriented nanocubes suggests the presence of either inclined screw dislocations or stacking faults. The 60° dislocation can be quickly excluded as the strain field about the dislocation line, oriented along the electron beam,

is not able to produce the extended contrast that is observed experimentally. While the faulted nature of the center of the nanocrystal relative to its edges far away from the defects is clear, it is important to consider the possibility of the inclined perfect screw dislocation. A stacking fault viewed such that the beam direction is in the plane of the stacking fault can be interpreted unambiguously. Screw dislocations distort the lattice due to mismatching planes normal to the line direction, characterized by the spiral staircase-like mismatch of the atomic bonds about the dislocation line. This strain generates broad strain contrast normal to the projected line direction will create a distorted lattice in projection whose contrast in the resulting HR-TEM image will be dependent on its location within the crystal. A slightly inclined stacking fault will similarly result in broad bright-dark contrast due to interference of the mismatched lattice in projection. Difficulty in zone axis alignment is created by the lack of beta tilt capability of the PicoIndenter as is the case of Figure 4.17 having a slight tilt about the [111] direction. This is further complicated by the rapidly changing projected thickness of the $[\bar{1}10]$-projected nanocube resulting in a non-uniform phase contrast along the defect. Experimental through-focal series of the nanocrystal depicted in Figure 4.17 reveal changing width of the broad dark-band lights of contrast in addition to apparent perfect 60° dislocations and stacking faults with associated partials which move along the (111) plane as defocus is changed.

The experimental focal series reconstruction was compared to Multislice simulations [3] of perfect screw dislocation and stacking faults in a 37 nm nanocube, Figure 4.18 and Figure 4.19, described in more detail in Appendix B. Slight rotation of 0 to 4° about the $[1\bar{1}\bar{1}]$ direction were considered due to the difficulty in aligning directly along the zone axis following compression. The $(1\bar{1}1)$-filtered images of the amplitude of the focal series reconstruction and of the Multislice exit waves are found in Figure 4.20. Fourier-filtered images were used to assist in identifying the faulted nature of the horizontally-oriented defect. The faults are more apparent if viewed in the page along the fringes. Fine detail in the Multislice simulations relative to the experimental focal series reconstructions may result from limited contrast or partial coherence of the electron beam in the experimental images.

Both perfect 60° and dissociated dislocations are present along the horizontal band of contrast in the experimental focal series reconstruction. A similar composition along

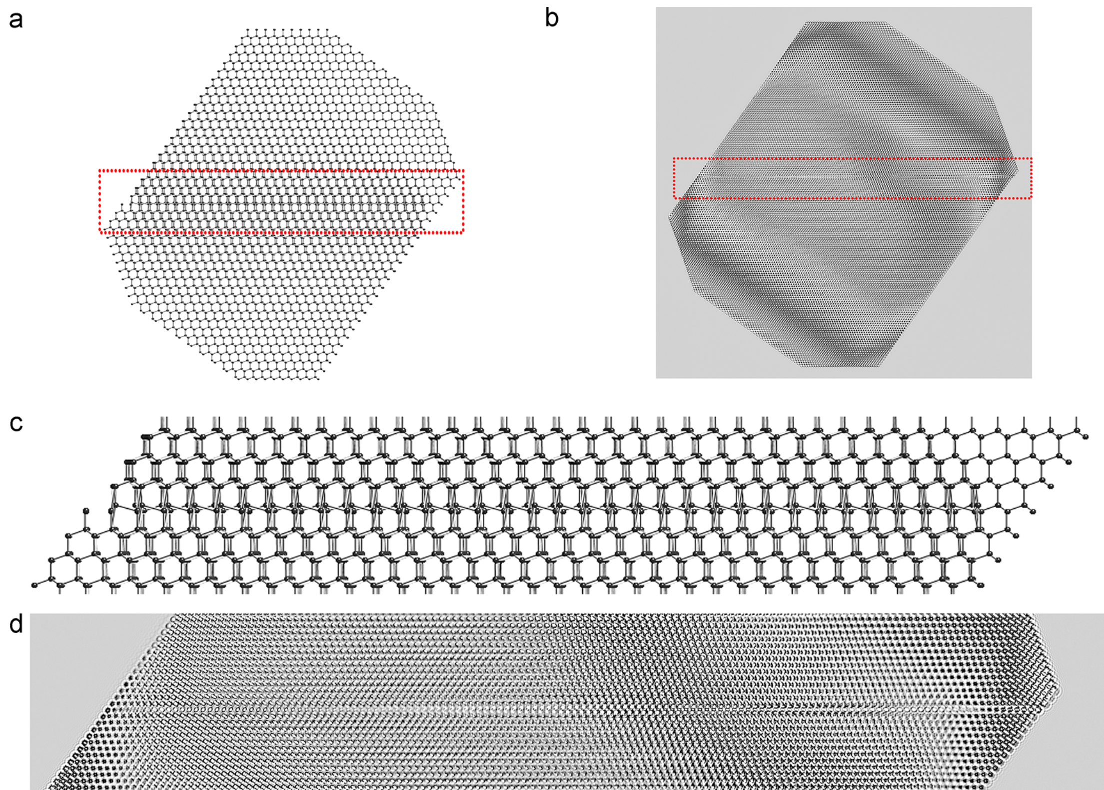

Figure 4.18: (a) Ball and stick model of a single $(1\bar{1}1)\,[10\bar{1}]$ screw dislocation in a [110]-oriented 37 nm nanocube and (b) the resulting amplitude of the exit wave. (c),(d) Magnified view of the screw dislocation.

the dislocation line or fault are seen in the amplitude component of the exit waves for single screw dislocations and stacking faults. Utilization of high-resolution, small field-of-view images can erroneously result in the determination that 60° and dissociated dislocations are present, which by design are not present within the simulated structures and cannot easily be separated. Great care must therefore be taken when interpreting the HR-TEM images and even focal series reconstructions of these defective crystals. The faulted nature of the $(1\bar{1}\bar{1})$ fringes far from the dislocation provides clear evidence of a stacking fault as opposed to a perfect dislocation such as the inclined screw.

It is generally understood that dissociated glissile dislocations must reside in the glide set [213] while any dissociated dislocations on the shuffle set are sessile. Unfortunately, the challenge of aligning the deformed nanocubes directly along the zone axis coupled

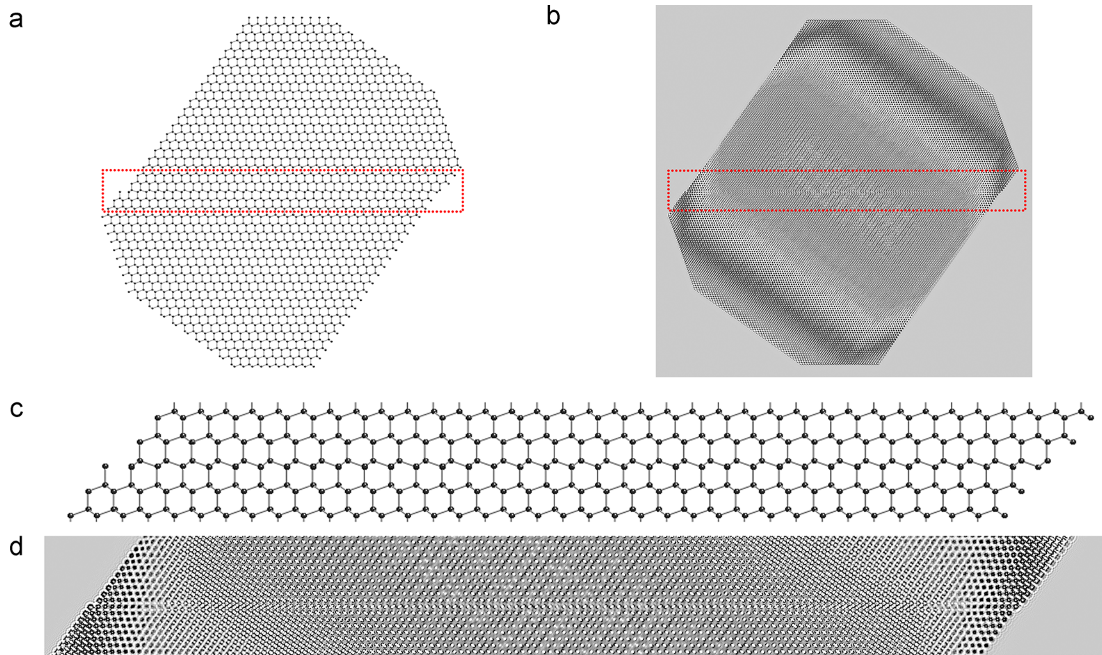

Figure 4.19: (a) Ball and stick model of a single $(1\bar{1}1)\,[1\bar{1}\bar{2}]$ partial dislocation in a [110]-oriented 37 nm nanocube and (b) the resulting amplitude of the exit wave. (c),(d) Magnified view of the partial dislocation.

with the 90° surface of the edge-on nanocube affecting local contrast have not made it possible to confirm the structure in these nanocubes. It can be seen, however, that the observed leading partial dislocations must play a dominate role in accommodating plasticity. As mentioned previously, flickering of the {111}-habit contrast bands which do not appear to multiply substantially prior to hardening suggests that the same slip bands are repeatedly slipping. For this to occur, the trailing partials must also be forming and passing through the nanocube. Additional leading partial must quickly nucleate on the same slip step as the contrast bands do not disappear. Why such a process would occur instead of deformation twinning, where leading partial are nucleated on adjacent slip planes without the formation of trailing partials, is not at present understood and must be a focus of future investigation.

Compression beyond the displacement excursion, Figure 4.21, results in activation of numerous parallel slip planes. The focal series construction and $(\bar{1}11)$-filtered image, Figure 4.21a,b, suggest that dislocation nucleation on non-neighboring planes takes

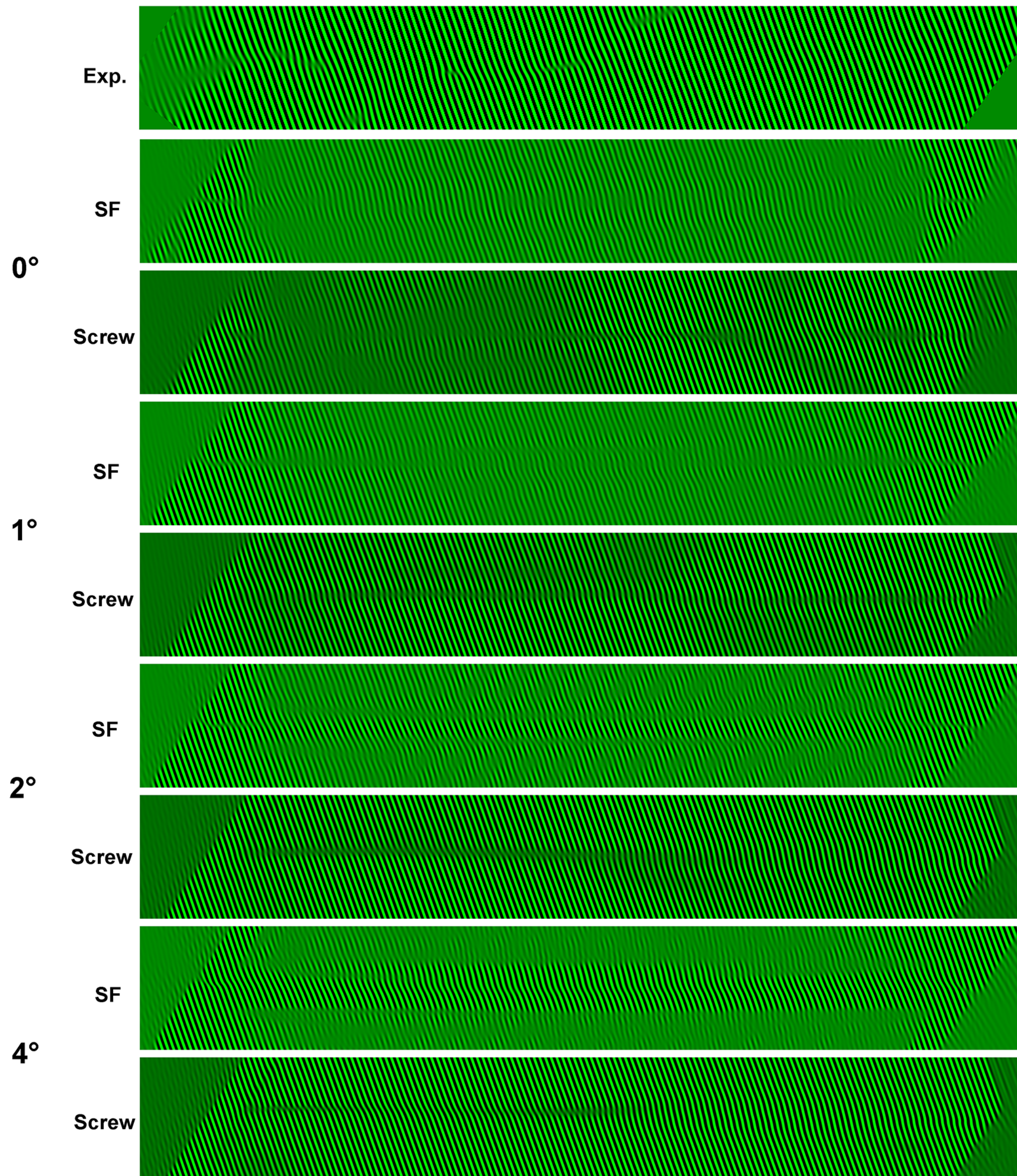

Figure 4.20: A comparison of the $(1\bar{1}\bar{1})$-filtered amplitude of the focal series reconstruction with the amplitude of the exit wave reconstructions for inclined $(1\bar{1}1)\,[10\bar{1}]$ screw dislocations and $(1\bar{1}1)\,[1\bar{1}\bar{2}]$ stacking faults in a 37 nm nanocrystal. Simulations were performed for an accelerating voltage of 200 keV, C_s of 2.0 mm, coherent incident wave function, α of 10 mrad, Δf between -200 nm and 200 nm with 20 nm defocus step.

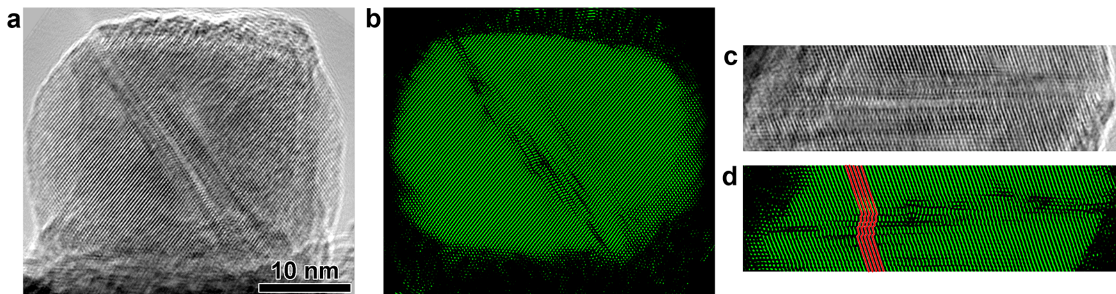

Figure 4.21: (a) Post-mortem focal series reconstruction and (b) respective $(\bar{1}\bar{1}1)$ Fourier-filtered images of $[\bar{1}10]$-oriented 28 nm nanocube compressed past the load drop after yield. Numerous, closely spaced, stacking faults on its (111) planes can be observed, highlighted in (c,d).

precedence over deformation twinning. This is supported by the *in-situ* imaging which identifies a discrete number of active slip planes with repetitive contrast changes between initial slip and the onset of hardening. A magnified view of the faulted region can be seen in Figure 4.21c,d with the faulted regions highlighted by the red lines. A slight rotation of the nanocube with respect to the electron beam occurred during compression, resulting in a misorientation for post-mortem analysis. While making direct determination of the nature and number of dislocations in the crystal is difficult, some qualitative analysis can still be performed. Stacking faults extend across the entirety of the nanocube and a small twinned region at the center. Alignment of the $(\bar{1}11)$ planes in top half of the cube with respect to the bottom in the projection of Figure 4.21c,d, suggests that an odd number of faults on the left side of the nanocube while an even number of faults exist on the right hand side.

Compression of a [110]-oriented nanocube imaged in dark-field with the g = $2\bar{2}0$ reflection selected can be seen in Figure 4.22. In DF-TEM, the incipient plasticity on the contact surface can be clearly seen, giving way to slip along an inclined {111} plane as evidenced by the horizontal Moiré fringes resulting from the relaxed crystal of the nanocube corner with respect to that of the strained core. Multislice simulations of a nanocube having one half strained relative to the other along a (111) slip plane, not pictured, demonstrated a strain mismatch of the two regions comparable to that of the strain at incipient plasticity, 7%.

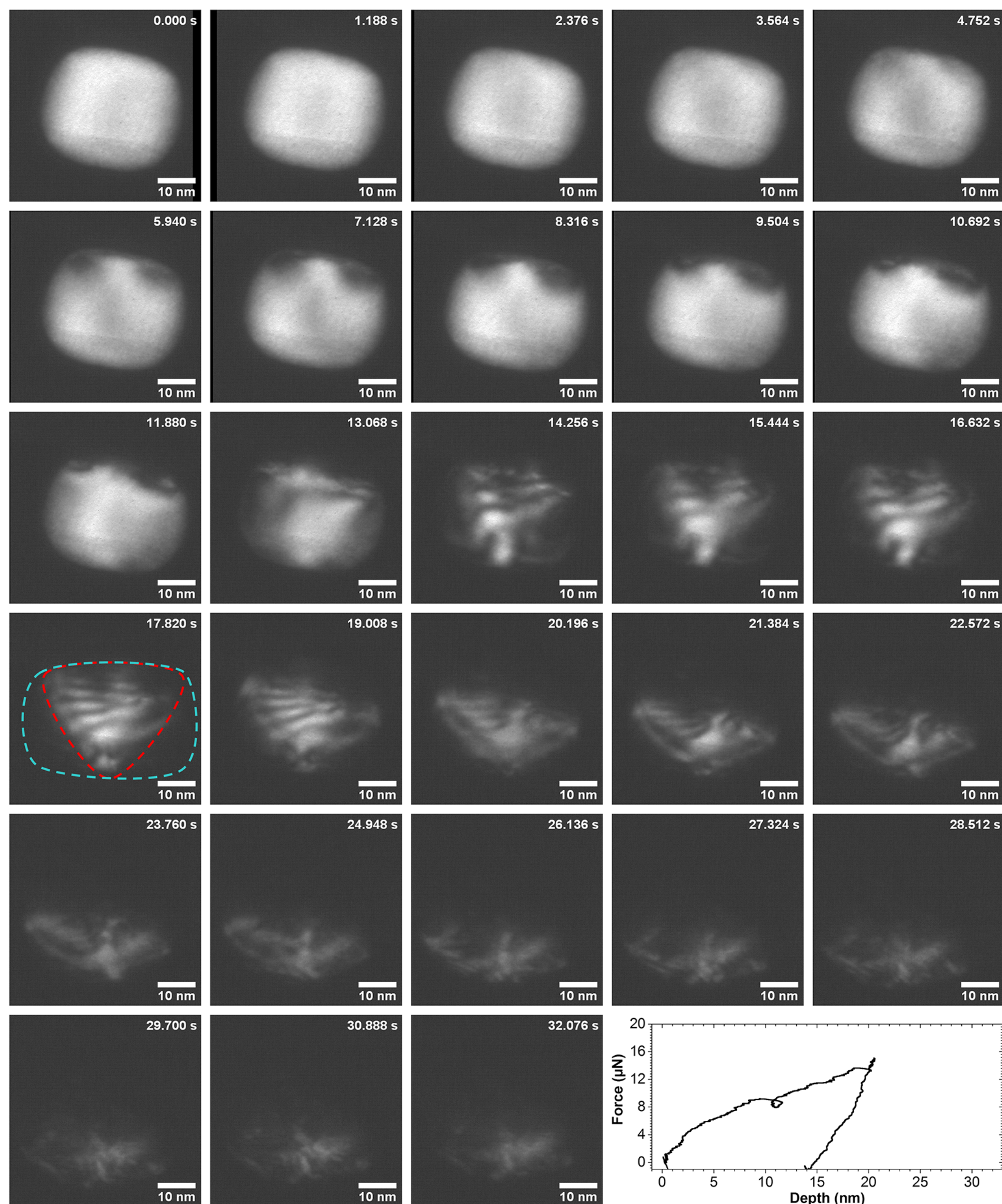

Figure 4.22: *In-situ* DF-TEM image of Si nanocube under [001] compression. Nanocube is oriented such that its [110] zone axis is along the beam direction, g = $2\bar{2}0$. The full, inclined slip plane, highlighted in red in 17.820 s frame, can be seen starting across the width of the top surface and extending to a corner of the lower surface of the nanocube whose outline is in blue.

Further evidence of partial dislocation activity can be found from post-mortem DF-TEM imaging and diffraction analysis of a nanocube compressed beyond its displacement excursion following yield, Figure 4.23. The 41 nm nanocube, initially defect free, contains bright-dark contrast on $(11\bar{1})$ planes following compression, Figure 4.23c. Corresponding CBED patterns before and after compression, Figure 4.23b,d, indicate the presence of faults on the $(11\bar{1})$ planes. This is more clear in the post-mortem selected area diffraction pattern, Figure 4.23e, containing a mirror pattern about the [111] direction in addition to satellite peaks representative of thin faulted regions. Post-mortem DF-TEM images of the 111, $11\bar{1}$, and 220 reflections of the crystal, Figure 4.23f-h, and the faulted 111_T and 220_T reflections, Figure 4.23i,j confirm the presence of $(11\bar{1})$ faults. Determination of the presence of isolated stacking faults or twin bands is not possible as the spatial resolution of DF-TEM about faulted planes is limited to a few nanometers, similar to the width of potential microtwins [1].

Contrast on {110} type planes have also been observed during compression of one [100]-oriented nanocube, Figure 4.24. The contrast, observed after the load drop moved sporadically, beginning at the top of the nanocube at about 10.5 s and eventually passing through the bottom of the cube around 25 s. Such sporadic movement on an unfavorite slip plane might suggest the formation of Lomer locks generated from two intersecting partial dislocations. The sporadic nature of the movement might suggest thermally assisted movement of the sessile dislocation through electron beam heating or heat generated from the gross deformation of the crystal. Focused studies on such a mechanism are required to provide a confident interpretation and one possibility is presented here.

Transition from perfect to partial dislocations. While plasticity in silicon subjected to low-stress, high-temperature deformation is mediated by the mobility of dislocations in the dissociated state, the abundance of evidence for plasticity in silicon at high-stress and low temperature has shown that plasticity is mediated by the nucleation of perfect dislocations, particularly under large confining pressures [213, 215]. Ostlund *et al* [14] reasoned that the ductile-to-brittle transition observed in their Si nanopillars may result from the nucleation of dissociated dislocations and the magnitude of their separation. In large pillars, the dissociation width is less than the length of the slip plain and the plasticity is limited by mobility of the slower trailing partial, therefore favoring brittle fracture. As the size is reduced, the leading partial may be able to exit the

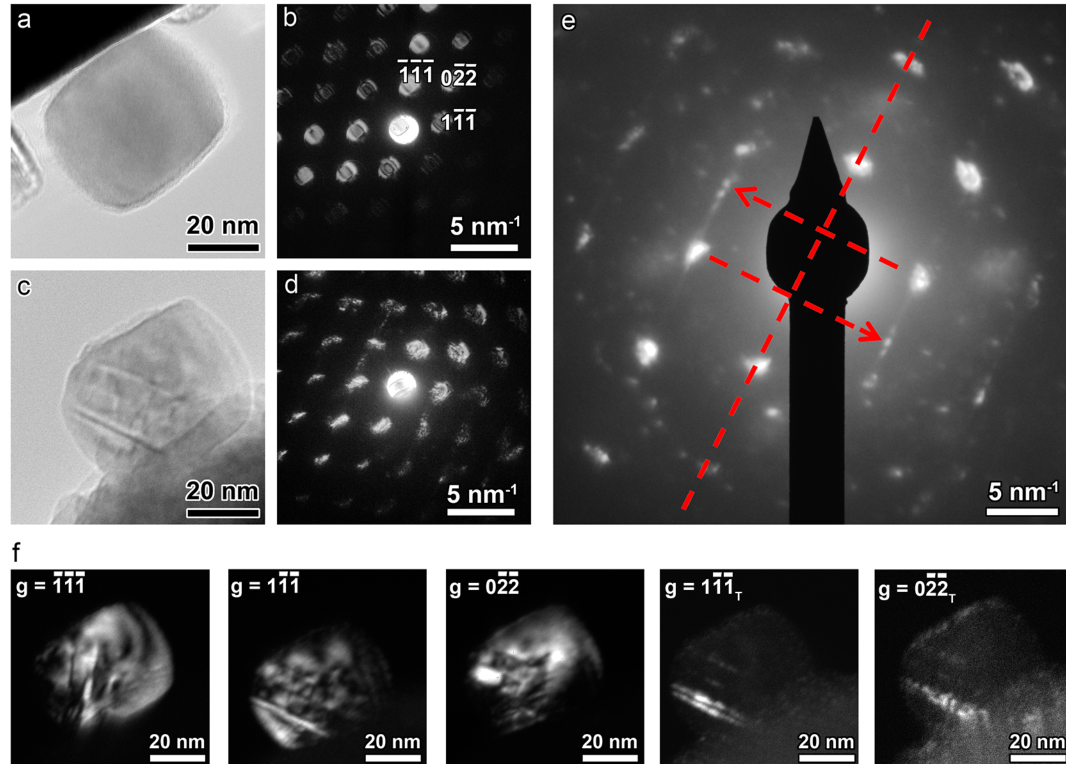

Figure 4.23: *Post-mortem* DF-TEM images of a $[01\bar{1}]$-oriented 41 nm Si nanocube after [001] compression. (a),(b) Pre-compression HR-TEM image and a corresponding CBED pattern. (c),(d) *Post-mortem* TEM image and a corresponding CBED pattern. Contrast bands are visible on $(11\bar{1})$ planes in the TEM image and as slight streaks along the [111] direction in the CBED pattern. (e) A selected area diffraction pattern aligned such that the diamond indenter contributes minimal diffraction. Additional spots along the [111] direction are indicative of faulting on $(11\bar{1})$ planes. (f) DF-TEM images using the $\bar{1}\bar{1}\bar{1}$, $1\bar{1}\bar{1}$, and $0\bar{2}\bar{2}$ reflections and the faulted $\bar{1}\bar{1}\bar{1}_T$ and $0\bar{2}\bar{2}_T$ reflections.

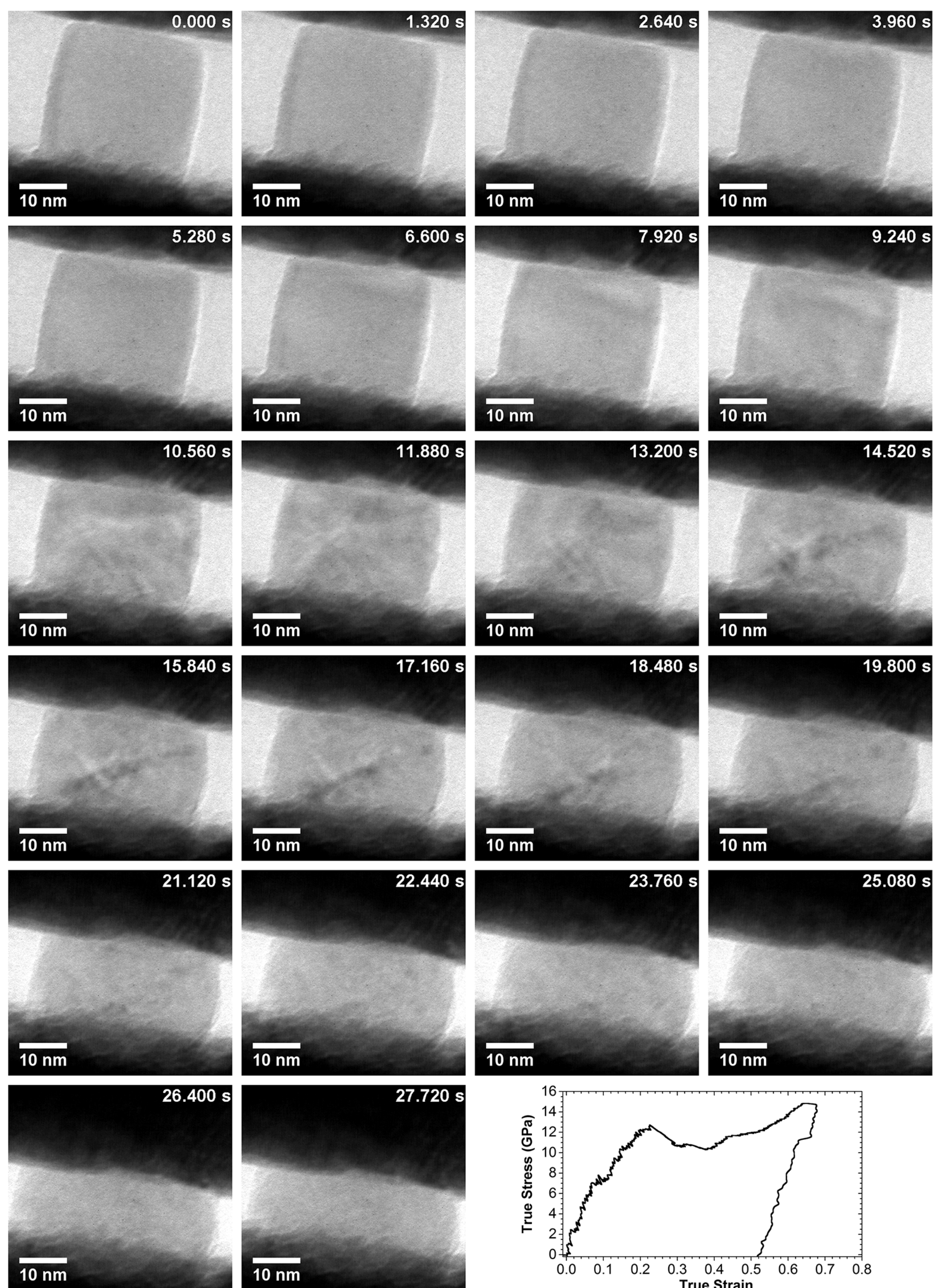

Figure 4.24: *In-situ* TEM image series and true stress versus true strain curve of a 30 nm particle whose [100] direction is oriented along the electron beam and whose slip planes are parallel to the beam direction. {110}-habit contrast can be observed. Downward translation of the contrast is sporadic in the video hinting at movement of Lomer locks (i.e. pinned {111}-habit dislocations).

crystal prior to nucleation of the trailing component. Korte and Clegg [215], however, have presented experimental evidence at 100 °C of the presence of predominately perfect dislocations within 2 µm pillars with small dissociation of screws having, a width of 4 nm and lengths of 40 nm, far below the ductile-to-brittle transition size reported by Ostlund *et al*.

Applying classical dislocation theory, Chen *et al* [230], compared the approximate critical shear stress τ_N required to nucleate perfect dislocations with that required to nucleate Shockley partial twinning dislocations τ_P. By combining the equations

$$\tau_N = \frac{2\alpha\mu b_N}{D} \tag{4.5}$$

and

$$\tau_P = \frac{2\alpha\mu b_P}{D} + \frac{\gamma}{b_p} \tag{4.6}$$

where μ is the shear stress (60 GPa for silicon), γ is the stacking fault energy (60 mJ m^{-2}), b_N and b_P are the burgers vectors to perfect and Shockley partial dislocations and α is equal to 1, a critical grain size for the transition between partial and perfect dislocations is found to be [230]

$$D_c = \frac{2\alpha\mu\left(b_N - b_P\right)b_P}{\gamma}. \tag{4.7}$$

For the case of silicon, the critical grain size is then 80 nm, or slightly above the crystal size examined within this work. While we did not have access to larger crystal for compression, the transition from perfect dislocation activity, or slightly dissociated dislocation activity, as seen by Korte and Clegg [215] and to our observation of partial dislocation activity is must fall between the two and this analysis provides a convenient, physical explanation for the observed transition.

4.3.4 The role of back stress in small volume strengths

Nanoscale materials capable of withstanding mechanical stresses approaching their theoretical limit are not new; however, the underlying mechanisms which enable such high strengths, particularly their dependence on length scale, are not fully understood [182, 187]. The potential for high-strength, high-ductility nanomaterials make possible a variety of new technologies such as durable MEMS devices through ductile

insulators. Particularly interesting is the demonstrated room temperature ductility of traditionally brittle materials at the nanoscale coupled with an observed increase in strength. Control and understanding of this mechanical behavior of confined materials is critical for the optimization and tunability of materials properties as nanoscale technologies mature.

Previous work by Garcia-Manyes and Guell [19] and Mook et al [20] found the contact stress in nanoscale silicon approaching and exceeding the theoretical strength E/10 = 16 GPa. The measured contact stress of 17 GPa for shallow indentations of silicon by a diamond indenter tip mounted to an AFM [19] is narrowly within the accepted limits of theoretical strength. Compression of Si nanospheres [20] presented an even more compelling case as the measured contact stresses appear to exceed the theoretical strength, particularly when considering that the triaxiality of stress is less in this case than indentation. In Figure 4.25 it can be seen that the contact stresses in both cases are comparable when relating the size of the plastically deformed Si spheres to the calculated plastic zone diameter $4a$ of the indented silicon. Using the estimate of yielding in [19] which occurs at 16 µN with a 75 nm tip, a hardness of 10.8 GPa was obtained which in terms of $H/3$ [19] gives a yield strength of 3.6 GPa. The plastic zone radius for nanoindentation was calculated using [231, 232]

$$R_p = \sqrt{\frac{3P}{2\pi\sigma_{ys}}} \tag{4.8}$$

where P is the applied load and σ_{ys} is the yield strength. Inserting the above values into Equation 4.8 gives a plastic zone radius of 45 nm. With their displacement δ of 3.2 nm one can calculate a contact radius of 21.7 nm such that $R_p = 2a$ where a is the contact radius of the indenter. Using $4a$ as a scaled plastic diameter to compare to the plastically deformed sphere diameter in Figure 4.25 is therefore reasonable.

This suggests that there is exists a strong correlation between plastic zone size and strength as in both cases stresses near the theoretical strength are maintained for length scales up to about 60 nm even after substantial plastic deformation. This was tentatively explained as being due to a pressure effect which would also increase the modulus of elasticity, however, in both cases the contact stress was well into the plasticity regime

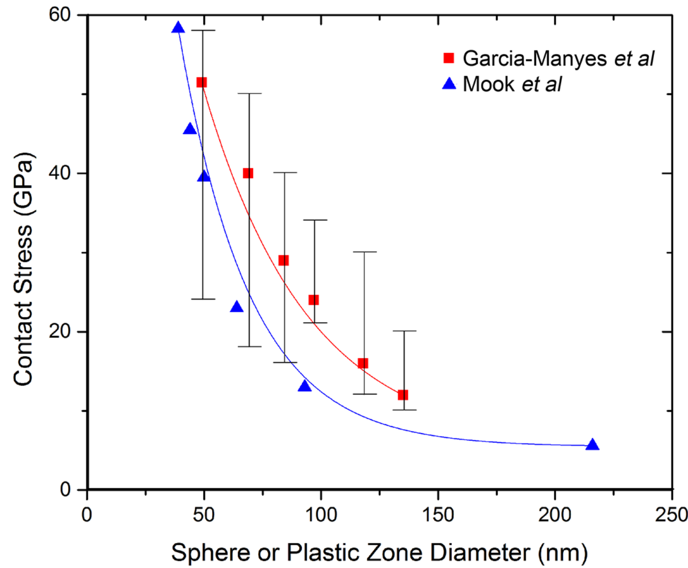

Figure 4.25: Calculated contact stress versus (blue) initial sphere radius of compressed spheres or (red) plastic zone diameter of nanoindentation of bulk silicon. Original data from [19, 20].

and previous studies have shown that the flow stress or hardness drops as dislocation plasticity is nucleated [233].

Similar observations have been made in other materials. The hardening rates $dP/d\delta$ for 33 nm and 12.5 nm films of Permalloy (80 Ni, 20 Fe) [192] were found to be 20 000 N m^{-1} to 33 000 N m^{-1}, respectively, far less than the value of 10 800 N m^{-1} predicted using Hertzian contact theory [234]. While the higher modulus of the c-axis sapphire substrate (400 GPa versus 200 GPa for Permalloy) may contribute, there are two additional factors to consider. Pile-up around the indenter would increase the contact area over that calculated and support more load. More importantly, the significance of back stress from emitted dislocations subsequently trapped in the small, constrained volume must be understood.

The finite size of nanoscale materials creates an inherent limitation on the number of possible dislocations and the small separation between dislocations produces large back stresses which have long been understood to impact strength [235–240]. Analysis of the discrete contribution of the back stress from dislocations as they nucleate and propagate within a material, however, has been beyond the reach of experiment. Here we present

direct experimental evidence of the contribution of back stresses due to dislocation pile-up following load drops during constant-displacement loading of a nanoscale geometry that was more easily interpretable: crystalline silicon nanocubes.

Using the data obtained for Section 4.3.1, we have analyzed the work hardening regime to compare the observed hardening to the back stresses calculated for geometrically necessary dislocations. After unloading a 37 nm cube the residual displacement was found to be approximately 22 nm. This would translate to approximately $\delta/b = 60$ dislocations if the full Burgers vector of 0.384 nm were considered.

In order to examine the back stresses exerted by dislocations nucleated in the Si nanocubes we developed a model associating plasticity with stress. Previously, tests on spheres and pillars could be fit with a dislocation pile-up model as given by [235],

$$\sigma = \frac{2\mu b N_{eff}}{\pi l_s (1-\nu)}. \tag{4.9}$$

Here, N_{eff} is an effective number of dislocations in a pile-up that would exert enough of a back stress to account for both the effective stress and a back stress, μ and ν are the elastic constants, b is the Burgers vector and l_s is the length scale of the sphere or pillar. This is repeated here for 37 nm silicon cube.

Using a refinement of Equation 4.9 we can estimate the back stress during compression of the Si nanocubes with dislocation activity on the $\{111\}\langle 1\bar{1}0\rangle$ slip system. This is illustrated in Figure 4.14b with dislocation emission starting at the top center of the cube where a stress concentration exists with growth in the $[1\bar{1}0]$ direction for perfect dislocations, as molecular dynamics models have predicted to occur at this length scale [197]. While it is not known exactly how far the first dislocation travels before it stops, a reasonable estimate would be that the distance traveled is the height of the cube h. Regarding the shear area, considering the large plastic deformation at the onset of hardening, one can estimate that the originally triangular shear surface has become compressed into a trapezoid of the form $A = {}^{a+b}/_{2}\sqrt{2}h_i$ where $a = \sqrt{2}w_i$ and $c = \sqrt{2}\,(w_i - h_i)$ where w_i and h_i are the instantaneous width and height of the particle. This gives an instantaneous shear area of the form

$$A_s = \left(2w_i h_i - h_i^2\right). \tag{4.10}$$

Accounting for compression, l_s becomes $\sqrt{2}h_i$. Upon resolving the force F_N in the normal direction required to resist the compressive force, one finds

$$F_N = F_S \sin\theta = \tau A_s \sin\theta. \tag{4.11}$$

With the nominal shear stress being about half of the applied stress, the back stress acting on the compressive stress is then the normal force acting on the cube face, w^2, such that

$$\sigma_{BS} = {}^{F_N}/_{w^2} = \frac{\mu b N_{eff} \sin\theta}{2\pi\left(1-\nu\right)} \frac{\left(w_i - h_i\right)}{w_i^2}. \tag{4.12}$$

Clearly this is an estimate not knowing the exact arrangement of dislocations or their number but is proposed to give a reasonable estimate of the back stress magnitude.

For the slip vector, $\sin\theta$ would be ${}^{\sqrt{2}}/_{2}$ allowing one to determine the back stress for each increment of dislocation emission associated with hardening beyond about 40% as seen in Figure 4.4. In our case, with uniaxial [001] compression and $\langle 101 \rangle$ slip, Equation 4.12 simplifies to

$$\sigma_{BS} = 17.9 h_0 \left(\epsilon - \epsilon_{confinement}\right) \frac{\left(2w_i - \left(1-\epsilon\right) h_0\right)}{w_i^2} \tag{4.13}$$

where the constant comes from the materials constants for silicon, $\mu = 80\,\text{GPa}$ and $\nu = 0.28$, $\epsilon_{confinement}$ is taken as the onset of hardening, and N_{eff} has been integrated into the equation as the geometrically necessary number of dislocations along $\mathbf{b} = {}^{a}/_{2}\langle 110 \rangle$,.

With this picture of repeated dislocation nucleation in such small cubes, it is clear from the in-situ imaging, Figure 4.8, that severely constrained plastic flow builds up large back stresses that contribute to the total flow stress. For such constrained volumes, it is proposed that the flow stress be given by

$$\sigma_{eff} = \sigma_{flow} - \sigma_{BS} \tag{4.14}$$

This is to be expected as it has been proposed for decades that the appropriate effective stress for dislocation velocities in equations of state should be the applied stress as reduced by a back stress [219, 235, 241–244]. In these constrained volumes

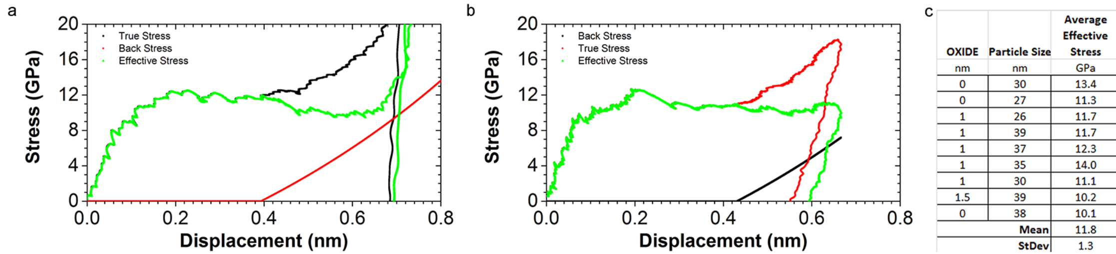

OXIDE	Particle Size	Average Effective Stress
nm	nm	GPa
0	30	13.4
0	27	11.3
1	26	11.7
1	39	11.7
1	37	12.3
1	35	14.0
1	30	11.1
1.5	39	10.2
0	38	10.1
	Mean	11.8
	StDev	1.3

Figure 4.26: True stress versus true strain curves, calculated back stress, and effective stress for (a) a 26 nm and (b) a 37 nm nanocube. (c) Table of mean effective stress for all nanocubes examined. The mean effective stress was found to be 11.8 GPa.

the continued motion of dislocations is limited by the size of the cube and plasticity is controlled by additional dislocation nucleation.

The final result is shown in Figure 4.26 where the compressive or applied stress is P/A, the back stress is Equation 4.12 and the difference is the effective stress as indicated in Equation 4.14. Figure 4.26a,b present the stress versus strain curves for two nanocubes 26 nm and 39 nm in size, respectively. It can be seen that the calculated back stress increases very closely with the resolved hardening, leading to an effective stress that is relatively constant. Examination of nine nanocubes gives a mean effective stress of 11.8 GPa, comparable to the observed flow stress in the nanocrystal described above. The compelling result, at least for initially dislocation free silicon nanocubes, is that the effective stress is nearly constant. Furthermore, this appears to be equal to the upper yield point for the initial dislocation yield as shown in Figure 4.10. This is consistent with previous data on silicon nanopillars in compression where the same stress for initial plasticity was reported for diameters ranging from 250 nm to 500 nm [14, 203]. For these very small volumes under compression it appears then that it may not be the initial yield strength that is length scale dependent but rather the flow stress which is back stress dependent in constrained flow. Additionally, it can be argued that the effective stress is that required for nucleating the next dislocation rather than being one associated with dislocation velocities. Such data will become necessary for appropriate validation of atomistic simulations as the temporal and temperature refinements become a reality [245–248].

4.3.5 Indenter Stability

The small size scale of the Si nanocubes examined here and the even small displacements required to resolve sub-1% strains in these volumes require a mechanical drive system with exceptional stability. Electron microscopes, capable of imaging with atomic resolution, are designed to minimize environmental effects creating vibrations through implementation of air tables, acoustic covers, and damping through mass. Specimen holders are designed so that they are rigid and made out of materials that have low thermal expansion coefficients. The requirements for a nano-manipulation specimen holder such as the PicoIndenter must also accommodate the indenter stage which must be able of macroscopic alignment (about 1 mm) while providing nanoscale precision for alignment to the region of interest. To enable this, the MEMS transducer is attached to a 3-axis piezoelectric crystal for 3-D nanoscale and microscale adjustments which is attached to a rod with macroscopic enabling displacements through a mechanical stage in the holder backend. The macroscopic adjustment and vacuum feedthrough requirements complicate stabilization of this long, narrow indenter assembly. As a result, a significant portion of the indenter shaft is suspended in vacuum beyond the final point of stabilization. The result in an instrument that is incredibly sensitive to acoustic interference which can cause the indenter tip to vibrate at the nanometer scale. While such vibrations have an insignificant effect for tensile testing or bending of long specimens, the vibrations can strongly affect the mechanical data and TEM imaging. Such lateral vibrations, if they were to occur while in contact with a 30 nm crystal, would amount to 10% transverse strain. This strain and the stresses responsible for them are not resolved by the axial load-sensing transducer. Additionally, these vibrations affect *in-situ* imaging of the deformation.

Early compression tests of Si nanospheres [197] and of the Si nanocubes examined here were performed with this few nanometer-amplitude vibration. The resulting force-displacement data exhibited significant load drops and were attributed to pop-in events [197] associated with dislocation bursts in confined volumes [47, 218, 249]. Stabilization of the indenter shaft by pressing it against the wall of the holder near the MEMS transducer was found to stabilize the indenter tip while greatly reducing the tip vibration below that resolvable by the TEM (i.e. below 1 Å, enabling allowing HR-TEM

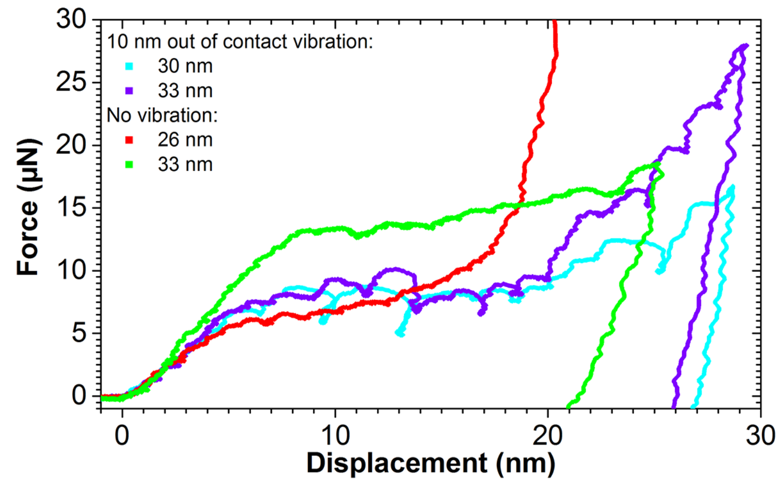

Figure 4.27: A comparison of force versus displacement curves for pillars with small lateral vibration, teal and violet, and after damping of the vibration well below 1 nm, red and green. Regular load-drops in the loading curve which could be mistakenly interpreted as pop-in events from dislocation bursts during stable compression rather than unresolved shear stresses contributing to deformation.

at the tip). The resulting load-displacement data was strikingly different from that obtained by a slightly vibrating tip, Figure 4.27. The Si nanocube compressions with a vibrating tip exhibit numerous load drops in addition to reduced yield strength. Eliminating the lateral vibration produced force-displacement curves that lacked any such load drops as were presented above. With the *in-situ* imaging capabilities the vibrations were discovered and likewise it was found from *in-situ* imaging that the elimination of these lateral vibrations yielded strikingly different results.

Following this observation, an effort was made in collaboration with Hysitron, Inc. to eliminate the nanoscale vibrations without affecting coarse adjustment capabilities. The development of a direct-drive coarse adjustment stage by Hysitron reduced the lateral vibrations from roughly 10 nm amplitude to below 5 nm while also significantly improving the ability to make small coarse adjustments. To reduce lateral vibrations further a polyimide foam having exceptional elasticity, low memory, and good vacuum capability was introduced between the indenter shaft and holder wall. The small pressure exerted on the indenter shaft was found to eliminate the vibrations while allowing coarse adjustment.

4.4 Conclusion

Silicon nanocubes, 20 nm to 65 nm in size and having {100} facets with slight edge/corner truncation were compressed along the [001] direction with a MEMS transducer. Force-displacement data obtained from the transducer were combined with spatial information obtained from *in-situ* TV-rate imaging in the transmission electron microscope. Large elastic strains of 7% were found for all nanocubes in this size range. Flow stresses of 11 GPa at a true strain of 20% were obtained before the strain was accommodated by nucleation of partial dislocations on the {111} slip planes. A size invariance of flow stress, strain, and modulus were observed throughout the size range examined, suggesting that a confinement regime has been attained where the reduction of critical size no longer impacts probability of dislocation nucleation at the surfaces. This is in contrast to tensile and bending tests of Si nanowires which have large surfaces areas compared to the nanocubes. Dislocation embryos, a few nanometers in size, were observed to form at incipient plasticity from which slip bands are emitted at the flow stress. Moiré fringes in the embryo suggest a significant strain gradient between the remaining crystal in projection and the embryo. The embryo structure could not be elucidated due to its small size and proximity to the indenter. It may be possible that hydrostatic forces develop at the compressed surface due to friction stresses, contributing to a β-Sn phase transition. Computational investigations of Si nanospheres with [212] and without [197] confinement found a β-Sn transition and formation of perfect $\langle 110 \rangle$ dislocations, respectively. A hybrid consideration of deconfinement of the nanocrystal walls in addition to friction stresses at the contact surfaces may provide valuable insight.

4.5 Future Directions

Understanding the mechanical response of confined volumes is not limited to intrinsic semiconductors but must be extended to electronically doped crystals. Electronic doping is known to influence plasticity in semiconductors through enhancement or reduction of charged double kink nucleation and mobility through changes in the band structure [241, 250–255]. This effect requires doping comparable to or greater than the intrinsic carrier concentration [256], which for the case of the Si nanocubes studied here is about 10^{-6} per nanocrystal. Investigation of doping effects on dislocation nucleation

is lacking as plasticity is mediated by dislocation mobility for the majority of size and temperature regimes examined. The ability to incorporate dopants into gas-phase synthesized nanocrystals [92, 257] provides an opportunity to study the potential influence of doping on nanoscale plasticity.

Germanium, another important Group IV semiconductor, has been shown to exhibit exceptional changes in electronic properties at a size scale similar to the Si nanocubes examined here [258], resulting from the exciton Bohr radius of 24 nm in Ge compared to 5 nm in silicon [259, 260]. As the effect of mid-gap states and shifting of the Fermi level resulting from electronic doping affect dislocation activity, it is reasonable to expect quantum confinement to also influence plasticity. Ge nanocubes can be synthesized by the same method used here to produce Si nanocubes [261, 262], allowing the mechanical response of a covalent crystal as the size is scaled towards the exciton Bohr radius to be probed. Due to challenges in efficient doping of nanocrystals resulting from self-purification [263] and dopant ionization energy [264], such a study may allow better isolation of band structure effects.

An additional, overarching complication for all *in-situ* testing not considered here is the effect of electron irradiation influencing the ductility in silicon. While few studies account for electron beam effects [18, 35, 265], the significant energy contribution of the electron beam through inelastic scattering events cannot be ignored. This has been studied in the case of plasticity in silica by Zheng *et al* [266] who demonstrated that even moderate electron irradiation provides enough heating, ionization and knock-on damage to allow the bond breaking and rearrangement necessary for plasticity [266,267]. In order to evaluate such an effect on these nanocubes, it is important to perform a complementary analysis without electron beam exposure. This is complicated by the need to carefully align the indenter to the nanocube which is a significant undertaking at this scale even with the electron beam. Successful compressions would not be monitored *in-situ*, making it difficult to determine the quality of uniaxial and uniform compression. Similarly, it will be difficult to convert to an accurate stress versus strain curve. Instead, considering the already well-characterized dependent of stress, and hence load, at yield with respect to nanocube size, it would be possible to compare the load at yield of a nanoparticle characterized prior to compression with and without exposure to the electron beam during compression.

Chapter 5

Changes in electronic structure of strontium titanate under uniaxial compression

5.1 Introduction and Background

Interest in supercapacitors and fast-switching nonvolatile memory has motivated investigation of the ferroelectric properties of the ABO_3 cousins. $BaTiO_3$ an other tetragonal perovskite structures owe their ferroelectric properties to distortion of the oxygen tetrahedra. Many of these materials, such as $SrTiO_3$ (STO), however are of the cubic perovskite structure at room temperature. Recently, it was demonstrated that STO can exhibit room temperature ferroelectricity when grown on a lattice mismatched substrate such as $DyScO_3$ [23], has opened the door to practical device integration and further catalyzing research [268–274].

Bulk STO_3 is in the cubic perovskite phase at room temperature with oxygen positioned at the face center positions, forming an octahedron around the body-centered titanium atom. The strontium atoms are positioned at the cube corners surrounded by four TiO_6 octahedra. Each Sr^{2+} ion is therefore coordinated by 12 O^{2-} ions. $SrTiO_3$ has mixed covalent-ionic character owing to hybridization of the O-2p states with the Ti-3d states while the Sr^{2+} and O^{2-} ions bond have ionic character. The structure

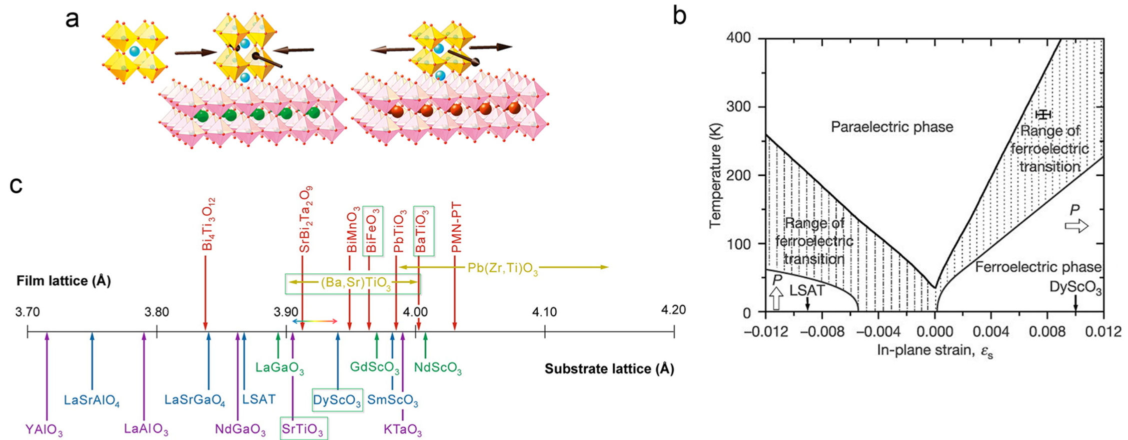

Figure 5.1: (a) Schematic of perovskite structure under biaxial compression and tension. (b) Strain phase diagram of $(001)_p$-oriented $SrTiO_3$. (c) A lattice constant number line of available ferroics and perovskite substrates. Few substrates are available near the R-T ferroelectric transition for $SrTiO_3$, limiting investigation of material properties across the transition. Adapted with permission from Schlom *et al* [21,22] and Haeni *et al* [23].

also has a unique character where the {100} surface can be comprised of TiO_2 or SrO, providing alternating anionic/cationic layers. This property is used heavily to develop well-defined surfaces for heteroepitaxy, however it creates significant issues for nanofabrication as discussed in Section 5.3.

Lattice distortion generated by substrate-induced biaxial strain, depicted in Figure 5.1a, shifts the ferroelectric transition temperature upward. As revealed by the phase diagram in Figure 5.1b, strains of +1% and greater result in room temperature ferroelectricity, with similar results seen in barium titanate [275]. Experimental study of the structure-property relationships as the strain state is controlled by traditional epitaxial growth is limited by the choice of substrates and hence selection of strain, Figure 5.1c [21]. Utilizing our experience in specimen preparation, *in-situ* mechanical testing and STEM imaging and spectroscopy we are working to better understand the ferroelectric transition. By compressing or bending nanopillars of STO fabricated from bulk, the electronic structure can be probed by STEM-EELS based on the Ti $L_{2,3}$ and O K edges. The state of strain can be determined instantaneously by determining instantaneous pillar length via ADF-STEM imaging between EELS acquisitions providing direct and localized information on the dependence of electronic structure on strain.

STO nanopillars must be fabricated with diameters substantially smaller than the inelastic mean free path of the electron in STO (λ =123 nm in order to reduce the effect of plural scattering events complicating interpretation of fine structure in the EEL spectra. Fabrication of STO nanopillars is complicated by the nature of the complex oxide. The alternating anion-cationic layers makes chemical etching impractical. Dry etching of structures with sufficiently small diameter and high aspect ratio is likewise infeasible. The focused ion beam approach used in Chapter 3 and Chapter 4 results in unacceptable amorphization and implantation of the surface, which would add spurious signal to that of the crystalline core. Here I present progress in developing an approach to fabrication that is capable of yielding STO nanopillars with diameters below 50 nm with aspect ratios exceeding 10:1 and having perfect crystalline surfaces. I also present preliminary results on the *in-situ* compression of STO with simultaneous STEM-EELS acquisition.

5.2 EELS fine structure of STO

The fine structure of EELS edges can provide a great deal of information on the local electronic and atomic structure of a material. The EELS edge contains the symmetry-projected partial density of unoccupied states related to the scattering atom, allowing one to probe the local chemical and structural environment of the atom. The titanium $L_{2,3}$ edge at 453 eV, shown in Figure 5.2, is sensitive to short-range coordination, namely its bonding with oxygen in addition to multiplet effects related to interactions between the core and valence band wave functions [276–278]. The Ti $L_{2,3}$ edge is split into four lines. These are transitions from the Ti $2p_{1/2}$ (L_2) and Ti $2p_{3/2}$ (L_3) levels to the narrow unoccupied $3d$ band. A crystal field effect, i.e. Coulomb field, splits these two lines further into t_{2g} and 3_g states [276, 279]. The peak positions, widths, asymmetry, peak ratios, and presence of satellite structures contain information on the bond ordering.

The crystal field splitting is caused by the length of the Ti-O bonds. In the cubic tetragonal phase, the octahedral crystal field splits five-fold degenerate d states in the conduction band are into two-fold degenerate e_g orbitals, directed at the ligands (σ-bonding character), and three-fold degenerate t_2g, directed between them (π-bonding character) [280] and having the higher energy-loss. As the lattice is strained, however,

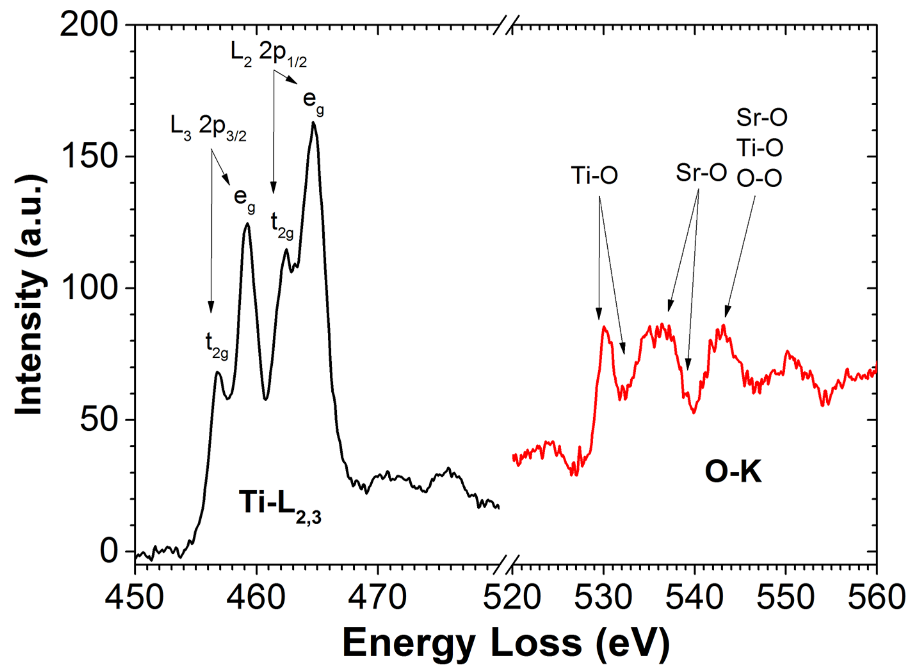

Figure 5.2: EELS spectrum acquired from the pillar in Figure 5.5 prior to compression with dispersion of 0.1 eV channel^{-1}. The Ti $L_{2,3}$ edge at 454 eV consists of the L_3 and L_2 peaks which are each split by the Coulomb field generated by the surrounding O atoms. The O K edge at 527 eV contains information related to bonding of oxygen with neighbor Ti and Sr atoms and is sensitive to bond length and bond angle.

the octahedral coordination of the oxygen is distorted along the c-axis. Compression of Ti-O bonds leads to a stronger crystal field, and hence larger splitting. Distortions from the octahedral symmetry will also increase the e_g:t_{2g} intensity ratio while decreasing their separation.

The field splitting of L_2 can be very small, on the order of 2 eV, requiring an EEL spectrometer with high resolution. The field splitting of L_3 is even smaller, however the relatively narrow peaks and ease of background fitting can provide better precision in measurement [281]. Shifts in the positions of satellite peaks residing approximately 5 eV beyond $L_{2,3}$ result from electron backscattering at neighboring atoms and can provide a more sensitive measure of lattice distortion [282].

The oxygen K edge with 527 eV onset, Figure 5.2, originates from transitions from the O 1s shell to unoccupied 2p states as allowed by the dipole selection rule. Hybridization of the O 2p states with the Sr and Ti 3d states modifies the unoccupied states, resulting in seven peaks in the O K edge The first two peaks are related to transitions to the 3d orbitals of the two nearest-neighbor Ti atoms and have a separation of about 2.4 eV. They are the result of the Coulomb field and are correlated with the Ti t_{2g} and e_g orbitals. The t_{2g}/e_g ratio is large for tight, linear-changed Ti-O-Ti bonds and decreases with distortion [283]. The third and fourth peaks are associated with Sr-O bonding of σ- and π-bonding character. Higher peaks have been ambiguously assigned to O-O bonding, and bonding to various Ti and Sr orbitals [280].

As can be seen, there is a significant amount of detail in each edge that is highly sensitive to the local atomic configuration. By monitoring the EEL spectra as the STO nanopillars are deformed, we hope to observe a transition that can be associated not only with deformation of the lattice but the R-T ferroelectric transition.

5.3 STO nanopillar fabrication

STO nanopillars were prepared by mechanically thinning 2 mm by 2 mm sections of single-side polished 500 µm thick Bulk STO cut by wafer saw and thinned by the wedge polishing method with 2° taper such that the thin edge was approximately 1 µm across. The STO wedge was then fixed to a PicoIndenter chair using M-Bond 610. [001] STO nanopillars were then fabricated along the thin edge of the STO wedge using the FEI Quanta 200 3D FIB in the University of Minnesota Nanofabrication Center. This instrument is currently capable of FIB milling only at 30 keV resulting in imaging resolution of approximately 10 nm and creating a 15 nm amorphous layer with visible damage extending to 30 nm, seen in inset of Figure 5.3a. For a target pillar diameter below 100 nm this process results in amorphization of 30% of the pillar and damage through more than 60% of the diameter.

Each pillar must have a diameter well below 100 nm for optimal STEM-EELS acquisition while having an aspect ratio of approximately 5:1 for mechanical stability. Thinning by FIB milling alone is not feasible in our case as damage must be reduced to minimize its contribution to the core loss signal of interest. This may be controlled by

reducing the ion accelerating voltage and beam current as is possible in state-of-the-art instruments or by subsequent chemical etching.

A post-FIB dip in a weak HF bath has been a common and effective approach to removing the amorphized layers of FIB lamellae and this approach was attempted for the nanopillars. 400 nm to 500 nm FIB pillars were etched in a solution of 30:1 deionized water (DI):10% buffered oxide etch (BOE) for 30 s, Figure 5.3b. While the HF etched the amorphous layer and reduced the pillar diameter, a layer of nanocrystalline material developed on the surface. In an attempt to remove this layer and further reduce pillar diameter, the specimen was etched for an additional 60 s in the BOE solution, Figure 5.3c-f, leading to a significant reduction in pillar diameter while leaving behind the nanocrystalline shell observed in the prior etch. STEM-EDX analysis, Figure 5.3g, revealed the material to be composed of Sr, Ti, Ga, F, C, and O suggesting that it is the solid byproduct of the reaction of HF with the surface while the nanopillar core, Figure 5.3h is comprised of Sr, Ti, and O.

The nanocrystalline layer on the nanopillar surface appears to be a solid precipitate resulting from the insoluble products of the HF reaction with $SrTiO_3$. The use substitution of HF for BOE, not pictured, was found to slightly reduce the amount of insoluble product however the result remained unacceptable. The addition of a small amount of hydrochloric acid, using a solution of 256:6:1 DI:HF:HCl and etch time of was found to completely eliminate formation of insoluble products as seen in the BF-TEM and DF-TEM images in Figure 5.4a,b. The reduction of Sr precipitates can be understood as $Sr(OH)_2$ reacts readily with both HF and HCl, the former creating an insoluble product while the latter forming a readily soluble product. TiO_2, however, is insoluble in both hydrochloric acid and water and reacts only weakly with hydrofluoric acid. Nevertheless, the result has been repeatable, producing pristine crystalline surfaces with atomic steps clearly visible in the high-resolution TEM image in Figure 5.4c.

Care must also be taken to eliminate hydrocarbon contamination as these specimens have been submerged in solvent. Samples not decontaminated prior to insertion into the microscope were found to build up a small layer of carbon on the surface. When etched again, the pillar surface appeared pitted and irregular, presumably due to the carbon shell formed during electron irradiation. A multi-hour bakeout at 125 °C to 150 °C under high vacuum and exposure to ozone plasma were both effective means of

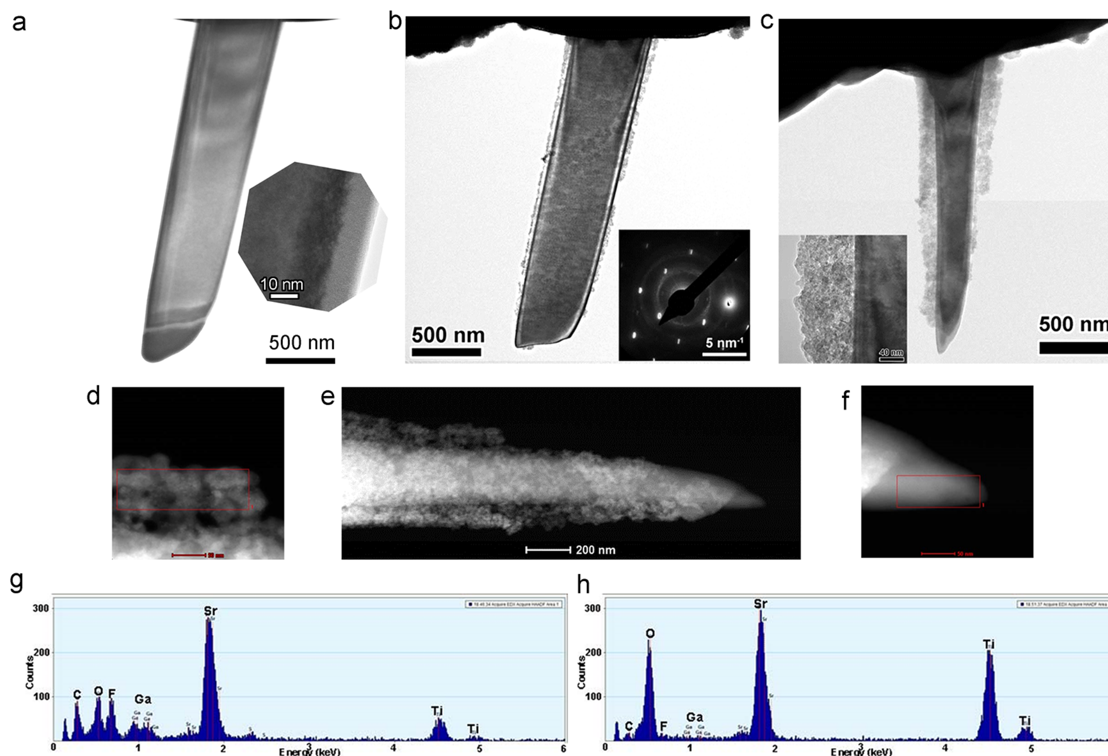

Figure 5.3: (a) As-fabricated nanopillar of STO produced by FIB milling with a 30 keV ion beam and, inset, a higher mangification image of the sidewall revealing a 15 nm amorphous layer and an additional 15 nm damaged layer. (b) The same pillar after etching in 300:1 BOE for 30 s. The amorphous layer has been removed but a nanocrystalline layer has developed. (c) The same pillar following an additional 60 s etch. (d-f) ADF-STEM images and (g,h) correlated STEM-EDX spectra of the nanocrystalline layer and the un-covered core at the tip of the pillar, respectively. The nanocrystalline material appears to be precipitation of insoluble products during etching.

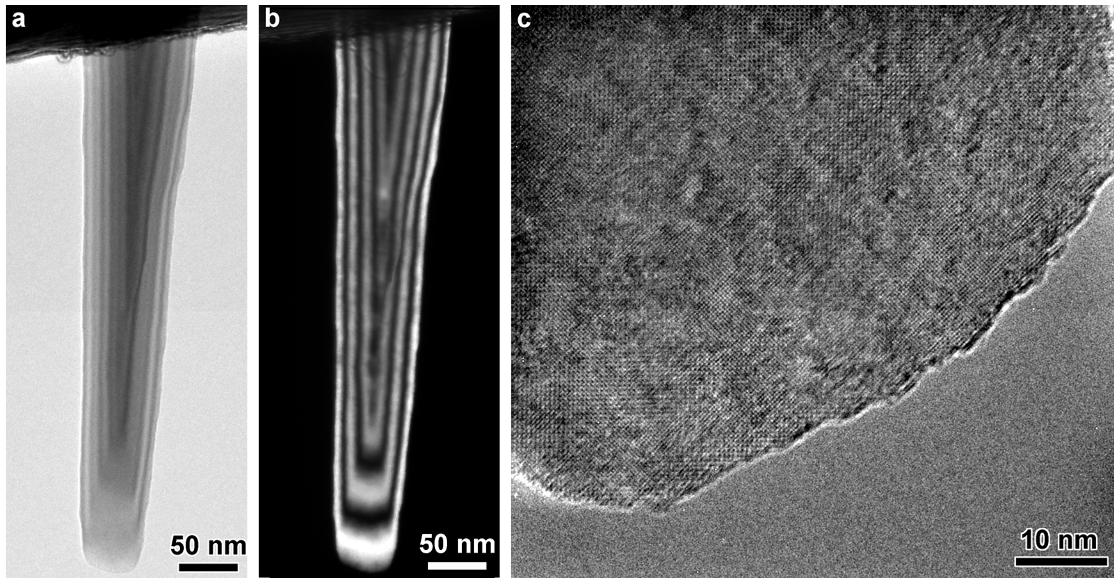

Figure 5.4: (a) BF-TEM and (b) DF-TEM using a g = 200 reflection of a nanopillar etched in a DI:HF:HCl solution. The pillar has well-developed crystalline surfaces and no sign of surface defects. (c) A HR-TEM image of the pillar tip demonstrating a the crystalline surface, composed of many surface steps but free of any apparent amorphous or damaged layer.

removing contamination and should be performed prior to to inspection after etching. The DI:HF:HCl etchant reduced the nanopillar diameter from 540 nm to 345 nm in 90 s with an aspect ratio better than 10:1. Etching of the same pillar for an additional 45 s in a reduction of diameter to 300 nm. The linear etch rate based on the limited data at present suggests an etch rate of $0.5\,\mathrm{nm\,s^{-1}}$ to $1.0\,\mathrm{nm\,s^{-1}}$. Initially etch rate appears higher, as would be expected due to the damaged surface of the pillar. Etch rate would also be expected to increase as diameter is reduced if the etchant preferentially attacks surface steps provided by the increasing surface curvature as the nanopillar diameter is reduced. Understanding the chemical reactions responsible for these results may have valuable implications for producing clean surfaces for epitaxial growth of perovskites. More intriguing for microscopists, this approach allows for the facile formation of relatively large-diameter nanopillars by FIB with high ion voltage and beam current which can be quickly reduced to sub-50 nm dimensions while generating high-quality crystalline surfaces with no evidence of damage. As evidenced here, nanopillars created in

a more than ten year old FIB can rival or beat the outcomes of state of the art, million dollar instruments.

5.4 Combined nanopillar STEM-EELS and compression

Compression of an approximately 500 nm long STO nanopillar having diameter of 50 nm at its tip and 100 nm at its base is demonstrated in Figure 5.5. In (a) the diamond indenter can be seen approaching the nanopillar within a FIB-machined well. In (b) the indenter has been aligned for uniaxial compression along the [001] direction of the pillar. In (c) ADF-STEM and HAADF-STEM images of the nanowire reveal the pillar has a faceted surface and no apparent defects. Upon contact with the indenter, bending contours become apparent in the ADF-STEM image. The Ti $L_{2,3}$ and O K edges were acquired via spectrum imaging with 0.1 eV channel^{-1} dispersion, 3.3 nm pixel size, and five 4 s integrations per pixel were performed stepwise across and then down the nanopillar as the pillar was compressed to a load of 30 µN by the diamond indenter, Figure 5.6. A full-pillar ADF-STEM image was acquired once per minute to account for indenter drift. Spectra were aligned and normalized to the first peak of the Ti $L_{2,3}$ edge, Figure 5.5d, and the local intensity difference relative to the EEL spectrum of the pre-deformed pillar, Figure 5.5, was used to determine the shift in electronic structure with strain. The pillar shown here fractured at an estimated strain below 0.5%, measuring from pillar tip to the apex of bright contrast in HAADF-STEM image of pillar, Figure 5.6 a due to indenter drift and bending.

5.5 Discussion and Future Directions

No clear difference has been resolved in the initial compression experiments, however much has been gained in terms of experimental procedure which will be applied to the research as the project moves forward. Small drift of the indenter tip over the duration of the STEM-EELS acquisition complicates determination of strain state. These early experiments focused on spectrum imaging with the intent of determining local strain along a uniaxially compressed pillar along its tapered length. This has not proven to be practical, however, due to the aforementioned indenter drift and challenge of

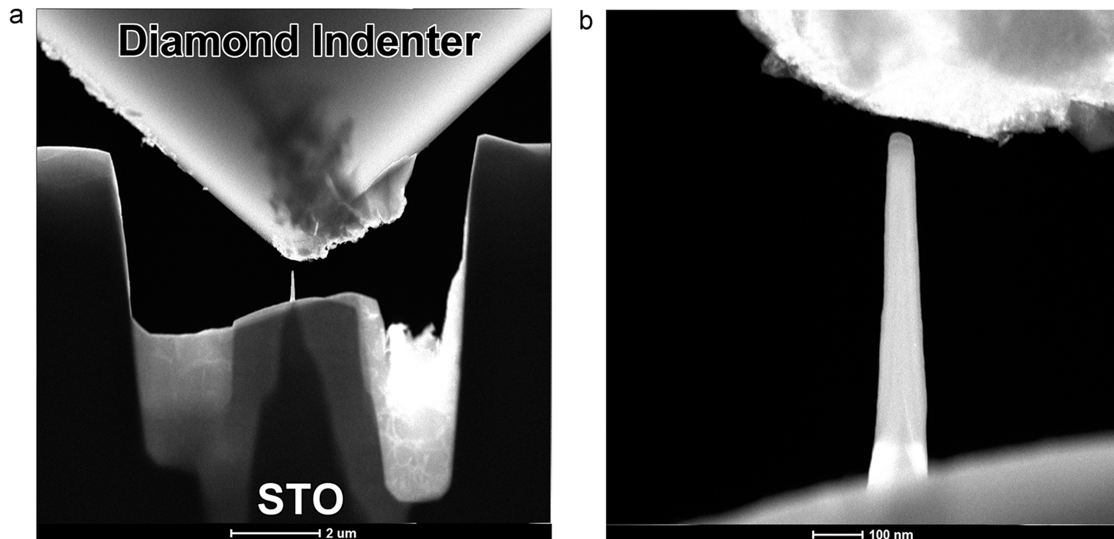

Figure 5.5: (a) Low-magnification ADF-STEM image of the diamond indenter approaching an STO pillar. (b) Higher-magnification image as the indenter is aligned with the pillar.

correcting for drift while performing spectrum imaging. Future experiments should focus on a well-defined region of the crystal under shorter time scales, which should reduce indenter drift and improve determination of strain under the probe. Manual collection of spectra while collecting ADF-STEM images between integrations will provide a rough determination of strain by measurement of pillar compression and allowing for any necessary correction for indenter drift. Upon completion of acquisition, the strain can be increased by applying higher load and repeating the process.

The simplest case for analysis and association with the biaxial strain states found in heteroepitaxial films will be the case of [001]-oriented uniaxial compression. The applied stresses in the [001] direction will result in a tensile strain in the plane normal. As the change in electronic structure has been directly associated with the physical distortion of the lattice [284, 285], these two cases should be analogous. $SrTiO_3$ has a Poisson ratio $\nu = 0.25$. Applying the Poisson relationship for conservation of volume under deformation to a 500 nm pillar, the 0.1% strain sensitivity necessary to probe the R-T FE transition would require a stable compression increment of just 2 nm. As opposed to compression, which is complicated by displacement stability and buckling, nanopillars

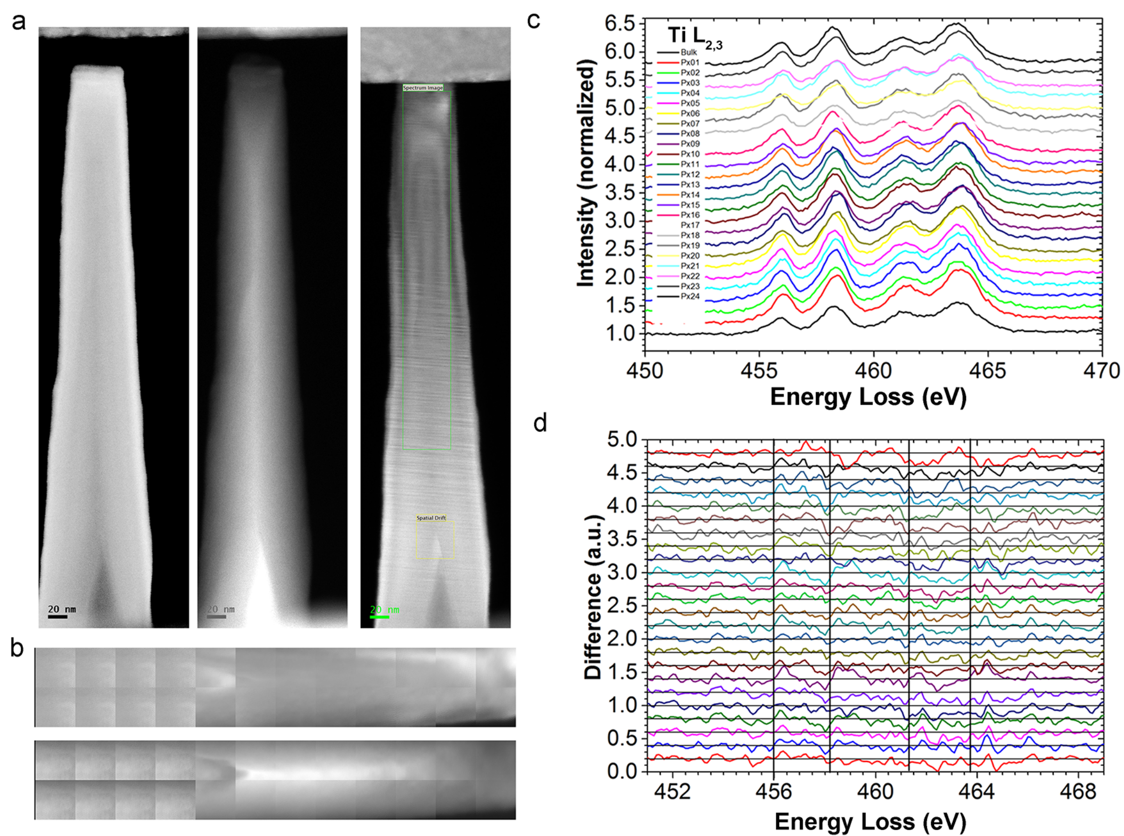

Figure 5.6: (a) ADF- and HAADF-STEM images of the pillar with the faceted surface visible in the HAADF-STEM image and an ADF-STEM image of the compressed nanopillar. (b) ADF/HAADF-STEM scans during spectrum imaging, rotated 90°from orientation in (a). (b) Core-loss spectra of the Ti $L_{2,3}$ edge during compression and (c) difference maps between the local spectrum and a reference spectrum acquired before compression. No clear change of state is seen in this early work.

can instead be bent, inducing a complex strain state with a compressive strain on the internal surface and a tensile strain on the external surface. A nanopillar of substantial enough length would not suffer from such great changes in strain with indenter drift as would a pillar in compression. Additionally, a large and continuous array of stain states could be probed within the same pillar across the diameter and along the length as the pillars are tapered.

Strain determination will be challenging due to limited options for determination. The most sensitive forms of strain measurement - CBED or nanobeam diffraction - are not possible as the insertion and retraction of the camera would affect the extremely vibration sensitive indenter as it is in contact with the nanopillar. HR-STEM may be possible as STO has a comfortably large atomic spacing for imaging in the Tecnai F30, however the PicoIndenter lacks beta tilt for good alignment to zone axes and the indenter will slightly bend the pillar in an unpredictable manner. While not nearly as accurate, measurement of strain using two well-defined points along the pillar, if present, can be used to estimate strain assuming uniaxial compression with no buckling of the pillar. Determination of the strain state will be essential, however, if a change in fine structure in the core-loss spectra are indeed found during nanopillar deformation.

As sample preparation of a challenging material structure has been resolved the next step relies on careful application of experience already gained. While a challenging project, the ability to probe the continuous electronic transition from the paralectric to ferroelectric phases in ABO_3 perovskites may provide powerful insights for strain engineering.

References

[1] Williams, D. & Carter, C. *Transmission electron microscopy: A textbook for materials science* (Springer Verlag, 2009).

[2] Kirkland. Computation of transmission electron micrographs. URL `http://people.ccmr.cornell.edu/~kirkland/`.

[3] Kirkland, E. *Advanced computing in electron microscopy* (Springer, 2010).

[4] Oh, Y., Asif, S. & Warren, O. Micromachined comb drive for quantitative nanoindentation. Google Patents (2012).

[5] Thimsen, E., Johnson, M., Zhang, X., Wagner, A. J., Mkhoyan, K. A., Leighton, C., Kortshagen, U. R. & Aydil, E. S. Nanocrystal networks assembled by aerosol deposition exhibiting high electron mobility without gate bias. *Nature Communications(under review)* (2014).

[6] Zhang, L. *et al.* Disproportionation of (mg,fe)sio3 perovskite in earths deep lower mantle. *Science* **344**, 877–882 (2014).

[7] Bapat, A., Anderson, C., Perrey, C. R., Carter, C. B., Campbell, S. A. & Kortshagen, U. Plasma synthesis of single-crystal silicon nanoparticles for novel electronic device applications. *Plasma Physics and Controlled Fusion* **46**, B97–B109 (2004).

[8] Spinella, C., Lombardo, S. & Priolo, F. Crystal grain nucleation in amorphous silicon. *Journal of Applied Physics* **84**, 5383–5383 (1998).

[9] Williams, J. S. & Elliman, R. G. Role of electronic processes in epitaxial recrystallization of amorphous-semiconductors. *Physical Review Letters* **51**, 1069–1072 (1983).

[10] Drosd, R. & Washburn, J. Some observations on the amorphous to crystalline transformation in silicon. *Journal of Applied Physics* **53**, 397–403 (1982).

[11] Anderson, C. *Enhanced crystallization of amorphous silicon thin films using embedded silicon nanoparticles.* Ph.d., University of Minnesota, Minneapolis (2008).

[12] Trask, J. *Enhanced Crystallization of Amorphous Silicon Thin Films by Nanocrystallite Seeding*. Ph.D. thesis, University of Minnesota (2013).

[13] Lu, S. Z. & Hellawell, A. Growth mechanisms of silicon in al-si alloys. *Journal of Crystal Growth* **73**, 316–328 (1985).

[14] Ostlund, F., Rzepiejewska-Malyska, K., Leifer, K., Hale, L. M., Tang, Y., Ballarini, R., Gerberich, W. W. & Michler, J. Brittle-to-ductile transition in uniaxial compression of silicon pillars at room temperature. *Advanced Functional Materials* **19**, 2439–2444 (2009).

[15] Gerberich, W. *et al.* Superhard silicon nanospheres. *Journal of the Mechanics and Physics of Solids* **51**, 979 – 992 (2003).

[16] Namazu, T., Isono, Y. & Tanaka, T. Evaluation of size effect on mechanical properties of single crystal silicon by nanoscale bending test using afm. *Microelectromechanical Systems, Journal of* **9**, 450–459 (2000).

[17] Tsuchiya, T. *et al.* Cross comparison of thin-film tensile-testing methods examined using single-crystal silicon, polysilicon, nickel, and titanium films. *Microelectromechanical Systems, Journal of* **14**, 1178–1186 (2005).

[18] Zhu, Y., Xu, F., Qin, Q., Fung, W. Y. & Lu, W. Mechanical properties of vapor-liquid-solid synthesized silicon nanowires. *Nano Letters* **9**, 3934–3939 (2009).

[19] Garcia-Manyes, S., Gell, A. G., Gorostiza, P. & Sanz, F. Nanomechanics of silicon surfaces with atomic force microscopy: An insight to the first stages of plastic deformation. *The Journal of Chemical Physics* **123**, – (2005).

[20] Mook, W. M., Nowak, J. D., Perrey, C. R., Carter, C. B., Mukherjee, R., Girshick, S. L., McMurry, P. H. & Gerberich, W. W. Compressive stress effects on nanoparticle modulus and fracture. *Physical Review B* **75**, 214112 (2007).

[21] Schlom, D. G., Chen, L.-Q., Eom, C.-B., Rabe, K. M., Streiffer, S. K. & Triscone, J.-M. Strain tuning of ferroelectric thin films. *Annual Review of Materials Research* **37**, 589–626 (2007).

[22] Schlom, D. G., Chen, L.-Q., Fennie, C. J., Gopalan, V., Muller, D. A., Pan, X., Ramesh, R. & Uecker, R. Elastic strain engineering of ferroic oxides. *MRS Bulletin* **39**, 118–130 (2014).

[23] Haeni, J. H. *et al.* Room-temperature ferroelectricity in strained srtio3. *Nature* **430**, 758–761 (2004).

[24] Watson, H. L. The electron microscope, a personal recollection.

[25] Orowan, E. Zur kristallplastizitt. iii - ber den mechanismus des gleitvorganges. *Zeitschrift fr Physik* **89**, 634–659 (1934).

[26] Taylor, G. I. The mechanism of plastic deformation of crystals. part i. theoretical. *Proceedings of the Royal Society of London. Series A, Containing Papers of a Mathematical and Physical Character* 362–387 (1934).

[27] Polanyi, M. ber eine art gitterstrung, die einen kristall plastisch machen knnte. *Zeitschrift fr Physik* **89**, 660–664 (1934).

[28] Suzuki, H. *Dislocations in solids* (VSP, 1985).

[29] Hirsch, P., Horne, R. & Whelan, M. Direct observations of the arrangement and motion of dislocations in aluminum. *Philosophical Magazine* **1**, 677 (1956).

[30] Bollmann, W. Interference effects in the electron microscopy of thin crystal foils. *Phys. Rev.* **103**, 1588–1589 (1956).

[31] Menter, J. The direct study by electron microscopy of crystal lattices and their imperfections. *Proceedings Of The Royal Society Of London Series A-mathematical And Physical Sciences* **236**, 119 (1956).

[32] Hirsch, P. 50 years of transmission electron microscopy of dislocations: Past, present, and future. *Herald of the Russian Academy of Sciences* **76**, 430–436 (2006).

[33] Wilsdorf, H. A study of dislocations in thin aluminum foils elongated in the electron microscope. In *Symposium on Advances in Electron Microscopy, ASTM STP*, 245, 43 (1958).

[34] Caillard, D. & Martin, J.-L. *Thermally activated mechanisms in crystal plasticity*, vol. 8 (Elsevier, 2003).

[35] Haque, M. & Saif, M. In-situ tensile testing of nano-scale specimens in sem and tem. *Experimental Mechanics* **42**, 123–128 (2002).

[36] Legros, M. In situ mechanical tem: Seeing and measuring under stress with electrons. *Comptes Rendus Physique* **15**, 224 – 240 (2014).

[37] Ross, F. M. Dynamic electron microscopy of semiconductor nanowire and quantum dot growth. Perspectives on Inorganic, Organic, and Biological Crystal Growth: From Fundamentals to Applications, 363–76 (American Insitute of Physics, New York, NY, USA, 2007).

[38] Lee, S., Im, J., Yoo, Y., Bitzek, E., Kiener, D., Richter, G., Kim, B. & Oh, S. H. Reversible cyclic deformation mechanism of gold nanowires by twinningdetwinning transition evidenced from in situ tem. *Nat Commun* **5** (2014).

[39] Kang, W. & Saif, M. T. A. In situ study of size and temperature dependent brittle-to-ductile transition in single crystal silicon. *Advanced Functional Materials* **23**, 713–719 (2013).

[40] Kobler, A., Kashiwar, A., Hahn, H. & Kbel, C. Combination of in situ straining and {ACOM} tem: A novel method for analysis of plastic deformation of nanocrystalline metals. *Ultramicroscopy* **128**, 68 – 81 (2013).

[41] Chisholm, C. *et al.* Dislocation starvation and exhaustion hardening in mo alloy nanofibers. *Acta Materialia* **60**, 2258 – 2264 (2012).

[42] Tang, D.-M. *et al.* Mechanical properties of si nanowires as revealed by in situ transmission electron microscopy and molecular dynamics simulations. *Nano Letters* **12**, 1898–1904 (2012).

[43] Wang, C.-C. *et al.* Sample size matters for al88fe7gd5 metallic glass: Smaller is stronger. *Acta Materialia* **60**, 5370 – 5379 (2012).

[44] Kiener, D. & Minor, A. M. Source truncation and exhaustion: Insights from quantitative in situ tem tensile testing. *Nano Letters* **11**, 3816–3820 (2011).

[45] Cao, Z. H., Liu, P., Meng, X. K., Tang, S. C. & Lu, H. M. In situ transmission electron microscopy observations of the crystallization of amorphous ge films. *Applied Physics a-Materials Science & Processing* **94**, 393–398 (2009).

[46] Oh, S. H., Legros, M., Kiener, D. & Dehm, G. In situ observation of dislocation nucleation and escape in a submicrometre aluminium single crystal. *Nature Materials* **8**, 95–100 (2009).

[47] Shan, Z. W., Li, J., Cheng, Y. Q., Minor, A. M., Syed Asif, S. A., Warren, O. L. & Ma, E. Plastic flow and failure resistance of metallic glass: Insight from in situ compression of nanopillars. *Phys. Rev. B* **77**, 155419 (2008).

[48] Han, X. D., Zheng, K., Zhang, Y. F., Zhang, X. N., Zhang, Z. & Wang, Z. L. Low-temperature in-situ large-strain plasticity of silicon nanowires. *Advanced Materials* **19**, 2112–2118 (2007).

[49] Deneen, J., Mook, W. M., Minor, A., Gerberich, W. W. & Carter, C. B. In situ deformation of silicon nanospheres. *Journal of Materials Science* **41**, 4477–4483 (2006).

[50] Batstone, J. L. Insitu crystallization of amorphous-silicon in the transmission electron-microscope. *Philosophical Magazine a-Physics of Condensed Matter Structure Defects and Mechanical Properties* **67**, 51–72 (1993).

[51] Wacaser, B. A., Dick, K. A., Johansson, J., Borgstrom, M. T., Deppert, K. & Samuelson, L. Preferential interface nucleation: An expansion of the vls growth mechanism for nanowires. *Advanced Materials* **21**, 153–165 (2009).

[52] Wacaser, B. A., Reuter, M. C., Khayyat, M. M., Wen, C.-Y., Haight, R., Guha, S. & Ross, F. M. Growth system, structure, and doping of aluminum-seeded epitaxial silicon nanowires. *Nano Letters* **9**, 3296–3301 (2009).

[53] Levi-Kalisman, Y., Falini, G., Addadi, L. & Weiner, S. Structure of the nacreous organic matrix of a bivalve mollusk shell examined in the hydrated state using cryo-tem. *Journal of Structural Biology* **135**, 8 – 17 (2001).

[54] Won, Y.-Y., Brannan, A. K., Davis, H. T. & Bates, F. S. Cryogenic transmission electron microscopy (cryo-tem) of micelles and vesicles formed in water by poly(ethylene oxide)-based block copolymers. *The Journal of Physical Chemistry B* **106**, 3354–3364 (2002).

[55] Li, Z., Kesselman, E., Talmon, Y., Hillmyer, M. A. & Lodge, T. P. Multicompartment micelles from abc miktoarm stars in water. *Science* **306**, 98–101 (2004).

[56] Ruault, M. O., Ridgway, M. C., Fortuna, F., Bernas, H. & Williams, J. S. Shrinkage mechanism of nanocavities in amorphous si under ion irradiation: An in situ study. *Nuclear Instruments and Methods in Physics Research Section B: Beam Interactions with Materials and Atoms* **206**, 912–915 (2003).

[57] Zhu, X. F., Williams, J. S., Conway, M. J., Ridgway, M. C., Fortuna, F., Ruault, M. O. & Bernas, H. Direct observation of irradiation-induced nanocavity shrinkage in si. *Applied Physics Letters* **79**, 3416–3418 (2001).

[58] Wu, Y. & Yang, P. Direct observation of vaporliquidsolid nanowire growth. *Journal of the American Chemical Society* **123**, 3165–3166 (2001).

[59] Stach, E. A. *et al.* Development of a nanoindenter for in situ transmission electron microscopy. *Microscopy and Microanalysis* **7**, 507–517 (2001).

[60] Evans, J. E., Jungjohann, K. L., Browning, N. D. & Arslan, I. Controlled growth of nanoparticles from solution with in situ liquid transmission electron microscopy. *Nano Letters* **11**, 2809–2813 (2011).

[61] Zheng, H., Claridge, S. A., Minor, A. M., Alivisatos, A. P. & Dahmen, U. Nanocrystal diffusion in a liquid thin film observed by in situ transmission electron microscopy. *Nano Letters* **9**, 2460–2465 (2009).

[62] Jonge, N. d., Peckys, D. B., Kremers, G. J. & Piston, D. W. Electron microscopy of whole cells in liquid with nanometer resolution. *Proceedings of the National Academy of Sciences* **106**, 2159–2164 (2009).

[63] de Jonge, N. & Ross, F. M. Electron microscopy of specimens in liquid. *Nat Nano* **6**, 695–704 (2011).

[64] Reimer, L. & Kohl, H. *Transmission electron microscopy: physics of image formation*, vol. 36 (Springer, 2008).

[65] Fultz, B. & Howe, J. *Transmission electron microscopy and diffractometry of materials* (Springer, 2012, p. 390.).

[66] Maas, A. & Hooijmaijers, H. *Scientific research in World War II: what scientists did in the war* (Routledge, 2009).

[67] Cowley, J. M. & Packard, S. D. Coherent nanodiffraction from phase objects: Carbon nanotubes. *Ultramicroscopy* **63**, 39–47 (1996).

[68] Hillyard, S. *Scanning transmission electron microscopy studies of indium gallium arsenide/gallium arsenide strained quantum wells and wires*. Ph.D. thesis, Cornell University (1996).

[69] Chuvilin, A., Kaiser, U., de Robillard, Q. & Engelmann, H. J. On the origin of holz lines splitting near interfaces: Multislice simulation of cbed patterns. *Journal of Electron Microscopy* **54**, 515–517 (2005).

[70] Rao, D. V. S., McLaughlin, K., Kappers, M. J. & Humphreys, C. J. Lattice distortions in gan on sapphire using the cbed-holz technique. *Ultramicroscopy* **109**, 1250–1255 (2009).

[71] Bch, A., Rouvire, J. L., Clment, L. & Hartmann, J. M. Improved precision in strain measurement using nanobeam electron diffraction. *Applied Physics Letters* **95**, – (2009).

[72] Lu, P. & Gauntt, B. D. Structural mapping of disordered materials by nanobeam diffraction imaging and multivariate statistical analysis. *Microscopy and Microanalysis* **19**, 300–309 (2013).

[73] Shah, A. B., Sivapalan, S. T., DeVetter, B. M., Yang, T. K., Wen, J., Bhargava, R., Murphy, C. J. & Zuo, J.-M. High-index facets in gold nanocrystals elucidated by coherent electron diffraction. *Nano Letters* **13**, 1840–1846 (2013).

[74] Yu, Z. H., Hahn, M. A., Calcines, J., Krauss, T. D. & Silcox, J. Study of the internal structure of individual cdse quantum rods using electron nanodiffraction. *Applied Physics Letters* **86**, 3 (2005).

[75] Thust, A., Coene, W., de Beeck, M. O. & Dyck, D. V. Focal-series reconstruction in hrtem: simulation studies on non-periodic objects. *Ultramicroscopy* **64**, 211 – 230 (1996).

[76] Koch, C. T. A flux-preserving non-linear inline holography reconstruction algorithm for partially coherent electrons. *Ultramicroscopy* **108**, 141 – 150 (2008).

[77] Koch, C. T. Towards full-resolution inline electron holography. *Micron* **63**, 69 – 75 (2014).

[78] Muller, D. A., Nakagawa, N., Ohtomo, A., Grazul, J. L. & Hwang, H. Y. Atomic-scale imaging of nanoengineered oxygen vacancy profiles in srtio3. *Nature* **430**, 657–661 (2004).

[79] Hillyard, S. & Silcox, J. Detector geometry, thermal diffuse-scattering and strain effects in adf stem imaging. *Ultramicroscopy* **58**, 6–17 (1995).

[80] Loane, R. F., Xu, P. & Silcox, J. Incoherent imaging of zone axis crystals with adf stem. *Ultramicroscopy* **40**, 121–138 (1992).

[81] Fitting, L., Thiel, S., Schmehl, A., Mannhart, J. & Muller, D. A. Subtleties in adf imaging and spatially resolved eels: A case study of low-angle twist boundaries in srtio3. *Ultramicroscopy* **106**, 1053–1061 (2006).

[82] Mkhoyan, K. A. *Scanning transmission electron microscopy of iii-v nitrides*. Ph.D. thesis, Cornell University (2004).

[83] Weyland, M. & Muller, D. Tuning the convergence angle for optimum stem performance. *FEI Nanosolutions* **1** (2005).

[84] Voyles, P. M., Muller, D. A., Grazul, J. L., Citrin, P. H. & Gossmann, H. J. L. Atomic-scale imaging of individual dopant atoms and clusters in highly n-type bulk si. *Nature* **416**, 826–829 (2002).

[85] Abe, E., Pennycook, S. J. & Tsai, A. P. Direct observation of a local thermal vibration anomaly in a quasicrystal. *Nature* **421**, 347–350 (2003).

[86] Batson, P. E. Simultaneous stem imaging and electron-energy-loss spectroscopy with atomic-column sensitivity. *Nature* **366**, 727–728 (1993).

[87] Ahn, C. *Transmission electron energy loss spectrometry in materials science and the eels atlas* (Wiley-VCH, 2004), 2 edn.

[88] Dori, L., Bruley, J., Dimaria, D. J., Batson, P. E., Tornello, J. & Arienzo, M. Thin-oxide dual-electron-injector annealing studies using conductivity and electron energy-loss spectroscopy. *Journal of Applied Physics* **69**, 2317–2323 (1991).

[89] Batson, P. E. Carbon 1s near-edge-absorption fine structure in graphite. *Physical Review B* **48**, 2608 (1993).

[90] Egerton, R. *Electron Energy-Loss Spectroscopy in the Electron Microscope* (Springer, 2011).

[91] Brydson, R. *Electron Energy Loss Spectroscopy.* Microscopy handbooks (Bios, 2001).

[92] Rowe, D. J., Jeong, J. S., Mkhoyan, K. A. & Kortshagen, U. R. Phosphorus-doped silicon nanocrystals exhibiting mid-infrared localized surface plasmon resonance. *Nano Letters* **13**, 1317–1322 (2013).

[93] Gresback, R., Kramer, N. J., Ding, Y., Chen, T., Kortshagen, U. R. & Nozaki, T. Controlled doping of silicon nanocrystals investigated by solution-processed field effect transistors. *ACS Nano* **8**, 5650–5656 (2014).

[94] Pi, X. D., Gresback, R., Liptak, R. W., Campbell, S. A. & Kortshagen, U. Doping efficiency, dopant location, and oxidation of si nanocrystals. *Applied Physics Letters* **92**, – (2008).

[95] Erwin, S. C., Zu, L., Haftel, M. I., Efros, A. L., Kennedy, T. A. & Norris, D. J. Doping semiconductor nanocrystals. *Nature* **436**, 91–94 (2005).

[96] Auchterlonie, G., McKenzie, D. & Cockayne, D. Using elnes with parallel eels for differentiating between a-si:x thin films. *Ultramicroscopy* **31**, 217 – 222 (1989).

[97] Batson, P., Kavanagh, K., Wong, C. & Woodall, J. Local bonding and electronic structure obtained from electron energy loss scattering. *Ultramicroscopy* **22**, 89 – 101 (1987).

[98] Batson, Philip Edward. Current trends for eels studies in physics. *Microsc. Microanal. Microstruct.* **2**, 395–402 (1991).

[99] Li, D., Bancroft, G., Kasrai, M., Fleet, M., Feng, X., Tan, K. & Yang, B. High-resolution si k- and l2,3-edge {XANES} of -quartz and stishovite. *Solid State Communications* **87**, 613 – 617 (1993).

[100] Scherzer, O. ber einige fehler von elektronenlinsen. *Zeitschrift fr Physik* **101**, 593–603 (1936).

[101] Scherzer, O. Spharische und chromatische korrektur von elektronen-linsen. *Optik* **2**, 114–132 (1947).

[102] Varela, M., Lupini, A., Benthem, K. v., Borisevich, A., Chisholm, M., Shibata, N., Abe, E. & Pennycook, S. Materials characterization in the aberration-corrected scanning transmission electron microscope. *Annual Review of Materials Research* **35**, 539–569 (2005).

[103] Haider, M., Rose, H., Uhlemann, S., Schwan, E., Kabius, B. & Urban, K. A spherical-aberration-corrected 200 kv transmission electron microscope. *Ultramicroscopy* **75**, 53 – 60 (1998).

[104] Krivanek, O., Dellby, N. & Lupini, A. Towards sub- electron beams. *Ultramicroscopy* **78**, 1 – 11 (1999).

[105] Krivanek, O., Nellist, P., Dellby, N., Murfitt, M. & Szilagyi, Z. Towards sub-0.5a electron beams. *Ultramicroscopy* **96**, 229 – 237 (2003).

[106] Vandenabeele, P. & Maex, K. Emissivity of silicon wafers during rapid thermal processing (1991).

[107] Nulman, J., Antonio, S. & Blonigan, W. Observation of silicon wafer emissivity in rapid thermal processing chambers for pyrometric temperature monitoring. *Applied Physics Letters* **56**, 2513–2515 (1990).

[108] Pigeat, P., Rouxel, D. & Weber, B. Calculation of thermal emissivity for thin films by a direct method. *Phys. Rev. B* **57**, 9293–9300 (1998).

[109] Kiener, D., Zhang, Z., turm, S., Cazottes, S., Imrich, P., Kirchlechner, C. & Dehm, G. Advanced nanomechanics in the tem: effects of thermal annealing on fib prepared cu samples. *Philosophical Magazine* **92**, 3269–3289 (2012).

[110] Shan, Z. W., Mishra, R. K., Syed Asif, S. A., Warren, O. L. & Minor, A. M. Mechanical annealing and source-limited deformation in submicrometre-diameter ni crystals. *Nature Materials* **7**, 115–119 (2008).

[111] Nowak, J., Beaber, A., Ugurlu, O., Girshick, S. & Gerberich, W. Small size strength dependence on dislocation nucleation. *Scripta Materialia* **62**, 819 – 822 (2010).

[112] Tian, L., Cheng, Y.-Q., Shan, Z.-W., Li, J., Wang, C.-C., Han, X.-D., Sun, J. & Ma, E. Approaching the ideal elastic limit of metallic glasses. *Nat Commun* **3**, 609 (2012).

[113] Wang, Y.-B. *et al.* Super deformability and youngs modulus of gaas nanowires. *Advanced Materials* **23**, 1356–1360 (2011).

[114] Chen, B. *et al.* Anelastic behavior in gaas semiconductor nanowires. *Nano Letters* **13**, 3169–3172 (2013).

[115] Voyles, P. M., Grazul, J. L. & Muller, D. A. Imaging individual atoms inside crystals with adf-stem. *Ultramicroscopy* **96**, 251–273 (2003).

[116] Walck, S. D. & McCaffrey, J. P. The small angle cleavage technique applied to coatings and thin films. *Thin Solid Films* **308309**, 399–405 (1997).

[117] Giannuzzi, L. A. & Stevie, F. A. *Introduction to focused ion beams: instrumentation, theory, techniques and practice* (Springer, 2005).

[118] McCaffrey, J., Phaneuf, M. & Madsen, L. Surface damage formation during ion-beam thinning of samples for transmission electron microscopy. *Ultramicroscopy* **87**, 97 – 104 (2001).

[119] Kiener, D., Motz, C., Rester, M., Jenko, M. & Dehm, G. {FIB} damage of cu and possible consequences for miniaturized mechanical tests. *Materials Science and Engineering: A* **459**, 262 – 272 (2007).

[120] Mayer, J., Giannuzzi, L. A., Kamino, T. & Michael, J. Tem sample preparation and fib-induced damage. *MRS Bulletin* **32**, 400–407 (2007).

[121] Bapat, A., Gatti, M., Ding, Y. P., Campbell, S. A. & Kortshagen, U. A plasma process for the synthesis of cubic-shaped silicon nanocrystals for nanoelectronic devices. *Journal of Physics D-Applied Physics* **40**, 2247–2257 (2007).

[122] Hawa, T. & Zachariah, M. R. Understanding the effect of hydrogen surface passivation and etching on the shape of silicon nanocrystal. *Journal of Physical Chemistry C* **112**, 14796–800 (2008).

[123] Sun, Y., Thompson, S. E. & Nishida, T. Physics of strain effects in semiconductors and metal-oxide-semiconductor field-effect transistors. *Journal of Applied Physics* **101**, – (2007).

[124] Dunand, D. C. & Mllner, P. Size effects on magnetic actuation in ni-mn-ga shape-memory alloys. *Advanced Materials* **23**, 216–232 (2011).

[125] Striemer, C. C., Gaborski, T. R., McGrath, J. L. & Fauchet, P. M. Charge- and size-based separation of macromolecules using ultrathin silicon membranes. *Nature* **445**, 749–753 (2007).

[126] Kirihara, A., Uchida, K. I., Kajiwara, Y., Ishida, M., Nakamura, Y., Manako, T., Saitoh, E. & Yorozu, S. Spin-current-driven thermoelectric coating. *Nature Materials* **11**, 686–689 (2012).

[127] Bi, L., Hu, J., Jiang, P., Kim, D. H., Dionne, G. F., Kimerling, L. C. & Ross, C. A. On-chip optical isolation in monolithically integrated non-reciprocal optical resonators. *Nature Photonics* **5**, 758–762 (2011).

[128] Scherrer, B., Heiroth, S., Hafner, R., Martynczuk, J., Bieberle-Htter, A., Rupp, J. L. M. & Gauckler, L. J. Crystallization and microstructure of yttria-stabilized-zirconia thin films deposited by spray pyrolysis. *Advanced Functional Materials* **21**, 3967–3975 (2011).

[129] Miikkulainen, V., Leskel, M., Ritala, M. & Puurunen, R. L. Crystallinity of inorganic films grown by atomic layer deposition: Overview and general trends. *Journal of Applied Physics* **113**, 021301 (2013).

[130] Longo, V., Verheijen, M. A., Roozeboom, F. & Kessels, W. M. M. Crystallization study by transmission electron microscopy of srtio3 thin films prepared by plasma-assisted ald. *ECS Journal of Solid State Science and Technology* **2**, N120–N124 (2013).

[131] Jang, J., Oh, J. Y., Kim, S. K., Choi, Y. J., Yoon, S. Y. & Kim, C. O. Electric-field-enhanced crystallization of amorphous silicon. *Nature* **395**, 481–483 (1998).

[132] Radnoczi, G., Robertsson, A., Hentzell, H. T. G., Gong, S. F. & Hasan, M. A. Al induced crystallization of a-si. *Journal of Applied Physics* **69**, 6394–6399 (1991).

[133] Im, J. S., Kim, H. J. & Thompson, M. O. Phase-transformation mechanisms involved in excimer-laser crystallization of amorphous-silicon films. *Applied Physics Letters* **63**, 1969–1971 (1993).

[134] Shah, A. V., Meier, J., Vallat-Sauvain, E., Wyrsch, N., Kroll, U., Droz, C. & Graf, U. Material and solar cell research in microcrystalline silicon. *Solar Energy Materials and Solar Cells* **78**, 469–491 (2003).

[135] Bertran, E., Sharma, S. N., Viera, G., Costa, J., St'ahel, P. & Cabarrocas, P. R. I. Effect of the nanoparticles on the structure and crystallization of amorphous silicon thin films produced by rf glow discharge. *Journal of Materials Research* **13**, 2476–2479 (1998).

[136] Mattoni, A. & Colombo, L. Crystallization kinetics of mixed amorphous-crystalline nanosystems. *Physical Review B (Condensed Matter and Materials Physics)* **78**, 075408 (2008).

[137] Girshick, S. L. & Chiu, C. P. Kinetic nucleation theory - a new expression for the rate of homogeneous nucleation from an ideal supersaturated vapor. *Journal of Chemical Physics* **93**, 1273–1277 (1990).

[138] Zellama, K., Germain, P., Squelard, S., Bourgoin, J. C. & Thomas, P. A. Crystallization in amorphous-silicon. *Journal of Applied Physics* **50**, 6995–7000 (1979).

[139] Iverson, R. B. & Reif, R. Recrystallization of amorphized polycrystalline silicon films on sio2 - temperature-dependence of the crystallization parameters. *Journal of Applied Physics* **62**, 1675–1681 (1987).

[140] Voutsas, A. T. A new era of crystallization: Advances in polysilicon crystallization and crystal engineering. *Applied Surface Science* **208**, 250–262 (2003).

[141] Street, R. A., Tsai, C. C., Kakalios, J. & Jackson, W. B. Hydrogen diffusion in amorphous-silicon. *Philosophical Magazine B-Physics of Condensed Matter Statistical Mechanics Electronic Optical and Magnetic Properties* **56**, 305–320 (1987).

[142] Mahan, A. H., Roy, B., Reedy, R. C., Readey, D. W. & Ginley, D. S. Rapid thermal annealing of hot wire chemical-vapor-deposited a-si : H films: The effect of the film hydrogen content on the crystallization kinetics, surface morphology, and grain growth. *Journal of Applied Physics* **99** (2006).

[143] Mahan, A. H., Johnson, E. J., Crandall, R. S. & Branz, H. M. Measurement of two deep h bonding levels in device quality glow discharge a-si:h. vol. 377 of *Materials Research Society Symposium - Proceedings*, 413–418 (Materials Research Society, San Francisco, CA, USA, 1995).

[144] Zafar, S. & Schiff, E. A. Spin equilibration in hydrogen depleted amorphous silicon. vol. 137-138 of *J. Non-Cryst. Solids (Netherlands)*, 323–6 (Netherlands, 1991).

[145] Zafar, S. & Schiff, E. A. Hydrogen and defects in amorphous silicon. *Physical Review Letters* **66**, 1493–6 (1991).

[146] Ganguly, G. & Matsuda, A. Defect formation during growth of hydrogenated amorphous-silicon. *Physical Review B* **47**, 3661–3670 (1993).

[147] Beyer, W. Diffusion and evolution of hydrogen in hydrogenated amorphous and microcrystalline silicon. *Solar Energy Materials and Solar Cells* **78**, 235–267 (2003).

[148] Mahan, A. H., Beyer, W., Williamson, D. L., Yang, J. & Guha, S. An explanation for the low-temperature h evolution peak in hydrogenated amorphous silicon films deposited 'on the edge of crystallinity'. *Philosophical Magazine Letters* **80**, 647–652 (2000).

[149] Cabarrocas, P. R., Gay, P. & Hadjadj, A. Experimental evidence for nanoparticle deposition in continuous argon-silane plasmas: Effects of silicon nanoparticles on film properties. *Journal of Vacuum Science & Technology a-Vacuum Surfaces and Films* **14**, 655–659 (1996).

[150] Cabarrocas, P. R. I. Towards high deposition rates of a-si-h - the limiting factors. *Journal of Non-Crystalline Solids* **166**, 37–42 (1993).

[151] Andujar, J. L., Bertran, E., Canillas, A., Campmany, J. & Morenza, J. L. Effect of substrate-temperature on deposition rate of rf plasma-deposited hydrogenated amorphous-silicon thin-films. *Journal of Applied Physics* **69**, 3757–3759 (1991).

[152] Bouchoule, A. *Dusty plasmas: Physics, chemistry, and technological impacts in plasma processing* (John Wiley & Sons Inc, 1999).

[153] Wagner, R. S. On the growth of germanium dendrites. *Acta Metallurgica* **8**, 57–60 (1960).

[154] Gilman, J. J. Direct measurements of the surface energies of crystals. *Journal of Applied Physics* **31**, 2208–2218 (1960).

[155] Chase, B. Fourier-transform raman-spectroscopy. *Analytical Chemistry* **59**, A881–& (1987).

[156] Skoog, D. A., Crouch, S. R. & Holler, F. J. *Principles of instrumental analysis* (Thomson Brooks/Cole, Belmont, CA, 2007).

[157] Ledinsky, M., Vetushka, A., Stuchlik, J., Mates, T., Fejfar, A., Kocka, J. & Stepanek, J. Crystallinity of the mixed phase silicon thin films by raman spectroscopy. *Journal of Non-Crystalline Solids* **354**, 2253–2257 (2008).

[158] Smit, C., Swaaij, R. A. C. M. M. v., Donker, H., Petit, A. M. H. N., Kessels, W. M. M. & Sanden, M. C. M. v. d. Determining the material structure of microcrystalline silicon from raman spectra. *Journal of Applied Physics* **94**, 3582–3588 (2003).

[159] Smith, D. L. *Thin-film deposition: Principles and practice* (McGraw-Hill, New York, New York, 1995).

[160] Smith, R. W. & Srolovitz, D. J. Void formation during film growth: A molecular dynamics simulation study. *Journal of Applied Physics* **79**, 1448–1457 (1996).

[161] Stout, P. J. & Kushner, M. J. Monte carlo simulation of surface kinetics during plasma enhanced chemical vapor deposition of sio2 using oxygen/tetraethoxysilane chemistry. *Journal of Vacuum Science & Technology A: Vacuum, Surfaces, and Films* **11**, 2562–2571 (1993).

[162] Rey, J. C., Cheng, L.-Y., McVittie, J. P. & Saraswat, K. C. Monte carlo low pressure deposition profile simulations. *Journal of Vacuum Science & Technology A: Vacuum, Surfaces, and Films* **9**, 1083–1087 (1991).

[163] Cho, J., Terry, S. G., LeSar, R. & Levi, C. G. A kinetic monte carlo simulation of film growth by physical vapor deposition on rotating substrates. *Materials Science and Engineering: A* **391**, 390–401 (2005).

[164] Hara, S., Izumi, S., Kumagai, T. & Sakai, S. Surface energy, stress and structure of well-relaxed amorphous silicon: A combination approach of ab initio and classical molecular dynamics. *Surface Science* **585**, 17–24 (2005).

[165] Pan, B. C. & Biswas, R. Structure and simulation of hydrogenated nanocrystalline silicon. *Journal of Applied Physics* **96**, 6247–6252 (2004).

[166] Donovan, E. P., Spaepen, F., Turnbull, D., Poate, J. M. & Jacobson, D. C. Heat of crystallization and melting-point of amorphous-silicon. *Applied Physics Letters* **42**, 698–700 (1983).

[167] Nocedal, J. & Wright, S. *Numerical optimization* (Springer, New York, 2006).

[168] Mullins, W. W. Theory of thermal grooving. *Journal of Applied Physics* **28**, 333–339 (1957).

[169] Ouyang, G., Wang, C. X. & Yang, G. W. Surface energy of nanostructural materials with negative curvature and related size effects. *Chemical Reviews* **109**, 4221–4247 (2009).

[170] Sakai, A., Tatsumi, T. & Ishida, K. Growth-kinetics of si hemispherical grains on clean amorphous-si surfaces. *Journal of Vacuum Science & Technology a-Vacuum Surfaces and Films* **11**, 2950–2953 (1993).

[171] Cayron, C., Den Hertog, M., Latu-Romain, L., Mouchet, C., Secouard, C., Rouviere, J. L., Rouviere, E. & Simonato, J. P. Odd electron diffraction patterns in silicon nanowires and silicon thin films explained by microtwins and nanotwins. *Journal of Applied Crystallography* **42**, 242–252 (2009).

[172] Xing, Y. R., Zhang, J. P., Wu, J. A., Liu, C. Z. & Wang, C. H. Phase transition of atomic structures on si(113) surface. *Surface Science* **232**, L215–L218 (1990).

[173] Aoyama, T., Goto, K., Yamazaki, T. & Ito, T. Silicon(001) surface after annealing in hydrogen ambient. *Journal of Vacuum Science & Technology a-Vacuum Surfaces and Films* **14**, 2909–2915 (1996).

[174] Dabrowski, J., Mussig, H. J. & Wolff, G. Atomic structure of clean si(113) surfaces: Theory and experiment. *Physical Review Letters* **73**, 1660–1663 (1994).

[175] Glaeser, A. M. Model studies of rayleigh instabilities via microdesigned interfaces. *Interface Science* **9**, 65–82 (2001).

[176] Wagner, R. S. & Treuting, R. G. Morphology and growth mechanism of silicon ribbons. *Journal of Applied Physics* **32**, 2490–2491 (1961).

[177] Faust Jr, J. W. & John, H. F. The growth of semiconductor crystals from solution using the twin-plane reentrant-edge mechanism. *Journal of Physics and Chemistry of Solids* **25**, 1407–1408 (1964).

[178] Haji, L., Joubert, P., Stoemenos, J. & Economou, N. A. Mode of growth and microstructure of polycrystalline silicon obtained by solid-phase crystallization of an amorphous-silicon film. *Journal of Applied Physics* **75**, 3944–3952 (1994).

[179] Kim, J. H., Lee, J. Y. & Nam, K. S. High-resolution transmission electron microscopy study of solid phase crystallized silicon thin films on sio2: Crystal growth and defects formation. *Journal of Applied Physics* **77**, 95–102 (1995).

[180] Venables, J. A. Atomic processes in crystal growth. *Surface Science* **299300**, 798–817 (1994).

[181] Humphreys, F. J. & Hatherly, M. *Recrystallization and related annealing phenomena* (Elsevier, Oxford, Oxford, 1995).

[182] Li, J., Shan, Z. & Ma, E. Elastic strain engineering for unprecedented materials properties. *MRS Bulletin* **39**, 108–114 (2014).

[183] Bedell, S., Khakifirooz, A. & Sadana, D. Strain scaling for cmos. *MRS Bulletin* **39**, 131–137 (2014).

[184] Htch, M. J. & Minor, A. M. Observing and measuring strain in nanostructures and devices with transmission electron microscopy. *MRS Bulletin* **39**, 138–146 (2014).

[185] Yildiz, B. stretching the energy landscape of oxideseffects on electrocatalysis and diffusion. *MRS Bulletin* **39**, 147–156 (2014).

[186] Yu, D., Feng, J. & Hone, J. Elastically strained nanowires and atomic sheets. *MRS Bulletin* **39**, 157–162 (2014).

[187] Zhu, T. & Li, J. Ultra-strength materials. *Progress in Materials Science* **55**, 710 – 757 (2010).

[188] Hashemi, P., Gomez, L. & Hoyt, J. Gate-all-around n-mosfets with uniaxial tensile strain-induced performance enhancement scalable to sub-10-nm nanowire diameter. *Electron Device Letters, IEEE* **30**, 401–403 (2009).

[189] Pott, V., Pott, V., Moselund, K., Moselund, K., Bouvet, D., De Michielis, L. & Ionescu, A. Fabrication and characterization of gate-all-around silicon nanowires on bulk silicon. *Nanotechnology, IEEE Transactions on* **7**, 733–744 (2008).

[190] Chu, M., Sun, Y., Aghoram, U. & Thompson, S. E. Strain: A solution for higher carrier mobility in nanoscale mosfets. *Annual Review of Materials Research* **39**, 203–229 (2009).

[191] Bhushan, B. & Koinkar, V. N. Nanoindentation hardness measurements using atomic force microscopy. *Applied Physics Letters* **64**, 1653–1655 (1994).

[192] Cordill, M. J. *et al.* Plasticity responses in ultra-small confined cubes and films. *Acta Materialia* **54**, 4515–4523 (2006).

[193] Vepek, S. Electronic and mechanical properties of nanocrystalline composites when approaching molecular size. *Thin Solid Films* **297**, 145 – 153 (1997).

[194] Sørensen, M. R., Brandbyge, M. & Jacobsen, K. W. Mechanical deformation of atomic-scale metallic contacts: Structure and mechanisms. *Phys. Rev. B* **57**, 3283–3294 (1998).

[195] Uchic, M. D., Dimiduk, D. M., Florando, J. N. & Nix, W. D. Sample dimensions influence strength and crystal plasticity. *Science* **305**, 986–989 (2004).

[196] Greer, J. R., Oliver, W. C. & Nix, W. D. Size dependence of mechanical properties of gold at the micron scale in the absence of strain gradients. *Acta Materialia* **53**, 1821 – 1830 (2005).

[197] Chrobak, D., Tymiak, N., Beaber, A., Ugurlu, O., Gerberich, W. W. & Nowak, R. Deconfinement leads to changes in the nanoscale plasticity of silicon. *Nature Nanotechnology* **6**, 480–484 (2011).

[198] Zhang, N. *et al.* Deformation mechanisms in silicon nanoparticles. *Journal of Applied Physics* **109**, – (2011).

[199] Gunol, J., Brochard, S. & Godet, J. Unexpected slip mechanism induced by the reduced dimensions in silicon nanostructures: Atomistic study. *Acta Materialia* **59**, 7464 – 7472 (2011).

[200] Godet, J., Pizzagalli, L., Brochard, S. & Beauchamp, P. Computer study of microtwins forming from surface steps of silicon. *Computational Materials Science* **30**, 16–20 (2004).

[201] Bradby, J. E., Williams, J. S., Wong-Leung, J., Swain, M. V. & Munroe, P. Nanoindentation-induced deformation of ge. *Applied Physics Letters* **80**, 2651–2653 (2002).

[202] Zheng, H. *et al.* Discrete plasticity in sub-10-nm-sized gold crystals. *Nat Communications* **1**, 144 (2010).

[203] Stauffer, D. D., Beaber, A., Wagner, A., Ugurlu, O., Nowak, J., Andre Mkhoyan, K., Girshick, S. & Gerberich, W. Strain-hardening in submicron silicon pillars and spheres. *Acta Materialia* **60**, 2471–2478 (2012).

[204] Minamisawa, R. A., Suess, M. J., Spolenak, R., Faist, J., David, C., Gobrecht, J., Bourdelle, K. K. & Sigg, H. Top-down fabricated silicon nanowires under tensile elastic strain up to 4.5. *Nature Communications* **3**, 1096 (2012).

[205] Zheng, K., Han, X., Wang, L., Zhang, Y., Yue, Y., Qin, Y., Zhang, X. & Zhang, Z. Atomic mechanisms governing the elastic limit and the incipient plasticity of bending si nanowires. *Nano Letters* **9**, 2471–2476 (2009).

[206] Wang, L., Zheng, K., Zhang, Z. & Han, X. Direct atomic-scale imaging about the mechanisms of ultralarge bent straining in si nanowires. *Nano Letters* **11**, 2382–2385 (2011).

[207] Stan, G., Krylyuk, S., Davydov, A. V., Levin, I. & Cook, R. F. Ultimate bending strength of si nanowires. *Nano Letters* **12**, 2599–2604 (2012).

[208] Gordon, M. J., Baron, T., Dhalluin, F., Gentile, P. & Ferret, P. Size effects in mechanical deformation and fracture of cantilevered silicon nanowires. *Nano Letters* **9**, 525–529 (2009).

[209] Hoffmann, S. *et al.* Measurement of the bending strength of vaporliquidsolid grown silicon nanowires. *Nano Letters* **6**, 622–625 (2006).

[210] Gerberich, W. W., Mook, W. M., Cordill, M. J., Carter, C. B., Perrey, C. R., Heberlein, J. V. & Girshick, S. L. Reverse plasticity in single crystal silicon nanospheres. *International Journal of Plasticity* **21**, 2391–2405 (2005).

[211] Pizzagalli, L., Godet, J., Gunol, J., Brochard, S., Holmstrom, E., Nordlund, K. & Albaret, T. A new parametrization of the stillingerweber potential for an improved description of defects and plasticity of silicon. *Journal of Physics: Condensed Matter* **25**, 055801 (2013).

[212] Valentini, P., Gerberich, W. W. & Dumitric, T. Phase-transition plasticity response in uniaxially compressed silicon nanospheres. *Physical Review Letters* **99**, 175701 (2007).

[213] J. Rabier, L. P. & Demenet, J. *Dislocations in Solids*, vol. 16 (Elsevier, 2010).

[214] Wagner, A. J., Anderson, C. M., Trask, J. N., Cui, L., Chov, A., Mkhoyan, K. A. & Kortshagen, U. R. Propagating nanocavity-enhanced rapid crystallization of silicon thin films. *Nano Letters* **13**, 5735–5739 (2013).

[215] Korte, S., Barnard, J. S., Stearn, R. J. & Clegg, W. J. Deformation of silicon - insights from microcompression testing at 25-500 c. *International Journal of Plasticity* **27**, 1853–1866 (2011).

[216] Guénolé, J., Godet, J. & Brochard, S. Plasticity in crystalline-amorphous core-shell si nanowires controlled by native interface defects. *Phys. Rev. B* **87**, 045201 (2013).

[217] Hirth, J. P. & Lothe, J. Theory of dislocations (1982).

[218] Li, J., Van Vliet, K. J., Zhu, T., Yip, S. & Suresh, S. Atomistic mechanisms governing elastic limit and incipient plasticity in crystals. *Nature* **418**, 307–310 (2002).

[219] Van Vliet, K. J., Li, J., Zhu, T., Yip, S. & Suresh, S. Quantifying the early stages of plasticity through nanoscale experiments and simulations. *Phys. Rev. B* **67**, 104105 (2003).

[220] Lee, H. J., Ni, H., Wu, D. T. & Ramirez, A. G. Grain size estimations from the direct measurement of nucleation and growth. *Applied Physics Letters* **87**, 1–3 (2005).

[221] Salehinia, I., Lawrence, S. & Bahr, D. The effect of crystal orientation on the stochastic behavior of dislocation nucleation and multiplication during nanoindentation. *Acta Materialia* **61**, 1421 – 1431 (2013).

[222] Li, J. The mechanics and physics of defect nucleation. *MRS Bulletin* **32**, 151–159 (2007).

[223] Gilman, J. J. Why silicon is hard. *Science* **261**, 1436–1439 (1993).

[224] Callahan, D. L. & Morris, J. C. The extent of phase transformation in silicon hardness indentations. *Journal of Materials Research* **7**, 1614–1617 (1992).

[225] Gridneva, I. V., Milman, Y. V. & Trefilov, V. I. Phase transition in diamond-structure crystals during hardness measurements. *physica status solidi (a)* **14**, 177–182 (1972).

[226] Needs, R. J. & Martin, R. M. Transition from beta-tin to simple hexagonal silicon under pressure. *Physical Review B* **30**, 5390–5392 (1984).

[227] Pharr, G., Oliver, W. & Clarke, D. The mechanical behavior of silicon during small-scale indentation. *Journal of Electronic Materials* **19**, 881–887 (1990).

[228] Domnich, V., Gogotsi, Y. & Dub, S. Effect of phase transformations on the shape of the unloading curve in the nanoindentation of silicon. *Applied Physics Letters* **76**, 2214–2216 (2000).

[229] Pharr, G., Oliver, W. & Harding, D. New evidence for a pressure-induced phase transformation during the indentation of silicon. *Journal of Materials Research* **6**, 1129–1130 (1991).

[230] Chen, M. W., Ma, E., Hemker, K. J., Sheng, H. W., Wang, Y. M. & Cheng, X. M. Deformation twinning in nanocrystalline aluminum. *Science* **300**, 1275–1277 (2003).

[231] Harvey, S., Huang, H., Venkataraman, S. & Gerberich, W. Microscopy and microindentation mechanics of single crystal fe3 wt. indentation. *Journal of Materials Research* **8**, 1291–1299 (1993).

[232] Robach, J. S., Kramer, D. E. & Gerberich, W. W. Determining yield stress via measurement of nanoindentation plastic zone radii. In *Symposium T Fundamentals of Nanoindentation & Nanotribology*, vol. 522 of *MRS Online Proceedings Library* (1998).

[233] Begau, C., Hartmaier, A., George, E. & Pharr, G. Atomistic processes of dislocation generation and plastic deformation during nanoindentation. *Acta Materialia* **59**, 934 – 942 (2011).

[234] Johnson, K. L. & Johnson, K. L. *Contact mechanics* (Cambridge university press, 1987).

[235] Eshelby, J., Frank, F. & Nabarro, F. Xli. the equilibrium of linear arrays of dislocations. *Philosophical Magazine Series 7* **42**, 351–364 (1951).

[236] Weertman, J. Steadystate creep through dislocation climb. *Journal of Applied Physics* **28**, 362–364 (1957).

[237] Hall, E. O. The deformation and ageing of mild steel: Iii discussion of results. *Proceedings of the Physical Society. Section B* **64**, 747 (1951). URL `http://stacks.iop.org/0370-1301/64/i=9/a=303`.

[238] Mott, N. F. The mechanical properties of metals. *Proceedings of the Physical Society. Section B* **64**, 729 (1951).

[239] Li, X., Wei, Y., Lu, L., Lu, K. & Gao, H. Dislocation nucleation governed softening and maximum strength in nano-twinned metals. *Nature* **464**, 877–880 (2010).

[240] Kim, J.-Y. & Greer, J. R. Tensile and compressive behavior of gold and molybdenum single crystals at the nano-scale. *Acta Materialia* **57**, 5245 – 5253 (2009).

[241] Brede, M. & Haasen, P. The brittle-to-ductile transition in doped silicon as a model substance. *Acta Metallurgica* **36**, 2003 – 2018 (1988).

[242] Mitchell, T., Peralta, P. & Hirth, J. Deformation by a kink mechanism in high temperature materials. *Acta Materialia* **47**, 3687 – 3694 (1999).

[243] Pizzagalli, L. & Beauchamp, P. Dislocation motion in silicon: the shuffle-glide controversy revisited. *Philosophical Magazine Letters* **88**, 421–427 (2008).

[244] Demenet, J. L., Rabier, J., Milhet, X., Hong, M. H., Pirouz, P., Stretton, I. & Cordier, P. Microstructures of 4hsic single crystals deformed under very high stresses. *Journal of Physics: Condensed Matter* **14**, 12961 (2002).

[245] Mendelev, M. I., Han, S., Srolovitz, D. J., Ackland, G. J., Sun, D. Y. & Asta, M. Development of new interatomic potentials appropriate for crystalline and liquid iron. *Philosophical Magazine* **83**, 3977–3994 (2003).

[246] Healy, C. J. & Ackland, G. J. Md simulations of compression of nanoscale iron pillars. In *Symposium XX Computational Studies of Phase Stability and Microstructure Evolution*, vol. 1369 of *MRS Online Proceedings Library* (2011).

[247] Hale, L. M., Zhou, X. W., Zimmerman, J. A., Moody, N. R., Ballarini, R. & Gerberich, W. W. Molecular dynamics simulation of delamination of a stiff, body-centered-cubic crystalline film from a compliant si substrate. *Journal of Applied Physics* **106**, – (2009).

[248] Kermode, J. R., Albaret, T., Sherman, D., Bernstein, N., Gumbsch, P., Payne, M. C., Csanyi, G. & De Vita, A. Low-speed fracture instabilities in a brittle crystal. *Nature* **455**, 1224–1227 (2008).

[249] Minor, A. M., Syed Asif, S. A., Shan, Z., Stach, E. A., Cyrankowski, E., Wyrobek, T. J. & Warren, O. L. A new view of the onset of plasticity during the nanoindentation of aluminium. *Nat Mater* **5**, 697–702 (2006).

[250] Patel, J. R. & Chaudhuri, A. R. Charged impurity effects on the deformation of dislocation-free germanium. *Phys. Rev.* **143**, 601–608 (1966). URL `http://link.aps.org/doi/10.1103/PhysRev.143.601`.

[251] John, C. S. The brittle-to-ductile transition in pre-cleaved silicon single crystals. *Philosophical Magazine* **32**, 1193–1212 (1975). URL `http://www.tandfonline.com/doi/abs/10.1080/14786437508228099`. `http://www.tandfonline.com/doi/pdf/10.1080/14786437508228099`.

[252] George, A. & Champier, G. Velocities of screw and 60 dislocations in n- and p-type silicon. *physica status solidi (a)* **53**, 529–540 (1979). URL `http://dx.doi.org/10.1002/pssa.2210530216`.

[253] Samuels, J. & Roberts, S. G. The brittle-ductile transition in silicon. i. experiments. *Proceedings of the Royal Society of London. A. Mathematical and Physical Sciences* **421**, 1–23 (1989). URL `http://rspa.royalsocietypublishing.org/content/421/1860/1.abstract`. `http://rspa.royalsocietypublishing.org/content/421/1860/1.full.pdf+html`.

[254] Alexander, H. & Teichler, H. *Dislocations*, 291–376 (Wiley-VCH Verlag GmbH, 2008). URL `http://dx.doi.org/10.1002/9783527619290.ch6`.

[255] Hirsch, P. B. A mechanism for the effect of doping on dislocation mobility. *J. Phys. Colloques* **40**, C6–117–C6–121 (1979). URL `http://dx.doi.org/10.1051/jphyscol:1979624`.

[256] Patel, J. R., Testardi, L. R. & Freeland, P. E. Electronic effects on dislocation velocities in heavily doped silicon. *Phys. Rev. B* **13**, 3548–3557 (1976). URL http://link.aps.org/doi/10.1103/PhysRevB.13.3548.

[257] Stegner, A. R., Pereira, R. N., Lechner, R., Klein, K., Wiggers, H., Stutzmann, M. & Brandt, M. S. Doping efficiency in freestanding silicon nanocrystals from the gas phase: Phosphorus incorporation and defect-induced compensation. *Phys. Rev. B* **80**, 165326 (2009). URL http://link.aps.org/doi/10.1103/PhysRevB.80.165326.

[258] Wilcoxon, J. P., Provencio, P. P. & Samara, G. A. Synthesis and optical properties of colloidal germanium nanocrystals. *Phys. Rev. B* **64**, 035417 (2001). URL http://link.aps.org/doi/10.1103/PhysRevB.64.035417.

[259] Maeda, Y., Tsukamoto, N., Yazawa, Y., Kanemitsu, Y. & Masumoto, Y. Visible photoluminescence of ge microcrystals embedded in sio2 glassy matrices. *Applied Physics Letters* **59**, 3168–3170 (1991).

[260] Cullis, A. G., Canham, L. T. & Calcott, P. D. J. The structural and luminescence properties of porous silicon. *Journal of Applied Physics* **82**, 909–965 (1997).

[261] Gresback, R., Holman, Z. & Kortshagen, U. Nonthermal plasma synthesis of size-controlled, monodisperse, freestanding germanium nanocrystals. *Applied Physics Letters* **91**, – (2007).

[262] Cernetti, P., Gresback, R., Campbell, S. & Kortshagen, U. Nonthermal plasma synthesis of faceted germanium nanocrystals. *Chemical Vapor Deposition* **13**, 345–350 (2007). URL http://dx.doi.org/10.1002/cvde.200606559.

[263] Norris, D. J., Efros, A. L. & Erwin, S. C. Doped nanocrystals. *Science* **319**, 1776–1779 (2008). URL http://www.sciencemag.org/content/319/5871/1776.abstract. http://www.sciencemag.org/content/319/5871/1776.full.pdf.

[264] Pereira, R. N., Stegner, A. R., Andlauer, T., Klein, K., Wiggers, H., Brandt, M. S. & Stutzmann, M. Dielectric screening versus quantum confinement of phosphorus donors in silicon nanocrystals investigated by magnetic resonance. *Phys. Rev. B* **79**, 161304 (2009). URL http://link.aps.org/doi/10.1103/PhysRevB.79.161304.

[265] Maeda, K. & Takeuchi, S. Chapter 54 enhancement of dislocation mobility in semiconducting crystals by electronic excitation. In Nabarro, F. & Duesbery, M. (eds.) *L12 Ordered Alloys*, vol. 10 of *Dislocations in Solids*, 443 – 504 (Elsevier, 1996). URL http://www.sciencedirect.com/science/article/pii/S157248599680009X.

[266] Zheng, K. *et al.* Electron-beam-assisted superplastic shaping of nanoscale amorphous silica. *Nat Commun* **1**, 24 (2010).

[267] Moore, N. W., Luo, J., Huang, J. Y., Mao, S. X. & Houston, J. E. Superplastic nanowires pulled from the surface of common salt. *Nano Letters* **9**, 2295–2299 (2009).

[268] Shi, Y. *et al.* A ferroelectric-like structural transition in a metal. *Nat Mater* **12**, 1024–1027 (2013).

[269] Garcia, V., Fusil, S., Bouzehouane, K., Enouz-Vedrenne, S., Mathur, N. D., Barthelemy, A. & Bibes, M. Giant tunnel electroresistance for non-destructive readout of ferroelectric states. *Nature* **460**, 81–84 (2009).

[270] Gruverman, A. *et al.* Tunneling electroresistance effect in ferroelectric tunnel junctions at the nanoscale. *Nano Letters* **9**, 3539–3543 (2009).

[271] Loetzsch, R. *et al.* The cubic to tetragonal phase transition in srtio3 single crystals near its surface under internal and external strains. *Applied Physics Letters* **96**, – (2010).

[272] Yuan, C., Ye, S., Xu, B. & Lei, W. Strain induced tetragonal srtio3 nanoparticles at room temperature. *Applied Physics Letters* **101**, – (2012).

[273] Wordenweber, R., Schubert, J., Ehlig, T. & Hollmann, E. Relaxor ferro- and paraelectricity in anisotropically strained srtio3 films. *Journal of Applied Physics* **113**, – (2013).

[274] Wordenweber, R., Hollmann, E., Kutzner, R. & Schubert, J. Induced ferroelectricity in strained epitaxial srtio3 films on various substrates. *Journal of Applied Physics* **102**, – (2007).

[275] Choi, K. J. *et al.* Enhancement of ferroelectricity in strained batio3 thin films. *Science* **306**, 1005–1009 (2004).

[276] Radtke, G. & Botton, G. A. Energy loss near-edge structures. In *Scanning Transmission Electron Microscopy*, 207–245 (Springer, 2011).

[277] de Groot, F. Multiplet effects in x-ray spectroscopy. *Coordination Chemistry Reviews* **249**, 31 – 63 (2005). Synchrotron Radiation in Inorganic and Bioinorganic Chemistry.

[278] Stoyanov, E., Langenhorst, F. & Steinle-Neumann, G. The effect of valence state and site geometry on ti l3,2 and o k electron energy-loss spectra of tixoy phases. *American Mineralogist* **92**, 577–586 (2007).

[279] Leapman, R. D. & Grunes, L. A. Anomalous $\frac{L_3}{L_2}$ white-line ratios in the $3d$ transition metals. *Phys. Rev. Lett.* **45**, 397–401 (1980).

[280] Zhang, Z., Sigle, W. & Rühle, M. Atomic and electronic characterization of the $a[100]$ dislocation core in $srtio_3$. *Phys. Rev. B* **66**, 094108 (2002).

[281] de Groot, F. M. F., Fuggle, J. C., Thole, B. T. & Sawatzky, G. A. 2p x-ray absorption of 3d transition-metal compounds: An atomic multiplet description including the crystal field. *Phys. Rev. B* **42**, 5459–5468 (1990).

[282] Leapman, R. D., Grunes, L. A. & Fejes, P. L. Study of the L_{23} edges in the $3d$ transition metals and their oxides by electron-energy-loss spectroscopy with comparisons to theory. *Phys. Rev. B* **26**, 614–635 (1982).

[283] Brydson, R., Sauer, H., Engel, W. & Hofer, F. Electron energy-loss near-edge structures at the oxygen k edges of titanium(iv) oxygen compounds. *Journal of Physics: Condensed Matter* **4**, 3429 (1992).

[284] Smith, M. B., Page, K., Siegrist, T., Redmond, P. L., Walter, E. C., Seshadri, R., Brus, L. E. & Steigerwald, M. L. Crystal structure and the paraelectric-to-ferroelectric phase transition of nanoscale batio3. *Journal of the American Chemical Society* **130**, 6955–6963 (2008).

[285] Lee, M. K., Nath, T. K., Eom, C. B., Smoak, M. C. & Tsui, F. Strain modification of epitaxial perovskite oxide thin films using structural transitions of ferroelectric batio3 substrate. *Applied Physics Letters* **77**, 3547–3549 (2000).

[286] Cowley, J. M. & Moodie, A. F. The scattering of electrons by atoms and crystals. I. A new theoretical approach. *Acta Crystallographica* **10**, 609–619 (1957).

[287] Loane, R. F., Xu, P. & Silcox, J. Thermal vibrations in convergent-beam electron diffraction. *Acta Crystallographica Section A* **47**, 267–278 (1991). URL `http://dx.doi.org/10.1107/S0108767391000375`.

[288] Gunawan, A. *Inelastic Scattering in STEM for Studying Structural and Electronic Properties of Chalcogenide-Based Semiconductor Nanocrystals.* Ph.D. thesis, University of Minnesota (2013).

Appendix A

Acronyms

- **TEM** – Transmission electron microscope
- **CTEM** – Conventional transmission electron microscope
- **STEM** – Scanning transmission electron microscope
- **EDX** – Energy dispersive X-ray spectroscopy
- **EELS** – Electron energy-loss spectroscopy
- **BF-TEM** – Bright-field TEM
- **DF-TEM** – Dark-field TEM
- **HR-TEM** – High-resolution TEM
- **CBED** – Convergent-beam electron diffraction
- **NBED** – Nanobeam electron diffraction
- **SAD** – Selected-area diffraction
- **SADP** – Selected-area diffraction pattern
- **HOLZ** – High-order Laue Zone
- **ADF-STEM** – Annular dark field STEM
- **HAADF-STEM** – High-angle annular dark field STEM
- **BF-STEM** – Bright-field STEM
- **a-Si:H** – Hydrogenated amorphous silicon
- **C1** – Condenser Lens 3

- **C2** – Condenser Lens 2
- **(S)TEM** – (Scanning) transmission electron microscope
- **FEG** – field emission gun
- **SFEG** – Schottky field emission gun
- C_s – Spherical aberration coefficient
- C_c – Chromatic aberration coefficient
- **CTF** – Contrast transfer function
- **CCD** – Charge-coupled device
- **ZLP** – Zero-loss peak
- **LSPR** – Localized surface plasmon resonance
- **ELNES** – Energy-loss near-edge structure
- **XAS** – X-ray absorption spectroscopy
- **XANES** – X-ray absorption near-edge fine structure
- **EXAFS** – extended X-ray absorption fine structure
- **FTIR** – Fourier transform infrared spectroscopy
- **SPC** – Solid-phase crystallization
- **SPE** – Solid-phase epitaxy
- **PECVD** – Plasma-enhanced chemical vapor deposition
- **HCDF** – Hollow-cone dark field
- **ZAP** – Zone axis pattern
- **JMAK** – Johnson-Mehl-Avrami-Kolmogorov
- **STO** – Strontium titanate ($SrTiO_3$)
- **FE** – Ferroelectric
- **FFT** – Fast Fourier transform

Appendix B

Simulation of screw dislocations and stacking faults

TEM images are strongly affected by aberration of the lenses and multiple (dynamical) scattering of electrons as they pass through the specimen. Conventional TEM images are particularly susceptible to these aberrations, making it impossible to directly interpret an CTEM image as discussed in Section 2.2.4. Comparison of experimental images to simulations that consider specimen structure and instrumental conditions are therefore critical when interpreting the atomic structure of a specimen. The Multislice method offers an efficient approach to simulating CTEM and STEM images and diffraction patterns based on calculation of the electron wave function as the electron beam passes through the specimen.

First developed by Cowley an Moodie [286], the Multislice method calculates the propagation of an incident electron beam or electron probe, described as a two-dimensional quantum mechanical wave packet, through an atomic structure which has been separated into thin slices. As the wave passes through each slice it experiences a local phase shift dependent on the projected atomic potential of all atoms in the slice. The resulting wave function is then propagated through vacuum to the next slice and the procedure is iterated until the electron beam passes through the sample. The exit wavefunction is then propagated through the objective lens, accounting for aberrations such as C_s and Δf which affect the final image. This approach allows the application of the weak phase approximation for thin specimens to be applied iteratively through a thick specimen. While the Multislice algorithm as implemented in most commercial software, e.g. TEMSIM [2], accounts for only elastic scattering, other scattering affects have been implemented over time such as the effects of temperature h based on thermal diffuse scattering due to phonons [287]. A thorough description of the Multislice algorithm and the theoretical underpinnings is presented in the text by Kirkland [3] and is also well-described and is expanded upon in the thesis by Gunawan [288].

The Multislice algorithm utilizes a solution to the non-relativistic 3-D Schrödinger equation for an electron wavefunction ψ and relies on the principle that the wavefunction of the high-energy electron beam can be separated into a part that varies with the electron wavelength and a part that varies slowly along the z-direction which is perturbed by the specimen potential. The electron wave function can then be described as

$$\psi\left(x,y,z\right)=\psi_s\left(x,y,z\right)\exp\frac{2\pi iz}{\lambda}, \tag{B.1}$$

where ψ_s is the slowly varying portion of the wavefunction and λ is the electron wavelength. Inserting this expression into the Schrödinger equation and solving for the slowly-varying portion of the wavefunction ψ_s under the influence of the specimen potential $V\left(x,y,z\right)$, one arrives at

$$\psi_s\left(x,y,z\right)=\exp\int_0^z\left(\frac{i\lambda}{4\pi}\nabla_{xy}^2+i\sigma V\left(x,y,z'\right)\right)dz'\psi_s\left(x,y,0\right), \tag{B.2}$$

where ∇_{xy}^2 is the sum of the second derivative with respect to the x and y directions, σ is the scattering cross-section of the incident electron, λ is the wavelength of the incident electron, and $V\left(x,y,z\right)$ is the specimen potential. Accounting for propagation between slices such that z becomes $z+\Delta z$ and integrating, (B.2) becomes [3]

$$\psi_s\left(x,y,z+\Delta z\right)=\exp\frac{i\lambda}{4\pi}\Delta z\nabla_{xy}^2+i\sigma\nu_{\Delta z}\left(x,y,z\right)\psi_s\left(x,y,z\right), \tag{B.3}$$

where $\nu_{\Delta z}\left(x,y,z\right)=\int_z^{z+\Delta z}V\left(x,y,z'\right)dz'$ is the projected atomic potential.

Taking $t\left(x,y,z\right)=\exp i\sigma\int_z^{z+\Delta z}V\left(x,y,z'\right)dz'$ to be the transmission function and applying the appropriate expansions, (B.3) can be expressed as

$$\psi_s\left(x,y,z+\Delta z\right)=\exp\frac{i\lambda}{4\pi}\Delta z\nabla_{xy}^2 t\left(x,y,z\right)\psi_s\left(x,y,z\right), \tag{B.4}$$

Applying a Fourier transform to (B.4) allows for simplification of the remaining exponential term, ultimately leading to an expression utilized by Multislice as the wave packet passes through the specimen layer-by-layer [3]

$$\psi_{n+1}\left(x,y\right)=p_n\left(x,y,\Delta z_n\right)\otimes\left[t_n\left(x,y\right)\psi_n\left(x,y\right)\right], \tag{B.5}$$

where $p_n\left(x,y,\Delta z_n\right)=\exp\frac{i\lambda}{4\pi}\Delta z\nabla_{xy}^2$ is the propagator function, $\otimes$ represents convolution, and $n=0,1,2,\cdots$ is the slice number in the specimen having thickness Δz_n. This equation represents the resulting wavefunction ψ_{n+1} of an incoming wavefunction ψ_n as it is modified by the potential $\nu_{\Delta z}$ of each slice as represented by the transmission function $t_n\left(x,y\right)$ and propagated through the free space between the slices by $p_n\left(x,y,\Delta z_n\right)$ as a small-angle outgoing wave, i.e. Fresnel diffraction.

The incident wave function is assumed to be a uniform plane wave for CTEM and for STEM is modeled as the sum of plane waves with varying angle of incidence. The CTEM exit wavefunction can then be modeled by a single propagation of the incident wavefunction. Calculation of the final image as projected by the objective lens is described in the next paragraph. A STEM image requires determination of the exit wavefunction for a probe positioned at each point in an image. The 2D-projected potential of the specimen $V(x, y, z)$ is calculated based on linear superposition of the relativistic Hartree-Fock potential for isolated atoms for each atom in the slice.

Objective lens aberrations, such as spherical and defocus, strongly affect the resulting image. These can be accounted for when imaging the transmitted wave function ψ_s through the objective lens as the product of the Fourier transform of the transmitted wave function Ψ_s and the transfer function of the objective lens $H_0(\mathbf{k})$ [3].

$$\Psi_s(\mathbf{k}) = FT[\psi_s(\mathbf{x})]\, \Psi_i(\mathbf{k}) = \Psi_s(\mathbf{k})\, H_0(\mathbf{k}), \tag{B.6}$$

where $\Psi_i(\mathbf{k})$ is the image wavefunction in the back focal plane of the objective lens. The transfer function of the objective lens $H_0(\mathbf{k})$ accounts for spherical aberration C_s, defocus Δf and objective aperture $A(k)$ through the aberration function $\chi(\mathbf{k})$, discussed in Section 2.2.3.

$$\begin{aligned} H_0(\mathbf{k}) &= \exp -i\chi(\mathbf{k}) A(\mathbf{k}) \\ \chi(\mathbf{k}) &= \pi\lambda k^2 \left(0.5 C_s \lambda^2 k^2 - \Delta f\right), \end{aligned} \tag{B.7}$$

where the aperture function $A(\mathbf{k})$ is defined by

$$\begin{aligned} A(\mathbf{k}) &= 1; \lambda k = \alpha < \alpha_{max} \\ &= 0; otherwise, \end{aligned} \tag{B.8}$$

where α_{max} is the maximum semi-angle allowed by the objective aperture.

The final image $g(x)$ is the magnitude squared of image wavefunction transmitted through the objective lens after inverse Fourier transformed back into real space as [3]

$$\psi_i(\mathbf{x}) = FT^{-1}[\Psi_i(\mathbf{k})]\, g(\mathbf{x}) = |\psi_i(\mathbf{x})|^2 = |\psi_s(\mathbf{x}) \otimes h_0(\mathbf{x})|^2, \tag{B.9}$$

where $h_0(\mathbf{x})$ is the complex point spread function of the objective lens, i.e. the inverse Fourier transform of the transfer function of the objective lens $H_0(\mathbf{k})$.

Focal- and thickness- series images are critical when determining the structure of an experimental image. In the case of the nanocubes described here, this is complicated by slight tilt off the crystallographic zone axes, extreme changes in thickness across the nanocube owing to the 90° surfaces when viewed along the $\langle 110 \rangle$ directions, and the likelihood of any dislocations to have a line direction not coincident with the beam direction. As was shown in Section 4.3.3 and is further discussed here, even a thorough

comparison of experimental images with Multislice simulations cannot necessarily provide an exclusive answer. The Multislice modeling is nevertheless a powerful tool in this case to guide interpretation of experimental data.

Multislice simulations of Si nanocubes having screw dislocations and stacking faults and variable rotation about the non-faulted {111} plane are presented here using software the TEMSIM from Kirkland [2]. All simulations are performed using conditions representative of the experimental configuration: an accelerating voltage of 200 keV, C_s of 2.0 mm, coherent incident wave function, α of 10 mrad, Δf between -200 nm and 200 nm and 20 nm defocus step. Side by side through-focal series of screw dislocations and stacking faults between 0° and 4°of tilt can be found in Figure B.1 through Figure B.4. Simulations were performed by Prashant Kumar on crystal structures generated by the author.

The single screw dislocation in Figure B.1 exhibits extended bright-dark contrast normal to the projected line direction while the apparent core structure is dependent on location along the line direction and defocus. Depending on conditions it can appear as a single stacking fault, extended stacking fault or twin while local regions can appear to contain perfect or dissociated 60° dislocations. The stacking fault appears as a single stacking fault whose local phase is dependent on location across the nanocube.

As the nanocube is rotated, the stacking fault develops a broad bright-dark contrast similar to the screw dislocation while the dislocation core appears to dissociate. The changing thickness of the nanocube and the change in relative thickness of the crystal above and below the stacking fault result in a complicated, location-dependent contrast similar to that described for the screw dislocation. Local examination of the structure using a Burgers circuit can lead to an erroneous observation of perfect and dissociated dislocations, extended stacking faults, and twins.

Comparison of the amplitude of the exit wave of the a focal series reconstruction to that of the Multislice simulations reveal contrast similar to the defocused images, Figure 4.20. It is evident that HR-TEM imaging of such a structure cannot objectively isolate perfect or dissociated 60° or screw dislocations which experimentally are likely even more complicated that the ideal structures examined here.

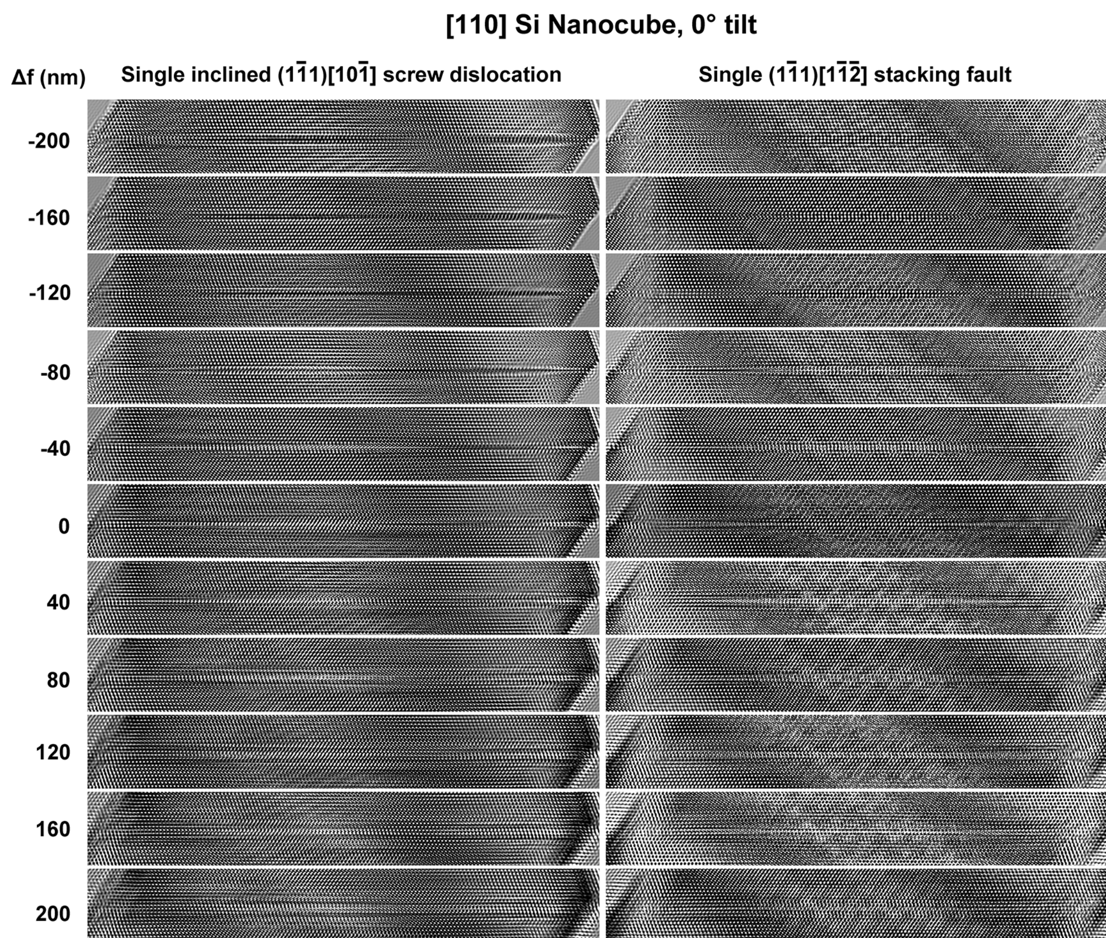

Figure B.1: Multislice through-focal series of screw dislocations and stacking faults in a [110]-oriented 37 nm nanocube having no tilt about the $[1\bar{1}\bar{1}]$ direction.

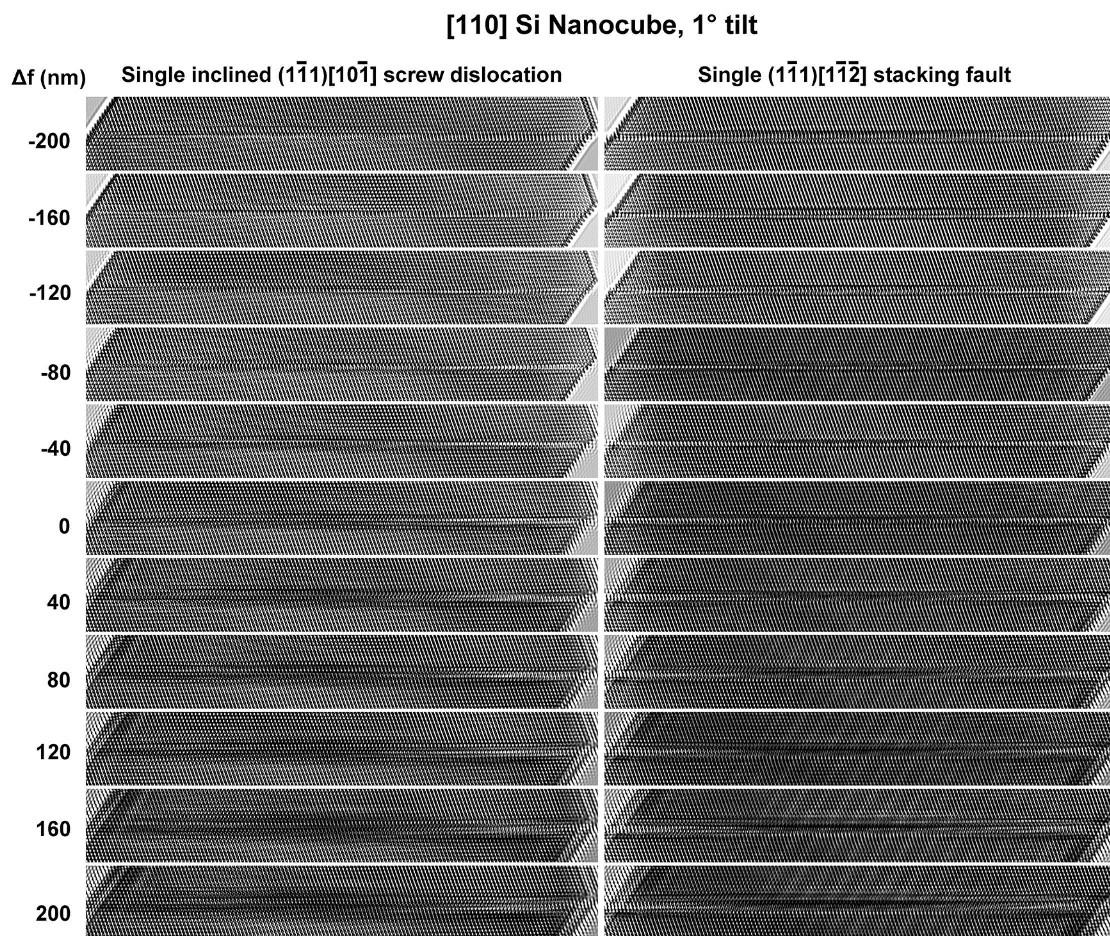

Figure B.2: Multislice through-focal series of screw dislocations and stacking faults in a [110]-oriented 37 nm nanocube having 1° about the [1$\bar{1}\bar{1}$] direction.

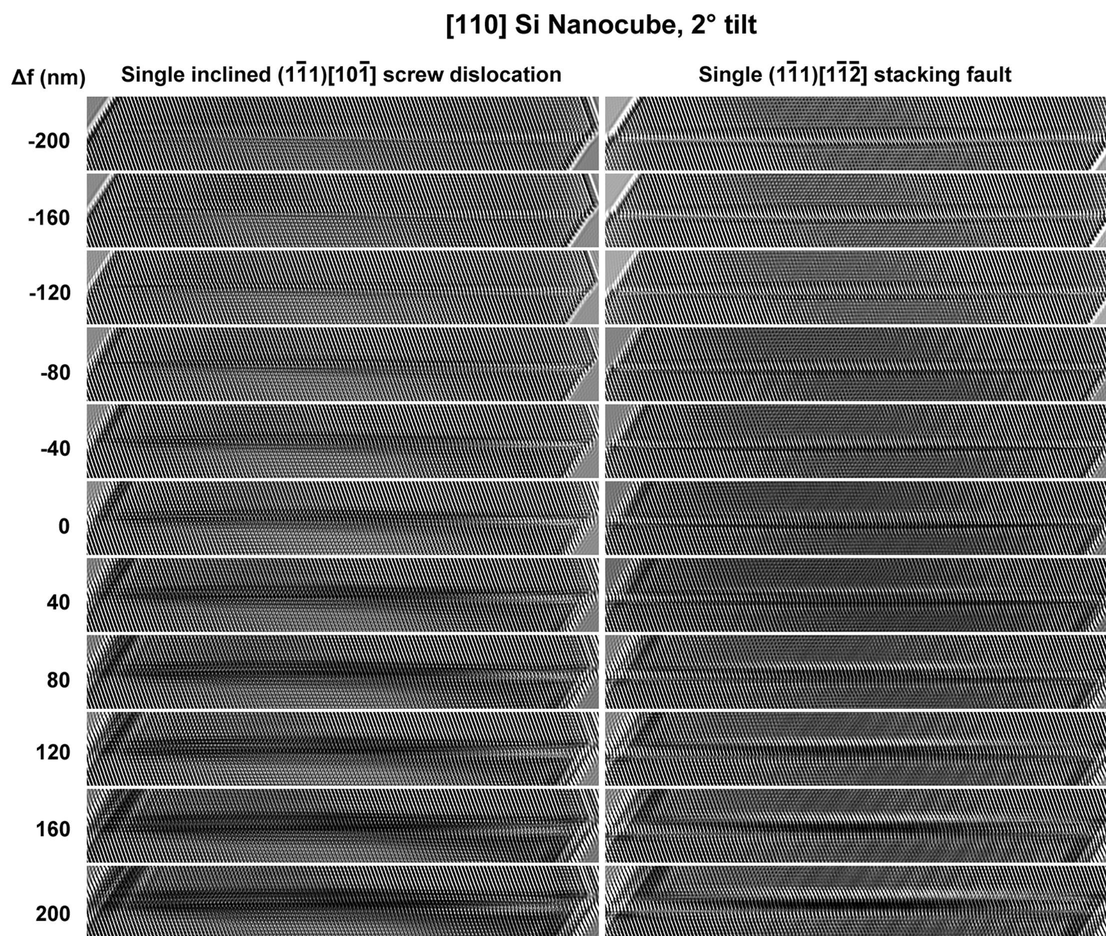

Figure B.3: Multislice through-focal series of screw dislocations and stacking faults in a [110]-oriented 37 nm nanocube having 2° about the [1$\bar{1}\bar{1}$] direction.

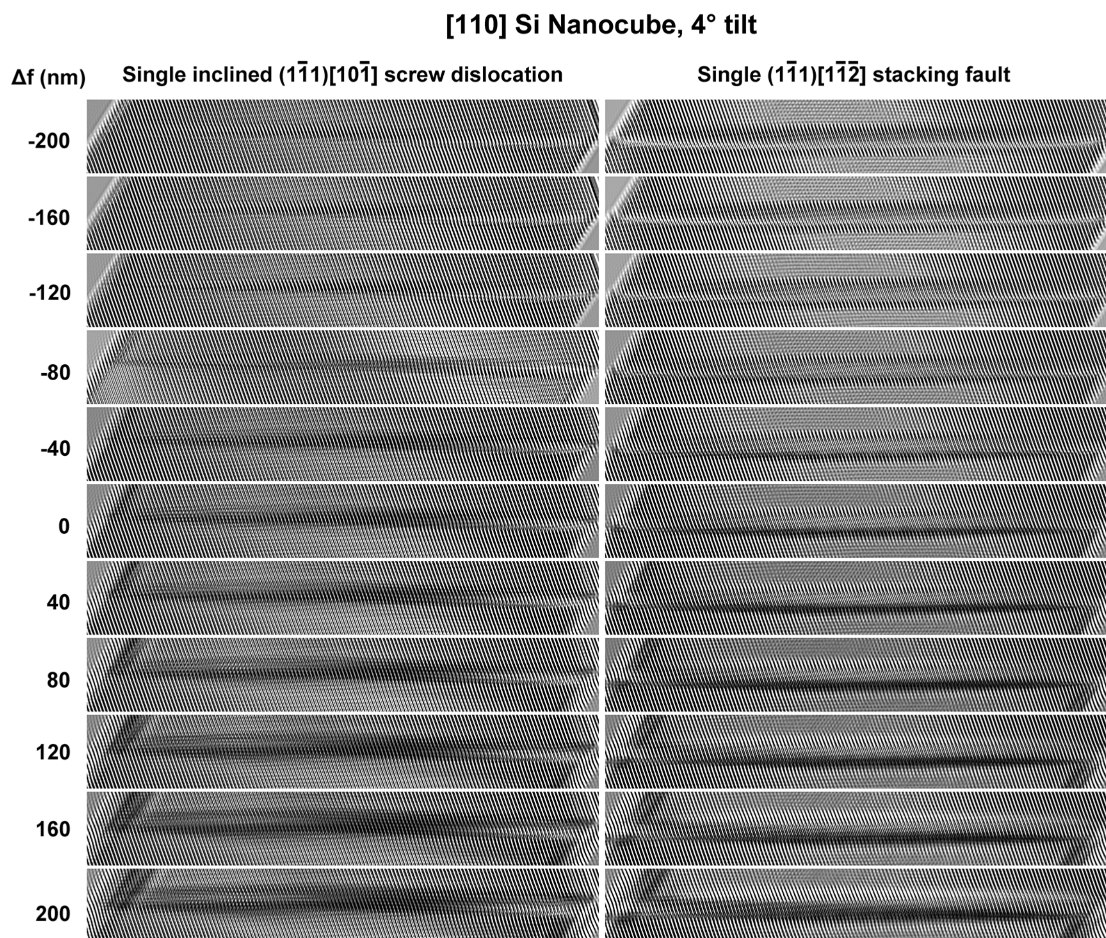

Figure B.4: Multislice through-focal series of screw dislocations and stacking faults in a [110]-oriented 37 nm nanocube having 4° about the $[1\bar{1}\bar{1}]$ direction.